# A study of the build-up region of megavoltage radiation beams

Wamied Abdel-Rahman

Physics Department
McGill University, Montreal
January 2004

A thesis submitted to McGill University in partial fulfillment of the requirements of the degree of Doctor of Philosophy

*Your file Votre référence*
*ISBN: 0-612-98189-4*
*Our file Notre référence*
*ISBN: 0-612-98189-4*

# Abstract

A phantom-embedded extrapolation chamber (PEEC) made of Solid Water™ was used for studying the buildup region of megavoltage radiation beams. We investigated the polarity effect produced in the PEEC and found that radiation induced currents, called the Compton current, were the dominant cause of the polarity effect in the PEEC. In the dose build-up region of megavoltage photon beams, the collecting electrode is the primary Compton current source and the magnitude of the current depends on the measurement depth, field size, and photon beam quality. The connecting cable acts as a secondary Compton current source that produces a very small Compton current which depends on the field size and the photon beam quality, becoming the dominant source when the PEEC is placed at depths greater than the depth of maximum dose. A study of the dose build-up region of megavoltage photon beams showed that the percentage depth ionizations obtained from measurements are higher than the percentage depth doses obtained with Monte Carlo (MC) techniques. To validate the MC-calculated percentage depth doses, the design of the PEEC was incorporated in the simulations. While the MC-calculated and measured percentage depth ionizations in the dose build-up region agreed with one another for the 6 MV, a non-negligible difference is observed for the 18 MV x-ray beam. A number of experiments and theoretical studies of various possible effects which could be the source of this discrepancy is investigated. We show that the contribution of contaminating neutrons and protons to the doses in the 18 MV x-ray beam is negligible. Moreover, the MC calculations using the XCOM photon cross sections database and the NIST bremsstrahlung differential cross sections do not explain the discrepancy between the MC calculations and measurement in the dose build-up region for the 18 MV and this discrepancy is yet to be further investigated.

# Résumé

Une chambre à extrapolation (PEEC), insérée dans un fantôme composé de matériau "Solid Water™", a été utilisée pour étudier la région d'accumulation de dose pour des faisceaux de rayonnements de photon d'énergie de l'ordre des méga volts. Nous avons étudié l'effet de polarité produit dans la PEEC et trouvé que les courants de radiation induits, appelé courants Compton, dominent l'effet de polarité de cette chambre. Dans la région d'accumulation de dose pour les faisceaux de photon l'électrode de collection est la principale source de courants Compton. Ces courants dépendent de la profondeur de la mesure, de la grandeur du champ et de la qualité du faisceau de photon. Le câble connecteur est la deuxième source de courants Compton produisant un très faible courrant Compton qui dépend de la grandeur du champ et de la qualité du faisceau de photon en région d'accumulation de dose. Ce courant devient la source dominante quand la PEEC est placée à des profondeurs plus grandes que la profondeur de dose maximum. Une étude de la région d'accumulation de dose pour les faisceaux de photons démontre que les courbes d'ionisation mesurées sont plus élevées que les courbes de rendement en profondeur obtenues par calculs basés sur les techniques Monte Carlo (MC). Pour effectuer les calculs MC de courbes de rendement en profondeur, le design de la PEEC a été incorporé aux simulations informatiques. Bien que dans la région d'accumulation de dose les courbes d'ionisation en profondeur mesurées et calculées par MC pour les faisceaux d'énergie 6 MV concordent, une différence non négligeable est observée pour les faisceaux d'énergie 18 MV. Plusieurs expériences et études théoriques des effets et causes possibles de cette différence sont présentées. Nous démontrons que la contribution à la dose des neutrons et des protons de contamination pour les faisceaux de 18 MV est négligeable. De plus, les calculs MC utilisant les sections efficaces de collision de photon de la base de données XCOM et les sections efficaces de collision bremsstrahlung de NIST n'expliquent pas les différences entre les calculs MC et les mesures pour la région d'accumulation de dose pour des énergies de 18 MV, lesquelles devront être l'objet d'études ultérieures.

# Original contribution

The thesis deals with relative dosimetry with ionization chambers in the dose build-up region of megavoltage photon beams and contains several experimental and theoretical approaches that represent an original contribution to current knowledge in clinical radiation dosimetry.

We are the first group to incorporate the design of the ionization chamber to validate the Monte Carlo calculated percentage depth doses (*PDD*s) in the dose build-up region of megavoltage photon beams. Our validation approach is based on comparing the MC-calculated and measured percentage depth ionizations (*PDI*s) in a phantom.

We extended to design of the phantom-embedded extrapolation chamber (PEEC), originally designed by Zankowski and later modified by Deblois, and built an aluminized Mylar front widow that can be mounted on the PEEC using two Derlin rings. The aluminized Mylar/Delrin ring allows dose measurements at a depth of 50 μm from the phantom surface.

We found and reported a coding error related to the bremsstrahlung production of positrons in the EGSnrc Monte Carlo (MC) system that may produce erroneous results when optimizing high-energy photon beams.

We have generated a text file called *pgs4pepr_xcom-full.dat* containing the XCOM database photon cross sections which are compiled by Berger, Hubbell, and Seltzer and is used by the PEGS4 user code. The *pgs4pepr_xcom-full.dat* allows MC calculations to be carried out with the XCOM photon cross sections.

We carried out an original experimental study of the polarity effect produced in the PEEC in megavoltage photon and electron beams and found that radiation induced currents, called the Compton current, were the dominant cause of the polarity effect in the PEEC.

To allow a theoretical study of the polarity effect, we developed an original MC user code, called the COMPTON/EGSnrc user code. The COMPTON user code contains a number of modifications to the standard NRC DOSRZnrc/EGSnrc user code. The main

feature of this code is monitoring the charge entering into, and exiting from, a particular region of interest in the radiation beam simulation, in addition to the absorbed dose in all regions.

# Acknowledgments

I would like to express my endless gratitude to my supervisor, Dr. Ervin B. Podgorsak, for his guidance and support throughout the completion of this work. He has always allowed me to work independently while maintaining his open door policy.

I would also like to thank the entire Medical physics staff who have always been eager to help. In particular, I am grateful to Dr. Jan Seuntjens and Dr. Frank Verhaegen for the help in many of the aspects related to the EGSnrc Monte Carlo system code. I would like to thank Robin Van Gils for machining the entrance window of the PEEC used in this project. I would like to acknowledge Pierre Léger, Joe Larkin, and Vlade Bobes who helped with the electronic aspects of the project. I would also like to thank Dr. François Deblois, Dr. Slobodan Devic, Michael Evans, Marina Olivares, William Parker, Horacio Patrocinio, and Dr. Tony Falco for their help and advice in various aspects of the project.

I express endless thanks to my fellow students Kristin Stewart, Emily Heath, Geneviève Jarry, Khalid Al-Yahya, Kamen Paskalev for their support, help, and discussions.

I would like to thank my parents, Dr. Tarig Abdel-Rahman and Zeinab Abdel-Rahim, as well as my beloved wife, Donya Abdel-Ghani, and my son Anmar for their endless love and support.

Finally, I would like to acknowledge the Research Institute of the McGill University Health Center for their financial support during the project.

# *TABLE OF CONTENTS*

# Chapter 1

# INTRODUCTION

## 1.1. INTRODUCTION

Medical physics is a branch of physics involved in the application of physics to medicine. The field marks its beginning with the discovery of x rays and radioactivity by Röntgen in 1895 (ref. 1-4) and Becquerel in 1896 (ref. 5-7), respectively. Since then, medical physics has evolved and branched into several subfields that are essential for the diagnosis and treatment of human disease. Today, the main branches of medical physics are: 1) *radiotherapy physics* which is concerned with treatment of cancer by ionizing radiation; 2) *diagnostic radiology physics* which is concerned with diagnostic imaging with x rays, ultrasound, and nuclear magnetic resonance (NMR); 3) *nuclear medicine physics* which deals with diagnostic imaging and treatment with unsealed radioisotopes; and 4) *health physics* which is concerned with radiation hazards and radiation protection.

Radiotherapy is one of three principal modalities used in treatment of cancer. The other two modalities are surgery and chemotherapy. Cancer treatment with radiotherapy is achieved by the killing of cancer cells using directly or indirectly ionizing radiation. Accurate radiation dose delivery to the prescribed target volume is of utmost importance in radiotherapy, and this is achieved through a long chain of complex procedures that involve equipment commissioning, equipment quality assurance, relative dose data measurements, output determination of clinical radiation beams, treatment planning, and patient setup verification prior to the actual dose delivery.

The radiation dose is delivered such that a precisely defined tumor volume receives a prescribed radiation dose, while the dose to healthy tissues surrounding the tumor volume is minimized. Failure to deliver the prescribed radiation dose to the tumor volume may result in failure to control the malignant disease, while failure to spare the surrounding healthy tissues may result in undesired and serious complications for the patient. Based

on an analysis of dose response data and evaluation of errors in dose delivery in a clinical setting the International Commission on Radiation Units and Measurements (ICRU) recommends an overall accuracy in tumor dose delivery of ±5%. While ±5% sounds like a relatively relaxed requirement, achieving this accuracy considering all parameters of the dose delivery is not a simple task.

### 1.1.1. Sources of clinical radiation beams

Photons and electrons are the most common ionizing radiation types used in radiotherapy. Other more exotic types, such as protons, neutrons, and heavy ions, may also be used, however, the high cost involved in producing such exotic beams limit the use of these modalities to a small number of specialized radiotherapy clinics around the world.

Ionizing radiation is delivered to tumor targets with radiation sources external to the patient (*teletherapy*) or with sealed radioactive sources placed inside the patient (*brachytherapy*). A typical teletherapy treatment machine is shown schematically in FIG. 1.1. The main components of the treatment machine are a *treatment couch patient support assembly* on which the patient is positioned and a *gantry*, both rotating around different axes that intersect at the machine *isocenter* (typically at 100 cm from the radiation source). The gantry holds the treatment head which incorporates a point-like radiation source and additional accessories for producing a collimated radiation beam.

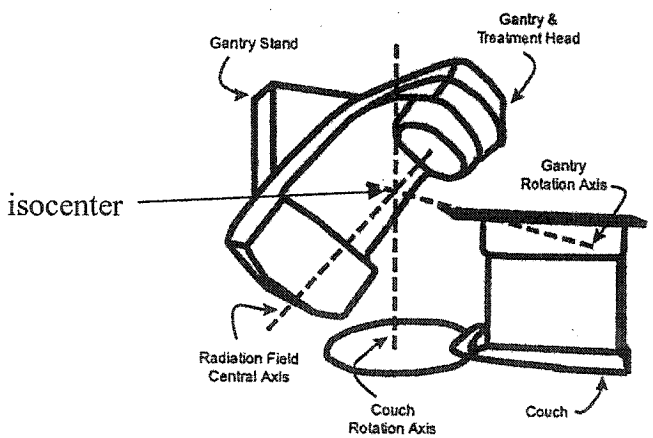


*FIG. 1.1. A schematic representation of a teletherapy machine.*

The sources of ionizing radiation in a teletherapy machine emit either continuous or pulsed radiation. Continuous radiation sources are either radioisotopes (the most common is cobalt-60) or machines producing low energy x rays using a constant potential to accelerate a steady electron current from a cathode (filament) to an anode (target) to produce continuous bremsstrahlung photons. The radiation source in medical linear accelerators (linacs) produces pulsed radiation with the linac's x-ray target bombarded by short bursts (lasting about 2 μs) at a typical pulse repetition frequency of 100 $s^{-1}$ of high energy electrons. Although continuous and pulsed radiations ionize media in the same manner, the response of ionization chambers (the most widely used dosimeters) depends strongly on the radiation source type.

## 1.2. RADIATION DOSIMETRY

Radiation dosimetry is the branch of radiation science that relates specific measurements made with a dosimeter to a determination of the energy deposited in a medium by radiation. Beginning with Röntgen's discovery of x rays in 1895 and continuing through the early 1900s, the basic technique for assessing radiation exposure to humans was to observe the redness (erythema) a given x-ray exposure induced in human skin. This technique was subjective, as well as insensitive, and could only afford crude, imprecise estimations of the radiation dose. In addition, it clearly had to be abandoned with the advent of megavoltage x-ray beams that were valued for their dose skin-sparing properties. Today, a number of physical radiation dosimetric quantities are used to describe radiation beams and are defined below with their commonly used units.

### 1.2.1. Radiation dosimetric quantities and units

#### *Fluence*

The *particle fluence* $\Phi$ for monoenergetic radiation particles having energy $E$ is defined as the quotient $dN$ by $dA$ where $dN$ is the number of particles intersecting a sphere of cross-sectional area $dA$

$$\Phi = \frac{dN}{dA}. \tag{1.1}$$

The common unit of particle fluence is $cm^{-2}$. Because the number of particles incident on the sphere remains the same, the particle fluence is independent of the incidence direction of the particles as shown in FIG.1.2.

The *planar particle fluence* is defined as the number of particles crossing a plane per unit area. Unlike particle fluence, the planar particle fluence has a dependence on the angle of incidence of the particle beam. The planar particle fluence is highest when the incidence of the particles is perpendicular onto the plane and decreases with oblique incidence of the particles.

Most clinical radiation beams are polyenergetic. For such beams, the *particle fluence spectrum* $\Phi_E(E)$ replaces the particle fluence $\Phi$ and is defined as

$$\Phi_E(E) = \frac{d\Phi}{dE}(E). \tag{1.2}$$

### *Energy fluence*

Radiation beams can also be characterized by the *energy fluence* $\Psi$ which is defined for monoenergetic particles as the product of the particle fluence $\Phi$ and the energy of the particles $E$

$$\Psi = \Phi \cdot E = \frac{dN}{dA} \cdot E. \tag{1.3}$$

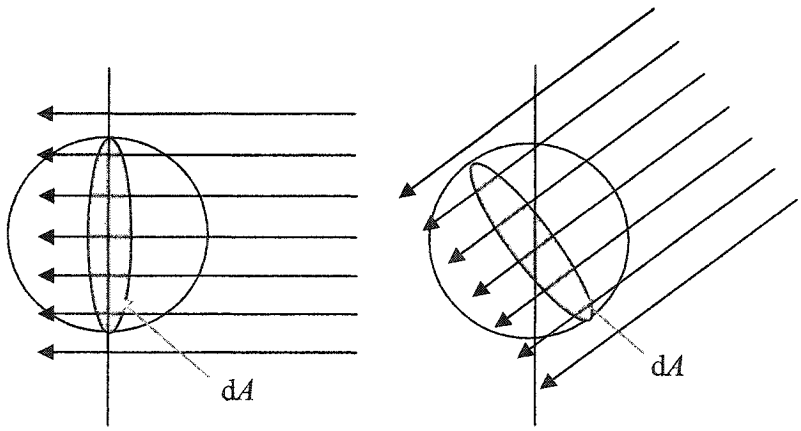


*FIG. 1.2. The definition of particle fluence Φ. The particle fluence is independence of the angle of incidence of the particles.*

Similarly to the particle fluence spectrum $\Phi_E(E)$, the energy fluence spectrum $\Psi_E(E)$ for a polyenergetic beam is given as

$$\Psi_E(E) = \frac{d\Psi}{dE}(E) = \frac{d\Phi}{dE}(E) \times E. \tag{1.4}$$

The fluence spectrum and energy fluence spectrum are generally difficult to measure for clinical external radiation beams and can be determined more easily through Monte Carlo techniques. Neither of the two quantities gives information on physical, chemical, and biological changes in the irradiated target of interest that the particular radiation source induces. Therefore, other dosimetric quantities such as those defined below are often used: *exposure* and *absorbed dose* for clinical applications and *equivalent dose* in health physics and radiation protection.

### Exposure

According to Reports 33 (ref. 8), 51 (ref. 9), and 60 (ref. 10) of the International Commission on Radiological Units and Measurements (ICRU), the exposure is defined as the sum of all charges of one sign $\Delta Q$ produced in air when all the electrons liberated by photons in a mass $\Delta m_{air}$ of air are completely stopped in air. Hence, the exposure $X$ is given by

$$X = \frac{\Delta Q}{\Delta m_{air}}. \tag{1.5}$$

Exposure is defined only for photon beams with energies below 3 MeV and only in air. The unit of exposure is the röntgen R, initially defined as 1 esu·cm$^{-3}$ of charge in air at STP, where STP stands for standard air temperature (273.2 K) and standard air pressure (101.3 kPa). Currently, the röntgen is defined as 1 R = 2.58×10$^{-4}$ C·kg$^{-1}$ air.

### Absorbed dose

The absorbed dose is the primary physical quantity in use today in dosimetry. Unlike exposure, absorbed dose can be defined for all types of ionizing radiation and for any material. The absorbed dose $D$, also called dose, is defined as the energy absorbed $\Delta E_{ab}$ per unit mass $\Delta m$ from any kind of ionizing radiation and in any medium

$$D = \frac{\Delta E_{ab}}{\Delta m}. \tag{1.6}$$

The old unit for the absorbed dose is the rad, defined as 100 erg/g, and the new unit is the gray (Gy) defined as 1 $J \cdot kg^{-1}$, where 1 Gy = 100 rad.

### *Equivalent dose*

It was recognized that a different amount of dose from different radiation types is needed to achieve a particular level of biological damage. Radiation having a high linear energy transfer $L_\infty$, a measure of how energy is transferred from radiation to exposed matter as a function of distance, often causes more damage per unit dose to biological systems. The International Commission on Radiological Protection (ICRP) Publication 60 (ref. 11), National Council on Radiation Protection and Measurements (NCRP) Report 108 (ref. 12), and the ICRU Report 51 (ref. 9) introduced the concept of equivalent dose $H$ for radiation protection purposes. The equivalent dose $H$ takes into account the different biological effectiveness of different kinds of radiation, and is defined as

$$H = w_R \cdot D, \tag{1.7}$$

where $w_R$ is a dimensionless radiation-weighting factor that depends on the radiation type and energy, and $D$ is the absorbed dose in the target. The radiation-weighting factor has been chosen as unity, *i.e.*, $w_R = 1$, for all radiations of low $L_\infty$ including x rays and gamma rays of all energies, as well as electron beams. For other types of radiation, $w_R$ is based on observed biological damage compared to damage by x rays or gamma rays for the same absorbed dose. Since $w_R$ is dimensionless, the SI units for equivalent dose are the same as for absorbed dose. However, to avoid confusion, the unit for equivalent dose has been given the special name Sievert (Sv) in the SI system. The old unit of the equivalent dose in the rem where 1 Sv = 100 rem.

## 1.2.2. Radiation dosimetry data in radiotherapy

In radiotherapy, the quantity of interest to be measured is usually the absorbed dose to medium $D_{med}$, particularly to water or tissue. Because the goal of radiotherapy requires delivering the prescribed dose to the target volume and sparing healthy tissues, many parameters must be considered before the actual treatment is delivered. The parameters

include determining the appropriate type and energy of radiation, the size, shape, and direction of incidence of radiation fields, and the correct dosage. The optimization of all these parameters to achieve a successful treatment is called *treatment planning*.

In treatment planning, 3 dimensional (3-D) dose distributions in the patient, required for plan evaluation, are calculated from superimposing 3-D dose distributions of every field used in the plan. Since a direct measurement of dose distributions in a patient is impossible, computerized treatment planning systems carry out the calculation of the 3-D dose distribution in a patient by relating the dose at every point in the patient to the dose at a reference point, usually taken to be the beam calibration point in a tissue- or water-equivalent phantom.

The link between the dose to a point in a patient and the dose at the reference pointing in phantom is achieved through the use of several dosimetric functions, usually measured in tissue-equivalent phantoms and the use of semi-empirical relationships that account for contour irregularities and tissue inhomogeneities in patients. These dosimetric functions in external radiation beams depend generally on the radiation beam energy and type; the radiation field size $A$; and optional beam modifiers, such as wedges and compensating filters. They also depend on the source-surface of phantom distance $SSD$, the depth $z$ inside the phantom, and on the off-axis distance from the beam central axis. Three of the most important basic dosimetric functions are discussed below, namely, the *relative dose factor*, the *percentage depth dose*, and the *off-axis ratio*. To understand the dependence of these dosimetric functions on various parameters, such as field size, energy, and position in phantom, for clinical external photon beams, it is useful to define first the concepts of primary dose and scattered dose.

### *Primary and scattered dose components*

The photon fluence at any geometrical point in the phantom is a combination of photons emitted from the radiation source, called *primary photons*, and photons produced in the irradiated phantom, called *scattered photons*. In this context, primary photons constitute photons emerging from the treatment head. The scattered photons, on the other hand, are produced in the phantom through one of three means: (*i*) interactions of primary photons

with phantom orbital electrons and atoms, (*ii*) bremsstrahlung x ray production through radiative losses by energetic electrons and positrons, and (*iii*) photons produced when an orbital electron of the medium annihilates a positron, producing one or two annihilation quanta. Consequently, at a given point in phantom the *primary dose component* is defined as the absorbed dose to medium resulting from energetic electrons released by the interactions of primary photons with the phantom, and the *scattered dose component* is defined as the absorbed dose to medium resulting from electrons released by interactions of scattered photons with the phantom.

### *The relative dose factor (RDF)*

The radiation output of clinical external radiation beams is referenced to dose to water at a reference geometrical point $P_{ref}$ on the beam central axis, characterized by ($z_{ref}$, $A_{ref}$, $f$), where $z_{ref}$ is the depth from the phantom surface usually selected at the depth of maximum dose $z_{max}$ along the beam central axis; $A_{ref}$ is the radiation field size on the phantom surface, usually a 10×10 cm$^2$ square field; and $f$ is the source-surface distance *SSD*, typically *SSD* = 100 cm.

In most cases patient treatments are carried out with regular fields other than $A_{ref}$ or irregular fields. Assuming a fixed *SSD*, the relative dose factor (*RDF*) for field size $A$ is defined as the ratio of the dose to point $P$ on the beam central axis characterized by $D_P(z_{max}, A, f, hv)$ to the dose $D_{P_{ref}}(z_{max}, A_{ref}, f, hv)$ at $P_{ref}$

$$RDF(A, hv) = \frac{D_P(z_{max}, A, f, hv)}{D_{P_{ref}}(z_{max}, A_{ref}, f, hv)}. \tag{1.8}$$

Figure 1.3 illustrates the definition of the *RDF*. Typical *RDF* values for cobalt-60 treatment units versus side of square field are plotted in FIG. 1.4. As the figure demonstrates, the *RDF* for photon radiation beams increases with increasing field size $A$ and is normalized to 1.00 for a 10×10 cm$^2$ field.

Because the collimator setting affects both the radiation output from the unit and the amount of dose deposited at $z_{max}$ by photons scattered from the medium, the *RDF* can be decomposed into two independent factors, namely, a collimator factor *CF* that describes the change in the radiation output or the fluence rate of primary photons and depends on

the collimator setting $A_c$, and a phantom scatter factor *SF* which describes the change in the amount of dose at $z_{max}$ deposited by in-phantom scattered photons and depends on the field size $A$ projected on the surface of the medium. Therefore, the *RDF* can be expressed as

$$RDF(A) = CF(A_c) \times SF(A). \tag{1.9}$$

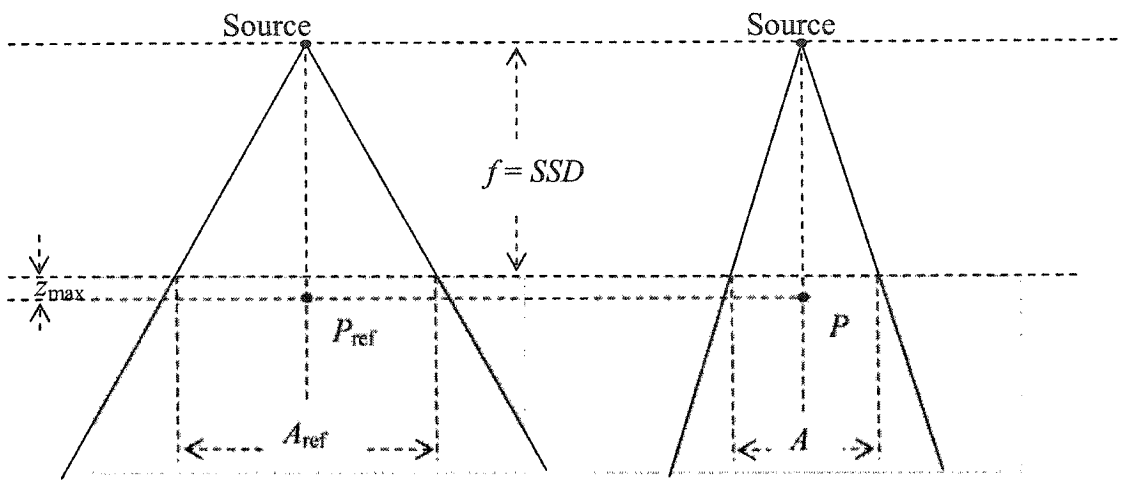


*FIG. 1.3. The definition and geometry for the relative dose factor RDF. Points $P_{ref}$ and P are at $z_{max}$, the source-surface distance is f, and the field sizes $A_{ref}$ and A are defined on the surface of the phantom.*

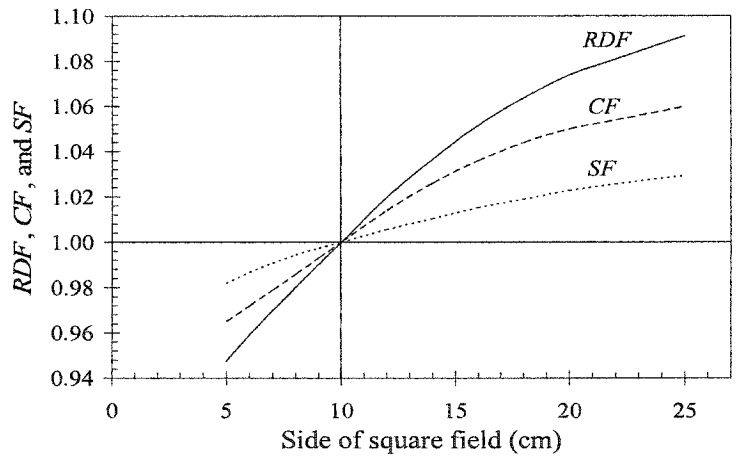


*FIG. 1.4. Typical values for the relative dose factor RDF, the collimator factor CF, and the scatter factor SF plotted as a function of the side of equivalent square fields for a cobalt-60 treatment unit. The RDF is the product of CF and SF. All three functions are normalized to 1 for a reference field of 10×10 $cm^2$.*

### *The percentage depth dose (PDD)*

One of the fundamental clinical dosimetric functions is the percentage depth dose (*PDD*). The definition of *PDD* is illustrated in FIG. 1.5. For a given field size $A$ defined on the surface of the phantom or patient and $SSD = f$, the *PDD*, expressed as a percentage, is the ratio of the dose at an arbitrary depth $z$ on the central axis of the beam to the maximum dose (point $P$ in FIG. 1.1.) also on the beam central axis. Thus, the *PDD* which depends on four parameters: $z$, $A$, $f$, and beam energy $hv$, is defined as follows

$$PDD(z, A, f, hv) = 100 \times \frac{D_Q}{D_P} = 100 \times \frac{\dot{D}_Q}{\dot{D}_P}, \tag{1.10}$$

where $D_Q$ and $\dot{D}_Q$ are the dose and dose rate, respectively, at point $Q$, and $D_P$ and $\dot{D}_P$ are the dose and dose rates, respectively, at point $P$.

Several *PDD* curves for different photon beams are shown in FIG. 1.6. As the figure illustrates, the depth $z_{max}$ at which the dose maximum occurs is a function of the beam energy. For low energy photon beams $z_{max}$ is at the phantom surface, while $z_{max}$ for high energy photon beams occurs deeper inside the phantom, the higher the beam energy the deeper is $z_{max}$ and the lower is the surface dose. The region between the phantom surface and $z_{max}$ is referred to as the *dose build-up region*. The build-up of dose in the superficial layers of patients in high energy photon beams provides skin sparing when target volumes located deep inside the patient are treated.

The build-up region for photon beams is a direct result of build-up in electron fluence in the first layers of the phantom. When a photon beam interacts with the first layers of the phantom, electrons are set in motion and, as they travel in the phantom, they deposit and deliver the dose along the path they follow. For low energy photon beams, these electrons do not possess enough energy to travel far from where they were originally set in motion and thus they deposit their energy locally. High energy photon beams, on the other hand, produce high energy electrons that can penetrate to deeper depths in the phantom and, as a result, a gradual build-up of electrons occurs with depth until electronic equilibrium is established close to $z_{max}$.

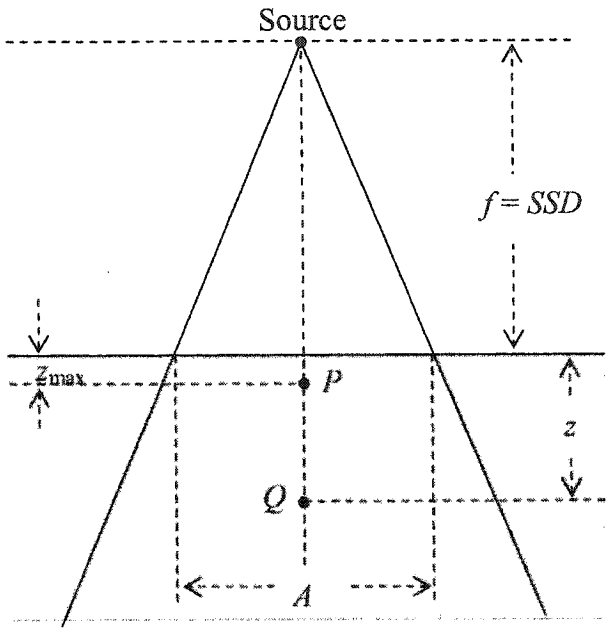


*FIG. 1.5. The definition and geometry for percentage depth dose (PDD). Point P is at $z_{max}$ and point Q is an arbitrary point on the beam central axis at depth z. The source-surface distance is f and the field size A is defined on the surface of the phantom.*

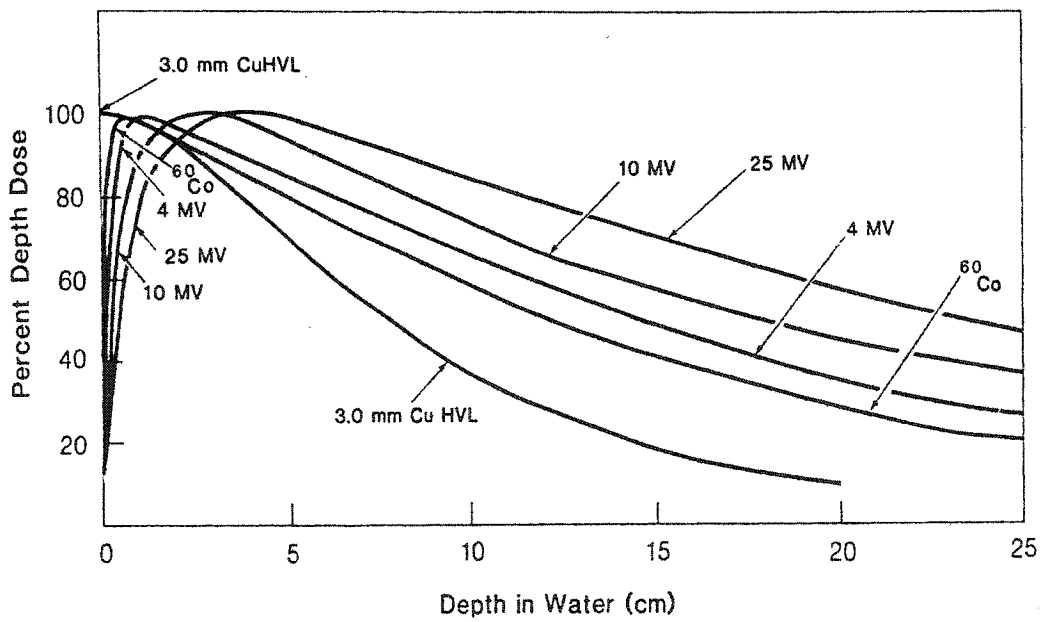


*FIG. 1.6. Percentage depth doses (PDD) in water for various clinical external radiation beams ranging from HVL 3.0 mm Cu to 25 MV x rays.*

The depth of maximum dose $z_{max}$ is an important parameter for characterizing *PDD* curves and through them the quality of photon beams. For megavoltage linac beams, $z_{max}$ in water depends on two parameters: beam energy $hv$, field size $A$. The primary dependence is on beam energy, and $z_{max}$ is often quoted only as a function of beam energy without much regard for the field size dependence. Thus, in the first approximation $z_{max}$ values for 4, 6, 10, 18 and 25 MV beams are quoted as 10, 15, 25, 35, and 40 mm, respectively (see TABLE 1.1). However, as shown by various investigators[13-15], $z_{max}$ of flattened linac beams also depends on field size. This dependence is illustrated for 6, 10, and 18 MV beams in FIG. 1.7. At all beam energies $z_{max}$ increases rapidly in the field size range from 1×1 to about 5×5 cm$^2$, reaches a saturation for fields around 5×5 cm$^2$, and then decreases gradually with an increasing field size, until around 30×30 cm$^2$, it returns to a value about equal to that for a 1×1 cm$^2$ field. For the small fields used in radiosurgery, the $z_{max}$ increase with field size is attributed to in-phantom scatter, while for large fields, the $z_{max}$ decrease with field size is attributed to contamination electrons[15] which originate in the flattening filter and are further scattered by the collimator jaws and air.

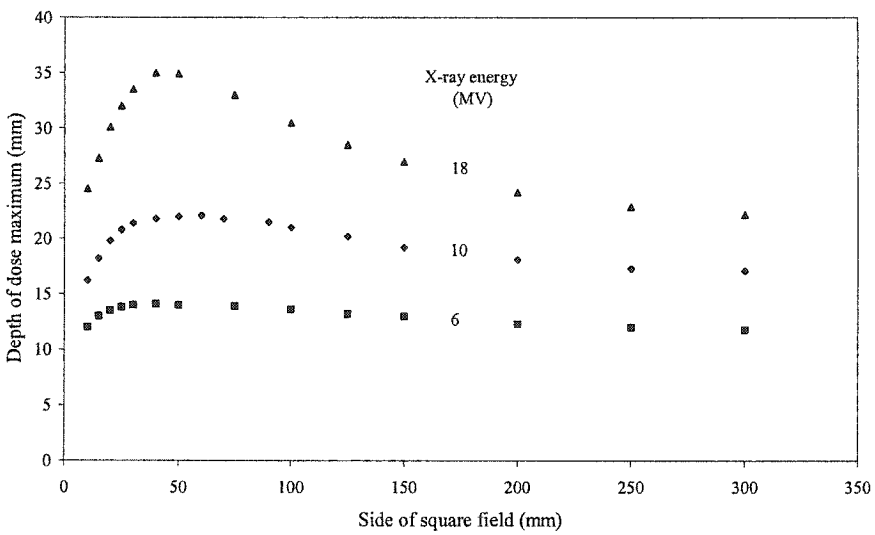


*FIG. 1.7. The variation of $z_{max}$ with square fields for 6, 10, and 18 MV x-ray beams[15]. Although $z_{max}$ is usually quoted in the literature as 15, 25, and 35 mm for 6, 10, and 18 MV x-ray beams regardless of the field size, experimental measurements revealed that $z_{max}$ varies slowly with field size and for a given photon beam energy has a maximum value for square fields of approximately 5×5 cm$^2$.*

TABLE 1.1. TYPICAL VALUES OF $z_{max}$ LISTED IN THE *BRITISH JOURNAL OF RADIOLOGY* SUPPLEMENT 25 (REF. 16) FOR VARIOUS PHOTON BEAMS.

| Photon Beam | $z_{max}$ (cm) |
|---|---|
| Cs-137 | 0.14 |
| Co-60 | 0.5 |
| 6 MV | 1.5 |
| 8 MV | 1.8 |
| 18 MV | 3.0-3.5 |

Beyond $z_{max}$, the decrease in *PDD* is mainly produced by the reduction of the primary photon fluence. The decrease in the primary photon fluence is due mainly to two factors: (1) attenuation of primary photons in the phantom, and (2) divergence of the radiation beam. The attenuation of primary photons in phantom reduces the photon fluence by a factor $e^{-\mu\ell}$, where $\mu$ is the linear attenuation coefficient and $\ell$ is the traversed phantom thickness beyond $z_{max}$, *i.e.*, $\ell = z - z_{max}$. In general, the lower the photon beam energy, the larger is $\mu$ resulting in a larger attenuation factor for the same traversed thickness in the phantom.

The decrease of photon fluence caused by the beam divergence is energy independent. The divergence of the radiation beam decreases the photon fluence at distance $R_2 = f + z$ from the source in comparison to the photon fluence at $z_{max}$ by a factor $(f + z_{max} / f + z)^2$. This is often referred to as the inverse-square law and the factor $(f + z_{max} / f + z)^2$ is referred to as the inverse-square factor *ISF*. If the parameters $z$, $A$, and $hv$ remain fixed, the primary dose component at $z$ relative to the primary dose component at $z_{max}$ increases with increasing $f$.

Finally, at any geometrical point in the phantom, the larger the field size $A$, the greater is the scattered dose component, which results in an increase in the *PDD*, if all other

parameters $z$, $f$, and $hv$ are kept constant. The dependence of the *PDD* on all four parameters $z$, $A$, $f$, and $hv$ is summarized in TABLE 1.2.

### *The off-axis ratio (OAR)*

To calculate the 3-D dose distributions in phantoms, off-axis dose profiles are required in conjunction with the *PDD*s. Off-axis dose profiles are usually measured perpendicularly to the beam central axis at various depths in the phantom. The off-axis ratio (*OAR*) dosimetric function is defined as the ratio of the dose to phantom at an off-axis point to the dose to phantom on the beam central axis at the same depth. Figure 1.8 plots *OAR*s at several depths in a water phantom at $SSD = 100$ cm for a $10\times10$ cm$^2$ open field 6 MV x-ray beam.

The volume dose matrix data that combine *PDD* data and *OAR* data at various depths can be used to calculate 2-D and 3-D dose distributions. The *OAR*s at depths $z_{max}$ and 10 cm are used to verify the compliance of the machine with specifications given by the manufacturer. Figure 1.8 also shows that the dose fall-off at the edge of the field is not sharp but extends over a region, typically a few millimeters, called the *penumbra* region. The penumbra shape is dependent on the finite size of the radiation source, energy and type of the radiation source, and on the depth in phantom. The dose in the region beyond the penumbral region, called the *umbra*, is generally small. The doses in the penumbral and umbral regions of the dose profile are in general produced by radiation transmitted through the jaws and the head shielding and by photons scattered in the patient.

TABLE 1.2. DEPENDENCE OF THE *PDD*, THE RELATIVE PRIMARY AND SCATTERED DOSE ON DEPTH $z$ BEYOND $z_{max}$, FIELD SIZE $A$, SOURCE-SURFACE DISTANCE $f$, AND PHOTON BEAM ENERGY $hv$.

| Varying parameter | Constant parameters | *PDD* |
|---|---|---|
| $z \uparrow$ | $A$, $f$, $hv$ | $\downarrow$ |
| $A \uparrow$ | $z$, $f$, $hv$ | $\uparrow$ |
| $f \uparrow$ | $z$, $A$, $hv$ | $\uparrow$ |
| $hv \uparrow$ | $z$, $A$, $f$ | $\uparrow$ |

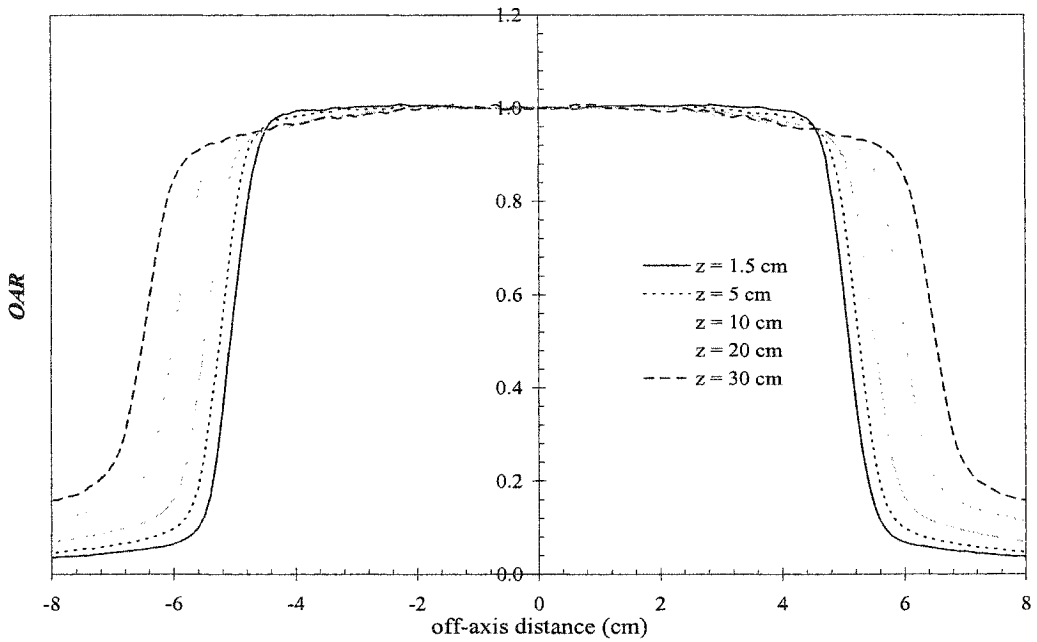


*FIG. 1.8. Off-axis ratio at 1.5, 5, 10, 20, and 30 cm depths for a 10×10 cm$^2$ open field produced by a 6 MV x-ray beam.*

## 1.3. RADIATION DOSIMETERS

*Radiation dosimeters* are instruments that measure directly or indirectly the dosimetric quantities or their time derivatives of ionizing radiation. These instruments must exibit at least one physical effect that is a function of the measured dosimetric quantity. A *dosimetry system* consists of a radiation dosimeter and its reader. The terms *absolute* and *relative dosimetry* are also used in the context of radiation measurement with *absolute dosimetry* providing a radiation related signal that leads directly to dose determination at a given point-of-interest and *relative dosimetry* providing a signal that leads to determination of dose only if the signal is first calibrated in a known radiation field .

A number of dosimetry systems are used today in medical physics: for example, ionization chamber systems, films, luminescence dosimeters, diamond detectors, and semiconductor dosimeters. A dosimeter must satisfy several desirable characteristics, such as accuracy, precision, linearity with measured dosimetric quantity, energy and dose rate dependence, directional dependence, and spatial resolution.

Because a particular dosimeter cannot satisfy all these characteristics, the choice of an appropriate dosimetry system depends on the particular application of interest, as well as on the convenience of use. For example, calorimeters are considered the most absolute dosimeters for measuring the absorbed dose to a medium, because they measure directly the energy deposited in the medium without the need for calibration in a known radiation beam. Yet, because of their relatively low sensitivity and high susceptibility to surrounding environmental conditions, calorimeters are generally reserved for calibrating radiation sources in standards laboratories. Calibration of clinical sources is generally carried out using calibrated ionization chambers. Furthermore, some dosimeters cannot meet a 2% accuracy recommended in absolute dosimetry but may have other advantages in other aspects, such as, for example, high spatial resolution, that make them superior in some relative dosimetry measurements.

### 1.3.1. Absolute dosimetry

The method for determining the dose at a point-of-interest in a medium, $D_{\text{med}}$, with any dosimeter can be generally expressed as

$$D_{\text{med}} = M \cdot C \cdot \prod_{\text{i}} K_{\text{i}}, \tag{1.11}$$

where $M$ is the measured dosimetric signal, $C$ is a conversion factor usually chosen such that the product $MC$ gives the dose to detector $D_{\text{det}}$, and $\prod_{\text{i}} K_{\text{i}}$ is a product of additional factors $K_{\text{i}}$ that are required to convert $D_{\text{det}}$ to $D_{\text{med}}$ in the absence of the detector.

As a demonstration of the use of Eq. (1.11), the absorbed dose to water $D_{\text{water}}$ measured with cavity ionization chambers in water is given as

$$D_{\text{water}} = Q_{\text{sat}} \cdot \frac{1}{m_{\text{air}}} \left( \frac{\overline{W}_{\text{air}}}{e} \right) \cdot \left[ \left( \frac{\overline{L}_{\Delta}}{\rho} \right)_{\text{air}}^{\text{water}} P_{\text{fl}} P_{\text{wall}} P_{\text{cel}} \right], \tag{1.12}$$

where $M$ is given as $Q_{\text{sat}}$ which is the *ionization produced in the air cavity*; $C$ is the quotient of the mean energy required to produce an ion pair in air per unit charge $\overline{W}_{\text{air}} / e$ and the air mass $m_{\text{air}}$ from which the charge $Q_{\text{sat}}$ is produced; and $\prod_{\text{i}} K_{\text{i}}$ is the product

of the mean restricted stopping power ratios of water-to-air $\left(\overline{L}_{\Delta}/\rho\right)_{\text{air}}^{\text{water}}$, a fluence perturbation factor $P_{\text{fl}}$, a wall perturbation factor $P_{\text{wall}}$, and a central electrode perturbation factor $P_{\text{cel}}$. Further details on dose measurement with ionization chambers are presented in Chapter 3. In clinics, absolute dosimetry techniques are usually applied only for calibrating radiation beams, *i.e.*, for determining the dose to the reference calibration point in phantom, while relative dosimetry techniques are used to obtain the dosimetric functions and the semi-empirical relationships required in treatment planning.

### 1.3.2. Relative dosimetry

Relative dosimetry techniques require dose measurements at two different geometrical points: a reference point $P_{\text{ref}}$ and a point-of-interest $Q$. Based on the general expression given in Eq. (1.11), the ratio of dose $D_{\text{Q}}$ at $Q$ to the dose $D_{\text{P}_{\text{ref}}}$ at $P_{\text{ref}}$ is given as

$$\frac{D_{\text{Q}}}{D_{\text{P}_{\text{ref}}}} = \frac{\left[M \cdot C \cdot \prod_{\text{i}} K_{\text{i}}\right]_{\text{Q}}}{\left[M \cdot C \cdot \prod_{\text{i}} K_{\text{i}}\right]_{\text{P}_{\text{ref}}}}, \tag{1.13}$$

which reduces to the ratio of measured dosimetric signals $M_{\text{Q}}/M_{\text{P}_{\text{ref}}}$ only if all other parameters do not change when moving from point $P_{\text{ref}}$ to point $Q$. When an ionization chamber is used in water, the general expression for relative dosimetric techniques becomes

$$\frac{D_{\text{water}}(Q)}{D_{\text{water}}(P_{\text{ref}})} = \frac{\left[Q_{\text{sat}} \cdot \left(\frac{\overline{L}_{\Delta}}{\rho}\right)_{\text{air}}^{\text{water}} P_{\text{fl}} P_{\text{wall}} P_{\text{cel}}\right]_{\text{Q}}}{\left[Q_{\text{sat}} \cdot \left(\frac{\overline{L}_{\Delta}}{\rho}\right)_{\text{air}}^{\text{water}} P_{\text{fl}} P_{\text{wall}} P_{\text{cel}}\right]_{\text{P}_{\text{ref}}}}. \tag{1.14}$$

An air-filled ionization chamber, because of its reliability and practicality, is the main instrument used in radiotherapy clinics for determining the output of clinical radiation beams (absolute dosimetry) and for the acquisition of relative dose data (relative dosimetry).

## 1.4. THESIS OBJECTIVE AND OUTLINE

### 1.4.1. Motivation and objective

During the past century, energies of photon beams used for external radiotherapy have progressed from low photon energies in superficial and orthovoltage x-ray beams to high energy photon beams. The use of high energy external photon beams in radiotherapy is valued for the skin sparing effect these beams provide. However, determining the dose at the skin surface either in an absolute manner or in a relative manner to the dose at $z_{max}$ has proven to be a challenge for medical physicists, especially if the dose tolerances recommended by the ICRU are to be met. Monte Carlo techniques provide satisfactory agreement with dose measurements for depths beyond $z_{max}$ for high energy photon beams; however, they give unsatisfactory agreement with measurements in the dose build-up region[17,18].

The source of this disagreement is not known yet. On the one hand, experimentalists are refining their measurement techniques, investigating other potential radiation sources that are not accounted for by Monte Carlo codes, and providing more accurate cross-sectional data that become the base for new and improved Monte Carlo codes. On the other hand, theoreticians are refining Monte Carlo transport algorithms, making them more accurate, faster, more efficient, and reliable.

In 2000, a new and improved Monte Carlo code known as the EGSnrc[19] was released. In this thesis, the dose in the build-up region for 6 and 18 MV x-ray beams is calculated with the new EGSnrc code and evaluated against measurements with a phantom-embedded extrapolation chamber (PEEC).

### 1.4.2. Thesis outline

The thesis is divided into two parts. Chapters 2 and 3 contain the necessary background material required for the thesis, and Chapters 4 through 6 describe the experimental work. Chapter 2 titled "*Basic radiation physics*" provides a summary of the various interactions of photons, neutrons, and charged particles with various dosimetric media, and the associated parameters, such as cross-sections and stopping powers, required for dose

calculations. Chapter 3 deals with *ionization chambers* and focuses on cavity theory required for dosimetry with cavity ionization chambers and on some practical aspects necessary for obtaining the dosimetric signal. A description of our custom-built phantom embedded extrapolation chamber PEEC, the primary apparatus used for the experimental work in this thesis, including evaluation of its mechanical and geometrical aspects is given in Chapter 4, which also describes the EGSnrc Monte Carlo system code. Chapter 5 presents an evaluation of the polarity effect in the PEEC in photon and electron beams, verifying our results using the COMPTON/EGSnrc MC user code which we developed. The direct comparison between the surface doses determined with the EGSnrc MC system code and PEEC measurements for 6 MV and 18 MV x-ray beams is provided in Chapter 6. Finally, Chapter 7 summarizes the results and gives recommendations for future work.

# REFERENCES


1. O. Glasser, J. C. Tucker, and M. Boveri, *Wilhelm Conrad Röntgen and the early history of the Roentgen rays* (Bale & Danielsson, London, 1933).
2. O. Glasser and W. C. Röntgen, *Dr. W. C. Röntgen* (C. C. Thomas, Springfield, I11., 1945).
3. W. C. Röntgen, A, Thomas, I. Isherwood et al., *The Invisible Light: 100 years of medical radiology* (Blackwell Science Ltd, Oxford; Cambridge, Mass., 1995).
4. F. H. Williams, *The Roentgen rays in medicine and surgery: as an aid in diagnosis and as a therapeutic agent designed for the use of practitioners and students* (Macmillin, New York, NY, 1901).
5. M. D. Blaufox, "Becquerel and the discovery of radioactivity: early concepts," Semin. Nucl. Med. **26**, 145-154 (1996).
6. J. Dutreix and A. Dutreix, "Henri Becquerel (1852-1908)," Med. Phys. **22**, 1869-1875 (1995).
7. J. Dutreix, "From x-rays to radioactivity and radium. The discovery and works of herni Becuerel (1851-1908)," Bull. Acad. Natl. Med. **180**, 109-181 (1996).
8. ICRU, "Radiation quantities and units," Report 33, International Commission on Radiation Units and Measurements, Washington, DC. (1980).
9. ICRU, "Quantities and units in radiation protection dosimetry," Report 51, International Commission on Radiation Units and Measurements, Bethesda, MD. (1991).
10. ICRU, "Fundamental quantities and units for ionizing radiation," Report 60, International Commission on Radiation Units and Measurements, Bethesda, MD. (1998).
11. ICRP, "1990 Recommendations of the ICRP," Publication 60, International Commission on Radiological Protection, Pergamon Press, Oxford and New York (1991).
12. NCRP, "Conceptual Basis for Calculations of Absorbed-Dose Distributions," Report 108, National Council on Radiation Protection and Measurements, Bethesda, MD (1991).
13. P.J. Biggs and C. C. Ling, "Electrons as the cause of the observed $d_{max}$ shift with field size in high energy photon beams" Med. Phys. **6**: 291-295 (1979).
14. G. Arcovito, A. Pieramattei, G. D'Abramo, and R. Andreassi, "Dose measurement and calculation of small fields for 9 MV x-ray" Med. Phys. **12**: 779-784 (1994).
15. K. E. Sixel, and E. B. Podgorsak, "Build-up region and depth of dose maximum of megavoltage x-ray beams" Med. Phys. **21**: 411-416 (1994).
16. A. L. Bradshow, "The variation of percentage depth dose and scatter factor with beam quality" Br. J. Radiol. Supplement 25 Appendix D: 125-130 (1996).
17. G. X. Ding, "Dose discrepancies between Monte Carlo calculation and measurement for high-energy photon beam at buildup region" *Int. Workshop on Recent Developments in Accurate Radiation Dosimetry* (Montreal, Canada, 10-13 OCT. 2001).
18. C. L. Hartmann Siantar *et al*, "Description and dosimetric verification of the PEREGRINE Monte Carlo dose calculation system for photon beams incident on a water phantom," Med. Phys. **28**, 1322-1337 (2001).
19. I. Kawrakow and D. W. O. Rogers, "The EGSnrc Code System: Monte Carlo simulations of electron and photon transport," Technical Report PIRS-701, National Research Council of Canada, Ottawa, Canada (2000).

# Chapter 2

# BASIC RADIATION PHYSICS

## 2.1. INTRODUCTION

Radiation physics is the science of ionizing radiation and its interaction with matter. Of special interest is the energy transferred from the radiation beam to matter in general and to biological material in particular. The unique effects of such interactions on the irradiated material, particularly on biological systems, have resulted in an extensive science dealing exclusively with a quantitative study of ionizing radiation and its effects. The results are used in applications of radiation beams in diagnostic and treatment of human diseases.

## 2.2. TYPES OF IONIZING RADIATION

As shown in FIG. 2.1, radiation is classified into two main categories: *ionizing* and *non-ionizing*. By definition, ionizing radiation is capable of ionizing matter. The International Commission on Radiation Units and Measurements (ICRU) Report 19 (ref. 1) categorized ionizing radiation into two groups in order to emphasize the differences between the interactions of charged particles and uncharged particles with matter. The two groups are:

- *Directly ionization radiation* which includes fast charged particles, such as electrons, positrons, protons, alpha-particles, heavy ions etc.. These particles deliver their energy to matter through Coulomb-force interactions with orbital atomic electrons along the charged particle's trajectory. Electrons and positrons are refereed to as light charged particles, while protons, alpha-particles, etc., are heavy charged particles

- *Indirectly ionizing radiation* which includes uncharged particles, such as x rays, gamma rays, and neutrons. These particles first transfer their energy to

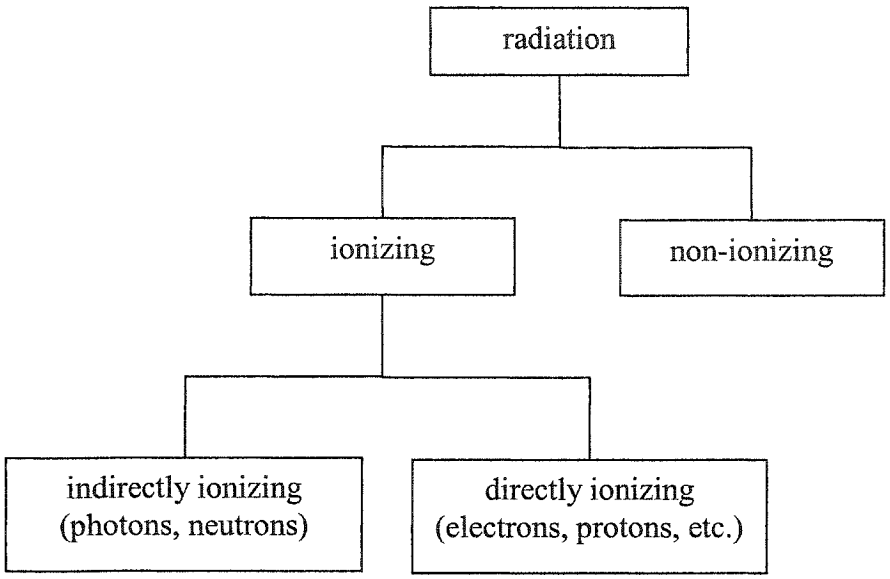


*FIG. 2.1. Classification of radiation as ionizing and non-ionizing radiation. Ionizing radiation is subdivided into directly ionizing and indirectly ionizing radiation.*

charged particles in the medium and the resulting fast directly ionizing charged particles then in turn deliver their energy to the medium.

Directly ionizing radiation deposits energy in matter through a one-step process (Coulomb interaction), while indirectly ionizing radiation deposits energy in matter through a two-step process in which the intermediate step involves producing directly ionizing particles.

## 2.3. INTERACTIONS OF PHOTONS WITH MATTER

### 2.3.1. Types of interactions

Depending on their origin, indirectly ionizing photon radiation can be further categorized into four groups:

- *Bremsstrahlung* (continuous x rays) which are produced by an acceleration or deceleration of light charged particles.
- *Characteristic x rays* (discrete) emitted in allowed transitions of atomic orbital electrons from a higher atomic orbit to a lower orbit.
- *Gamma rays* (discrete) emitted through nuclear transitions in gamma decay.

- *Annihilation radiation* emitted through positron annihilation with an orbital electron.

There are various processes by which photons may interact with matter. The probability for a particular interaction to take place depends on the energy $h\nu$ of the incident photon and on the atomic number $Z$ of the medium. Photons may interact with the atom as a whole (photoelectric effect, Rayleigh scattering), with the nucleus (pair production, photonuclear interactions, resonance elastic scattering), or with a tightly or loosely bound orbital electron (Compton scattering, triplet production). In this context, a tightly bound electron is an orbital electron with a binding energy $E_b$ comparable to, but smaller than, the energy $h\nu$ of the incident photon; *i.e.*, $E_b \lesssim h\nu$. On the other hand, a loosely bound or free electron is an orbital electron with a binding energy much smaller than the energy of the incident photon; *i.e.*, $E_b << h\nu$.

The outcome of the photon interaction with matter depends on the undergoing interaction process. In photoelectric effect, pair and triplet production, as well as in photonuclear processes the incident photon disappears, while in Compton and Rayleigh scattering processes the incident photon is scattered. Furthermore, photoelectric effect, Compton scattering, pair production, and triplet production result in transfer of energy to electrons. Protons and neutrons are usually released from nuclei in photonuclear interactions.

### 2.3.2. Photoelectric effect

In a *photoelectric* interaction the incident photon is completely absorbed by an atom, and an orbital electron called a *photoelectron* is ejected. Most of the energy of the incident photon is transferred to the ejected orbital electron and only a small fraction of the photon energy is absorbed by the atom to conserve momentum. To overcome its binding energy in a given shell, the photoelectron expends some of the transferred energy in escaping the atom and its kinetic energy $E_K$ immediately after it escapes the atom is essentially equal to the incident photon energy $h\nu$ minus its atomic binding energy; *i.e.*, $E_K = h\nu - E_b$. The atom is left in an excited state with a vacancy in the shell from which the photoelectron was ejected and it relaxes either radiatively through emission of *characteristic* photons or

non-radiatively through emission of Auger and Coster-Kronig electrons (see Section 2.6.1).

The angle $\theta$ at which the photoelectron is emitted relative to the photon's direction of incidence depends on the energy of the incident photon. At low photon energies ($h\nu \leq 20$ keV) photoelectrons are ejected primarily at right angles to the direction of the incident photon, while for photon energies above 1 MeV photoelectrons are emitted mainly in the forward direction.

The theoretical derivation of the photoelectric effect cross section is quite difficult due to the complications arising from the binding of the orbital electron. No single closed formula describes accurately the photoelectric effect cross section over a wide range of incident photon energies. However, satisfactory analytical expressions, applicable only in several photon energy regions and based on experimental results, were presented by Evans[2] and Hubbell[3]. Because the whole atom participates in the interaction, the photoelectric effect interaction is usually described by the atomic cross section ${}_a\tau$. The atomic cross section for photoelectric effect ${}_a\tau$ as a function of the incident photon energy $h\nu$ and the atomic number $Z$ can be expressed as

$$ {}_a\tau \cong k\frac{Z^n}{(h\nu)^m}, \tag{2.1}$$

where $k$ is a constant. In the energy region $h\nu \leq 0.1$ MeV, ${}_a\tau$ varies roughly as $Z^4$ and $(h\nu)^{-3}$, *i.e.*,

$$ {}_a\tau \propto \frac{Z^4}{(h\nu)^3}. \tag{2.2}$$

At photon energies greater than 5 MeV, ${}_a\tau$ becomes approximately inversely proportional to the energy of the incident photon $h\nu$.

The atomic cross sections for the photoelectric effect ${}_a\tau$ in lead, copper, and carbon as a function of the incident photon energy are presented in FIG. 2.2. The curves exhibit discontinuities, known as *absorption edges*, which arise whenever the energy of the incident photon $h\nu$ matches the ionization potential of electrons in the K-shell, and the subshells of L, M, .... shells. Referring to FIG. 2.2, the K-edge for lead occurs at 88 keV corresponding to the binding energy of the K-shell electrons. If the energy of the incident

photon $h\nu$ is just below 88 keV, the K-shell electrons cannot participate in the photoelectric process and only electrons in the higher shells can do so.

The magnitude of the sudden increase in the atomic photoelectric cross section at the K-edge in comparison to the remaining 80 electrons in a lead atom indicates the importance of the contribution of the K-shell electrons to the atomic photoelectric cross section. The K-shell electrons contribute to more than 75% of the total photoelectric effect cross section, suggesting a strong dependence of the photoelectric process on the binding energy of the orbital electron. Similarly, the L-shell for lead shows a step function increase at the corresponding three energy levels in the L-shell ( $L_I$ at 15.9 keV, $L_{II}$ at 15.2 keV, and $L_{III}$ at 13.0 keV).

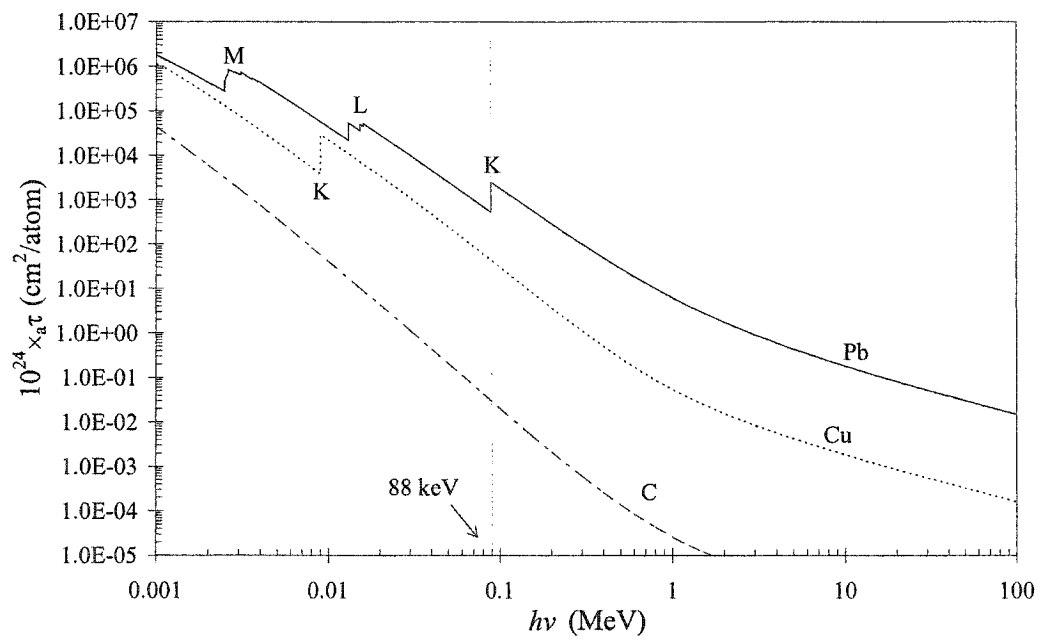


*FIG. 2.2. Atomic cross sections for the photoelectric effect ${}_a\tau$ in carbon, copper, and lead as a function of the incident photon energy hv. The graph illustrates the K, L, and M absorption edges for lead, and the K absorption edge for copper.*

### 2.3.3. Compton scattering

In *Compton scattering* interactions, a photon of energy $h\nu$ interacts with an orbital, essentially free and stationary, electron. The incident photon is scattered with a lower

energy $h\nu'$ at an angle $\theta$ with respect to the incident photon direction; the orbital electron (Compton or recoil electron) receives an energy of $E_k = h\nu - h\nu'$ and recoils at angle $\phi$. Similarly to the photoelectric effect, after the interaction the atom is left with a vacancy in one of its atomic shells.

The kinematics of the Compton scattering interaction is derived simply by applying the relativistic laws of energy and momentum conservation to get

$$h\nu' = h\nu \frac{1}{1+\varepsilon(1-\cos\theta)}, \tag{2.3}$$

$$E_K = h\nu \frac{\varepsilon(1-\cos\theta)}{1+\varepsilon(1-\cos\theta)}, \tag{2.4}$$

and

$$\cot\phi = (1+\varepsilon)\tan\left(\frac{\theta}{2}\right), \tag{2.5}$$

where $\varepsilon$ is the normalized incident photon energy

$$\varepsilon = \frac{h\nu}{m_e c^2}, \tag{2.6}$$

with $m_e c^2$ the rest energy of the electron ($m_e c^2 = 0.511$ MeV).

The electronic cross section for Compton scattering ${}_e\sigma$ was derived by Klein and Nishina[4,5] who expanded the Thompson's classical photon-electron scattering theory[4] by applying Dirac's relativistic theory of the electron. The Klein-Nishina expression for the differential cross section of Compton scattering $\mathrm{d}_e\sigma$ per unit solid angle per electron for photon energy of $h\nu$ scattered at angle $\theta$ is

$$\frac{\mathrm{d}_e\sigma}{\mathrm{d}\Omega} = \frac{r_e^2}{2}\left(\frac{\nu'}{\nu}\right)^2\left(\frac{\nu}{\nu'} + \frac{\nu'}{\nu} - \sin^2\theta\right), \tag{2.7}$$

where $r_e$ is the classical electron radius ($r_e = e^2/(4\pi\varepsilon_0 m_e c^2) = 2.818\times10^{-15}$ m). By integrating Eq. (2.7) over all scattering angles $\theta$, the electronic cross section ${}_e\sigma$ is given by the following relationship

$${}_e\sigma = 2\pi r_e^2\left\{\frac{1+\varepsilon}{\varepsilon^2}\left[\frac{2(1+\varepsilon)}{1+2\varepsilon} - \frac{\ln(1+2\varepsilon)}{2\varepsilon}\right] + \frac{\ln(1+2\varepsilon)}{2\varepsilon} - \frac{1+3\varepsilon}{(1+2\varepsilon)^2}\right\}. \tag{2.8}$$

The electronic cross sections for Compton scattering ${}_e\sigma$ for an orbital electron in carbon, copper, and lead atoms as well as for an unbound (free) electron (Eq. (2.8)) are plotted in FIG. 2.3. At very low photon energies the binding of an orbital electron to the atom will generally reduce the electron's probability of interacting with an incident photon through the Compton process; however, for photon energies above 1 MeV the effect of the binding of the orbital electron to the atom on Compton cross section is negligible.

### 2.3.4. Pair and triplet production

In pair and triplet production interactions, a photon interacts with the Coulomb field of a nucleus or an orbital electron, respectively. The photon disappears and an electron-positron pair is created.

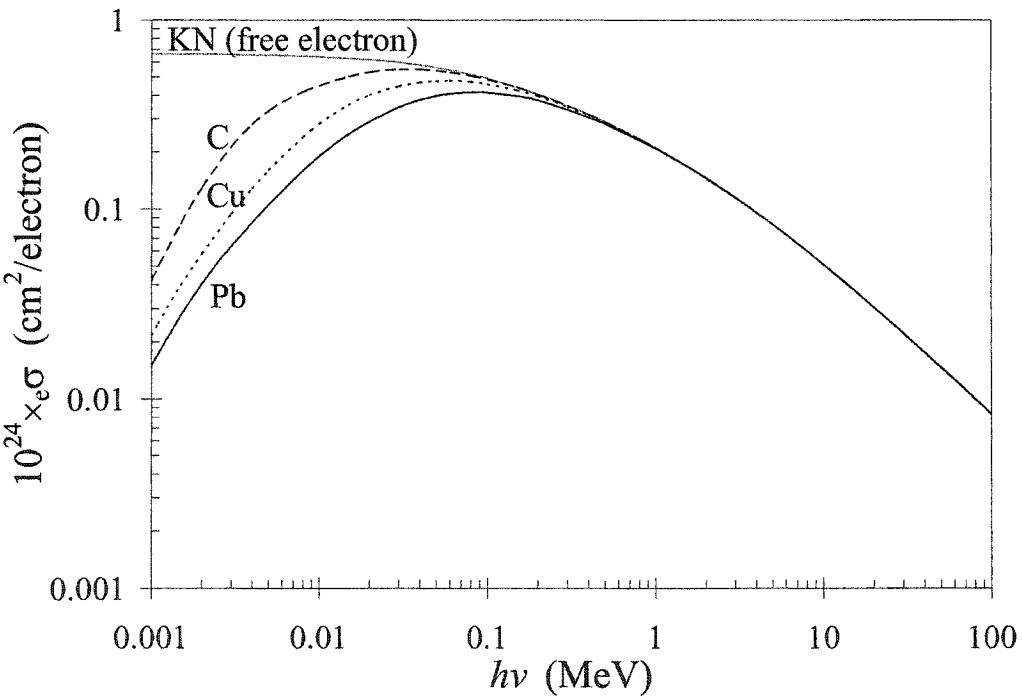


*FIG. 2.3. Electronic cross sections for Compton scattering ${}_e\sigma$ in carbon, copper, and lead as a function of the incident photon energy hν. The curve labeled KN is the Klein-Nishina Compton electronic cross section for an unbound (free) electron, given in Eq. (2.8).*

Part of the photon energy undergoing a pair production interaction is expended for creating the electron-positron pair and the remaining photon energy is distributed

between the kinetic energies of the electron $E_{K_e}$ and the positron $E_{K_p}$, while a negligible amount of energy is transferred to the nucleus to conserve momentum. Because the photon interacts with the nucleus in the pair production process, no vacancy is created in the atomic shells.

A photon undergoing a triplet production interaction spends part of its energy in creating the electron-positron pair; however, here the remaining photon energy is transferred to the kinetic energy distributed among the three particles (the electron-positron pair and the orbital electron in whose field the interaction occurs). Hence, triplet production interactions create a vacancy in one of the atomic shells, because the orbital electron gains sufficient energy to overcome its binding energy to the atom and leaves the atom.

In contrast to the photoelectric effect and Compton scattering interactions, a photon must have an energy above a well established threshold value to be able to interact with media through the pair and triplet production processes. The threshold photon energy can be calculated using the invariance relationship $E_{\text{tot}}^2 - (pc)^2 = \text{Inv.}$, evaluated before and after the interaction. For pair production, the threshold photon energy is equal to the energy required to create the electron-positron pair, with a small correction, *i.e.*, $h\nu_{\text{thr}}(\text{pair}) = 2m_e c^2(1 + m_e c^2 / m_A c^2) \approx 2m_e c^2 = 1.022$ MeV, where the rest energies for the electron and the nucleus are $m_e c^2$ and $m_A c^2$, respectively. The threshold energy for triplet production is $h\nu_{\text{thr}}(\text{triplet}) = 4m_e c^2 = 2.044$ MeV.

The atomic differential cross section for pair production $\mathrm{d}_a\kappa_{\text{PP}}$, based on a theory by Bethe and Heitler[6], is given by

$$\mathrm{d}_a\kappa_{\text{PP}} = \frac{\sigma_0 Z^2 P}{h\nu - 2m_e c^2}\,\mathrm{d}E_{K_p}, \tag{2.9}$$

where $\sigma_0 = r_e^2/137$ and the parameter $P$ is mainly a function of the incident photon energy $h\nu$ having a small dependence on the atomic number $Z$. By integrating Eq. (2.9) over all possible values of the positron kinetic energy $E_{K_p}$, the atomic differential cross section ${}_a\kappa_{\text{PP}}$ can be written as

$${}_a\kappa_{\text{PP}} = \sigma_0 Z^2 \bar{P}, \tag{2.10}$$

where the parameter $\overline{P}$ varies roughly as a logarithmic function of $h\nu$.

The atomic cross section for triplet production ${}_a\kappa_{TP}$ is smaller than ${}_a\kappa_{PP}$ for the same atom. It can be calculated roughly from ${}_a\kappa_{TP}$ using

$$ {}_a\kappa_{TP} \cong \frac{{}_a\kappa_{PP}}{CZ}, \tag{2.11}$$

where $C$ is a parameter that depends on $h\nu$. At very large photon energies $C$ approaches 1 and rises slowly with decreasing energy to reach a value of about 2 at 5 MeV.

For dosimetric applications, ${}_a\kappa_{PP}$ and ${}_a\kappa_{TP}$ are usually combined into a single cross section ${}_a\kappa$, usually referred to as the pair-production cross section. The contribution of ${}_a\kappa_{TP}$ to the total pair production cross section ${}_a\kappa$ depends on $Z$ and $h\nu$ but generally ${}_a\kappa_{PP}$ contributes more than 99% to ${}_a\kappa$ in high $Z$ materials. For low $Z$ materials, the contribution of ${}_a\kappa_{TP}$ becomes more significant. For example, in carbon $(Z = 6)$ ${}_a\kappa_{TP}$ is about 8% of ${}_a\kappa$ at 10 MeV; its contribution increases with increasing $h\nu$ and approaches 16% an very high photon energies. Atomic cross sections for pair production ${}_a\kappa_{PP}$ and triplet production ${}_a\kappa_{TP}$ in carbon, copper, and lead are shown in FIG. 2.4.

### 2.3.5. Rayleigh (coherent) scattering

In Rayleigh scattering interactions the photon is scattered by the combined action of the whole atom. This event is also called coherent scattering since the photon essentially loses none of its energy, while the atom moves just enough to conserve the total momentum of the system. The photon scattering angle with respect to the direction of the incident photon depends on both $Z$ and $h\nu$, but most photons are usually redirected through a small angle making this process difficult to detect in wide-beam geometries.

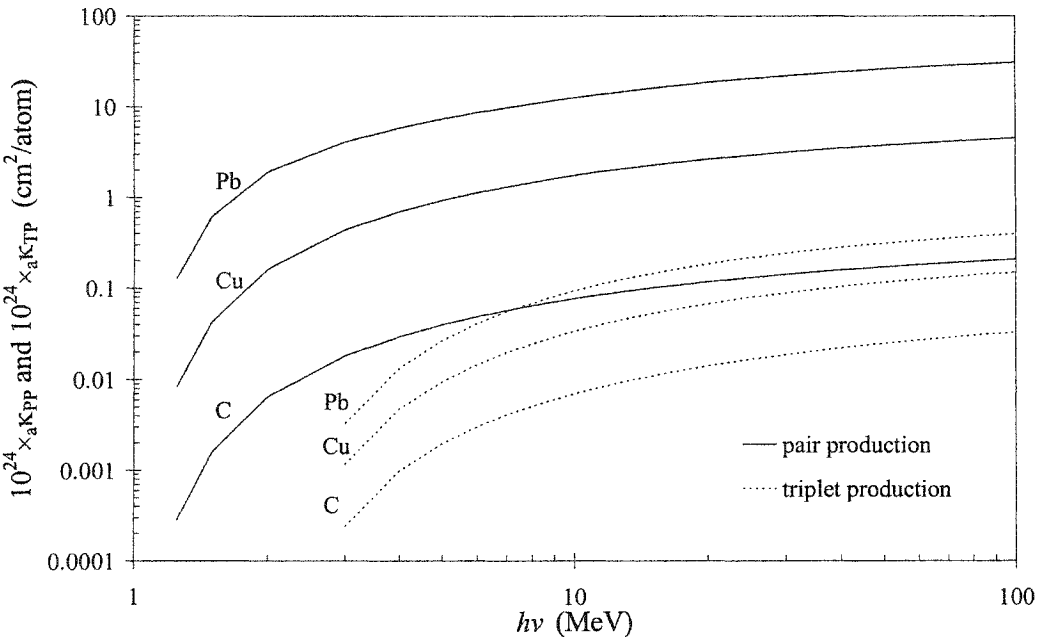


*FIG. 2.4. Atomic cross sections for pair production ${}_a\kappa_{PP}$ and triplet production ${}_a\kappa_{TP}$ in carbon, copper, and lead as a function of incident photon energy. The threshold photon energies for pair production and triplet production are 1.022 MeV and 2.044 MeV, respectively. At 10 MeV, the contribution of ${}_a\kappa_{TP}$ to the total pair production cross section ${}_a\kappa$ is 1%, 2%, and 8% for lead, copper, and carbon, respectively.*

The differential atomic cross section for Rayleigh scattering $d_a\sigma_R$ is obtained by multiplying the Thompson's scattering differential cross section by an atomic form factor[7], containing a parameter $x = \frac{1}{\lambda}\sin(\frac{\theta}{2})$, as follows

$$\frac{d_a\sigma_R}{d\Omega} = \frac{r_e^2}{2}\left(1+\cos^2\theta\right)\left[F(x,Z)\right]^2. \tag{2.12}$$

For small values of $\theta$ the form factor $F(x,Z)$ approaches $Z$, while, for large values of $\theta$, it has a value close to zero.

Figure 2.5 presents the atomic cross section for Rayleigh scattering ${}_a\sigma_R$ in lead, copper, and carbon. In general, ${}_a\sigma_R$ is approximately proportional to $Z^2$ and to $(h\nu)^{-2}$. The relative importance of Rayleigh scattering in comparison to other photon interactions is small and often negligible, especially in the megavoltage energy range.

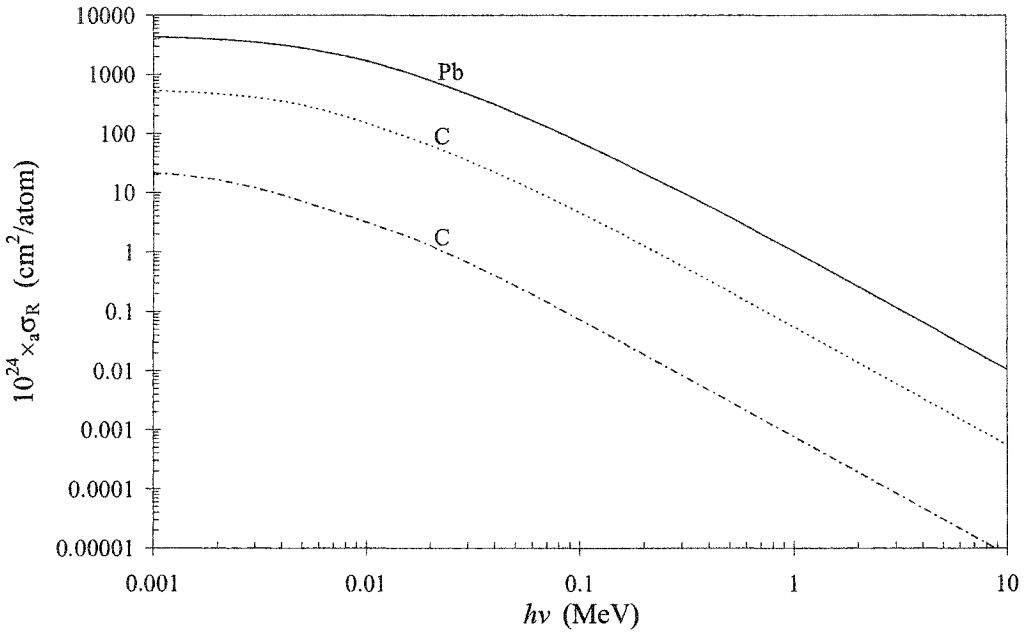


*FIG. 2.5. Atomic cross sections for Rayleigh (coherent) scattering* ${}_a\sigma_R$ *in carbon, copper, and lead.*

Although FIG. 2.5 shows that ${}_a\sigma_R$ is maximum at photon energies of the order of a few keV, a 1 keV photon has a much greater probability to interact with media through the photoelectric process, since the atomic cross section for photoelectric ${}_a\tau$ is about 1000 times larger than that for ${}_a\sigma_R$ at 1 keV.

### 2.3.6. Photonuclear interactions

In photonuclear interactions, an energetic photon interacts with the atomic nucleus which then emits a proton [(γ,p) reaction] or a neutron [(γ,n) reaction]. The kinetic energy of the ejected nucleon essentially equals the energy of the incoming photon minus the nucleon's binding energy. Photonuclear reactions (γ,p) may thus be considered a nuclear Compton effect when the photon's energy is much larger than the binding energy of the nucleon. Similarly to pair and triplet production, photonuclear reactions have a threshold photon energy below which no reaction can take place. The threshold energy is different from the average binding energy per nucleon and lies in the energy region between 6 and 16 MeV for most stable middleweight and heavyweight isotopes (the average binding

energy per nucleon for most nuclei is between 7 and 9 MeV). A notable exception is the deuteron with a photonuclear threshold energy of 1.2 MeV.

The (γ,n) interaction has a greater practical importance compared to the (γ,p) interaction because the released neutrons may lead to problems in radiation protection. For clinical x-ray generators producing high energy photon beams with energies above 10 MV, the emerging beam will be contaminated with neutrons; and the degree of neutron contamination will depend on the beam energy and on the design of the generator. Hence, the presence of neutrons must be considered in room and equipment shielding design, especially since neutrons propagate through mazes much more effectively than photons do.

Furthermore, photon absorption by very heavy nuclei can also induce fission. In various isotopes of thorium, uranium and plutonium, the threshold photon energy for photofission occurs between 5 and 5.5 MeV.

The probability of photonuclear and fission reactions is much smaller than the combined probabilities for the other photon interactions, namely, photoelectric, Rayleigh and Compton scattering, as well as pair and triplet production. Therefore, photonuclear and fission reactions are usually not considered in the calculation of the absorbed energy in the irradiated medium. The cross section for photonuclear reactions and photofission is on the order of $10^{-27}$ cm$^2$/atom, in comparison with typical photoelectric, Compton scattering, and pair production atomic cross sections on the order of $10^{-24}$ cm$^2$/atom.

### 2.3.7. Total mass attenuation coefficient $(\mu/\rho)$

In radiation physics, it of often more practical to convert the electronic and atomic cross sections for a particular interaction into macroscopic quantities, such as linear or mass attenuation coefficients. The mass attenuation coefficient for a particular interaction can be calculated by multiplying the corresponding atomic cross section by the conversion factor $N_A/A$, where $A$ is the atomic mass of the medium (in g/g-atom), and $N_A$ is Avogadro's constant ($N_A = 6.022\times10^{23}$ atoms/g-atom). Note that the atomic cross

section for Compton scattering ${}_a\sigma$ for a particular medium is equal to the Compton electronic cross section ${}_e\sigma$ multiplied by the atomic number of the medium $Z$.

The total mass attenuation coefficient $\mu/\rho$ is the sum of the individual mass attenuation coefficients for the various processes by which photons interact with matter. Since photonuclear reactions have a cross section several orders of magnitude lower than that for the other processes, in principle we can ignore them and write

$$\mu/\rho = (\tau/\rho) + (\sigma/\rho) + (\sigma_R/\rho) + (\kappa/\rho), \tag{2.13}$$

where $\kappa/\rho$ is the sum of the pair and triplet production mass attenuation coefficients and $\tau/\rho$, $\sigma/\rho$, and $\sigma_R/\rho$ are the mass attenuation coefficients for the photoelectric effect, Compton scattering, and Rayleigh scattering processes, respectively. Data for photon interaction cross sections and mass attenuation coefficients in various elements and compounds of interest are found in many references, the most notable are data compiled by McMaster[8], Storm and Israel[9], and Hubbel[10,11].

Figure 2.6 plots the mass attenuation coefficient $\mu/\rho$ and the partial attenuation coefficients $\sigma_R/\rho$, $\tau/\rho$, $\sigma/\rho$, and $\kappa/\rho$ as a function of photon energy $h\nu$ in water and lead based on data from the National Institute of Standards and Technology (NIST) [XCOM: Photon Cross Sections Database] compiled by Berger, Hubbell, and Seltzer. The XCOM photon cross sections database is available online at the following URL address:

*http://physics.nist.gov/PhysRefData/Xcom/Text/XCOM.html*

The relative contributions $\sigma_R/\rho$, $\tau/\rho$, $\sigma/\rho$, and $\kappa/\rho$ to $\mu/\rho$ for water and lead are shown in FIG. 2.7.

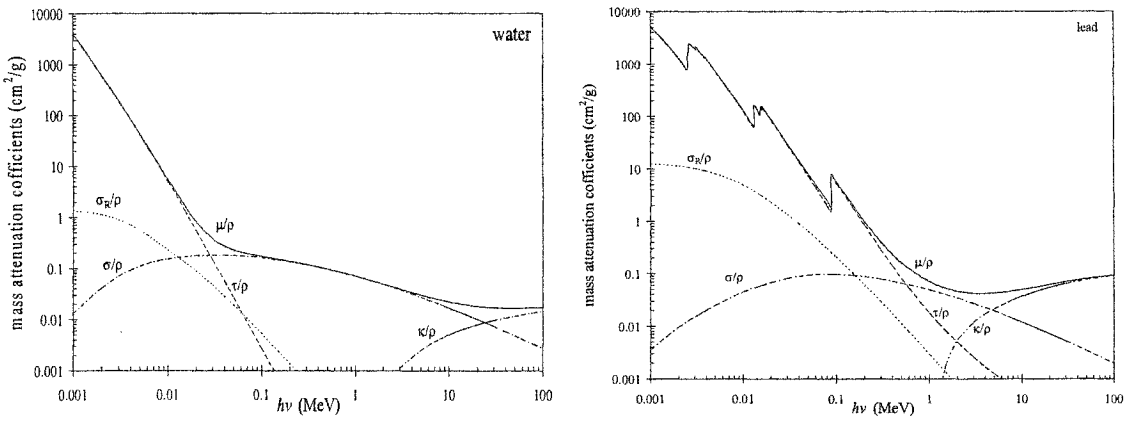


*FIG. 2.6. The total mass attenuation coefficient and the partial mass attenuation coefficients (photoelectric, Compton and Rayleigh scattering, and total pair production) for water and lead.*

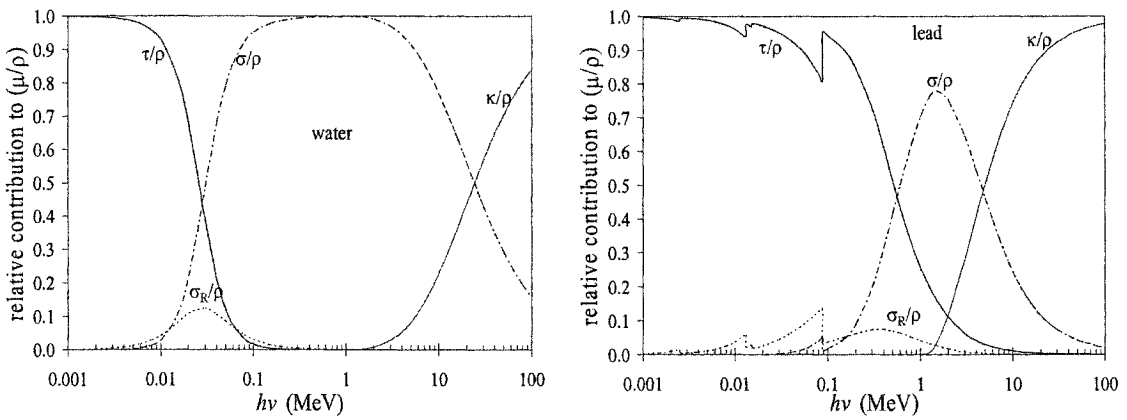


*FIG. 2.7. Relative contribution of photoelectric $\tau/\rho$, Compton $\sigma/\rho$ and Rayleigh $\sigma_R/\rho$ scattering, and pair production $\kappa/\rho$ mass attenuation coefficients to the total mass attenuation coefficient for water and lead.*

### 2.3.8. Mass energy transfer coefficient ($\mu_{tr}/\rho$) and kerma calculation for photons

The various processes by which photons interact with media result in transferring part or all of the interacting photon energy (except in Rayleigh scattering) to energetic charged particles with a very small amount of energy transferred to the atom as a whole. In general, any kinetic energy transferred to the atom or ionized atom is negligible. The energetic charged particle can be either an orbital electron (in photoelectric effect and Compton scattering) or an electron-positron pair (in pair production) or both (in triplet

production). Moreover, the ejected orbital electron loses part of its energy gained from the interaction to overcome its atomic binding energy. In post-irradiation processes, some of this "lost" energy may be given to an Auger electron produced in the de-excitation of the atom. At high photon energies, the energy dispensed by the ejected orbital electron to overcome its atomic binding energy is negligible in comparison to the energy gained by the interaction, and one can assume that the total energy transferred from the photon is essentially carried by the ejected orbital electron.

In radiation dosimetry the energy absorbed by matter exposed to radiation is of great interest and importance. For a photon fluence incident on a medium, the fraction of the incident photon energy that is transferred from the incident photons to electrons in the medium is found by the mass energy transfer coefficient $\mu_{tr}/\rho$, which is related to the mass attenuation coefficient $\mu/\rho$ through

$$\frac{\mu_{tr}}{\rho} = \frac{\mu}{\rho} \cdot \frac{\overline{E_K}}{h\nu}, \tag{2.14}$$

where $\overline{E_K}$ is the mean energy transferred to charged particles (electrons and positrons), averaged over a large number of interactions. Similarly to the method used in Eq. (2.13), we may express $\mu_{tr}/\rho$ as the sum of the individual mass energy transfer coefficients for the photoelectric $\tau_{tr}/\rho$, Compton $\sigma_{tr}/\rho$, and pair production $\kappa_{tr}/\rho$ processes

$$\mu_{tr}/\rho = (\tau_{tr}/\rho) + (\sigma_{tr}/\rho) + (\kappa_{tr}/\rho). \tag{2.15}$$

The mass energy transfer coefficient for Rayleigh scattering is essentially zero, since, in Rayleigh scattering, no energy is transferred to electrons.

The mass energy transfer coefficient $\mu_{tr}/\rho$ allows a direct calculation of an important dosimetric quantity called *kerma* $K$. Kerma, an acronym for kinetic energy released in matter, is associated with indirectly ionization radiation only (photons and neutrons). For a photon beam having a photon energy fluence spectrum $\Psi_{h\nu}(h\nu)$ present at point $Q$ in an irradiated medium, the *kerma* $K$ at $Q$ is given by

$$K = \int_0^{h\nu_{max}} \Psi_{h\nu}(h\nu) \left(\frac{\mu_{tr}}{\rho}\right)_{h\nu,Z} \mathrm{d}(h\nu). \tag{2.16}$$

### 2.3.9. Mass energy absorption coefficient $(\mu_{ab}/\rho)$

Secondary charged particles (electrons or positrons) produced by photons interacting in an absorbing medium lose their energy through Coulomb collisions with orbital electrons in the medium or nuclei of the medium. Electron-orbital electron interactions may result in excitations and ionizations of atoms (collision loss), while the electron-nucleus interactions result in bremsstrahlung loss by the electron (radiative loss). The absorbed dose in medium is attributed only to the collision losses. If the fraction $g$ of the secondary electron kinetic energy is lost to bremsstrahlung production, the mass energy absorption coefficient $\mu_{ab}/\rho$ can be related directly to the mass energy transfer coefficient $\mu_{tr}/\rho$ as

$$\frac{\mu_{ab}}{\rho} = \frac{\mu_{tr}}{\rho}(1-g). \tag{2.17}$$

In dosimetry the mass energy absorption coefficient $\mu_{ab}/\rho$ plays an important role in calculating the absorbed dose in a medium exposed to photon radiation. The absorbed dose in a biological medium is of great importance in treatment of cancer with radiation and in health physics. Whereas the mass attenuation coefficient $\mu/\rho$ and the mass energy transfer coefficient $\mu_{tr}/\rho$ are evaluated based on $h\nu$ and $Z$ of the medium where the photon interaction actually takes place, $\mu_{ab}/\rho$ must be evaluated based also on the medium surrounding the point of interaction.

When the point of interaction is surrounded by the same homogenous medium of radius $r$ equal to at least the maximum range of charged particles produced by the interaction, the fraction $g$ is evaluated based on the same $Z$ used in evaluating $\mu/\rho$ and $\mu_{tr}/\rho$. Table of $\mu_{ab}/\rho$ data are calculated based on this assumption. Consequently, one must not use such data in evaluating the dose near interfaces between dissimilar media.

## 2.4. INTERACTIONS OF NEUTRONS WITH MATTER

### 2.4.1. Types of interactions

Similarly to photons, neutrons may penetrate matter without interacting or they may interact with matter through several possible means: *elastic*, *inelastic*, and *nonelastic scattering* with nuclei, *neutron capture* by nuclei, or by causing *spallation*. In dosimetry, the importance of each of these reactions for a given neutron energy is governed by the following :

1) the relative abundance in the particular medium of the isotopes involved in the reactions.
2) the relative reaction cross section.
3) the type and energy of the reaction products.

In *elastic scattering* a neutron collides with a nucleus of mass $M$ that recoils with an angle $\phi$ with respect to the neutron's initial direction of incidence. During the interaction, an energy $\Delta E_K$ is transferred to the struck nucleus. For a neutron with a kinetic energy $E_K$ before the collision, the energy transferred to the nucleus of rest mass $M$ is given by the following relationship

$$\Delta E_K = E_K \frac{4Mm_n}{(M+m_n)^2}\cos^2\phi, \tag{2.18}$$

where $m_n$ is the neutron rest mass ($m_n = 939.6\,\mathrm{MeV}/c^2$). If scattering is isotropic in the center-of-mass system[12], the average energy transferred to the nucleus $\overline{\Delta E_K}$ becomes

$$\overline{\Delta E_K} = E_K \frac{2Mm_n}{(M+m_n)^2}, \tag{2.19}$$

while the maximum transferred energy $\Delta E_{max}$ is

$$\Delta E_{max} = E_K \frac{4Mm_n}{(M+m_n)^2}. \tag{2.20}$$

For the four most important constituent elements of tissue (H, C, N, and O), the mean energy transfers $\overline{\Delta E_K}$ are $0.5E_K$, $0.142E_K$, $0.124E_K$, and $0.083E_K$ to H, C, N, and O atoms, respectively. The neutron elastic scattering cross section[13-15] generally decreases

with increasing neutron energies (except at resonance peaks). At low energies, the decrease in elastic cross sections is rapid and becomes slower at higher neutron energies.

In *inelastic scattering*, a neutron is "temporarily" captured by a nucleus and then re-emitted with a lower energy and in a direction different from the incident direction. The nucleus is left in an excited state and will de-excite by emitting high energy gamma rays within a time range of nanoseconds to seconds. Cascade gamma ray emissions are also possible in the event that the nucleus is excited to levels greater than the first excitation level[16].

*Nonelastic scattering* refers to neutron reactions with nuclei resulting in the emission of particles other than a single neutron, for example, $O^{16}(n,\alpha)C^{13}$. Cross sections for noneleastic scattering processes become significant at neutron energies above 5 MeV. The emitted protons and alpha particles resulting from the nuclear interactions are of special importance, because they deposit their energies near the reaction site. Additionally, in most of nonelastic scattering reactions, de-excitation of the nuclei through emission of gamma rays follows the nuclear reaction.

Thermal neutrons, *i.e.*, neutrons with energies $E_K \leq 0.5$ eV, may be captured by a nucleus leading to the emission of a proton or gamma rays; a process known as *neutron capture*. In tissue two important reactions are of particular importance, namely, the $N^{14}(n,p)C^{14}$ and $H^1(n,\gamma)H^2$ reactions. The emitted proton ($E_{K_p} = 0.58$ MeV) and the recoil $C^{14}$ nucleus ($E_{K_{C^{14}}} = 0.04$ MeV), resulting from the thermal neutron reaction with nitrogen, deposit an energy of 0.62 MeV locally. The neutron-hydrogen reaction produces a 2.2 MeV gamma ray that generally interacts in a remote location. Even though the cross section for neutron-nitrogen capture ($\sigma_N = 1.84\times10^{-28}$ m$^2$/atom) is greater than that for the neutron-hydrogen capture process ($\sigma_H = 0.332\times10^{-28}$ m$^2$/atom), the probability for neutron-hydrogen capture in tissue is greater, because of the relative abundance of hydrogen atoms to nitrogen atoms in tissue (41 to 1).

Neutrons with sufficiently high energies may cause a nucleus to fragment, resulting in the ejection of several particles as well as nuclear fragments. This process is referred to as

*spallation* and becomes significant only at neutron energies of about 100 MeV or greater. Most of the energy released from the spallation process is carried by the heavy fragments that eventually deposit their kinetic energies locally. However, neutrons and de-excitation gamma rays produced by spallation usually carry some of the released energy to a remote location.

### 2.4.2. Kerma calculation for neutrons

Unlike in photon beams, it is customary to describe neutron beams in terms of the particle fluence spectrum $\Phi_{E_K}(E_K)$ rather than the energy fluence spectrum $\Psi_{E_K}(E_K)$. For a monoenergetic neutron fluence $\Phi$ undergoing a specific type of interaction with a particular atom in a point in medium, the *kerma* $K_i$ in a small mass $m$ is expressed as

$$K_i = \Phi \sigma_i \frac{N}{m} \overline{(\Delta E_K)_i} . \tag{2.21}$$

where $\sigma_i$ is the interaction cross section, $N$ the number of target atoms in the irradiated mass, and $\overline{(\Delta E_K)_i}$ the mean energy transferred to charged particles through the particular interaction. The product $\sigma_i N/m$ summed over all possible interactions is simply the mass attenuation coefficient for neutrons $\mu/\rho$ in the material. Following the same convention as for photon beams, we may define the mass energy transfer coefficient $\mu_{tr}/\rho$ for neutrons as the product of the mass attenuation coefficient $\mu/\rho$ and the fraction of the neutron energy transferred to charged particles $\overline{\Delta E_K}/E_K$. When all possible interactions are considered, the total *kerma* $K$ in mass of medium $m$ is expressed as

$$K = \Phi \left( \frac{\mu_{tr}}{\rho} \right) E_K , \tag{2.22}$$

where $E_K$ is the kinetic energy of the neutron beam.

The ICRU Report 13 (ref. 17), based on Caswell[18], tabulates data of the product $(\mu_{tr}/\rho)E_K$, called the *neutron kerma factor* $F_n$, instead of $\mu_{tr}/\rho$. The neutron kerma factor $F_n$ values in several elements and media of importance in dosimetry as a function of neutron energy are plotted in FIG. 2.8. Because of the presence of resonance peaks in

neutron nuclear reaction cross sections, $F_n$ is generally not a smooth function of the kinetic energy $E_K$ and the atomic number of the medium $Z$. Unlike in photon interaction cross sections, interpolation of $F_n$ versus $Z$ must generally not be used as means to determine the $F_n$ values for other elements or media; however, the interpolation of $F_n$ versus $E_K$ can be employed in regions where resonance peaks are absent. The kerma $K$ at point $Q$ in the medium resulting from a neutron fluence spectrum $\Phi_{E_K}(E_K)$ present at $Q$ can be calculated using the kerma factor $F_n$ as follows

$$K = \int_0^{E_{max}} \Phi_{E_K}(E_K)\ F_n(E_K, Z)\ dE_K . \tag{2.23}$$

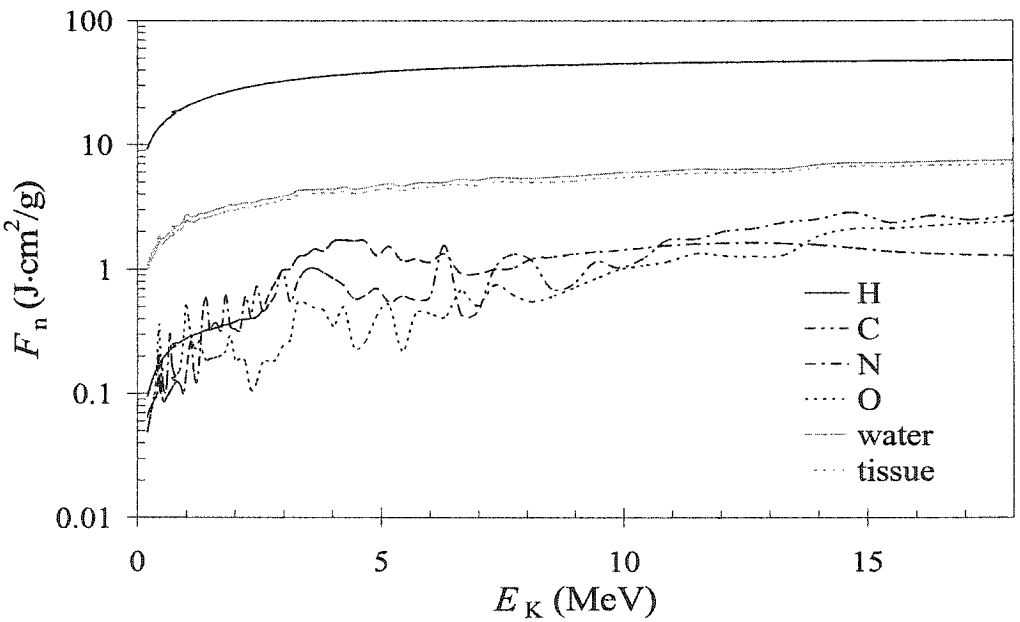


*FIG. 2.8. The neutron kerma factor $F_n$ against kinetic energy $E_K$ in H, C, N, O, water, and tissue based on the ICRU Report 13 (ref. 17) data.*

## 2.5. INTERACTIONS OF CHARGED PARTICLES WITH MATTER

A charged particle, through its associated electrical field, interacts with one or more orbital electrons or with the nucleus of every atom it passes. Hence, unlike photons and neutrons, charged particles cannot pass through a layer of matter without some type of interaction. Most of these individual interactions result in a small transfer of energy from by the incident charged particle to the medium. Charged particles having kinetic energies of a few MeV would undergo about $10^5$ interactions before losing all of their kinetic energy in the medium. Hence, it is convenient to think that charged particles lose their energy, as they move through medium, gradually and continuously. This continuous process of charged particle energy loss is referred to as the *continuous slowing down approximation* (CSDA).

### 2.5.1. Types of interactions

Charged particle Coulomb-force interactions can be characterized in terms of the classical impact parameter $b$ with respect to the classical size of the atom $a$, as illustrated in FIG. 2.9. Depending on the magnitude of $b$ in comparison to $a$, one of three types of charged particle interactions dominates, namely soft collisions, hard collisions, and interactions with the nuclear Coulomb field.

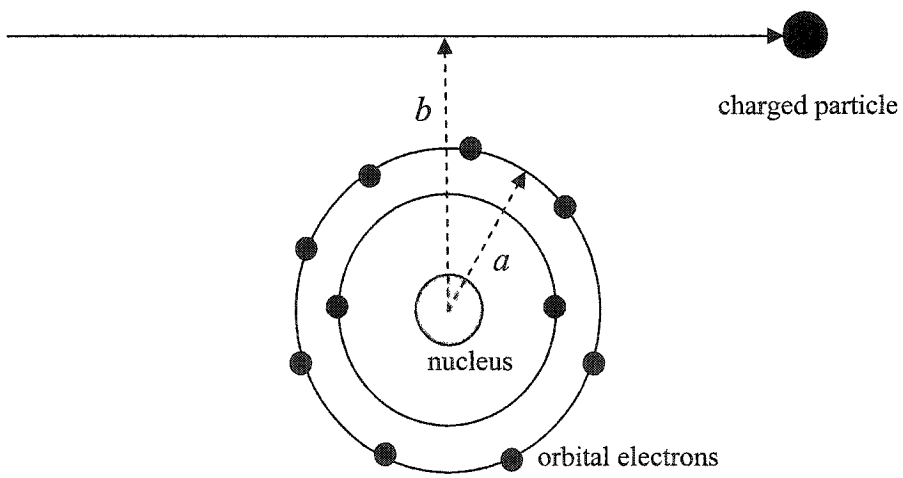


*FIG. 2.9. The classical atomic radius a and the impact parameter b are used to characterize charged particle interaction with an atom. Soft collision: $b >> a$; hard collision $b \approx a$; nuclear collision: $b << a$.*

*Soft collisions* refer to interactions of distant charged particles with a particular atom, *i.e.*, for $b >> a$. The individual atom interacts as a whole with the passing charged particle and may become excited or ionized, if an orbital electron is ejected. Charged particles dispense approximately half of their total kinetic energy into media through a large number of soft collisions.

When the impact parameter $b$ is on the order of the classical atomic radius $a$, the charged particle may interact directly with a single orbital electron. This type of interaction is referred to as a *hard collision*. The orbital electron, knocked-out by the charged particle is called a delta ($\delta$) ray. It gains a considerable amount of kinetic energy from the impact and travels through the medium on a path of its own, while interacting with other atoms in the medium. Although a charged particle undergoes only a small number of hard collisions compared to the number of soft collisions before losing all of its kinetic energy, the amounts of energy lost by the charged particle through these two processes are generally comparable. The ejection of a $\delta$ ray will be followed by emission of characteristic x rays or by ejection of Auger electrons, just as if the orbital electron had been ejected by a photon interaction or captured by the nucleus.

In situations where the impact parameter $b$ of a charged particle is much smaller than the atomic radius $a$, the charged particle mainly interacts with the nuclear Coulomb field. This type of interaction is very important for energetic electrons and positrons and essentially negligible for heavy charged particles. In most events (~98% of such encounters), the electron is elastically scattered and no emission of x rays or excitation of the atom occurs. The elastically scattered electron will lose an insignificant amount of energy in order to conserve momentum in the collision. Hence, the elastic scattering does not transfer energy to the medium but it is an important mechanism for deflecting electrons from their original path. In the remaining 2% of the electron-nucleus encounters, the electron is inelastically scattered by the nucleus and suffers a significant deceleration in the nuclear field. This results in a change of electron's direction of motion and is accompanied by an emission of a high energy photon. The emitted photon is referred to as *bremsstrahlung photon*, a Germen term for "braking radiation".

## 2.5.2. Stopping power

Under CSDA, the average energy loss $dE_K$ by a charged particle traversing a medium through any type of interaction per unit of path length $dx$ is called the *linear stopping power* $S$. The *mass stopping power* $S/\rho$ is obtained by dividing the linear stopping power by the density $\rho$ of the traversed medium; hence

$$\frac{S}{\rho} = \frac{1}{\rho}\frac{dE_K}{dx}. \tag{2.24}$$

The mass stopping power $S/\rho$ can be subdivided into the *mass collision stopping power* $(S/\rho)_{col}$ which accounts for the energy lost by the charged particle through hard and soft collisions only (collision loss) and the *mass radiative stopping power* $(S/\rho)_{rad}$ which accounts for the bremsstrahlung production energy losses (radiative loss). The separation of $S/\rho$ into collision and radiative parts is important in dosimetry, since both components contribute differently to the absorbed dose in the medium. The energy lost through collisions contributes to the absorbed dose in the volume surrounding the charged particle track, whereas bremsstrahlung photons carry energy away from the point of interaction; therefore, radiative losses do not contribute to the local dose. Because radiative losses are only important for electrons and positrons, $(S/\rho)_{rad}$ for heavy charged particles is essentially zero and the total mass stopping power equals the collision stopping power.

Based on theoretical derivations by Livingston and Bethe[19], Bloch[20], Lindhard[21], Anderson *et al.*[22], Ritchie and Brandt[23], and Ashley[24-25], the ICRU Report 37 (ref. 26) in section 2.2 provides formulae from which $S/\rho$ for heavy charged particles can be calculated. The mass stopping power $S/\rho$ for protons and alpha particles in water, based on the ICRU Report 37, is shown in FIG. 2.10.

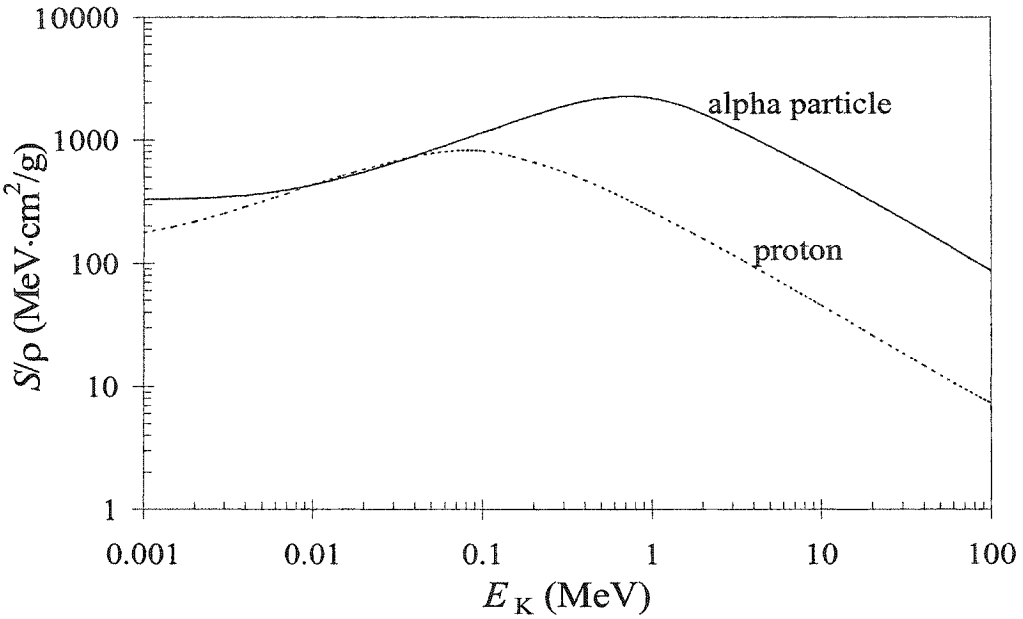


*FIG. 2.10. Mass stopping powers for alpha particles and protons in water against the kinetic energy $E_K$, based on the ICRU Report 37 (ref. 26).*

In addition, the ICRU Report 37 (ref. 26) in Section 2.3 provides means for calculating $(S/\rho)_{col}$ for electrons and positrons, based on the work by Bethe[6,27], Rohrlich and Carlson[28], and Uehling[29]. Data for electrons $(S/\rho)_{rad}$ can be found in the ICRU Report 37 (ref. 26) in Section 9. The mass collision stopping power $(S/\rho)_{col}$ and the mass radiative stopping power for electrons in water as a function of the kinetic energy $E_K$, based on the ICRU Report 37, are shown in FIG. 2.11.

### 2.5.3. Radiation yield

The fraction of the initial energy of the charged particle that is converted into bremsstrahlung is called the *radiation yield* $Y(E_K)$. Since radiative losses are important only for electrons and positrons, the radiation yield for heavy charged particles is essentially zero.

The radiation yield $Y(E_0)$ for an electron of initial kinetic energy $E_0$ is given by

$$Y(E_0) = \frac{1}{E_0}\int_0^{E_0} y(E_K)\,dE_K, \tag{2.25}$$

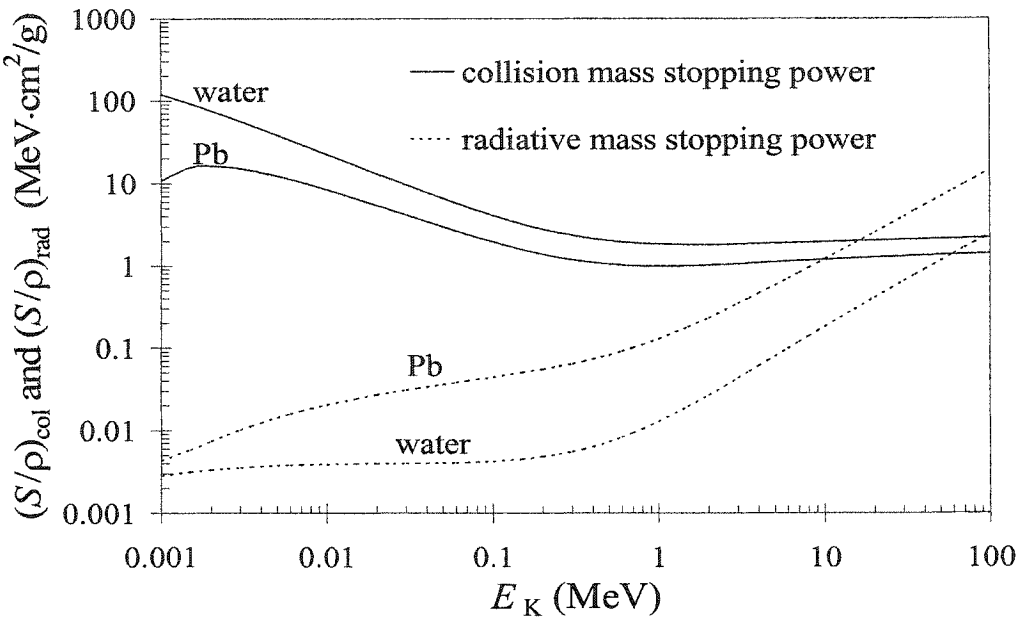


*FIG. 2.11. Collision and radiative mass stopping powers for electrons in water as a function of the kinetic energy $E_K$, based on the ICRU Report 37 (ref. 26).*

where $y(E_K)$ is the instantaneous radiation yield which is defined as

$$y(E_K) = \frac{(S/\rho)_{rad}}{S/\rho}. \tag{2.26}$$

Because the mass stopping powers $(S/\rho)_{rad}$ and $S/\rho$ are essentially based on the CSDA, Eqs. (2.25) and (2.26) characterize the radiation yield of the primary charged particle only. Any bremsstrahlung produced by secondary orbital electrons is not included. By contrast, the $g$ factor that relates $\mu/\rho$ and $\mu_{tr}/\rho$ for photon beams in Eq. (2.17) is the fraction of the radiative energy loss to the total energy loss of all primary electrons of energy $E_0$ that are generated by the photon beam including radiative losses by all secondary electrons generated from the interaction of the primary electrons with the medium.

### 2.5.4. Charged particle range

The expectation value of the pathlength that a charged particle will follow until it losses all of its kinetic energy and completely stops is defined as the *particle range* $\Re$. Under the assumption that charged particles lose their energy continuously, the range of a charged particle $\Re_{\mathrm{CSDA}}$ with an initial kinetic energy $E_0$ is defined as

$$\Re_{\mathrm{CSDA}} = \int_0^{E_0} \frac{\mathrm{d}E_{\mathrm{K}}}{(S/\rho)}. \tag{2.27}$$

Discrete and discontinued energy losses of charged particles may also take place, but for practical purposes $\Re_{\mathrm{CSDA}}$ is assumed to be equal to $\Re$. The *projected range* $\langle t \rangle$ of a charged particle is defined as the expectation value of the farthest depth of penetration of the charged particle in its initial direction.

### 2.5.5. Restricted mass collision stopping power

When a charged particle interacts with orbital electrons through soft and hard collisions, secondary electrons are released. These secondary electrons will have a kinetic energy ranging from zero to a maximum possible energy. The maximum possible energy transferred to secondary electron from a primary charged particle depends on the mass and type of the primary charged particle, as well as on its kinetic energy $E_{\mathrm{K}}$. For electrons, the maximum energy transferred $\Delta E_{\max}$ is $E_{\mathrm{K}}/2$ (incident electron and orbital electron are indistinguishable particles); for positrons, $\Delta E_{\max}$ is $E_{\mathrm{K}}$ (incident positron and orbital electron have identical masses but are distinguishable particles); and for heavy charged particles, such as protons, $\Delta E_{\max}$ is given by

$$\Delta E_{\max} = \frac{2m_{\mathrm{e}}M^2c^2\gamma^2\beta^2}{(m+M)^2 + 2mM(\gamma-1)}, \tag{2.28}$$

where $m_e$ is the electron rest mass and $M$ is the rest mass of the heavy charged particle.

In dosimetry, one is often interested in the energy absorbed in a predefined volume of matter. Since a primary charged particle interacting in the predefined volume will essentially produce a spectrum of secondary electrons, some of these secondary electrons may have a sufficient kinetic energy to leave the particular volume of interest when this

volume of interest is smaller than the maximum range of the secondary electrons. In radiobiology, for example, the volume of interest becomes on the order of the cell size and the use of $(S/\rho)_{col}$ to calculate the absorbed dose will always overestimate the energy deposited within the volume of interest.

The restricted mass collision stopping power $L_\Delta/\rho$, unlike $(S/\rho)_{col}$, accounts only for the energy that is deposited in a particular volume of interest by secondary electrons with energies up to a cut-off energy Δ. The choice of Δ depends on the chosen volume size for the particular application. In radiobiology, for example, Δ would appropriately be the energy of an electron that has a range $\Re$ of the order of the dimension of a typical cell. Consequently, the concept of restricted collision stopping power has become a useful concept in transport algorithms for charged particles in Monte Carlo simulation codes. Algorithms will track the transport of a charged particle till its energy falls below the chosen cut-off energy Δ, where all the particle energy is then deposited in the local region. Figure 2.12 compares $L_\Delta/\rho$ for selected cut off energies Δ to the unrestricted mass collision stopping power $(S/\rho)_{col}$ for electrons in water as a function of kinetic energy. The ICRU Report 37 (ref. 26) in Section 7 provides means for evaluating the restricted stopping power for electrons and positrons in any medium.

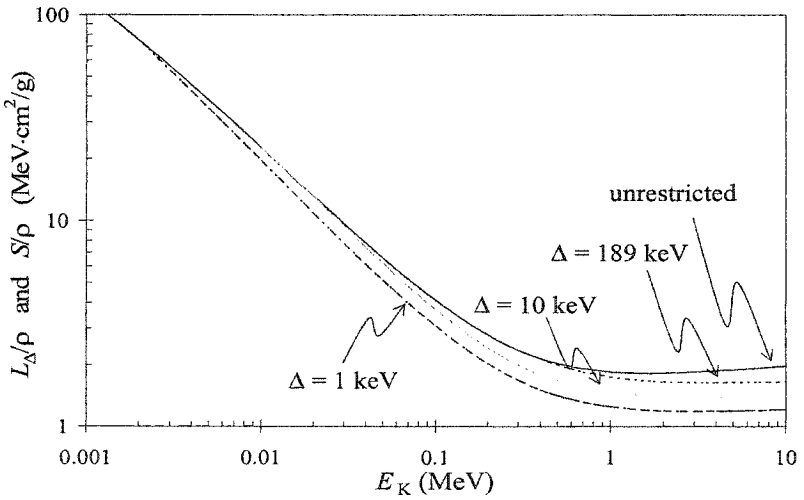


*FIG. 2.12. Comparison of unrestricted mass collision stopping powers and restricted mass collision stopping powers in water for electrons as a function of the electron kinetic energy $E_K$ for various values of the cut-off energy Δ.*

## 2.6. POST-INTERACTION PROCESSES

Photoelectric effect, Compton scattering, and triplet production processes can supply an orbital electron with an energy that exceeds the electron atomic binding energy. The event leads to the ejection of the orbital electron; hence, transforming the atom into a positive ion with a vacancy in its atomic shells. *Vacancies* in atomic shells can also be produced by Coulomb interactions of an energetic charged particle with orbital electrons, by electron capture and internal conversion nuclear decay processes, by annihilation of an orbital electron with a positron, and through Auger effect. Eventually the atom relaxes to its ground state by electrons from higher orbital shells filling the shell vacancies, resulting in the emission of characteristic photons or Auger electrons. The process is repeated several times, the vacancy cascades to the outer shell, and the positive ion eventually attracts an electron from its surroundings and reverts to a neutral atom.

Pair production and triplet production are followed by the *annihilation* of the positron with a "free" and stationary electron producing two annihilation photons, most commonly with an energy of 0.511 MeV each and emitted 180° from each other to satisfy the conservation of charge, energy, and momentum. In-flight positron annihilation may also occur and will produce one or two photons with energies exceeding 0.511 MeV.

## 2.7. SUMMARY

Photons, neutrons, and charged particles interact with media differently. The main processes by which photons interact with matter are: the *photoelectric effect*, *Compton* and *Rayleigh scattering*, and *pair* and *triplet production*. The cross sections and the attenuation coefficients for each of these interactions are a function of the incident photon energy and the atomic number $Z$ of the medim (see Table 2.1). At low photon energies, most photons interact with matter through the photoelectric effect; at 1 MeV Compton scattering dominates, and pair production becomes important at photon energies exceeding 10 MeV.

Neutrons interact with media through several processes. At very low energies, *neutron capture* is the most probable interaction. *Inelastic* and nonelastic scattering processes take place at neutron energies exceeding 2.5 MeV and 5.0 MeV , respectively, and become

important at neutron energies of about 10 MeV . For neutron energies above 20 MeV *nonelastic scattering* and *spallation* become important.

Charged particles interact with matter through *soft* and *hard collisions*. Electrons and positrons may, in addition, interact with nuclei, thereby generating bremsstrahlung radiation in the process referred to as *radiative collisions*.

In dosimetry, the absorbed dose in a homogeneous medium for a radiation beam depends on the radiation type and energy. For photon beams, the dose is calculated by using the mass energy absorption coefficient $\mu_{ab}/\rho$; for neutron beams, the neutron kerma factor $F_n$ is used; while for charged particles, restricted mass collision stopping powers are used.

TABLE 2.1. DEPENDENCE OF PHOTOELECTRIC, COMPTON AND RAYLEIGH SCATTERING, AND THE TOTAL PAIR PRODUCTION MASS ATTENUATION COEFFICIENTS ON THE ATOMIC NUMBER OF THE ATTENUATING MEDIUM $Z$ AND THE PHOTON ENERGY $h\nu$.

| interaction | Photoelectric | Compton | Pair production | Rayleigh |
|---|---|---|---|---|
| mass attenuation coefficient for given effect | $\frac{\tau}{\rho} \approx\!\propto \frac{Z^3}{(h\nu)^3}$ | $\frac{\sigma}{\rho} \approx\!\propto \frac{Z^0}{h\nu}$ | $\frac{\kappa}{\rho} \approx\!\propto Z\ln(h\nu)$ | $\frac{\sigma_R}{\rho} \approx\!\propto \frac{Z}{(h\nu)^2}$ |

# REFERENCES


1. ICRU, "Radiation quantities and units," Report 19, International Commission on Radiation Units and Measurements, Bethesda, MD (1971).
2. R. D. Evans, "X-ray and gamma ray interactions," In *Radiation dosimetry*, edited by F. H. Attix and W. C. Roesch (Academic Press, New York, 1968), Vol. 1, pp. 93-155.
3. J. H. Hubbell, "Photon Cross Sections, Attenuation Coefficients and Energy Absorption Coefficients from 10 keV to 100 GeV," Report NSRDS-NBS29, U.S. National Bureau of Standards (1969).
4. R. D. Evans, *The Atomic Nucleus* ( McGraw-Hill, Malabar, Florida, 1982).
5. O. Klein and Y. Nishina, "Über die streuung von Strahlung durch freie Elktronen nach der neuen relativistischen Quantendynamik von Dirac," Physik **52**, 853-868 (1929).
6. H. Bethe and W. Heitler, "On the stopping of fast particles and on the creation of positive electrons," Proc. Roy. Soc. A. **146**, 83-112 (1934).
7. J. H. Hubbell, W. J. Veigele, E. A. Briggs et al., "Atomic form factors, incoherent scattering functions and photon scattering cross section," J. Phys. Chem. Ref. Data **4**, 471-538 (1975).
8. W. H. McMaster, N. K. Del Grande, J. R. Mallett, and J. H. Hubbell, "Compilation of x-ray cross sections," Report UCRL-50174, Section 11, Rev.1, Univ. of Calif., Livermore, CA (1969).
9. E. Storm and H. I. Israel, "Photon cross sections from 1 keV to 100 MeV for elements from $Z$ = 1 to $Z$ = 100," In *Nuclear Data Tables*, (Academic Press, New York, NY, 1970), Vol. A7, pp.565-681.
10. J. H. Hubbell, H. A. Gimm, and I. Øverbø, "Pair, triplet and total cross sections for 1 MeV-100 GeV photons in elements $Z$ = 1-100," J. Phys. Chem. Ref. Data **9**, 1023-1147 (1980).
11. J. H. Hubbell, "Photon mass attenuation and energy absorption coefficients from 1 keV to 20 MeV," Int. J. Appl. Rad. Isot. **33**, 1269-1290 (1982).
12. M. D. Goldberg, V. M. Way, and J. R. Stehn, *Angular distributions in neutron-induced reactions* Brookhaven Natl. Lab. Rept. BNL-400 2nd ed., Vol. I (1962).
13. D. J. Hughes and R. B. Schwatrz, *Neutron cross sections* Brookhaven Natl. Lab. Rept. BNL-325 2nd ed. (1958).
14. D. J Hughes, B. A. Magurno, and M. K. Brussel, *Neutron cross sections* Brookhaven Natl. Lab. Rept. BNL-325 Suppl. 1 2nd ed. (1960).
15. J. R. Stehn, M. D. Goldberg, B. A. Magurno, and R. Wiener-Chasman, *Neutron cross sections* Brookhaven Natl. Lab. Rept. BNL-325 Suppl. 2. Vol. I (1964).
16. F. Ajzenberg-Selove and T. Lauritsen, "Energy levels of light nuclei," Nucl. Phys. **11**, 1 (1959).
17. ICRU, "Neutron fluence, neutron spectra and kerma," Report 13, International Commission on Radiation Units and Measurements, Washington, D.C. (1969).
18. R. S. Caswell, J. J. Coyne, and M. L. Randolph, "Kerma factors for neutron energies below 30 MeV," Rad. Res. **83**, 217 (1966).
19. M. S. Livingston and H. A. Bethe, "Nuclear physics," Rev. Mod. Phys. **9**, 282 (1937).
20. F. Bloch, "Zur bremsung rasch bewegter Teilchen beim Durchgang durch Materie," Ann. Phys. **16**, 285 (1933).

21. J. Lindhard, "The Barkas effect, or $Z_1^3 - Z_1^4$ corrections to stopping of swift charged particles," Nucl. Instrum. Meth. **132**, 1 (1976).

22. H. H. Andersen, J. F. Bak, H. Knudsen, and B. R. Nielsen, "Stopping power of Al, Cu, Ag, and Au for MeV hydrogen , helium, and lithium ions. $Z_1^3$ and $Z_1$ proportional deviations from the Bethe formula," Phys. Rew. **B16**, 1929 (1977).

23. R. H. Ritchie and W. Brandt, "Projectile charge dependence of stopping powers," Phys. Rev. **A17**, 2102 (1978).

24. J. C. Ashley, R. H. Ritchie, and W. Brandt, "$Z_1^3$ effect in the stopping power of matter for charged particles," Phys. Rev. **B5**, 2393 (1972).

25. J. C. Ashley, R. H. Ritchie, and W. Brandt, "$Z_1^3$ dependents stopping power and range contributions," Phys. Rev. **A8**, 2402 (1973).

26. ICRU, "Stopping powers for electrons and positrons," Report 37, International Commission on Radiation Units and Measurements, Bethesda, MD. (1984).

27. H. Bethe," Zur Theorie des Durchgangs schneller Korpuskularstrahlen durch Materie," Ann. Physik. **5**, 325 (1930).

28. F. Rohrlich and B. C. Carlson, "Positron-electron differences in energy loss and multiple scattering," Phys. Rev. **93**, 38 (1953).

29. E. A. Uehling, "Penetration of heavy charged particles in matter," Annual Rev. Nucl. Sci. **4**, 315 (1954).

# Chapter 3

# DOSE DETERMINATION WITH IONIZATION CHAMBERS

## 3.1. GAS-FILLED RADIATION DETECTORS

A typical gas-filled radiation detector with associated basic circuitry is shown schematically in FIG. 3.1. The instrument works on the principle that as radiation passes through a specific gas, ionization of gas atoms and molecules occurs. When a high voltage is applied between two electrodes placed in the gas-filled space, the positive ions are attracted to the negative electrode (cathode) and the free electrons (or negative ions in electro-negative gases) travel to the positive electrode (anode). The charges are collected by the anode and cathode resulting in a small current in the associated electric circuit. By placing a very sensitive current-measuring device into the circuit, the small ionization current is measured and displayed as a signal that is proportional to the radiation dose.

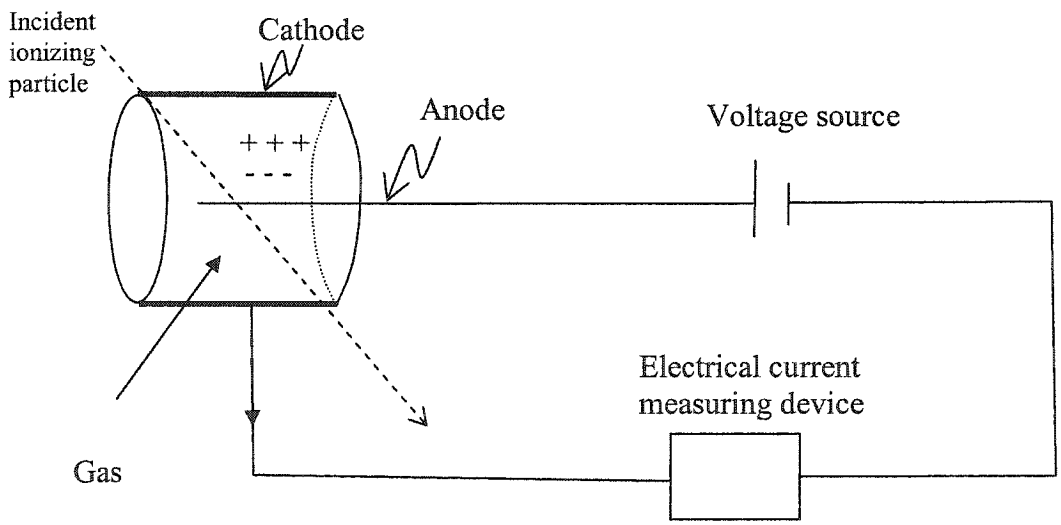


*FIG. 3.1. A schematic representation of a gas-filled radiation detector and associated circuitry.*

The magnitude of the signal produced in a gas-filled radiation detector depends on the incident particle type, fluence, and energy, as well as on the type of gas and magnitude of the applied voltage between the two electrodes. A typical graph of the variation of the pulse height generated in a gas-filled ionization chamber for alpha and beta radiation as a function of the applied voltage across the electrodes is shown in FIG. 3.2. In general, the pulse height increases with the increase in the applied voltage, but a careful analysis of the signal shows distinctive regions which predetermine the operation mode of the gas-filled radiation detector. Although for practical purposes a particular gas-filled radiation detector is operated only at one or a few of these regions, analyzing the full signal curve of FIG. 3.2 may help in understanding many ionization chamber dosimetry phenomena, such as ionic recombination, charge mobilities under the influence of an electric field, and charge multiplication, that govern the output signal of the detector[1-3].

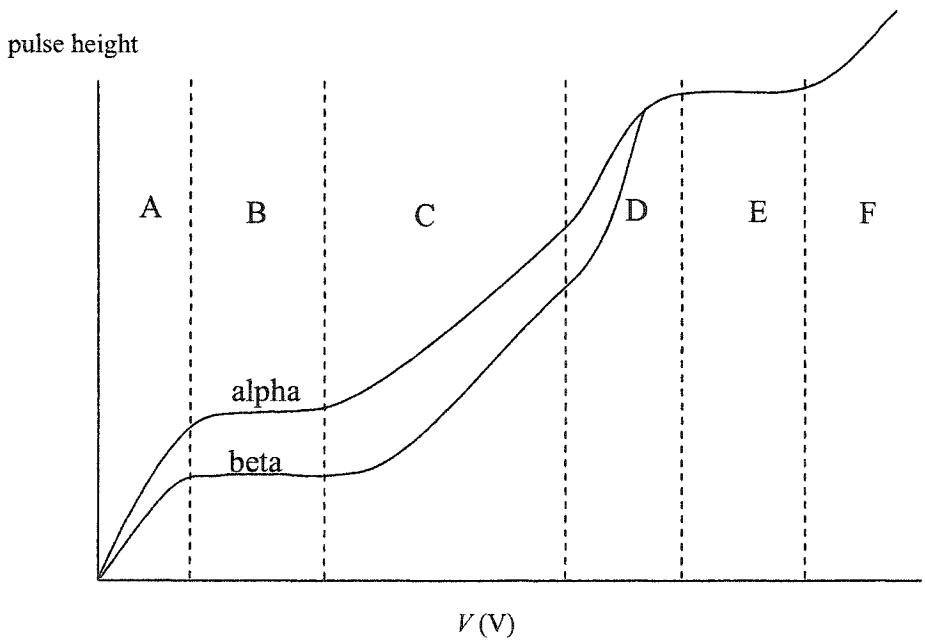


*FIG. 3.2. Variation of pulse height as a function of applied voltage in a gas-filled radiation detector. Region A is the recombination region; region B the saturation region; region C the proportionality region; region D the limited proportionality region; region E the Geiger-Müller region; and region F the continuous discharge region.*

- **Region A (recombination region):** When an incident ionizing particle interacts with a gas, positive ions and electrons (or negative ions) are produced. The applied voltage in this region is very low, such that many of the produced ion pairs recombine before they reach the electrodes. As the applied voltage is increased in this region, the drift velocity of the ions increases significantly. Hence, there is a corresponding decrease in the time available for ions to recombine, resulting in a sharp and almost linear increase in the pulse height measured by the detector. In addition, ions, as a result of collisions with other gas molecules, move toward the electrodes with a velocity that is directly proportional to the electric field strength. Gas-filled radiation detectors are not operated in this region of response for practical reasons; however, an analysis of the signal curve in this region helps in understanding the mechanisms of ionic recombination and charge mobility. Moreover, the pulse height produced in this region depends on the incident particle type and energy, in addition to the applied voltage. As shown in FIG. 3.2, a heavy alpha particle in general produces more ion pairs in air compared to a beta particle and this results in a larger measured signal in this region.

- **Region B (ionization chamber region):** The applied voltage in this region is sufficiently high so that only a small number of ionic recombinations occur. As the applied voltage is increased, the pulse height increases slowly and asymptotically approaches a saturation value $Q_{\text{sat}}$. This saturation value corresponds to the measured pulse height, if no ionic recombination or any other charge loss mechanism and no charge gain take place in the gas. Creating an ion pair in a gas requires a specific energy per unit charge $\left(\overline{W}_{\text{air}} / e\right)$. Consequently, this saturation value $Q_{\text{sat}}$ is of high interest for assessing many dosimetric quantities of interest, such as the exposure, air-kerma, and dose. Gas-filled detectors, operating in this response region, are referred to as *ionization chambers*. Ionization chambers are widely used in dosimetry, primarily for source output calibration in standards laboratories

and for radiation beam output calibration in radiotherapy clinics. Similarly to the recombination region A, the pulse height of the detector in this region depends on the incident charge particle type and energy, and on the applied voltage across the electrodes. The signal versus voltage relationship in regions A and B of FIG. 3.2 is commonly referred to as the *saturation curve*.

- **Region C (proportionality region):** In this region, the applied voltage is sufficiently high so that ions and electrons produced in the gas by the initial incident particle gain sufficient energy to produce new ion pairs as they collide with other gas molecules in moving toward the appropriate electrodes. This process is referred to as *charge gain* or *charge multiplication*. In the cylindrical detector, shown schematically in FIG. 3.1, the *charge multiplication* is limited to the region surrounding the anode where the electric field is the strongest. When drifting electrons enter this region they gain sufficient kinetic energy between successive collisions with gas molecules to become directly ionizing particles. The electrons released from these ionizing events may gain sufficient kinetic energy to produce additional ionizations and so on. As a result, an electron avalanche, often called the *Townsend avalanche*, arrives at the anode from each primary ionization produced by the incident ionizing particle.

  The radius of the cylindrical gas volume in which *charge multiplication* can occur expands with the increase in the applied voltage. The pulse height of the signal becomes proportional to the initial number of ion pairs produced in the gas by the incident ionizing particle and may be up to 1000 times larger than the initial charge. The factor by which the ionization increases is known as the *gas amplification factor* and it depends on the chamber design, the gas used, and on the magnitude of the applied voltage. Gas-filled detectors operating in this response region are called *proportional counters*. A typical *proportional counter* operates with a voltage high enough such that signal amplification takes place in the "multiplication" region confined to a fraction of a millimeter only around the central electrode. If a few primary ionizations are

produced in the gas volume, there will be no interactions between the avalanches and it is reasonable to assume that each avalanche produces the same signal at the anode. Consequently, the measured signal is directly proportional to the number of initial ion pairs produced by the incident particles. Because of charge multiplication, a *proportional counter* cannot provide any information about the energy deposited in the sensitive volume of the detector by the incident particle. Instead, it may be used as a counting device, if individual ionization events can be recorded separately.

- **Region D (limited proportionality region):** As the voltage is further increased, the region in which charge multiplication commences becomes larger and interactions between avalanches originating from different primary ionization events can take place. Because electrons are more mobile and are collected quickly in comparison with positive ions, the rapid collection of electrons leaves a "positive ion sheath" surrounding the anode. With increasing electric fields, the build-up of charges at the electrodes will eventually start to disturb and reduce the electric field inside the detector volume. As a result, the proportionality feature of the detector is lost in this region until it reaches a stage where no further charge multiplication can take place and the response of the detector becomes independent of the charge type and energy. For this reason, region D is referred to as the region of limited proportionality, and it has no practical applications in nuclear and medical physics.

- **Region E (Geiger-Müller region):** When the detector response becomes independent of the charge type and energy, it enters an operational region known as the Geiger-Müller (GM) region (region E) and the detector is referred to as a GM survey meter. The Geiger-Müller region starts at voltages in the range of several 1000 V and extends over a region of 200 to 300 V. The applied voltage depends on the size of the central electrode and the cylindrical geometry of the chamber. In this region, the response of the detector becomes independent of the applied voltage across the electrodes and even a

minimally-ionizing particle will produce a very large pulse. In the GM region, the initial *Townsend avalanche* produced by an ionization event builds up rapidly. As the electrons produced reach the central electrode, the remaining "positive ion sheath" reduces the electric field strength in the charge multiplication volume; hence, charge multiplication is terminated. However, the effects of the initial *Townsend avalanche* propagate throughout the gas and may result in a successive number of following avalanches. These following avalanches are thought to be triggered by exited neutral atoms, produced by collisions with drifting charges, or by the cathode after it neutralizes the positive ions. The excited atoms may emit photons in the ultraviolet region that may initiate further avalanches, while the cathode (post-neutralization of a positive ion) may emit an electron that starts an avalanche directly, or a photon that produces a photoelectron elsewhere. For this reason, GM detectors use special means of quenching the discharge. One method, called external quenching, uses a large resistance between the anode and the high-voltage supply to reduce the potential difference after each pulse. The disadvantage of this method is that a substantial amount of time ($\sim 10^{-3}$ s) has to pass before the detector returns to its original operating voltage and this makes the detector relatively slow.

Another more commonly used method is internal quenching where an appropriate gas that has a complex molecule with lower ionization potential than the counting gas is used. When a positive ion of the counting gas collides with a molecule from the quenching gas, the quenching gas molecule transfers an electron to the counting gas thereby neutralizing it. The positive quenching gas ions when reaching the cathode spend their energy in dissociating rather than producing secondary electrons. Organic gases, such as ethyl alcohol, are suitable for internal quenching; however, they are consumed by the dissociation and this limits the life-time of the GM detector ($\sim 10^{9}$ counts). The halogens chlorine and bromine, when used as quenching gases, extend the lifetime of the detector because they recombine after dissociation and become available for other dissociation-recombination cycles.

- **Region F (continuous discharge):** When the applied voltage is increased further beyond the Geiger-Müller region, a steady discharge current flows through the detector. The applied voltage is so high that, once ionization takes place in the gas, a continuous discharge of electricity follows in the detector making this region unsuitable for radiation detection.

As FIG. 3.2 suggests, the applied voltage across the sensitive volume pre-determines the gas-filled detector's application. For example, if the energy fluence and dose output of a radiation source are to be measured, a detector operating in the ionization region (*ionization chamber*) is suitable for this task, since, at higher voltages, charge multiplication perturbs the initial signal produced by the incident ionizing particle leading to an overestimation of the energy deposited in the sensitive volume. On the other hand, a gas-filled radiation detector operating in the Geiger-Müller region is suitable for detecting very small activities produced by radionuclides or measuring very low radiation exposures of interest in radiation protection.

The ionization chamber is the most widely used gas-filled detector in radiotherapy clinics. Such chambers are available in a variety of designs for different applications and in general make use of air as the ionization gas medium. In the remaining sections of this chapter, several practical aspects associated with air-filled ionization chambers are discussed. In many instances, these aspects may be applied when the ionization chamber is filled with a gas other than air or a liquid.

## 3.2. AIR-FILLED IONIZATION CHAMBERS

A variety of different air-filled ionization chambers is available for various purposes in radiation dosimetry. The most common are: (*i*) the standard free-air ionization chambers, (*ii*) cavity chambers, and (*iii*) extrapolation chambers.

A *standard free-air ionization chamber* is mainly used in standards laboratories for measuring the *exposure rate* in air or the *air-kerma rate in air* for calibrating a radiation source. The chamber is based on collecting all ions produced by a radiation beam in a defined volume of air resulting from the direct transfer of energy from photons to primary electrons.

A typical clinic today depends mainly on *cavity ionization chambers* for relative and absolute dosimetry. Calibrated cavity ionization chambers used in absolute dosimetry must have a calibration coefficient traceable to a national primary standards laboratory (PSDL). This implies that the chamber was calibrated either (*i*) directly at the PSDL or at an accredited dosimetry calibration laboratory (ADCL), or (*ii*) at a secondary standards dosimetry laboratory (SSDL). All these calibration laboratories must trace their calibration to a PSDL. The calibration coefficient of a cavity ionization chamber could be also obtained through a cross-calibration in a "user secondary standard laboratory" with another ionization chamber having a calibration coefficient obtained from a PSDL, ADCL, or SSDL.

In addition, cavity ionization chambers are used for many relative dose measurements in radiotherapy clinics, such as measurement of collimator factors, relative dose factors, dose profiles, and percentage depth doses. Usually each task of a relative dose measurement is carried out with ionization chambers designed for the specific task at hand. Cylindrical and parallel-plate cavity chambers are the most common types of cavity ionization chambers used in radiotherapy.

A *phantom-embedded extrapolation chamber* (PEEC) is a variable air volume extrapolation chamber built as an integral part of the phantom in which the dose is measured. This type of chamber was initially used as a relative dosimeter to determine the dose at the surface of a phantom or at an interface between two different media. Recently, it was shown[4,5] that extrapolation chambers can also serve as absolute radiation dosimeters in output measurement of megavoltage photon and electron beams without the need for a calibration coefficient traceable to a PSDL.

Other ionization chambers that are of some interest to radiotherapy are *well chambers* used for calibration of radioactive sources for brachytherapy and *transmission chambers* used for monitoring the dose output from medical linear accelerators.

### 3.2.1. Standard free-air ionization chamber

A standard free-air ionization chamber[6] is specifically designed for measuring the *exposure* rate in air or the *air-kerma rate in air*. Figure 3.3 is a schematic diagram of a

typical free-air ionization chamber. Its operation relies on collecting the total ionization charge produced in a known volume of air by a well defined narrow x-ray beam. The chamber consists on one side of three coplanar plates (two guard plates on either side of the collecting plate all maintained at the same potential) and, opposite to the three plates a parallel polarizing plate. The chamber is kept inside a case shielded by lead to prevent scattered photons and stray radiation from reaching the sensitive air volume of the chamber. The shielding case has an entrance diaphragm with a circular aperture of area $A_0$.

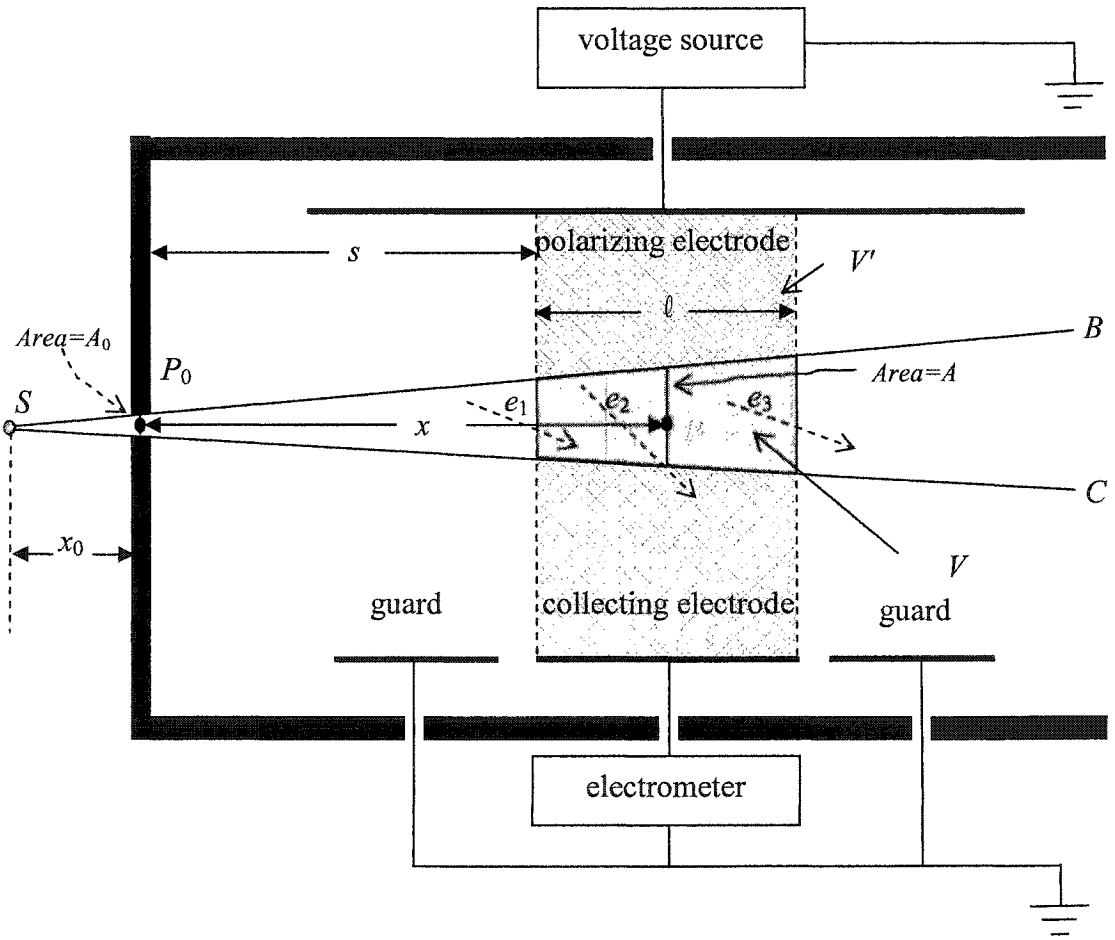


*FIG. 3.3. A schematic diagram of a typical standard free-air ionization chamber. The charge collecting volume is V' and the ideal volume is V where secondary electrons $e_2$ are produced for collection. When charge particle equilibrium is established, the number of $e_3$ electrons produced in V and escaping collection in V' is balanced by ($e_1$) electrons produced outside of V and entering V'.*

When photons emitted by the source $S$ aligned with the entrance diaphragm interact with air molecules, energetic electrons are produced. An energetic electron will further interact with air molecules through various mechanisms described in Section 2.5.1. It will eventually lose its kinetic energy and produce an ionization track in air along its path. The exposure in the volume $V$ which is a truncated cone with a cross sectional-area $A$ at its mid-point $P$ and a length $\ell$ that equals the length of the collecting plate would be determined directly, if all charges produced by photons interacting in the volume $V$ were collected and the resulting charge is divided by the mass of air contained in the volume $V$.

All ionizations produced by secondary electrons originating from the volume $V$ should be collected in order to determine the exposure in $V$; examples of such electrons are illustrated by $e_2$ in FIG. 3.3. However, the ions collected by the electrode may not be this particular set of ions as some electrons, illustrated by $e_3$ in FIG. 3.3, that are produced by photon interactions in the volume $V$ escape this volume and produce ions that are not collected by the collecting electrode. Therefore, only part of the ionization produced by these electrons is collected. In addition, some ions which are generated by electrons, illustrated by $e_1$ in the FIG. 3.3, originally produced outside of the volume $V$ are collected. If the distance $s$ from the aperture to the collecting volume is sufficiently large (about 10 cm for 300 keV photons), electronic equilibrium is established and ionizations lost from the volume $V$ by $e_3$-type electrons are compensated by ionization gain from $e_1$-type electrons produced outside of $V$.

Referring to FIG. 3.3, it can be shown[7] that the exposure $X_{P_0}$ at the aperture (point $P_0$) is

$$X_{P_0} = \frac{Q_{sat}}{M_c} e^{\mu s}, \tag{3.1}$$

where $M_c = \rho_{air} A_0 \ell$ and $Q_{sat}$ is the gas ionization produced in the volume $V$.

Although standard free-air ionization chambers allow a direct measurement of exposure with an accuracy of about ±0.5% for low-energy photon beams, their use is limited to standards laboratories because of their bulkiness and lack of mobility. Furthermore, because of size and shielding considerations, the use of standard free-air ionization

chambers use is limited to photon beams below 3 MeV. A 3 MeV photon beam would require the total length of the guard and collecting electrode to be over 3 m and an air gap of 1.5 m between the center of the collecting volume and the aperture will attenuate the beam by more than 5%. At high photon energies, other techniques based on cavity ionization chambers and calorimeters are used to quantify radiation beams.

### 3.2.2. Cavity ionization chambers and cavity theories

A cavity ionization chamber, in contrast to a standard free-air ionization chamber, may be used to determine the absorbed dose in any medium and for any radiation source beam. Determining the absorbed dose in a medium with a cavity ionization chamber relies on first determining the absorbed dose in the gas in the chamber cavity and then relating this dose to that which would be absorbed in the medium in the absence of the ionization chamber (see Fig. 3.4).

Several "cavity" theories which relate the dose in a measuring gas surrounded by a medium to the dose in the unperturbed medium were developed, most notably by W. H. Bragg[8] and W. H. Gray[9] and subsequently improved by L. V. Spencer and F. H. Attix[10].

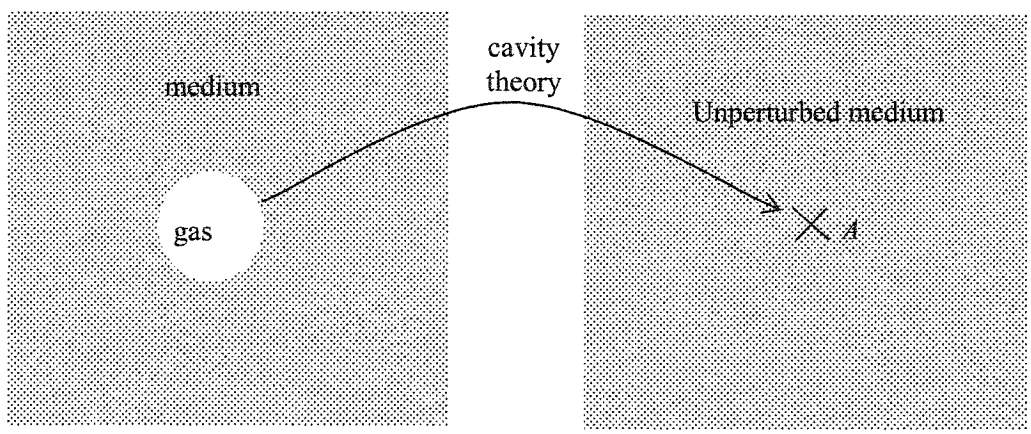


*FIG. 3.4. The absorbed dose at point A in the unperturbed medium is determined from the absorbed dose in the small gas cavity placed at point A using an appropriate cavity theory.*

### *Bragg-Gray cavity theory*

When a mono-energetic electron beam of fluence $\Phi$ and kinetic energy $E_K$ passes through an interface between two media, $g$ and $m$, as shown in FIG. 3.5, the absorbed dose in the $g$ side of the interface is given by

$$D_g = \Phi \times (S/\rho)_g, \tag{3.2}$$

and the absorbed dose on the $m$ side of the interface is

$$D_m = \Phi \times (S/\rho)_m, \tag{3.3}$$

where $(S/\rho)_g$ and $(S/\rho)_m$ are the mass collision stopping powers for electrons of energy $E_K$ traveling in media $g$ and $m$, respectively.

If backscatter at the interface is ignored, the electron fluences at either side of the interface are identical; hence, $D_g$ and $D_m$, resulting from electrons with kinetic energy $E$, are related through the following relationship

$$\frac{D_m}{D_g} = (S/\rho)_g^m, \tag{3.4}$$

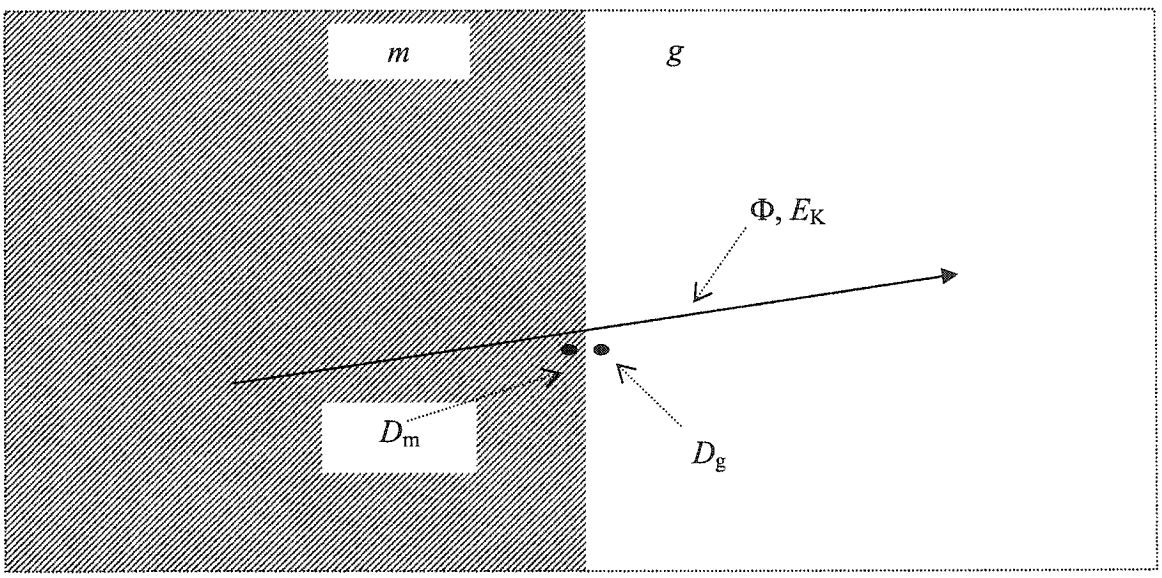


*FIG 3.5. A mono-energetic electron beam of fluence $\Phi$ and kinetic energy $E_K$ passing through an interface between media m and g. Assuming $\Phi$ to be continuous across the boundary, the dose ratio $D_m/D_g$ equals the corresponding ratio of mass collision stopping powers.*

where $(S/\rho)_g^m$ represents the ratio of mass collision stopping powers for electrons in media $m$ and $g$ evaluated at energy $E_K$.

Equation (3.4) can be extended to relate the absorbed dose in a thin layer or "cavity" (Fig. 3.6) of medium $g$ sandwiched between regions containing a different medium $m$ to the dose in the surrounding medium $m$ in the absence of the $g$-layer (cavity), if two conditions are satisfied:

The first condition requires that *the thickness of the g-layer in the configuration is very small in comparison with the range of charge particles striking it such that its presence does not perturb the charged particle fluence.* This condition is usually satisfied when heavy charged particles (primary or secondary to a neutron beam), which undergo little scattering, cross the cavity as long as the $g$-layer thickness is small compared to the range of the heavy charged particles. However, the presence of such a small cavity may perturb significantly the electron fluence unless the atomic number of medium $g$ is close to that of medium $m$.

The second condition requires that *the absorbed dose in the cavity $D_g$ is deposited entirely by the charged particles crossing it*, implying that indirectly ionizing radiation, such as photons and neutrons, do not interact in the g-layer. Thus, all charged particles producing ionization in the cavity must originate outside of the cavity. For neutron beams, the second condition tends to be more difficult to satisfy, especially if the g-layer is hydrogenous, thus having a large neutron interaction cross section.

For an electron beam with an energy spectrum crossing the $g$-layer, the dose in the $g$-layer from all electrons is related to the dose in the surrounding medium $m$ through the following relationship

$$\frac{D_m}{D_g} = \left(\overline{S}/\rho\right)_g^m, \tag{3.5}$$

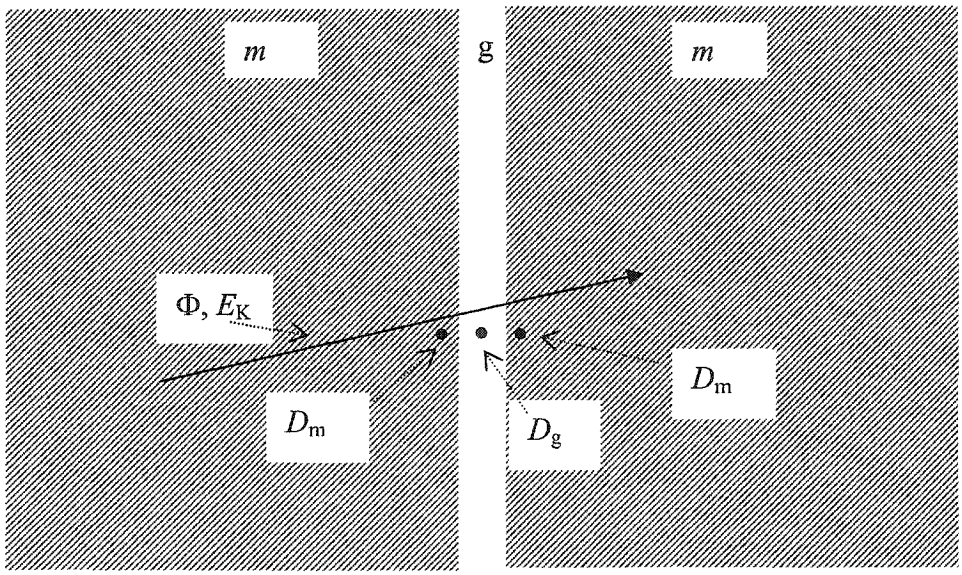


*FIG. 3.6. A mono-energetic electron beam of fluence $\Phi$ and kinetic energy $E_K$ passing through a thin layer of medium g (cavity) sandwiched between regions containing medium m. Assuming $\Phi$ to be continuous across layer g and both interfaces, the dose ratio $D_m/D_g$ equals the corresponding ratio of mass collision stopping powers.*

where $(\bar{S}/\rho)_g^m$ is the ratio of the *mean* mass electron collision stopping powers in media *m* and *g*. The Brag-Gray relationship implies that from the point of view of the electron fluence, the cavity does not exist. In medium *g*, the mean mass electron stopping power is given by

$$(\bar{S}/\rho)_g = \frac{\int_0^{E_{max}} \Phi_E(E_K)\,(S/\rho)_g\,dE_K}{\int_0^{E_{max}} \Phi_{E_K}(E_K)\,dE_K} = \frac{D_g}{\Phi_{tot}}, \tag{3.6}$$

and in medium *m*, it is given by

$$(\bar{S}/\rho)_m = \frac{\int_0^{E_{max}} \Phi_{E_K}(E_K)\,(S/\rho)_m\,dE_K}{\int_0^{E_{max}} \Phi_{E_K}(E_K)\,dE_K} = \frac{D_m}{\Phi_{tot}}, \tag{3.7}$$

where $\Phi_{tot}$ is the total fluence of electrons. Because of the smooth variation of the collision stopping power with energy, it is often possible (although not rigorously correct)

to calculate first the average energy from the electron fluence spectrum and then use the ratio of stopping powers evaluated at this average energy.

### *Spencer-Attix derivation of Bragg-Gray cavity theory*

While developing an improved cavity theory, L. V. Spencer and F. H. Attix[10] re-derived the Bragg-Gray cavity theory through a different approach based on investigating the behavior of the electron spectrum under conditions of charged particle equilibrium (CPE). The absorbed dose in the unperturbed medium, when CPE exists and bremsstrahlung radiation is neglected can be stated as

$$D_{\mathrm{m}} \overset{\mathrm{CPE}}{=} NE_{\max}, \tag{3.8}$$

where $N$ is the number of charged particles per gram emitted from an infinite homogeneous medium *m,* each particle having a kinetic energy $E_{\max}$. At such points, the dose $D_{\mathrm{m}}$ can be rewritten in terms of the equilibrium charged particle fluence spectrum $\Phi^{\mathrm{eq}}_{E_{\mathrm{K}}}(E_{\mathrm{K}})$ as

$$D_{\mathrm{m}} = \int_0^{E_{\max}} \Phi^{\mathrm{eq}}_{E_{\mathrm{K}}}(E_{\mathrm{K}}) \left(S/\rho\right)_{\mathrm{m}} \mathrm{d}E_{\mathrm{K}}. \tag{3.9}$$

The equilibrium charged particle fluence $\Phi^{\mathrm{eq}}_{E_{\mathrm{K}}}(E_{\mathrm{K}})$ can be easily obtained by equating Eqs. (3.8) and (3.9) and differentiating with respect to $E_{\max}$; hence,

$$\Phi^{\mathrm{eq}}_{E_{\mathrm{K}}}(E_{\mathrm{K}}) = \frac{N}{\left(S/\rho\right)_{\mathrm{m}}}. \tag{3.10}$$

When a small cavity filled with medium $g$ is placed in medium $m$, the same equilibrium charged particle fluence $\Phi^{\mathrm{eq}}_{E_{\mathrm{K}}}(E_{\mathrm{K}})$ that exists in the medium $m$ will cross the cavity leading to the following relationship for the absorbed dose in the cavity $D_{\mathrm{g}}$

$$D_{\mathrm{g}} = \int_0^{E_{\max}} \Phi^{\mathrm{eq}}_{E_{\mathrm{K}}}(E_{\mathrm{K}}) \left(S/\rho\right)_{\mathrm{g}} \mathrm{d}E_{\mathrm{K}} = N \int_0^{E_{\max}} \left(S/\rho\right)^{\mathrm{g}}_{\mathrm{m}} \mathrm{d}E_{\mathrm{K}} \tag{3.11}$$

and the ratio of the dose in $m$ to the dose in $g$ is found by dividing Eq. (3.11) by Eq. (3.8) to get

$$\frac{D_g}{D_m} = \frac{1}{E_{max}} \int_0^{E_{max}} (S/\rho)_m^g dE . \tag{3.12}$$

The Spencer-Attix derivation of the Bragg-Gray cavity theory can be generalized to include the energy escaping through bremsstrahlung radiation produced by electrons in the medium. The absorbed dose in the medium in this case can be rewritten as

$$D_m \overset{CPE}{=} NE_{max}[1 - Y_m(E_{max})], \tag{3.13}$$

in which $Y_m(E_{max})$ is the radiation yield in medium *m* for charged particles of energy $E_{max}$. The dose in medium *m* is then given by

$$D_m = \int_0^{E_{max}} \Phi_{E_K}^{eq}(E_K) \left(S_{col}/\rho\right)_m \, dE_K , \tag{3.14}$$

and the dose in the cavity filled with medium *g* is given by

$$D_g = \int_0^{E_{max}} \Phi_{E_K}^{eq}(E_K) \left(S_{col}/\rho\right)_g \, dE_K , \tag{3.15}$$

where $\left(S_{col}/\rho\right)_g$ and $\left(S_{col}/\rho\right)_m$ are the mass collision stopping powers for electrons of energy $E_K$ traveling in media *g* and *m*, respectively.

Since the presence of the cavity does not affect the fluence spectrum of crossing electrons in the Bragg-Gray cavity theory, the equilibrium fluence, as given by Eq. (3.10), essentially remains unchanged and the Spencer-Attix formalism of the Bragg-Gray cavity theory may be rewritten in the following form to account for the bremsstrahlung production in the medium

$$\frac{D_g}{D_m} = \frac{1}{E_{max}[1 - Y_m(E_{max})]} \int_0^{E_{max}} (S_{col}/\rho)_m^g \, dE_K . \tag{3.16}$$

### *Spencer-Attix cavity theory*

Experiments[11] had shown that the Bragg-Gray cavity theory did not predict accurately the ionization produced in an air-filled cavity chamber, especially when ionization chambers with walls of high atomic number were used. These experiments had shown that: 1) the measured ionization density in the air cavity depends on the electrode separation and 2) for very small electrode separations the measured ionization density of the air cavity

chamber irradiated in a calibrated radiation beam did not match the calculated ionization density based on the Bragg-Gray cavity theory. In 1955, L. V. Spencer and F. H. Attix[10] proposed a cavity theory using a more general method than did Bragg and Gray.

The stopping power ratio in the Bragg-Gray cavity theory is evaluated under the assumption of the *Continuous Slowing Down Approximation* (CSDA) upon which the collision stopping powers are based. In reality, energetic δ rays are produced in electron-electron collisions, which then join the flux of electrons that are crossing the cavity and their presence enhances the equilibrium spectrum at lower electron energies. Hence, the Spencer-Attix cavity theory goal was to modify the Brag-Gray cavity theory by incorporating the effects of the energetic δ rays so as to account for the observed variation of ionization density with cavity size, at least for Bragg-Gray cavities. For practical applications, a fairly simple model was developed by Spencer and Attix and a more sophisticated theory was developed by Burch[12] at about the same time.

The Spencer-Attix cavity theory is based on the following assumptions: (1) validity of the Bragg-Gray conditions, (2) the absence of bremsstrahlung generation, and (3) the condition that the cavity does not perturb the total electron fluence (including $\delta$ rays). In addition, the size of a cavity containing medium $g$ is characterized by a parameter $\Delta$ which is taken to be the mean energy of electrons with projected ranges just large enough to cross the cavity.

The equilibrium spectrum $\Phi_{E_K}^{eq,\delta}(E_K)$ of electrons including $\delta$ rays generated in the surrounding medium $m$ and crossing the cavity can be divided into two components:

- A "fast" group of electrons having kinetic energies equal to or greater than $\Delta$. This group of electrons is capable of carrying energy away and can therefore transport energy. In fact, electrons in this group of electrons can cross the cavity if they strike it.
- A "slow" group of electrons with kinetic energies below $\Delta$. These electrons are assumed to have zero range, thus they drop their energy "on the spot". Hence they are assumed not to be able to enter the cavity, nor to transport energy.

As a result, only the "fast" group of electrons contributes to the dose in the cavity.

Dose determination with the Spencer-Attix cavity theory takes into account the fluence spectrum which includes $\delta$ electrons having energies between $\Delta$ and the maximum energy transfer possible in a single electron-electron collision, namely $E_K/2$. (Note that electrons with energies less than $\Delta$ cannot enter the cavity). In a particular region of interest, the so-called "fast" electrons, including their secondaries, are allowed to slow down and deposit their energy in the medium according to their stopping powers. However, the locally deposited energy by these primary electrons and their secondaries must be restricted to secondary electrons with energies below $\Delta$. A secondary electron with a kinetic energy exceeding $\Delta$ carries its energy to a region other than the local region of interest (consequently, it becomes a primary electron in the other region of interest). Therefore, the restricted stopping power $L_\Delta/\rho$ has to be used in the cavity theory. The ratio $D_m/D_g$ according to the Spencer-Attix cavity theory with Nahum's track-ends, is given by

$$\frac{D_m}{D_g}^{CPE} = \frac{\int_\Delta^{E_{max}} \Phi_{E_K}^{eq,\delta}(E_K)\,(L_\Delta/\rho)_m\,dE_K + TE_m}{\int_\Delta^{E_{max}} \Phi_{E_K}^{eq,\delta}(E_K)\,(L_\Delta/\rho)_g\,dE_K + TE_g} = \left(\bar{L}_\Delta/\rho\right)_g^m, \tag{3.17}$$

where $\left(\bar{L}_\Delta/\rho\right)_g^m$ is the ratio of the mean restricted stopping powers for *m* and *g*.

Although for commercially used cavity ionization chambers the mean restricted mass stopping powers are evaluated with $\Delta = 10\,\text{keV}$, it turns out that the ratio of the mean restricted mass stopping powers is relatively independent of the choice of $\Delta$. The track-end terms $TE_m$ and $TE_g$ in Eq. (3.17) account for the energy deposited at the end of tracks by electrons that have an initial energy between $\Delta$ and $2\Delta$ which can have an energy drop below $\Delta$ and, thereby, lose their total remaining energy locally. Track-end terms were approximated by Nahum[13] as

$$TE_m = \Phi_{E_K}^{eq,\delta}(\Delta)\left(\frac{S(\Delta)}{\rho}\right)_m \Delta \tag{3.18}$$

and

$$\mathrm{TE}_g = \Phi_{E_K}^{eq,\delta}(\Delta)\left(\frac{S(\Delta)}{\rho}\right)_g \Delta . \tag{3.19}$$

Equations (3.18) and (3.19) express the portion of the track where the energy of the electron is below $\Delta$. The amount of energy per unit mass deposited by such electrons is equal to the product of $\Delta$ and the electron spectrum with the unrestricted stopping powers both evaluated at the threshold energy $\Delta$. Since an electron with an energy $\Delta$ can transfer a maximum energy $\Delta/2$ in a single electron-electron collision, the unrestricted stopping power has to be used for evaluating the TE terms. Track-end energy deposition contributes about 5% to 10% of the total dose.

### *General cavity theory for photon beams*

Both the Bragg-Gray and Spencer-Attix cavity theories require the dose in the cavity to be deposited by electrons generated outside the cavity in the surrounding medium. In some situations, indirectly ionizing radiation beams can produce a significant number of primary electrons by directly interacting with the cavity gas. For a photon beam, the production of primary electrons in the cavity increases with increasing cavity size and decreasing photon energy. Under charged particle equilibrium conditions, for very large cavities or at sufficiently low photon energies where most of the cavity dose is deposited by primary electrons generated in the cavity, the ratio $D_m / D_g$ depends purely on the ratio of the mass energy absorption coefficients $(\bar{\mu}_{ab}/\rho)_g^m$ evaluated for media *m* and *g* at the photon beam energy, and is given by

$$\frac{D_m}{D_g} = (\bar{\mu}_{ab}/\rho)_g^m . \tag{3.20}$$

While the Spencer-Attix cavity theory applies to small cavities, Eq. (3.20) may be regarded as the dose ratio limit when the cavity size becomes large. In an intermediate cavity, the dose deposited in the cavity is a result of primary electrons generated in both the medium and in the cavity. Burlin[14] proposed a simple weighting method in which the ratio of the dose to medium and the dose to the cavity is given by the following two-component model

$$\frac{D_g}{D_m} = d\left(\bar{L}_\Delta / \rho\right)_m^g + (1-d)\left(\bar{\mu}_{ab} / \rho\right)_m^g, \tag{3.21}$$

with $d$ a parameter that corresponds to the average value of electron fluence reduction in the medium and related to the cavity size. In one extreme, $d$ approaches unity for small cavities and in the other, $d$ approaches zero for large cavities. The parameter $d$ is expressed as

$$d = \frac{\int_0^L \Phi_{E_K}^{eq,\delta}(E_K)\, e^{-\beta \ell}\, d\ell}{\int_0^L \Phi_{E_K}^{eq,\delta}(E_K)\, d\ell} = \frac{1-e^{-\beta L}}{\beta L}, \tag{3.22}$$

where $\beta$ is an effective attenuation coefficient corresponding to the reduction in particle fluence from the medium through $(1-d)$ and the increase in fluence through interactions within the cavity; $L$ is the mean cavity size, and $\ell$ is the distance of any point in the cavity from the boundary.

### 3.2.3. Absolute dosimetry with a cavity ionization chamber in photon beams

Before clinical use, the output of an external clinical radiation beam must be calibrated. This basic output calibration is but one of the important links constituting the chain in accurate dose delivery to the patient. The objective of calibrating an external radiation clinical beam is to determine the absorbed dose rate at a reference point in water (usually at $z_{max}$) under a specific reference geometrical irradiation condition. The reference geometrical irradiation conditions are usually defined to be: (*i*) an *SSD* of 100 cm and (*ii*) a field size of 10×10 $cm^2$ on the phantom surface, as illustrated in FIG. 3.7.

For superficial and orthovoltage x rays as well as for isotope teletherapy beams, the dose rate is specified in cGy/min; for linacs in cGy/monitor unit (cGy/ MU). In order to meet the requirement of the International Commission on Radiation Units and Measurements (ICRU) that the overall accuracy in the dose delivery be within ±5%, the calibration of external radiation beams must be carried out with an accuracy better than ±2% in the measured absorbed dose.

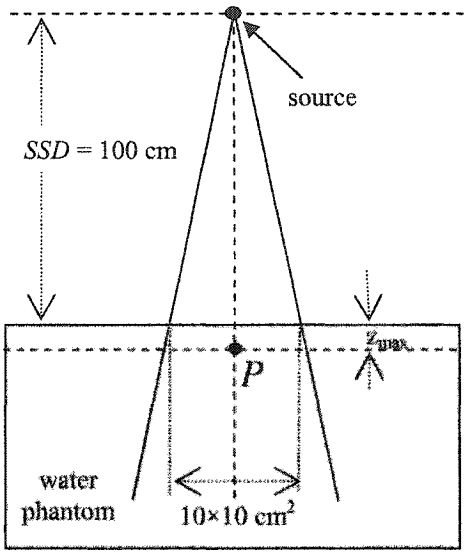


*FIG. 3.7. Basic beam output calibration setup in externel beam radiotherapy. The dose rate is determined at point P which is at a depth $z_{max}$ in a water phantom irradiated by a source located at a distance SSD from the surface of the phantom and producing a $10\times10$ cm$^2$ field at the surface of the phantom.*

In principle, any cavity ionization chamber with a well known cavity volume size from which all charges $Q_{\text{sat}}$ are collected may be used directly for this task. The procedure would be to calculate first the dose in the cavity $D_{\text{g}}$ from $Q_{\text{sat}}$ through the relationship

$$D_{\text{g}} = \frac{Q_{\text{sat}}}{m}\left(\overline{W}_{\text{gas}}/e\right). \tag{3.23}$$

In the absence of the chamber wall, the absorbed dose to the medium $D_{\text{m}}$ is calculated from $D_{\text{g}}$ through the direct application of the Spencer-Attix cavity theory according to Eq. (3.17).

For photon beams, if the wall is thick enough to stop all electrons generated in the medium from reaching the gas cavity, the wall may be considered as a large cavity and the dose in medium $D_{\text{m}}$ is related to the dose in the wall $D_{\text{wall}}$ through

$$D_{\text{m}} = D_{\text{wall}}\left(\bar{\mu}_{\text{ab}}/\rho\right)^{\text{m}}_{\text{wall}} = D_{\text{g}}\left(\bar{L}_{\Delta}/\rho\right)^{\text{wall}}_{\text{g}}\left(\bar{\mu}_{\text{ab}}/\rho\right)^{\text{m}}_{\text{wall}} = \frac{Q_{\text{sat}}}{m}\left(\overline{W}_{\text{gas}}/e\right)\left(\bar{L}_{\Delta}/\rho\right)^{\text{wall}}_{\text{g}}\left(\bar{\mu}_{\text{ab}}/\rho\right)^{\text{m}}_{\text{wall}}, \tag{3.24}$$

in which the wall may now be considered as the "medium" in the basic Spencer-Attix cavity theory.

An additional correction factor is usually applied to Eq. (3.24) to account for the undesirable perturbations of the radiation beam fluence caused by the presence of the chamber wall. Firstly, the chamber wall perturbs the photon fluence at the point of measurement. Since chamber walls are generally made of a material different from that of the medium, the wall attenuates the primary photon beam and generates scattered photons differently than does the medium. Depending on the choice of the wall material, gas, and the type of medium, the photon fluence in the cavity may be higher or lower and a wall correction factor $A_{\text{wall}}$ accounts for the difference in the photon fluence produced by the presence of the chamber. Secondly, the wall generates secondary electrons that result from the interaction of photons with the wall. In addition, depending on the wall thickness, the wall may prevent electrons produced in the medium from entering the gas cavity. Hence, some of the ionization in the gas will be produced by electrons originating in the medium and some ionization in the gas will come from electrons generated in the wall.

The use of very thin walls with physical characteristics similar to the medium would practically eliminate the perturbation effects produced by the wall. For a typical cavity ionization chamber only a fraction $\alpha$ of electrons that ionize the gas are generated in the wall, and the basic Spencer-Attix cavity theory relation of Eq. (3.17) and large cavity theory relation of Eq. (3.24) can be combined to estimate the dose to the medium $D_{\text{m}}$ as follows

$$D_{\text{m}} = D_{\text{g}}[\alpha\left(\bar{L}_{\Delta}/\rho\right)_{\text{g}}^{\text{wall}}\left(\bar{\mu}_{\text{ab}}/\rho\right)_{\text{wall}}^{\text{m}} + (1-\alpha)\left(\bar{L}_{\Delta}/\rho\right)_{\text{g}}^{\text{m}}]. \tag{3.25}$$

Large changes in the value of $\alpha$ produce only a small effect on the dose calculated with Eq. (3.25). Values for $\alpha$ were measured by Lempert[15] and the data can be obtained from the AAPM TG-21 calibration protocol (ref. 16). Finally, including perturbation correction for a photon beam we get the following expression for $D_{\text{m}}$

$$D_{\text{m}} = \frac{Q_{\text{sat}}}{m}\left(\bar{W}_{\text{gas}}/e\right)\left[\alpha\left(\bar{L}_{\Delta}/\rho\right)_{\text{g}}^{\text{wall}}\left(\bar{\mu}_{\text{ab}}/\rho\right)_{\text{wall}}^{\text{m}} + (1-\alpha)\left(\bar{L}_{\Delta}/\rho\right)_{\text{g}}^{\text{m}}\right]A_{\text{wall}}. \tag{3.26}$$

### 3.2.4. Absolute dosimetry with a cavity ionization chamber in electron beams

In electron beams, because electron scattering behavior in the low density gas cavity medium differs from that in the higher density surrounding medium, it was pointed out by Harder[17] that two possible effects can affect the dose measurement when the Spencer-Attix cavity theory is applied directly:

Firstly, because an electron is more likely to be scattered into the cavity from the denser surrounding medium than to be scattered out by the lower density gas, the number of electrons traversing a cavity present in a medium is greater than the number of electrons that would be traversing the same volume filled by the medium; thereby increasing the dose in the gas relative to the dose in the medium. Secondly, an electron's path through the lower density gas cavity is straighter than it would in the denser filling medium; hence, the dose in the gas cavity is decreased relative to the dose in the medium. These two effects due to the "scattering" perturbations are incorporated into a single correction factor $P_{fl}$ that is applied to the Spencer-Attix dose relationship as follows

$$D_m = \frac{Q_{sat}}{m}\left(\bar{W}_{gas}/e\right)\left(\bar{L}_\Delta/\rho\right)_g^m P_{fl}. \tag{3.27}$$

The magnitude of $P_{fl}$ depends on the cavity shape and orientation with respect to the direction of the incident electron beam, and the surrounding medium. For a parallel-plate cavity chamber having a 1-2 mm electrode separation and used in a water-equivalent medium, $P_{fl}$ may be taken as unity[18]; for other chamber designs and sizes its values can be found in many references[19].

### 3.2.5. Absolute dosimetry using a calibrated cavity ionization chamber

The calibration of clinical photon and electron radiation beams is usually carried out with a calibrated cavity ionization chamber, having a calibration coefficient traceable to a PSDL, in conjunction with a calibration protocol. Avoiding the use of uncalibrated cavity ionization chambers in absolute dosimetry arises from the difficulty in accurately determining the sensitive air-mass volume in the cavity ionization chamber from which

the charge $Q_{sat}$ is collected. The sensitive air-mass volume is not necessarily equal to the geometrical cavity volume in the chamber. In order to determine the sensitive air-mass accurately one must carefully analyze the electric field established inside the polarized chamber. To overcome this problem, cavity ionization chambers, when used as absolute dosimeters, are calibrated against a standard free-air ionization chamber or against a calibrated cavity ionization chamber with a calibration factor traceable to a PSDL. This practice removes the need for knowing accurately the sensitive air-mass volume in cavity volume.

The procedures to be followed when calibrating an external clinical radiation beam are available in numerous international and national radiation dosimetry protocols. Generally, the choice of which protocol to use is left to individual departments. In North America protocols developed by the *American Association of Physicists in Medicine* (AAPM) are in widespread use; protocols developed by the *International Atomic Energy Agency* (IAEA), on the other hand, are popular in the rest of the world. Generally, the AAPM and IAEA dosimetry protocols are based on same basic knowledge and data and provide very similar results.

Most calibration protocols used today are based on calibrated cavity ionization chambers and one of three main protocol types:

1. Procedures based on exposure measurements in a phantom ($C_\lambda$) (ref. 20).
2. Procedures based on exposure in air or air-kerma in air calibrations and Spencer-Attix cavity theory [AAPM TG-21 (ref. 16), AAPM TG-25 (ref. 21), and IAEA TRS-277 (ref. 22-24)].
3. Procedures based on absorbed dose in medium calibrations [AAPM TG-51 (ref. 25) and IAEA TRS-398 (ref. 26)].

The first approach was used prior to 1980 and, because of the limitation of the concept of exposure to low energy photon beams, it is now only used for calibrating kilovoltage x-ray beams. The latter two protocol types were established after 1980 and are used to determine the absorbed dose to water with the procedure depending on the chamber dimensions and on the radiation type and energy. They cover several distinct beam types and energy ranges, such as: (*i*) low energy (superficial) photon beams; (*ii*) medium energy

photon beams (orthovoltage); (*iii*) megavoltage photon beams; (*iv*) electron beams below 10 MeV; and (*v*) electron beams equal to or above 10 MeV.

Before attempting to calibrate the output of a given ionizing radiation beam, one must first select a dosimetry calibration protocol appropriate for the radiation beam and ensure that the appropriate calibration coefficient for the cavity ionization chamber is available. The protocol then guides the user through a chain procedure with an ultimate goal of determining the absorbed dose to medium. A typical calibration chain procedure involves specifying the beam quality for photon and electron beams and determining the appropriate calibration coefficient for the chamber to be used for calibration of the particular beam, chamber reading correction factors, and the phantom correction factors. Several important basic chamber calibration coefficients are discussed below.

## 3.2.6. Basic cavity ionization chamber calibration coefficients

### *Exposure calibration coefficient* $N_X$

The exposure calibration coefficient $N_X$ of a cavity ionization chamber is defined as

$$N_X = \frac{X}{M}, \tag{3.28}$$

where $X$ is the exposure (in Roentgen) and $M$ is the measured signal (in coulomb) corrected for ionic recombination and polarity effects. The $N_X$ calibration coefficient of a particular cavity chamber is obtained by calibrating the chamber directly against a standard free-air ionization chamber in a standards laboratory or by indirect cross-calibration against a calibrated cavity ionization chamber in a "user" laboratory. Because $N_X$ is generally sensitive to the quality of the photon beam, the exposure calibration coefficient for a cavity chamber is specified for different photon beam qualities. The typical unit of $N_X$ is R/nC.

### *Air-kerma calibration coefficient* $N_K$

The air-kerma calibration coefficient $N_K$ of a cavity ionization chamber cannot be obtained directly through an irradiation of the chamber in a photon beam, since the

quantity kerma is not directly measurable. However, $N_K$ is related to $N_X$ through the following relationship

$$N_K = \frac{(K_{air})_{air}}{M} = N_X \frac{(\overline{W}_{air}/e)}{(1-g)}, \tag{3.29}$$

where $(K_{air})_{air}$ is the *air-kerma in air* and $g$ is the bremsstrahlung fraction (for cobalt-60 gamma rays $g = 0.003$, for superficial x rays $g = 0$). The typical unit of $N_K$ is cGy/nC. Multiplying the air-kerma calibration coefficient $N_K$ for a particular chamber by the measured signal $M$ gives the *air-kerma in air*.

### *Absorbed dose-to-air calibration coefficient* $N_{gas}$ *or* $N_{D,air}$

$N_{gas}$ ( in the AAPM notation) or $N_{D,air}$ (in the IAEA notation) calibration coefficient is a unique characteristic of each cavity ionization chamber, because it is closely related to the air-sensitive volume $V$ of the particular chamber. It is defined as

$$N_{gas} = \frac{D_{air}}{M} = \frac{(\overline{W}_{air}/e)}{\rho_{air} V}, \tag{3.30}$$

with $M$ again the measured signal and $\rho_{air}$ the air density.

Since $(\overline{W}_{air}/e)$ is assumed to be constant for all radiotherapy beam energies, $N_{gas}$ is also constant for all beam energies. It is related to the *air-kerma in air* calibration coefficient $N_K$ through the following relationship

$$N_{gas} = N_K \frac{(1-g)}{(\overline{\mu}_{ab}/\rho)^{air}_{wall} (\overline{L}_{\Delta}/\rho)^{wall}_{air} K_{wall} K_{comp} K_{cel}}, \tag{3.31}$$

with $K_{wall} = A^{-1}_{wall}$ a photon fluence perturbation correction factor; $K_{comp}$ a correction factor for the production of electrons in the chamber components other than the wall material, such as buildup caps, that contributes to the dose in the gas $D_{gas}$; and $K_{cel}$ a correction factor required when a particular cylindrical chamber has a central electrode made of a material different than that of the wall.

***Absorbed dose-to-water calibration coefficient*** $N_{D,w}$

Since the goal of output calibration of an external clinical radiation beam is to determine the dose in medium $D_m$, a series of correction coefficients must be applied for the previously mentioned air-based calibration coefficients ($N_X$, $N_K$, and $N_{gas}$) to convert the measured quantities $X$, $(K_{air})_{air}$, $D_{air}$, respectively, into $D_m$. It is more appropriate and logical to calibrate the output of the radiation beam in terms of a calibration coefficient $N_{D,med}$ that relates the signal reading of the chamber directly to the quantity of interest $D_m$. For a water phantom we can relate the dose in water $D_w$ to the absorbed dose-to-water calibration coefficient $N_{D,w}$ through

$$D_w = MN_{D,w}. \tag{3.32}$$

Similarly to $N_X$ and $N_K$, the absorbed dose-to-water calibration coefficient $N_{D,w}$ depends on the quality of the radiation beam. A standards laboratory usually provides an absorbed dose-to-water calibration coefficient $N_{D,w}^{Co-60}$ for a cobalt-60 beam or, alternatively, the user may calculate it from $N_X^{Co-60}$, $N_K^{Co-60}$, and $N_{gas}$ calibration coefficients. The absorbed dose-to-water calibration coefficient $N_{D,w}^{Q}$, for any particular photon beam of quality Q, is related to $N_{D,w}^{Co-60}$ through a quality coefficient $k_Q$ defined as

$$k_Q = \frac{N_{D,w}^{Q}}{N_{D,w}^{Co-60}}. \tag{3.33}$$

## 3.2.7. Relative dosimetry with cavity ionization chambers

While absolute dosimetry is restricted to calibrated cavity ionization chambers, relative dosimetry can be performed with uncalibrated cavity ionization chambers. In many circumstances, where the dose conversion factors required to convert the response of a particular cavity chamber into absorbed dose in Grays remain constant, the ratio of the absorbed dose in two points at different irradiation conditions is equivalent to the ratio of the cavity chamber signal response (corrected for ionic recombination and polarity

effects) positioned at these points of interest. On the other hand, in instances where the dose conversion factors vary with chamber position, these factors cannot be ignored and must be considered. For example:

- For central axis *PDD*s in photon beams, the restricted stopping power ratio $\left(\overline{L}_{\Delta}/\rho\right)_{g}^{m}$ is essentially independent of depth at depths beyond $z_{max}$. At depths shallower than $z_{max}$ (In the region between phantom surface and $z_{max}$), however, $\left(\overline{L}_{\Delta}/\rho\right)_{g}^{m}$ varies by up to 2% depending on the field size and energy. Hence, the chamber response at a particular depth in the build-up region must be multiplied by the corresponding average stopping power ratio of the electron spectrum traversing that depth before obtaining the *PDD* in the build-up region, as ignoring the $z$ dependence of the restricted stopping power ration may result in erroneous dose measurements in the dose build up region.
- Similarly, in electron beams $\left(\overline{L}_{\Delta}/\rho\right)_{g}^{m}$ varies significantly as a function of depth for all depths (*i.e.*, electron energy) and the measured signal must be corrected by using the appropriate stopping power ratios. For electron beams with energies less than 10 MeV, Harder proposed the following simple relationship for the mean electron energy $\overline{E}(z)$ at depth $z$ (ref. 21)

$$\overline{E}(z) = \overline{E}(0)(1 - z/R_{p}), \tag{3.34}$$

where $\overline{E}(0)$ is the mean electron energy at the phantom surface and $R_{p}$ is the practical range of the electron beam.

### 3.2.8. Phantom-embedded extrapolation chamber (PEEC)

Extrapolation chambers are parallel-plate ionization chambers with variable air-volume that offer a simple and practical alternative to other methods for dose determination in the medium. Because extrapolation chambers may have cavity sizes as small as 0.5 mm, they can measure the dose with a good depth resolution; an important feature in regions where the dose changes rapidly with depth. In addition, adjusting the thickness of the gas cavity allows extrapolating the ionization density to zero thickness; thus removing any perturbations caused by the presence of the cavity at the measurement point.

### *Absolute dosimetry with the PEEC*

In 1937, Failla[27] proposed the use of extrapolation chambers in clinical dosimetry, and since then, they were used for surface dose measurement in low energy[28], orthovoltage[27], and megavoltage[29] x-ray beams and in dosimetry for beta rays[30-31]. A specially designed extrapolation chamber embedded in a polystyrene phantom was developed in 1955 by Genna and Laughin[32] for calibrating a cobalt-60 clinical beam. In addition, calibrations of clinical megavoltage photon and electron beams were carried out by Klevenhagen[33] with a Lucite-based PEEC, and Zankowski and Podgorsak[4] with a Solid Water™-based PEEC. Recently, Deblois and collegues[5] measured the absorbed dose in bone-equivalent material with a hybrid PEEC.

In absolute dosimetry, determining the dose to medium $D_m$ using a PEEC is based on a modified Spencer-Attix cavity theory such that the ratio $Q_{sat}/m$ is replaced by the ionization gradient $\frac{1}{\rho_g A}\frac{dQ_{sat}}{ds}$. Hence, $D_m$ is expressed as

$$D_m = \frac{1}{\rho_g A}\frac{dQ_{sat}}{ds}\left(\bar{W}_{gas}/e\right)\left(\bar{L}_\Delta/\rho\right)_g^m, \tag{3.35}$$

where $\rho_g$ is the gas density, $A$ is the effective area of the collecting electrode determined through capacitance measurements, and $dQ_{sat}/ds$ is the measured charge gradient with respect to relative displacement of electrodes. By making the PEEC an integral part of the medium and using very thin electrodes made of a material with a similar atomic number to that of the medium, several correction factors, such as $A_{wall}$, normally associated with the use of commercially available cavity ionization chambers become negligible and are not considered in the dose determination with the PEEC.

### *Relative dosimetry with the PEEC*

The use of extrapolation chambers for dose measurements in the build-up region of high energy photon beams has two advantages. Firstly, a good depth dose resolution can be achieved and, secondly, any perturbations resulting from the presence of a finite cavity size can be removed.

In principle, a good resolution can be achieved by a parallel-plate cavity ionization chamber with fixed electrode separation. However, such a chamber will always exhibit an over-response resulting from side wall scatter into the sensitive gas volume. The magnitude of the over-response depends on the design of the chamber; a chamber with smaller guard rings will have a greater over-response. On the other hand, extrapolation of the ionization density measured with an extrapolation chamber to zero cavity thickness removes the side wall scatter over-response from the measured data.

For accurate relative depth dose measurements, the use of the PEEC was suggested by Nilsson[34]. Initially, Velkely[35] obtained "over-response" correction factors intended to be applied to all types of cavity ionization chambers based on build-up dose measurement with an extrapolation chamber although Nilsson[34], later, showed that correction factors are specific to a particular chamber design and depend on the size of the guard ring, plate separation and chamber volume. For example, Mellenberg[36] showed that the over-response of a Markus-type parallel-plate chamber in a phantom irradiated with 4 MV x rays may result in an over-estimation of the surface dose by a factor of two. Other investigators[37] were able to obtain correction factors to be used for surface dose measurements with other commercial parallel-plate chambers.

## 3.3. AIR-FILLED IONIZATION CHAMBERS: PRACTICAL ASPECTS.

Dosimetry with air-filled ionization chambers is based on an accurate determination of the ionization in the air cavity produced by irradiation. The exposure $X$ may be calculated directly from the ionization measurement, and *air-kerma in air* and *dose to air* can be obtained through the accurate knowledge of $(\overline{W}_{air}/e)$. Since the measured signal of an irradiated chamber not only depends on the radiation beam but also on many other factors, such as environmental conditions, collection efficiency of the chamber, and other non-dosimetric signals, a number of correction factors correcting the measured signal are required to account for these effects.

### 3.3.1. Mean ionization and excitation energy of a gas $\overline{W}_{gas}/e$

In dosimetry, collisions by charged particles interacting with atomic orbital electrons through Coulomb-force are the most important means by which atoms can be ionized or excited, since the dose is deposited almost entirely by charged particles. Since these collisions can, in addition to ionization, also produce excited atoms where an orbital electron is raised to a higher energy level rather than ejected from the atom, the excitation energy must be considered as part of the deposited dose. This energy going into excitation of atoms in the medium decreases the ionization efficiency of the charged particle; hence, the number of ions created by the charged particle cannot be calculated simply by dividing the initial kinetic energy $E_0$ of the charged particle by the ionization potential of the atom.

To overcome this difficulty the ionization efficiency of the charged particle is expressed in terms of a quantity $W$ defined as the mean energy spent by the charged particle of initial kinetic energy $E_0$ to produce an ion pair in the medium. Therefore, the quantity $W$ is expressed as

$$W = \frac{E_0}{\overline{N}}, \tag{3.36}$$

where $\overline{N}$ is the average number of ions produced by the charged particle having an initial kinetic energy $E_0$ and stopping in the medium.

To take into account radiative losses by charged particles, the ICRU Report 19 (ref. 38) alternatively defined $W$ as

$$W = \frac{E_0(1-g)}{\overline{N}(1-g')}, \tag{3.37}$$

where $g$ is the fraction of energy lost by the charged particle in bremsstrahlung production and $g'$ is the fraction of ions produced by the bremsstrahlung radiation.

When a large number $n$ of charged particles having different initial kinetic energies irradiate the medium, the average value of $\overline{W}$ may be defined as

$$\bar{W} = \frac{\sum_{i=1}^{n} E_i(1-g_i)}{\sum_{i=1}^{n} \bar{N}_i(1-g_i')}, \tag{3.38}$$

analogous to Eq. (3.37) where $E_i(1-g_i)$ is the kinetic energy of the *i*-th charged particle excluding bremsstrahlung losses and $\bar{N}_i(1-g_i')$ is the average number of ions created by the *i*-th charged particle by collision losses. For heavy charged particles, $g_i$ and $g_i'$ are practically zero, whereas for electrons $g_i$ is approximately equal to $g_i'$. For indirectly ionizing radiation beams, *i.e.*, photons and neutrons, the quantity $\bar{W}$ may still be defined and used but it commonly refers to the secondary charged particles produced in the medium by the indirectly ionizing particle.

The quantity $\bar{W}$, in general, is difficult to calculate for a gas from first principles and it is more practical to obtain its value experimentally. Experimental values of $\bar{W}$ for various gasses and various charged particles are compiled in the ICRU Report 31 (ref. 39) where a value of 33.85 eV/*ion pair* was recommended for dry air to be used with photon and electron beam irradiations independent of their energies. The currently accepted value of $\bar{W}_{air}$, obtained by Boutillon and Perroche[40], is 33.97 eV/*ion pair*. In dosimetry, the quantity $\bar{W}_{air}/e = 33.97\ \text{J}\cdot\text{C}^{-1}$ is a more convenient form of expressing the $\bar{W}_{air}$-value, since it directly relates the quantities air-kerma and exposure.

The value of $\bar{W}_{air}/e$ for humid air is less than the recommended value of 33.97 $\text{J}\cdot\text{C}^{-1}$. The dependence of $\bar{W}_{air}/e$ on the relative humidity was reported by Niatel[41]. In general, the value of $\bar{W}_{air}/e$ is about 0.997 of the recommended value for dry air over the range 15-75% relative humidity and, in most circumstances, this perturbation is ignored.

### 3.3.2. Temperature and pressure corrections

Ionization chambers used in radiation dosimetry use air as the ionization medium from which ions are collected when irradiated by an ionizing beam. Usually, air-filled ionization chambers are open to the atmosphere. Since the amount of ionization produced

essentially depends on the mass of air in the chamber, any environmental condition changes must be accounted for.

When measuring dosimetric quantities, such as *exposure*, *air-kerma in air*, and *dose to air*, the mass of air in the irradiated ionization chamber must be known. The density of air in an ionization chamber open to the atmosphere at temperature $T$ and pressure $p$ is approximately given by

$$\rho_{T,p} = \rho_{0,760} \frac{273.15}{273.15 + T(^{\circ}\mathrm{C})} \times \frac{p(\mathrm{mmHg})}{760}, \tag{3.39}$$

where $\rho_{0,760} = 1.293 \text{ kg} \cdot \text{m}^{-3}$ is the air density at standard temperature and pressure (STP), *i.e.*, $T = 0\ ^{\circ}\mathrm{C}$ and $p = 760$ mmHg (101.3 kPa). A PEEC used as an absolute dosimeter requires the user to determine the air density with Eq. (3.39).

Additionally, calibrated cavity ionization chambers may be used for exposure or dose assessment in atmospheric conditions different from the atmospheric conditions prevailing at the time they were calibrated. Hence, the calibration coefficient of a cavity ionization chamber is given for a specific reference temperature $T_r$ and reference pressure $p_r$ with $p_r = 101.3$ kPa and $T_r = 20\ ^{\circ}\mathrm{C}$ in Europe and $T_r = 22\ ^{\circ}\mathrm{C}$ in North America. When used for absolute dosimetry, readings obtained by a calibrated cavity chamber must be normalized to the reference temperature and pressure. Typical measurements with calibrated cavity ionization chambers are often conducted at atmospheric conditions that are not considerably different from the reference conditions and a first order correction $P_{T,p}$ based on the ideal gas equation can be applied to the reading of the chamber as follows

$$P_{T,p} = \frac{273.15 + T}{273.15 + T_r} \times \frac{p_r}{p}, \tag{3.40}$$

where $T$ and $T_r$ are in degrees Celsius. Conceptually, $P_{T,p}$ may be viewed as predicting the charge that would be measured by the chamber, if the irradiation took place at the reference temperature and reference pressure, $T_r$ and $p_r$, respectively.

Moreover, temperature may cause expansion of the chamber; hence, altering slightly the physical dimensions of the chamber, and may have some influence on the electrometer being used as an integral part of the dosimetry system. These effects are very small and usually assumed negligible. In relative dosimetry measurements carried out in a short period of time where changes in atmospheric environmental conditions are negligible, temperature and pressure correction factors are not required.

### 3.3.3. Ionic recombination and diffusion losses

In general, the charge collected $Q(V)$ by a polarized ionization chamber operating at a polarizing potential $V$ is less than the charge $Q_{sat}$ produced in the gas by the radiation beam due to initial and general recombination charge loss mechanisms, as well as, ionic diffusion against the electric field established in the chamber. As a result, it is necessary to estimate the collection efficiency $f(V)=Q(V)/Q_{sat}$ of the ionization chamber at the applied voltage $V$ and apply a correction factor $P_{ion}(V)=f^{-1}(V)$ to the measured charge $Q(V)$ to obtain the required dosimetric quantity $Q_{sat}$.

In summary, based on the linear behavior[42] near saturation of $1/Q$ versus $1/V$ in pulsed radiation beams produced by linacs, and $1/Q$ versus $1/V^2$ in continuous radiation beams produced by cobalt-60 teletherapy units, the two-voltage method is commonly used for determining the correction factor $P_{ion}$. The method involves measuring the charge in the irradiated chamber when two different voltages $V_H$ and $V_L$ are applied.

For pulsed radiation beams, the two-voltage technique gives the following result for $P_{ion}$

$$P_{ion}(V_H)=\frac{1-(V_H/V_L)}{(Q_H/Q_L)-(V_H/V_L)}, \tag{3.41}$$

and for continuous radiation beams, the two-voltage technique becomes

$$P_{ion}(V_H)=\frac{1-(V_H/V_L)^2}{(Q_H/Q_L)-(V_H/V_L)^2}, \tag{3.42}$$

where $Q_H$ and $Q_L$ are the measured charges at $V_H$ and $V_L$ voltages, respectively. Most calibration protocols recommend a polarization potential of 300 V for $V_H$ an $V_H/V_L \geq 2$.

### 3.3.4. Polarity effect

In many cases, the measured signal from an irradiated ionization chamber at one polarity does not equal the measured signal when the polarity is reversed. There are many possible causes[42] for this commonly-observed polarity effect. Generally, the possible causes can be divided into two categories: 1) voltage-independent polarity effects and 2) voltage-dependent polarity effects.

*Voltage-independent polarity effects* are mainly produced by radiation interactions taking place directly in various chamber components. These interactions produce a non-dosimetric charge and will add to, or subtract from, the ionization collected from the ionized gas cavity depending on the polarity setting of the chamber at the irradiation time as well as on the irradiation geometry. One important chamber component producing such a polarity effect is the collecting electrode. As illustrated in FIG. 3.8, a residual charge $Q_{\text{elec}}$ is produced on the collecting electrode resulting from: 1) the emission of secondary electrons from the electrode by high energy electrons and photons and 2) low energy electrons coming to a complete stop and landing on the collecting electrode.

Ignoring ionic losses in the cavity, the charge measured when the polarity of the chamber is positive $M_{\text{pos}}$ equals the sum of the dosimetric charge $Q_{\text{sat}}$ and the residual charge $Q_{\text{elec}}$. Similarly, the charge measured by the negatively-polarized chamber $M_{\text{neg}}$ is equal to the sum of the dosimetric charge $-Q_{\text{sat}}$ and the residual charge $Q_{\text{elec}}$. The dosimetric charge $Q_{\text{sat}}$ is calculated by taking half of the difference between $M_{\text{pos}}$ and $M_{\text{neg}}$, *i.e.*,

$$Q_{\text{sat}} = \frac{M_{\text{pos}} - M_{\text{neg}}}{2}. \tag{3.43}$$

The non-dosimetric charge $Q_{\text{elec}}$ that produces the polarity effect can be estimated as follows

$$Q_{\text{elec}} = \frac{M_{\text{pos}} + M_{\text{neg}}}{2}. \tag{3.44}$$

If ionic losses in the cavity are considered, we get instead of Eq. (3.43) the following relationship

$$Q(V) = \frac{M_{\text{pos}} - M_{\text{neg}}}{2} = Q_{\text{sat}} \times f(V). \tag{3.45}$$

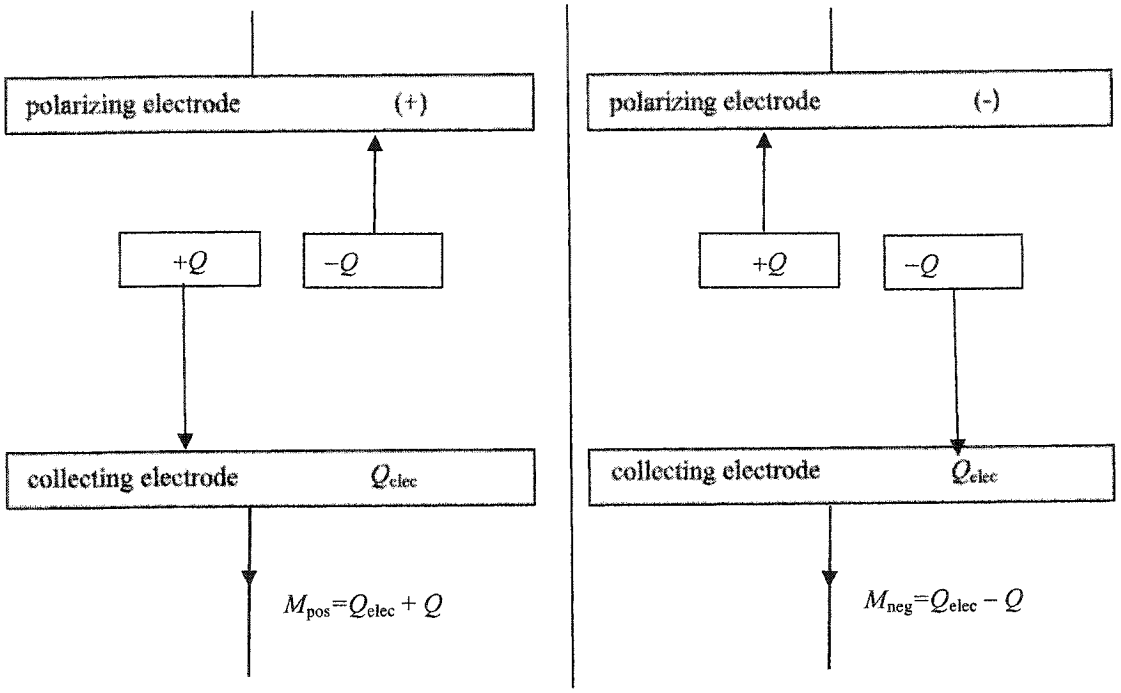


*FIG. 3.8. Ilustration of the polarity effect produced by the collecting electrode of a polarized ionization chamber placed in the path of the irradiation beam. The radiation beam creates, in addition to the positive and negative charges in the gas, a residual charge on the collecting electrode.*

Equation (3.45) may be applied to correct for all voltage-independent polarity effects that are produced by components other than the collecting electrode, such as connecting wires and cables. It should be pointed out that determining $Q(V)$ from the average of the absolute values of $M_{pos}$ and $M_{neg}$, a common procedure in dosimetry, leads to erroneous $Q(V)$ values in situations where $Q_{elec}$ exceeds $Q(V)$.

In photon beams, photon interactions (photoelectric effect and Compton scattering) cause the loss of electrons from the collecting electrode. In the build-up region, these lost electrons are not fully compensated by the arrival of electrons ejected from the upper layers of the phantom. As a result, $|M_{pos}|$ will be greater than $|M_{neg}|$. For depths beyond $z_{max}$, because of the presence of electronic equilibrium $Q_{elec} \approx 0$ and both positive and negative polarities yield the same reading.

In electron beams, the loss of electrons in the collecting electrode is mainly produced by hard collisions between the incident electrons and orbital electrons of the electrode. The sign and magnitude of $Q_{elec}$ depends on the depth at which the chamber is placed. Very close to the surface, the number of "knocked-out" electrons is greater than the number of electrons landing on the collecting electrode. As we go further in depth, the number of "knocked-out" electrons will diminish, while more electrons will stop on the collecting electrode. For this reason, the positive and negative polarity ionization curves for electron beams cross each other several times between the surface and the practical range of the electrons.

*Voltage-dependent polarity effects* include: 1) variation of the sensitive air mass volume of the chamber due to distortion of the electric field lines by space charge[43] or by a potential difference between the collecting electrode and the guard rings[44], 2) difference in the collection efficiency of a chamber resulting from the different mobilities of positive and negative ions[45], especially for cylindrical or spherical ionization chambers.

These effects may either vary the effective air volume from which the dosimetric charge is collected or change the collection efficiency of the chamber when the polarity is reversed. Correcting for voltage-dependent polarity effects is not as simple as correcting for voltage-independent polarity effects. The user may still use chambers exhibiting voltage-dependent polarity effects as long as these effects have a very small impact on the dosimetric signal.

## 3.4. SUMMARY

Ionization chambers are air-filled radiation detectors operating with voltages high enough to collect most of the ionization in the air-sensitive volume produced by the radiation. Three types of air-filled ionization chambers are used in dosimetry: *standard free-air ionization chambers*, *cavity ionization chambers*, and *phantom-embedded extrapolation chambers* (PEEC). While free-air ionization chambers are used mainly in standards laboratories, cavity ionization chambers and PEECs are used in absolute dosimetry and relative dosimetry measurements in radiotherapy clinics in conjunction with appropriate cavity theories.

For absolute dosimetry measurements, *e.g.*, output calibration of external clinical radiation beams, a calibrated cavity ionization chamber having a calibration coefficient traceable to a primary standards dosimetry laboratory in conjunction with a calibration protocol must be used. Suitable chamber calibration coefficients are: (*i*) exposure in air or *air-kerma in air* calibration coefficient used with appropriate calibration protocols with procedures based on exposure in air *or air-kerma in air* calibrations in conjunction with the Spencer-Attix cavity theory, or (ii) an absorbed *dose-to-water* calibration coefficient used in conjunction with an appropriate dosimetry protocol.

For relative dosimetry measurements, the choice of a particular chamber design depends on the task at hand. In most cases, a cylindrical cavity ionization chamber with a cavity volume of 0.6 $cm^3$ is sufficient for relative dosimetry. However, some circumstances require specially designed cavity chambers with a parallel-plate design or smaller volume, or the use of an extrapolation chamber instead.

When ionization chambers are used as radiation dosimeters, various effects, such as ionic recombination, polarity, and environmental conditions, must be considered by the user. Depending on the task at hand and the particular chamber used, the user might need to consider all of these effects or only a few of them.

# REFERENCES


1. G. G. Eichholz and J. W. Poston, *Principles of Nuclear Radiation Detection* (Ann Arbor Science, Ann Arbor, Michigan, 1979).
2. K. S. Krane, *Introductory Nuclear Physics* (John Wiley & Sons, Toronto, Canada, 1988).
3. E. W. Emery, "Geiger-Mueller and proportional counters," in *Radiation dosimetry*, edited by F. H. Attix, W. C. Roesch, and E. Tochilin (Academic Press, New York, 1966), Vol. 2, pp. 73.121.
4. C. E. Zankowski and E. B. Podgorsak, "Calibration of photon and electron beams with an extrapolation chamber," Med. Phys. **24**, 497-503 (1977).
5. F. Deblois, W. Abdel-Rahman, J. P. Seuntjens, and E. B. Podgorsak, "Measurement of absorbed dose with a bone-equivalent extrapolation chamber," Med. Phys. **29**, 433-440 (2002).
6. H. Wyckoff and F. H. Attix, "Design of free-air ionization chambers," Handbook 64, National Bureau of Standards, Washington, D.C.,(1957).
7. F. H. Attix, *Introduction to radiological physics and radiological dosimtry* (John Wiley & Sons, New York, 1986).
8. W. H. Bragg, "Consequences of the corpuscular hypothesis of the gamma and x rays, and the ranges of beta rays," Phil. Mag. **20**, 385 (1910).
9. L. H. Gray, "Absorption of penetrating radiation," Proc. Roy. Soc. A. (London) **122**, 647 (1929).
10. L. V. Spencer and F. H. Attix, "A theory of cavity ionization," Radiat. Res. **3**, 239-254 (1955).
11. F. H. Attix, L. De La Vergne, and V. H. Ritz, "Cavity ionization as a function of wall material," J. Res. **60**, 235 (1958).
12. P. R. J. Burch, "Cavity ionization chamber theory," Rad. Res. **4**, 361 (1955).
13. A. E. Nahum, "Extension of the Spencer-Attix Cavity Theory to 3 media situation for Electron beams," in *Dosimetry in Radiotherapy*, edited by IAEA (IAEA, Vienna, 1988), Vol. 1, pp. 87-115.
14. T. E. Burlin, "The measurement of exposure dose for high energy radiation with cavity ionization chambers," Phys. Med. Biol. **3**, 197-206 (1959).
15. G. Lempert, R. Nath, and R. J. Schulz, "Fraction of ionization from electrons arising in the wall of an ionization chamber," Med. Phys. **10**, 1-3 (1983).
16. AAPM Task Group 21 of the Radiation Therapy Committee, "A protocol for the determination of the absorbed dose from high-energy photon and electron beam," Med. Phys. **10**, 741-771 (1983).
17. D. Harder, " Einfluss der Vielfachstreuung von Elektronen auf die Ionization in gas gefüllten Hohlräumen," Biophysik **5**, 157 (1968).
18. ICRU, "Radiation dosimetry: Electrons with energies between 1 and 50 MeV," Report 35, International Commission on Radiation Units and Measurements, Washington, D. C. (1972).
19. K. Johansson, L. Mattson, L. Lindborg, and H. Svensson, "Absorbed-dose determination with ionization chambers in electron and photon beams having energies between 1 and 50 MeV," Report IAEA-SM 222/35, International Atomic Energy Agency, Vienna (1977).

20. ICRU, "Determination of absorbed dose in a patient irradiated by beams of X or gamma rays in radiotherapy procedures," ICRU Report 24, International Commission on Radiation Units and Measurements, Washington, D. C. (1976).

21. Task Group 25 American Association of Physicists in Medicine, "Clinical electron beam dosimetry," Med. Phys. **18**, 73-109 (1991).

22. International Atomic Energy Agency, *Absorbed dose determination in photon and electron beams: An international code of practice* (IAEA Technical Reports Series No. 277, Vienna, 1987).

23. Institute of Physics & Engineering in Medicine & Biology, "The IPEMB code of practice for the determination of absorbed dose for x-rays below 300 kV generating potential (0.035 mm AL-4mm Cu HVL; 10-300 kV generating potential). Institution of Physics and Engineering in Medicine and Biology," Phys. Med. Biol. **41**, 2605-2625 (1996).

24. Institute of Physics & Engineering in Medicine & Biology, "The IPEMB code of practice for electron dosimetry for radiotherapy beams of initial energy from 2 to 50 MeV based on air-kerma calibration. Institution of Physics and Engineering in Medicine and Biology," Phys. Med. Biol. **41**, 2557-2603 (1996).

25. P. R. Almond, P. J. Biggs, B. M. Coursey, W. F. Hanson, M. Saiful Huq, R. Nath, and D. W. O. Roger, "AAPM's TG-51 protocol for clinical reference dosimetry of high- energy photon and electron beams," Med. Phys. **26**, 1847-1870. (1999).

26. International Atomic Energy Agency, *Absorbed Dose Determination in External Beam Radiotherapy based on Absorbed-Dose-to-Water Standards: An international code of practice* (IAEA Technical Reports Series No. 398, Vienna, 2000).

27. G. Failla, "Measurement of tissue dose in terms of the same unit for all ionizing radiations," Radiology **29**, 202-215 (1937).

28. J. Böhm and U. Schneider, "Review of extrapolation chamber measurements of beta rays and low energy x-rays," Radiat. Prot. Dosim. **14**, 193.198 (1986).

29. D. J. Manson, D. Velkley, J. A. Purdy et al., "Measurements of surface dose using build-up curves obtained with an extrapolation chamber," Radiology **15**, 473.474 (1975).

30. R. Loevinger, "Extrapolation chamber for measurement of beta sources," Sci. Instr. **24**, 907-914 (1953).

31. C. G. Soares, "Calibration of ophthalmic applicators at NIST: a revised approach," Med. Phys. **18**, 787-793 (1991).

32. S. Genna and J. S. Laghlin, "Absolute calibration of cobalt 60 gamma-ray beam," Radiology **65**, 394-405 (1955).

33. C. Klevenhagen, "Determination of absorbed dose in high-energy electron and photon radiations by means of an uncalibrated ionization chamber," Phys. Med. Biol. **36**, 239-253 (1991).

34. B. Nilsson and A. Montelius, "Fluence perturbation in photon beams under nonequilibrium conditions," Med. Phys. **13**, 191-195 (1986).

35. D. E. Velkley, D. J. Manson, J. A. Purdy, and G. D. Oliver, "Build-up region of megavoltage photon radiation sources," Med. Phys. **2**, 14-19 (1975).

36. D. E. Mellenberg, "Determination of build-up region over-response corrections for a Markus-type chamber", Med. Phys. **17**, 1041-1044 (1990).

37. N. B. J. Tannous, W. F. Gagnon, and P. R. Almond, "Buildup region and skin-dose measurements for Therac 6 linear accelerator for radiation therapy," Med. Phys. **8** 378-381 (1981).

38. ICRU, "Radiation quantities and units," Report 19, International Commission on Radiation Units and Measurements, Washington, D. C. (1971).

39. ICRU, "Average energy required to produce an ion pair," Report 31, International Commission on Radiation Units and Measurements, Washington, D. C. (1979b).

40. M. Boutillon and A.-M. Perroche, "Effect of a change in the stopping-power values on the *W* value recommended by ICRU for electrons in dry air," Bureau International des poids et Mesures, Sèvres, Rept. CCEMRI(I)/85-8.

41. M. T. Niatel, "Etude experimentale de l'influence de la vapeur d'eau sur l'ionisation produite dans l'air," Comptes Rendus Acad. Sci. Paris **268**, 1650 (1969).

42. J. W. Boag, "Ionization chambers," in *Radiation dosimetry*, edited by F. H. Attix, W. C. Roesch and Tochilin (Academic Press, Ney Yory, 1966), Vol. 2, pp. 1-72

43. J. W. Boag, "Space charge distortion of the electric field in a plane parallel ionization chamber," Phys. Med. Bio. **8**, 461-467 (1963).

44. J. W. Boag, "Distortion of the electric field in an ionization chamber due to a difference in potential between guard ring and collector," Phys. Med. Bio. **9**, 25-32 (1964a).

45. A. C. Lapsley, "Effect of space charge on saturation properties of ionization chambers," Rev. Sci. Instr. **24**, 602 (1953).

# Chapter 4

# EXPERIMENTAL APPARATUS

## 4.1. PHANTOM-EMBEDDED EXTRAPOLATION CHAMBER

### 4.1.1. General design of the chamber

The phantom-embedded extrapolation chamber (PEEC) used in our experiments was originally designed by Zankowski and Podgorsak[1-5] and built in the mechanical shop of the Medical Physics department of the McGill University Health Centre (MUHC). The PEEC has a parallel-plate geometry and the electrode separation can be varied continuously from a fraction of a mm to about 1 cm. Zankowski and Podgorsak[5] showed that the device can be used as an alternative method to calibrated cavity ionization chambers for calibrating high energy clinical radiation beams. The PEEC was originally made entirely of Solid Water™ material (model 457; Gammex-RMI, Middleton, WI). The composition and radiological properties of Solid Water™ can be found in many references in the literature[6-10].

Deblois[11] subsequently modified the design of the original PEEC by attaching a stepping motor onto the mobile piston, thus allowing the control of the piston position through a computer. He also changed the electrode and piston material and used the hybrid PEEC for dose measurements in materials other than Solid Water™.

Figure 4.1 shows a schematic diagram of the PEEC including the standard electrical operation diagram. The PEEC assembly forms a 30×30×10 $cm^3$ Solid Water™ block with a cylindrical aperture of 7 cm bored parallel to the direction of the beam in the center of the Solid Water™ block. A movable cylindrical piston also made of Solid Water™ fills the cylinder bore in the block. The movable piston is designed such that a smaller cylinder made of any material can be mounted on top of the piston. This particular design of the piston allows dose measurements in materials other than Solid Water™. Currently,

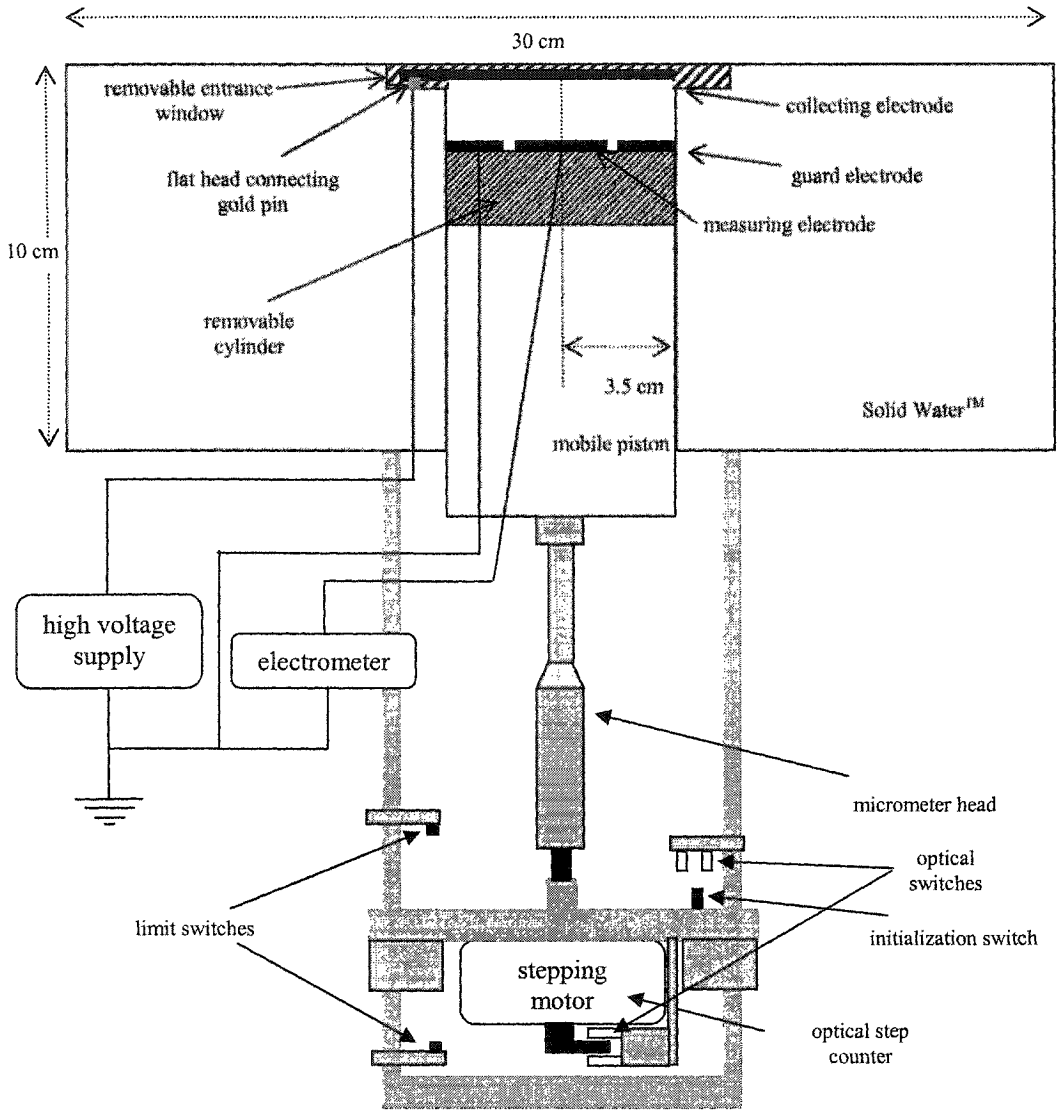


*FIG. 4.1. Schematic representation of the PEEC.*

the piston consists of a 0.5 cm thick Solid Water™ cylindrical disk and a 2 cm thick cylindrical disk made of a bone equivalent material (model SB3; Gammex-RMI, Middleton, WI).

The removable entrance window on the top of the PEEC assembly together with the cylindrical removable piece mounted on the piston define the sensitive air volume of the chamber. In our work, two different entrance windows and a Solid Water™ removable cylinder were used. The Solid Water™ removable cylinder was part of the original design of the PEEC. The collecting electrode and the guard electrode are made of a thin layer

(50 μm) of graphite dag that is spray-painted directly onto the top of the cylinder. The first entrance window, designed by Zankowski, is made of Solid Water™ having a thickness of 0.2 cm above the sensitive air volume of the chamber. Graphite dag is spray-painted onto the inside of the Solid Water™ entrance window to form the polarizing electrode. For some of our experiments, we designed a second removable entrance window made of a thin aluminized Mylar (polyethylene terephthalate) foil stretched between two Delrin (polyoxymethylene) rings.

The bottom of the movable piston of the PEEC is attached to a micrometer head through a ball-bearing mechanism. The micrometer head is directly connected to the stepping motor which in turn sits on a holder that slides on two vertical cylindrical tracks as the motor shaft rotates the micrometer head in one direction or the other. The two vertical cylindrical tracks hold the movable piston and the stepping motor assembly onto the Solid Water™ block. To minimize backscatter radiation from all extracameral non-phantom materials, principally the motion-controlled piston assembly, the stepping motor and its holder are located at least 10 cm from the chamber sensitive volume. In addition, all metallic components of the PEEC are made of aluminum ($Z = 13$) rather than higher $Z$ materials.

Based on the standard circuitry of ionization chambers, the collecting electrode of the PEEC is connected to ground through a calibrated electrometer (model 35617; Keithley, Cleveland, OH), while the guard ring is connected to ground directly. A variable voltage power supply (model 248; Keithley, Cleveland, OH) providing a variable bias of up to ±5000 V was connected to the polarizing electrode on the removable entrance windows through a flat head gold pin.

### 4.1.2. Electrode construction

The electrodes on the Solid Water™ entrance window and on the 0.5 cm thick disk of Solid Water™ are constructed from thin uniform layers of graphite dag (Aquadag; Acheson Colloids (Canada), Ltd., Ontario), spray-painted with a pressurized airbrush (Eclipse; Iwata, Japan) directly onto the Solid Water™ surface. Each applied dag layer corresponds to a thin ~10 μm layer. The layer is sanded and polished to ensure uniform

deposition of graphite across the surface and to remove surface irregularities. The process is repeated when an additional layer is applied till the resistance across the electrode falls below 30 Ω corresponding to a graphite thickness of the order of 50 μm.

Before the graphite electrode is spray-painted onto the 0.5 cm thick Solid Water™ disk, small spring-loaded gold-plated pins are pushed through small holes and the flat closed end of the spring-loaded pins is leveled with the disk surface. These spring-loaded pins are used as contact points for small gold pins welded to triaxial cables in the chamber circuitry. After the disk surface is spray-painted with the graphite dag, two independent graphite-conducting surfaces are produced using a lathe to etch a small circular groove into the graphite layer. The inner thin graphite disk corresponds to the collecting electrode and the outer disk corresponds to the guard rings; each having its own spring-loaded pin.

The Solid Water™ entrance window is made of a 9.7 cm diameter Solid Water™ disk having a thickness of 4 mm. The thickness of the central area of the disk with 7.3 cm diameter is reduced to 2 mm onto which the graphite electrode is deposited. The entrance window is mounted to the top of the Solid Water™ block and is fastened with nylon screws. The polarizing electrode, when the entrance window is fastened, touches a spring-loaded brass pin which is connected to the high-voltage power supply.

The Mylar entrance window is made of an aluminized Mylar disk-shaped foil and two Delrin rings. The combined thickness of the Mylar layer and the thin conducting aluminum layer is 50 μm, making the electrode suitable for surface dose measurements. The Delrin rings have an outer diameter of 9.7 cm and an inner diameter of 7.3 cm for the bottom ring and 7.2 cm for the top ring. The thickness of the bottom ring is 2 mm having an additional 2 mm thick ridge with a radial thickness of 1 mm starting from the inner diameter of the ring. The top ring has a thickness of 2 mm, thus producing a uniform 4 mm thick Delrin ring when both (top and bottom) rings are assembled together. This particular design of the Delrin entrance window ensures the flatness of the aluminized Mylar foil when the foil is held in place between both rings. It was not possible to construct the rings with these particular dimensions from Solid Water™, because the rings break easily during the machining process. The bottom ring has a small hole so that

the aluminized Mylar foil makes contact with the spring-loaded brass pin, when the entrance window is fastened to the Solid Water™ block.

After the machining of the Delrin rings, a thin layer of epoxy glue (5 minute epoxy syringe glue; Lepage, Henkel Canada Corporation, Brampton, Ontario) was applied to the bottom ring, and the Mylar foil was pressed onto the bottom ring, in such a way that the conducting aluminum layer faces the conducting graphite layer on the Solid Water™ disk when the entrance window assembly is fixed to the Solid Water™ block. Both removable entrance windows (the Solid Water™ and the aluminized Mylar) are shown schematically in FIG. 4.2 and the physical properties of the materials are summarized in TABLE 4.1. The removable entrance windows were affixed to the Solid Water™ block using 6 nylon screws.

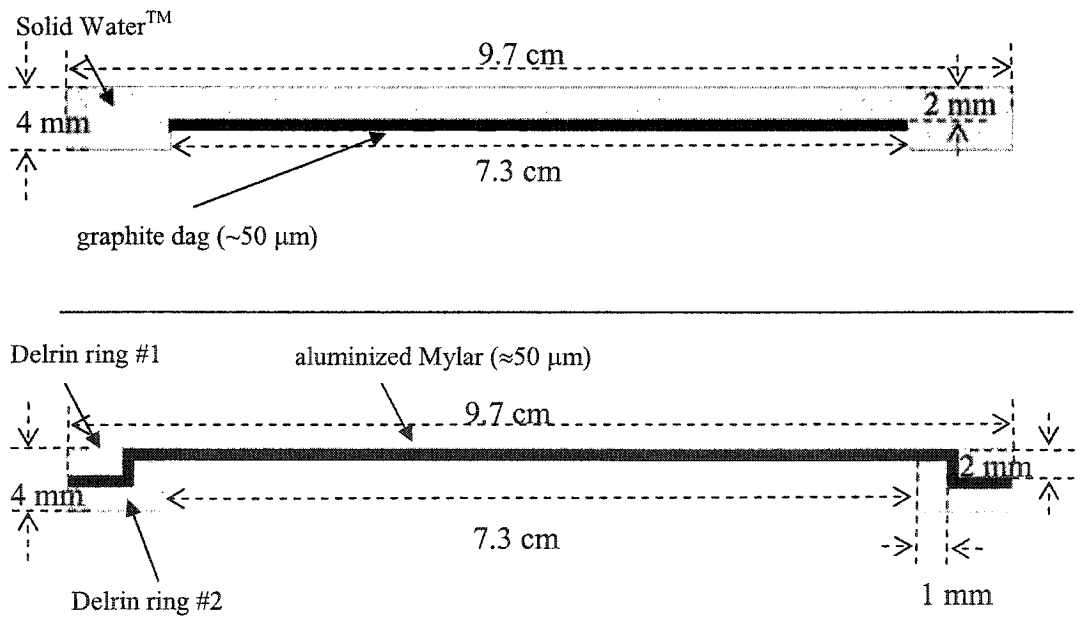


*FIG. 4.2. Schematic representation of the Solid Water™ entrance window (top) and the aluminized Mylar entrance window (bottom).*

TABLE 4.1. PHYSICAL PROPERTIES AND COMPOSITION OF MATERIALS USED IN CONSTRUCTING THE SOLID WATER™ AND ALUMINIZED MYLAR REMOVABLE ENTRANCE WINDOWS.

| | graphite | Solid Water™ | Mylar | aluminum | Delrin |
|---|---|---|---|---|---|
| $\rho$ (g/cm$^3$) | 1.7 | 1.035 | 1.4 | 2.702 | 1.425 |
| composition | % | % | % | % | % |
| H | | 8.09 | 4.1959 | | 6.7135 |
| C | 100 | 67.22 | 62.5017 | | 40.0017 |
| N | | 2.4 | | | |
| O | | 18.84 | 33.3025 | | 53.2848 |
| Al | | | | 100 | |
| Ca | | 2.32 | | | |
| Cl | | 0.13 | | | |

### 4.1.3. Computer-controlled system

Deblois[11] modified the original PEEC assembly to simplify the acquisition of data through the use of a personal computer (486 PC compatible). The computer controls remotely the operation of the PEEC through two different interfaces; namely, (*i*) a parallel interface for controlling the stepping motor and (*ii*) a GPIB (IEEE Std 488.2-1992; Institute of Electrical and Electronic Engineers, New York, NY) interface which controls all standard IEEE-488 instruments.

The stepping motor attached to the movable piston is controlled through an aluminum box containing the print circuit and power supply for the stepping motor. The motor control box sits next to the personal computer and is connected to the personal computer parallel port. A 10 m long 9-wire shielded cable connects the PEEC stepping motor to its aluminum control box.

A miniature serial to an IEEE-488 controller (Micro 488/p-901 rev 1.0; IOtech Inc, Cleveland, OH) is used to control all standard IEEE-488 instruments. For the PEEC, the IEEE-488 instruments are a Keithley 35617 electrometer and a high voltage power supply (Keithley 248). This GPIB interface converts the RS-232 serial port commands from the computer into an IEEE-488 bus talker, listener, and controller for up to 8 IEEE-488 instruments on a daisy chain cable. Some of our measurements with the PEEC required the use of a separate reference chamber for monitoring the radiation output from the linac. The reference chamber was connected to a second electrometer (model 6517A; Keithley,

Cleveland, OH) through a triaxial cable connection which was capable of providing a variable bias of up to ±1000 V. The Keithley 6517A electrometer, when used in our measurements, was also controlled by the personal computer through the GPIB bus. A schematic diagram of the computer-controlled system is shown in FIG. 4.3.

The computer programs for controlling all auxiliary instruments (the stepping motor, the Keithley 248 power supply, and the Keithley 6517A and 35617 electrometers) were written in the basic language (QuickBasic™ v.4.5; Microsoft, Remond, WA). Many of these programs are menu-driven and allow the user to visualize and analyze the results on the screen and also to write results of interest to text files.

### 4.1.4. Remote control for the PEEC piston

The piston movement is controlled through the stepping motor. A sequence of pulses produced by the aluminum control box rotates the stepping motor through one step in either direction, and the position of the motor within one rotation is monitored constantly by an optical switch attached to the shaft of the motor. It takes 200 steps for the stepping motor to complete one revolution which corresponds to a micrometer displacement of 0.5 mm.

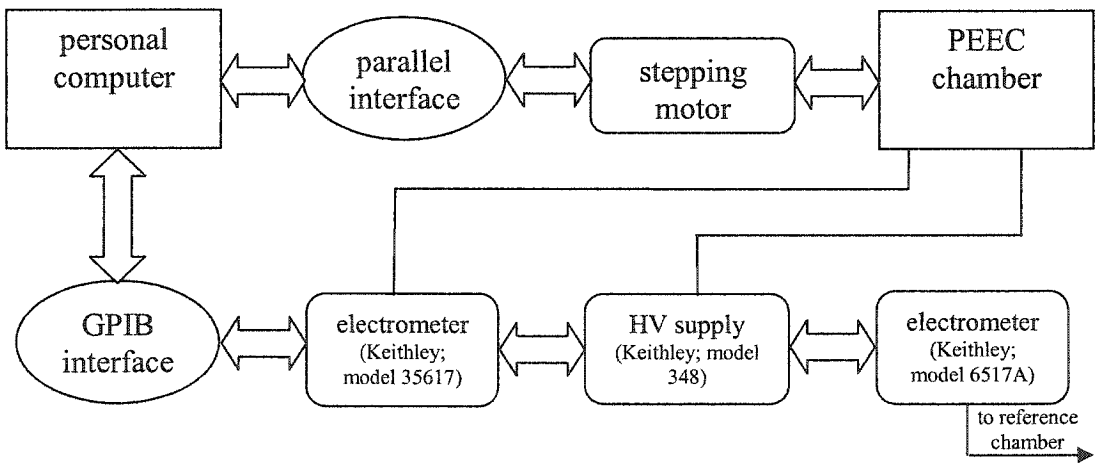


*FIG. 4.3. Schematic diagram of the computer-controlled system for measurements with the PEEC and a reference chamber.*

Optical switches indicated on FIG. 4.4 are electronic devices having a U-shape and are used in conjunction with an optical barrier. One arm has an optical light source called the emitter, while an optical sensor called the detector is mounted on the other arm opposite to the emitter. The detector acts as a conductor when it detects light emitted from the emitter. On the other hand, when an optical barrier comes between the two arms, the detector acts as a capacitor.

Two optical switches are used for the PEEC piston control; one is mounted on the shaft below the stepping motor, thus monitoring the rotation of the shaft, and the other is mounted on one of the vertical tracks, as also shown in FIG. 4.1. The second switch is movable on the track and is fastened with a set of screws to select the minimal operation distance between the electrodes $s_0$, usually set to correspond to an electrode separation $s$ between 0.5 – 1.0 mm. This initial position of the piston is defined to be the position at which both optical switches act as conductors. As the stepping motor rotates, the micrometer is displaced by a relative distance $s_{rel}$ and the optical switch on the vertical track becomes a conductor. The optical switch below the stepping motor acts as conductor at most relative displacements and becomes occasionally a capacitor when its optical barrier mounted on the shaft comes directly between the switch emitter and the detector. This occurs after every complete shaft revolution from the initial position of the piston and is used to monitor the performance of the piston assembly. Figure 4.4 shows schematically the principle of operation of the two optical switches.

Additionally, two physical limiting switches are installed on the piston's assembly. The constant exposure of the optical switches to radiation degrades their performance and the switches must be replaced eventually. The bottom physical limiting switch acts as a safe-guard in case that the optical switches fail in order to prevent a direct contact of the electrodes. The top physical limiting switch determines the maximum traveling distance of the piston which is usually set to correspond to an electrode separation $s$ of about 12 mm.

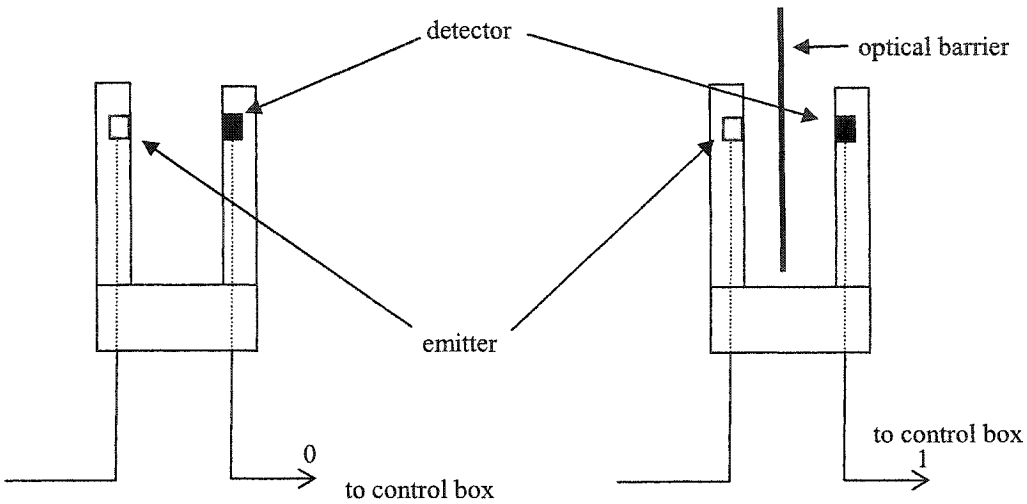


*FIG. 4.4. Schematic diagram of the operation of an optical switch. When an optical barrier comes between the emitter and the detector, the device acts as a capacitor rather than a conductor.*

### *Reproducibility of the piston control system*

The reproducibility of the piston's motion and linearity of the relation between the position requested by the positioning subroutine and the reading of the micrometer were verified extensively. The agreement between the software-requested position and the displacement reading from the micrometer is nearly perfect (see FIG. 4.5) with a slope of $1.000 \pm 0.001$. At very low positions, however, a small deviation from linearity is observed. To avoid this problem, the PEEC is usually operated at positions relatively far from $s_0$.

In addition, a small hysteresis effect of the piston motion was observed. When going in one direction of movement, the reproducibility of the desired positions was excellent; however, this hysteresis effect occurs only if one has to go back in position and then forward again. This effect on the micrometer motion is thought to be due to some "play" in its mechanism, and the effect is avoided, if the piston is always moved in the same forward direction during signal measurements. In situations where a position lower than the piston's current position is required, a new initialization to $s_{rel} = 0$ position was made.

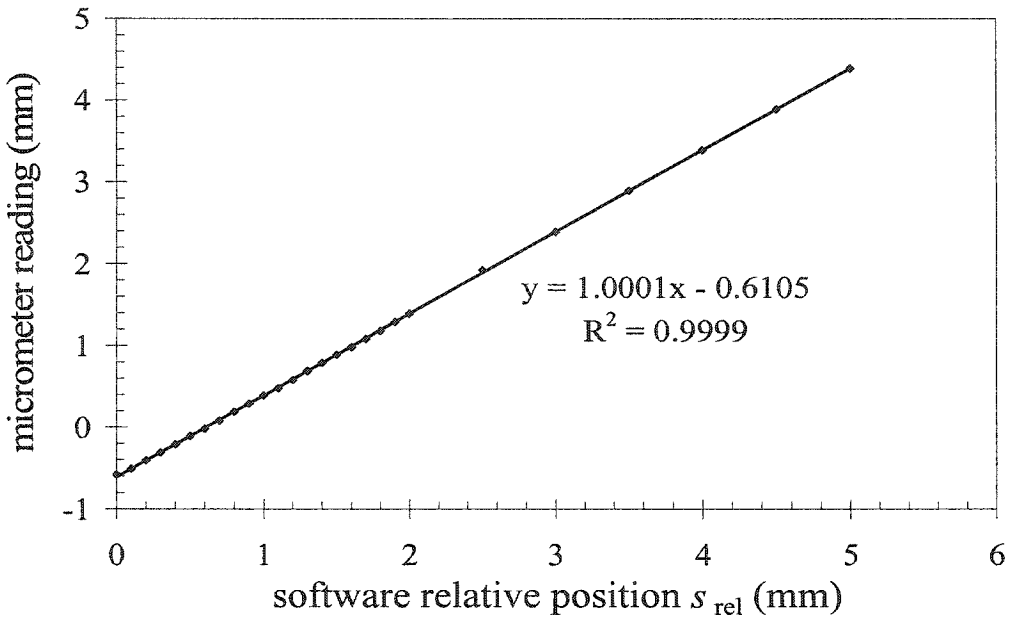


*FIG. 4.5. Comparison of software-requested position with the micrometer reading.*

### 4.1.5. Determination of the collecting electrode area

The successful dosimetry operation of the PEEC strongly depends on the precise knowledge of the effective area $A$ of the collecting electrode. Because of the finite width of the groove that separates the collecting electrode and the guard ring, the effective area $A$ of the collecting electrode is determined more accurately through electrical means rather than relying on measuring the physical dimension of the collecting electrode.

The capacitance $C$ of a parallel-plate ionization chamber with a sufficiently large guard-ring approaches the capacitance of two infinite parallel-plates and is given by

$$C = \frac{\Delta Q}{\Delta V} = \varepsilon_0 \frac{A}{s}, \tag{4.1}$$

where $\varepsilon_0$ is the electrical permittivity of vacuum ($8.85\times10^{-12}$ F·m$^{-1}$); $s$ is the separation between the electrodes ($s = s_o + s_{rel}$); and $\Delta Q$ is the variation in measured charge for a $\Delta V$ change in polarizing voltage.

Since the initial position $s_o$, which corresponds to the minimum electrode separation achievable for a particular optical switch position, is not accurately known, the effective area $A$ of the collecting electrode is determined by first measuring the capacitance $C$ of

the chamber at different relative displacements $s_{rel}$, then plotting the inverse capacitance $1/C$ versus $s_{rel}$. Rearranging Eq. (4.1) as

$$\frac{1}{C} = \frac{\Delta V}{\Delta Q} = \frac{s_0 + s_{rel}}{\varepsilon_0 A}, \tag{4.2}$$

the slope of the linear fit of $1/C$ versus $s_{rel}$ is $(\varepsilon_0 A)^{-1}$ and the x-intercept is the minimum electrode separation $s_0$. This procedure for the determination of the effective area $A$ is usually repeated for both polarities and before every use of the chamber.

The effective area $A$ of the collecting electrode can be determined accurately using a few capacitance measurements $\Delta Q/\Delta V$ (typically 5) at several selected electrode separations $s_{rel}$ (typically 5). After the PEEC became part of the computer-controlled system, automatization of capacitance measurements made this process less time-consuming, more practical, and, more importantly, allowed a comprehensive study of the performance of the PEEC to be conducted.

Two QBasic programs, each for a different polarity, were written to automate the determination of the effective area $A$ with the computer-controlled system. As a safety feature, the polarity setting of the Keithley 248 high voltage power supply can be set only manually from a switch located at the rear of the device, preventing any control of the polarity setting from its GPIB interface. The automatization capacitance programs control the piston position through the stepping motor and the applied voltage produced by the Keithley 248 high voltage power supply on the polarizing electrode, and read the charge measured by the electrometer.

At each piston position, the program sequence is as follows: 1) set polarizing voltage at a reference voltage of ±50 V; 2) wait for 5 s to allow the system to stabilize; 3) read the reference charge $Q_{50}$; 4) set the polarizing voltage at $V$; 5) wait for 5 s to allow the system to stabilize; 6) read the charge $Q_V$; and 6) calculate the capacitance $C = (Q_V - Q_{50})/(V \mp 50)$. This sequence is then repeated for a different polarizing potential $V$. The programs can take a total of 25 $\Delta Q/\Delta V$ measurements (5 measurements of $\Delta Q/\Delta V$ per 5 separations) in a period of 15 min.

### *Linearity of piston control system*

The automatization of the PEEC enabled us to conduct a comprehensive capacitance study of the chamber and evaluation of the movable piston performance. With the Solid Water™ entrance window mounted, 100 capacitance measurements were acquired at 100 different relative electrode separations $s_{rel}$ ranging from 0 to 4 mm, with $\Delta V$ ranging from 4 to 400 V. The data measurements took about 3 days for each polarity.

A plot of the inverse of the capacitance $C$ averaged over the 100 measured $\Delta Q/\Delta V$ points versus the relative electrode separation $s_{rel}$ for both polarities is shown in FIG. 4.6. The effective area $A$ of the collecting electrode was determined to be $4.618\times10^{-4}$ m$^2$ and $4.602\times10^{-4}$ m$^2$ for positive and negative chamber polarities, respectively. The averaged area of the collecting electrode, consequently, was $4.610 \pm 0.016$ cm$^2$.

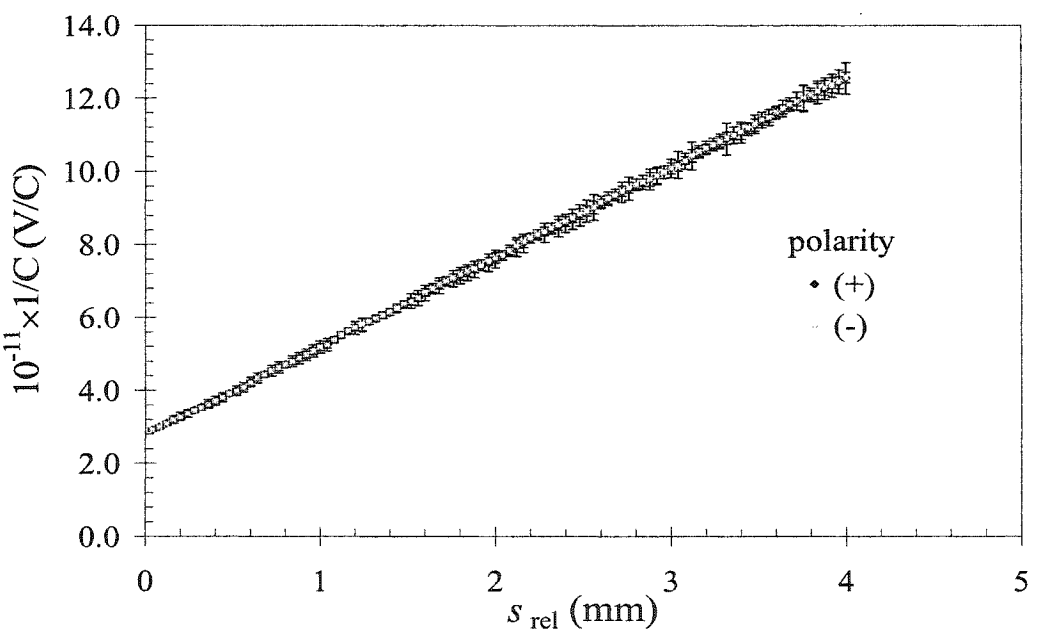


*FIG. 4.6. Inverse capacitance as a function of relative electrode displacement for PEEC with Solid Water™ entrance window in place.*

Theoretically, the capacitance $C$ of the PEEC can be calculated with Eq. (4.1) if $A$ and $s$ are known. To evaluate any possible systematic positioning errors of the piston control system, the effective area $A$ and the minimum electrode separation $s_o$, both determined from capacitance measurements were used to calculate the theoretical capacitance $C_{theor}$ at a particular relative electrode separation $s_{rel}$ following the relationship given by Eq. (4.2). At all $s_{rel}$ for which $\Delta Q/\Delta V$ measurements where collected, the difference between the calculated $C_{theor}$ and measured $C_{meas}$ that is based on 100 measured $\Delta Q/\Delta V$ points at the particular $s_{rel}$ divided by $C_{theor}$ is plotted against $s_{rel}$ in FIG. 4.7. The plot shows a similar periodic pattern for both polarities with a period corresponding to one complete revolution of the piston. This systematic error is possibly produced by an inherent non-linear motion of the micrometer screw. The magnitude of this error is within 0.5% at most positions beyond the first 0.5 mm displacement. This relatively large discrepancy at very small electrode separations coincides with results of a direct comparison of software-requested position with micrometer readings shown in FIG. 4.5.

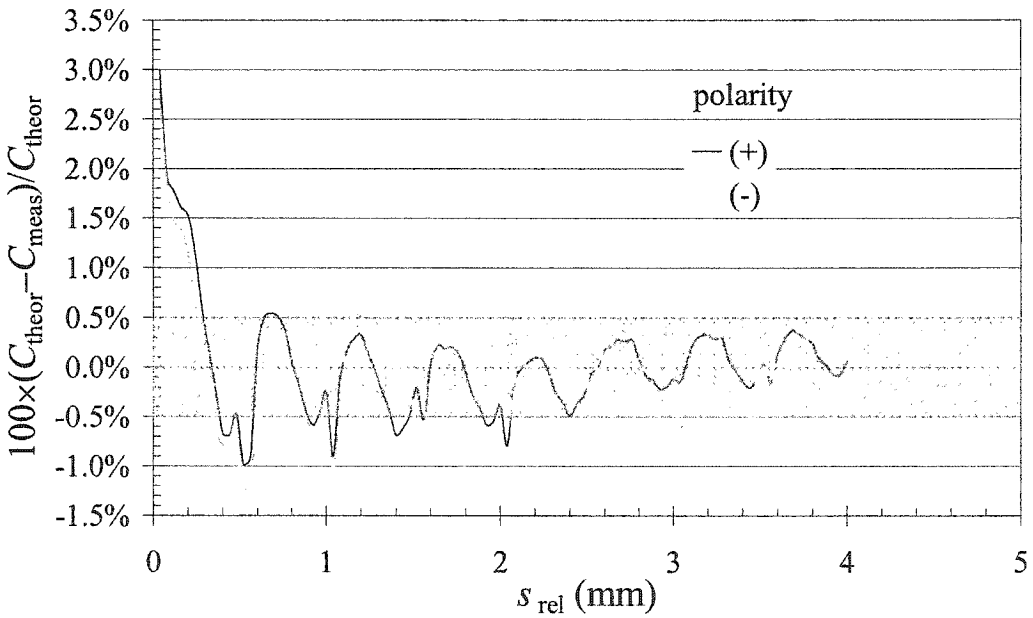


*FIG. 4.7. Evaluation of systematic positioning errors by the piston control system, where $C_{th}$ is the theoretical capacitance calculated from the effective area A and the minimum electrode separation $s_o$, and $C_{meas}$ is the measured capacitance.*

### 4.1.6. Leakage measurement with the PEEC

The charge recorded by an electrometer connected to a polarized ionization chamber exposed to a radiation beam is produced mainly but not exclusively by ionization in the gas. Direct radiation interactions with various chamber components and leakage currents produced in the associated circuitry also contribute to the measured signal. The dosimetric signal of interest to a physicist is provided by the gas ionization, and any signal due to leakage current or due to direct radiation interactions with chamber components must be removed from the signal recorded by the electrometer in order to obtain the correct dosimetric signal.

To verify that leakage currents did not significantly affect our measurement by the PEEC in a radiation beam, the PEEC leakage current was measured as a function of the polarizing voltage for 1.2 mm, 2 mm, and 4 mm electrode separations and no irradiation of the chamber. The magnitude of the polarizing voltage was increased from 50 V to 1500 V in steps of 50 V in all measurements. 1000 current readings were acquired at a particular voltage using a QBasic program with the PEEC connected to the computer-controlled system. Figure 4.8 plots the leakage current, averaged over 1000 readings for the PEEC.

Some scans [(-) 2 mm, (-) 4 mm] produced a stable leakage current essentially independent of the applied voltage, with an average current of about -0.13 pA. The leakage currents in other scans, although varying with voltage, were on the average about 1 order of magnitude smaller than those of scans with the stable current. Additionally, the "stability" of a particular scan seems to be independent of the electrode separation $s$ as well as the polarity of the chamber, and more likely depending on the electrometer environmental conditions. Nevertheless, analyzing all data, the leakage currents of the PEEC are much smaller than currents measured in radiation beams, since the dosimetric current readings measured with PEEC are typically 1 nA, *i.e.*, four orders of magnitude higher than the maximum leakage current of 0.1 pA. A conclusion was made that leakage signals did not affect appreciably the dosimetric signal measured with the PEEC and were thus ignored in our data analysis.

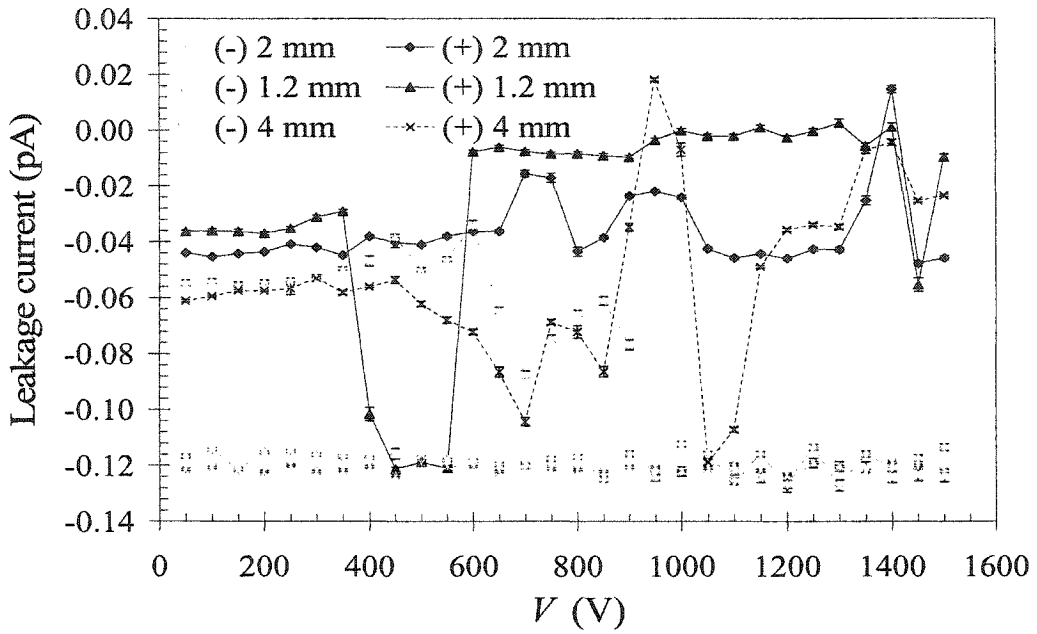


*FIG. 4.8. Average leakage current of the PEEC against the polarizing voltage. The data were collected for electrode separations of 1.2 mm, 2 mm, and 4 mm, using the Solid Water™ entrance window. At each polarizing voltage setting and electrode separation, the average value over 1000 current measurements is well below current signals (on the order of 1 nA) measured in a radiation beam.*

### 4.1.7. Calibration of the electrometers and power supplies

To analyze saturation curves of ionization chambers accurately, one must verify the performance of the voltage power supply and the response of the reading electrometer. The polarization delivered by the Keithley (model 348) power supply was cross-calibrated with a high precision voltmeter (model; Keithley, Cleveland, Ohio), and the Keithley power supply was found to deliver voltages within their specifications (within ±0.5 V). This would induce a small polarization error in the measurements of the order of 1% only at very low polarizing voltages; however, near saturation where the measured currents vary slowly with change in polarizing voltage, the small error in the bias voltage has a negligible effect on measurements.

Both electrometers (Keithley model 35617 and Keithley model 6517A) were calibrated using a calibrated picoampere current source (model 261; Keithley, Cleveland, Ohio) with a calibration factor traceable to a standards laboratory (National Research Council,

Ottawa, Canada). The current source was set to produce ±1.000 nA in an interval of 100.0 s to deliver a total output of 100.0 nC. The current source was connected to the electrometer via a relay switch. The timing device was a universal timer which includes a relay triggered by an internal pulse-counter driven by a synchronized internal clock. The electrometers read the delivered charge to within ±0.01%.

## 4.2. MONTE CARLO CALCULATION SYSTEM

### 4.2.1. Introduction

Monte Carlo methods, instead of addressing clear-cut mathematical problems, attempt to develop methods for simulating complicated processes. A computer code written specifically to simulate a particular problem can be used to calculate numerical solutions and draw statistical conclusions for the problem. In radiotherapy physics and radiation dosimetry, Monte Carlo methods have been used by manufacturers for designing treatment units by manufacturers and by clinics and research institutes for solving complex dosimetric problems. Radiation beams are transported through a particular geometry of interest, while possible interactions of radiation with matter are modeled by simulating the possible trajectories and energy depositions of individual particles, also called histories, using tabulated cross sections for the different possible interactions. By simulating millions of histories transported through the pre-defined geometries, macroscopic measurable quantities, such as the absorbed dose in matter, can be calculated even for the most complex situations involving treatment of real patients.

Many Monte Carlo software packages, specifically developed for application in medical physics, are currently available commercially. A typical Monte Carlo software package used in medical physics will have the following components:

- interaction cross-section data for photons and electrons/positrons
- particle transport algorithms
- geometry modeling
- simulation data analysis tools

These various packages usually fall into two main categories based on the algorithms for transporting electrons. The two categories are the "Class-I" Monte Carlo systems and the

"Class-II" Monte Carlo systems. In both classes, electrons are transported in discrete steps, but the difference between the two classes is based on the type of interactions that take place during the individual steps.

In *"Class-I" Monte Carlo systems*, an electron in a single step loses an amount of energy that corresponds to the energy lost through all possible mechanisms (soft and hard collisions as well as radiative losses). The magnitude of the energy loss in a single step is calculated based on unrestricted total stopping powers. The electrons are transported following a pre-determined energy loss grid, yet a "Class-I" algorithm can be sophisticated enough to generate secondary particles (electrons or bremsstrahlung photons) for each individual step and account for the angular deflection and energy-loss straggling. The popular ETRAN (Electron TRANsports) code developed by Berger and Seltzer[12] is an example of a "Class-I" Monte Carlo system.

In *"Class-II" Monte Carlo systems*, an electron in a single step loses its energy only through one interaction type (radiative, soft or hard collision) that is sampled by the code. These algorithms use cross sections for hard collisions and radiative losses to determine the next interaction point for the transported electron. The code then moves the electron based on the continuous slowing down approximation (CSDA) to the interaction point and the particular electron losses an energy in the process that is determined by the restricted stopping powers and is directly deposited as dose into the geometry. At the interaction point, a "catastrophic" event, either a hard collision or bremsstrahlung interaction, occurs and the code generates the secondary particles that are released from that particular interaction (δ-rays for hard collisions and bremsstrahlung x-rays for radiative losses) and accounts for angular deflections. In a single electron transport step, the cross sections, hence, the distance to the next interaction point, are evaluated at the initial electron kinetic energy, meanwhile the cross sections at the next interaction point are essentially different, since the electron must lose some energy between interactions (soft collisions). Class-II codes use several "tricks" to remove this particular problem. Codes based on EGS[13-15] (Electron-Gamma-Shower) series are classified as "Class-II" Monte Carlo systems.

## 4.2.2. The EGS Monte Carlo code system

### *History*

The EGS Monte Carlo system, a "Class-II" code system, was originally developed at the Stanford-Linear Accelerator Centre (SLAC) by Ford and Nelson[13]. The EGS code system was formally introduced as a package in 1978, referred to as the EGS3. In 1985, the EGS4 (ref. 14) was released with major improvements to its predecessor EGS3 and was capable of transporting electrons and photons down to 1 keV.

The EGS4 code system was developed by Nelson, Hirayama, and Rogers and included a separate data preparation code PEGS4 that generates data files with extensions **.pegs4dat* containing photon cross section data and electron restricted and unrestricted stopping powers for all elements with $Z = 1$ to 100, as well as for compounds and mixtures. In 2000, the EGSnrc[15] system code with major improvements to its predecessor the EGS4 code became available.

All EGS Monte Carlo codes are written entirely in MORTRAN3 (MORe forTRAN) and packages that rely on the EGS Monte Carlo system code come with a MORTRAN3 pre-compiler which converts a MORTRAN3 code into a FORTRAN77 code.

### *Structure of EGS code systems*

A typical EGS code system consists of two separate sections; one, written by the user and referred to as the USER code, contains a main program with additional subroutines that define: (1) a particular geometry or geometries for the simulation; and (2) scoring quantities of interest. The other section, referred to as the EGS code, consists of subroutines governing the transport of particles and contains the physics for particle transport.

The user code is linked to the EGS code through COMMON variables, such as particle energy and type. To make the user codes versatile, they are programmed to initially read an input file containing user control data, such as the number of histories and the dimensions and materials of the geometries. Figure 4.9 illustrates the typical structure of an EGS program.

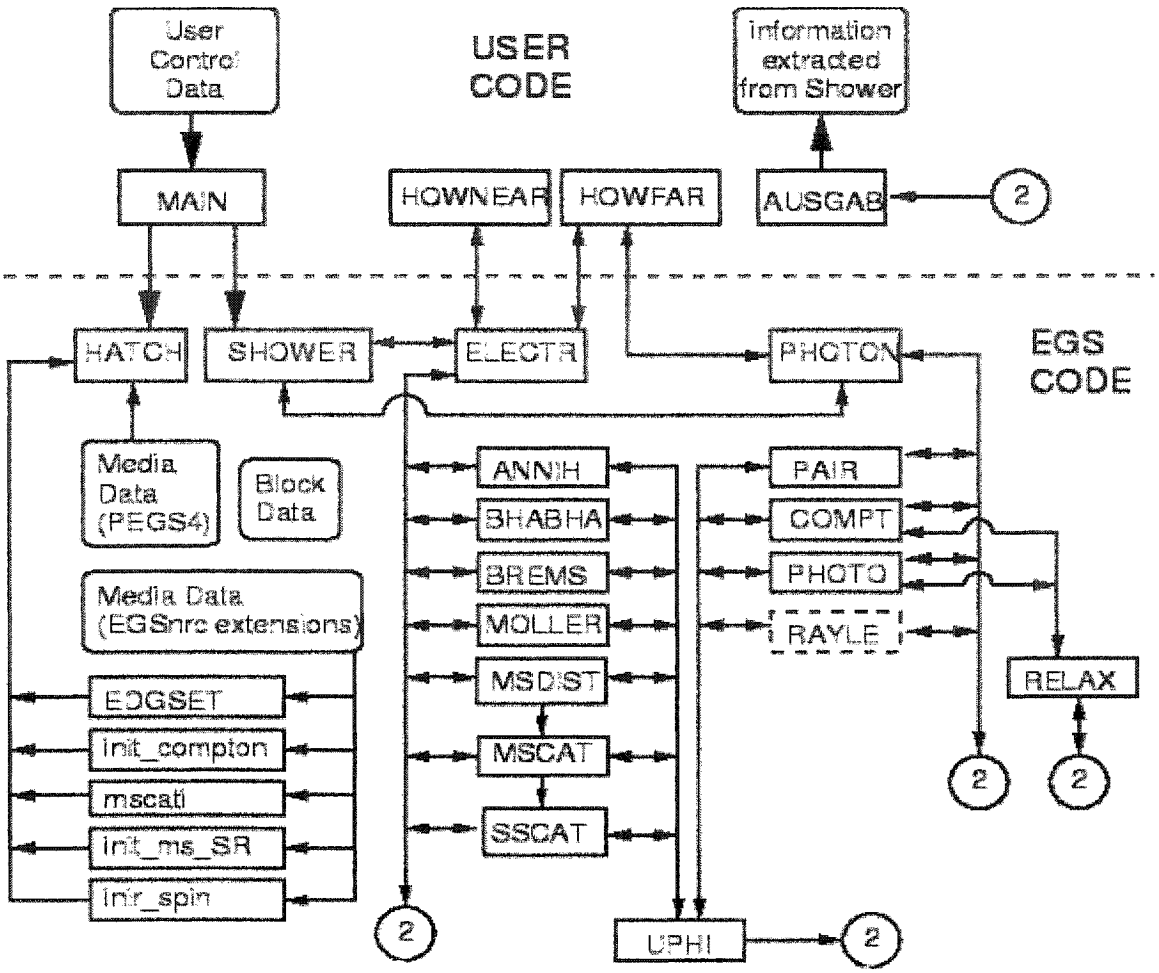


*FIG. 4.9. A block diagram of a typical structure of an EGS program. The user must write a user code which contains the MAIN subroutine and define the geometries as well as the scoring quantities. The user code is linked to the EGS code, which contains the physics for transporting radiation in the defined geometries, through COMMON variables.*

Usually a simulation of the irradiation process is carried out with many variance reduction techniques. For example, photons may cross a particular region of interest without interacting. To achieve a reasonable statistical variance, a large number of photons must be transported through that particular region, thereby increasing the calculation time significantly. To overcome this problem, a technique called photon forcing forces all photons to interact in the particular region while reducing their statistical weight. The statistical weight is calculated based on the attenuation coefficient for the photon energy and the distance between the current photon position and the region boundary along the direction of motion of the photon.

Secondary particle enhancement is another variance reduction technique. Instead of creating a single secondary particle following a particular interaction, $N$ secondary particles are created, each with a statistical weight of $1/N$. In the EGSnrc system code, many of these common variance reduction methods are implemented directly into the EGS code and are available to the user. In older EGS system codes the user had to include variance reduction subroutines in the user code section.

### 4.2.3. PEGS4

Many of the cross-sections of photon interactions and stopping powers for electrons that are required by the EGS code for transporting radiation in media are read from a separate input file prepared by a separate program called PEGS4. The program prepares all necessary data specially formatted for direct use by EGSnrc. A typical PEGS4 data file contains data from which the linear attenuation coefficients for photoelectric $\tau$, Rayleigh scattering $\sigma_R$, and total pair production $\kappa$, as well as the restrictive stopping powers $L_\Delta/\rho$, and radiative stopping powers $(S/\rho)_{rad}$ are calculated by the EGS code for materials constituting the simulation geometries. In contrast the Compton scattering cross sections are calculated by the EGS code based on the Klein-Nishina equation given by Eq. (2.8).

For photons, the PEGS4 program can generate the linear attenuation coefficients for photoelectric, Rayleigh scattering, and total pair production interactions for elements, with $Z = 1$ to 100, compounds, and mixtures, using tables of atomic cross-sections for all elements with atomic numbers ranging from 1 to 100. These tables cover a large energy interval ranging from a few keV to several GeV. The atomic cross-section tables are read from the *pgs4pepr.dat* file that is available with the EGS package, and were compiled from data provided by Storm and Israel[16]. We have generated an additional file, called the *pgs4pepr_xcom-full.dat*, that contains the cross-section data compiled by Berger, Hubbell, and Seltzer[17]. The data, also known as the XCOM database, can be downloaded from the following URL address:

*http://physics.nist.gov/PhysRefData/Xcom/Text/XCOM.html*

The PEGS4 program also generates tables of restricted stopping powers $L_\Delta / \rho$ and radiative stopping powers $S_{rad} / \rho$ that are necessary for a "Class-II" Monte Carlo code system. The data are calculated based on methods adopted by the ICRU Report 37 (ref. 18).

The user must provide an input file for the PEGS4 for each element, compound, and mixture of interest that contains: (*i*) the physical parameters for the material (density, constituent elements and their percentage weights in compound or mixtures, etc.), (*ii*) calculation options (including Rayleigh scattering cross sections, restricted stopping powers or total stopping powers), and (*iii*) cut-off energies for the restricted stopping powers. By default, the program prepares the table with a preset number of 70 energy bins but the user provides the energy range in the input file. When the program is successfully executed, the data are stored in a file with the **.pegs4dat* extension. Often one has to combine several generated **.pegs4dat* files into a single file containing all materials requested by the EGS code in the simulation.

### 4.2.4. Standard NRC user codes included with the EGSnrc Monte Carlo system code

The EGSnrc Monte Carlo system code package comes with five of the standard NRC (National Research Council Canada) user codes. The codes are the DOSRZnrc, DOSXYZnrc, SPRRZnrc, CAVRZnrc, and FLURZnrc. These user codes, in conjunction with the EGS code, simulate the passage of electrons, positrons, and photons in a generalized geometry, either right cylindrical (RZ) or Cartesian (XYZ).

These standard NRC user codes are optimized for scoring a specific quantity of interest. DOSRZnrc and DOSXYZnrc codes are optimized for scoring absorbed dose in the predefined geometry, while the SPRRZnrc code calculates the mean restricted stopping power ratios $\left(L_\Delta / \rho\right)_{med_2}^{med_1}$ throughout the defined geometry. The FLURZnrc is optimized to score the fluence spectra, and the CAVRZnrc is optimized to calculate quantities of interest associated with ionization chambers irradiated with photon beams, such as the $A_{wall}$ correction factor.

Once these standard NRC user codes are compiled, the executable programs require the particular user to create an input file containing the size and material components of the geometry of interest, the source location, energy and type, Monte Carlo transport options (cut-off energies and physics options), number of histories to simulate, random number seeds, and the desired output quantities and format.

For simulating radiotherapy radiation beams including high-energy electron and photon beams, cobalt-60 beams, and orthovoltage beams, a special program called the BEAMnrc is used. The BEAMnrc greatly simplifies the modeling of radiotherapy machines, because it contains various predefined geometric structures, called component modules (CM) which are used as building blocks for the entire source geometry. The user, when modeling a radiotherapy machine, constructs the entire geometry for the simulation by selecting several appropriate CMs, each corresponding to a particular component of the treatment machine, such as the jaws, target, applicators, scattering foils, mirrors, monitoring ionization chambers, etc. Once the user has constructed the treatment machine using the CMs, the BEAMnrc program generates an appropriate user code. After the code is compiled, the user provides an input file, similarly with the standard NRC user codes, containing the appropriate dimensions and materials for each CM, source type and energy, transport options, output options, etc.

One of the very interesting and important outputs of the BEAMnrc is a phase-space file which lists all particles that have reached a particular plane at a particular position $z$. For each particle, the particle's type, energy, location on the phase-space plane $(x, y)$, velocity vector $(v_x, v_y, v_z)$, statistical weight $w$, and the latch are scored. The latch is an 8 bit variable that is used to label additional features of the particle. The latch feature can be used to flag regions of interest where the particular particle has interacted or was created. With the latch feature, the user, for example, can differentiate between particles scattered from the jaws or applicators that have reached the phase-space file. Since a phase-space file, containing millions of particles, statistically represents the output of the simulated treatment machine, one can reuse all particles contained in the phase-space file as an input source for a different user code. This procedure is an efficient way for calculating dose distributions in phantoms located far from the original radiation source. For

example, if one is to calculate the percentage depth dose (*PDD*) in water at an *SSD* of 100 cm, the first step would be to simulate the treatment machine and obtain a phase-space file located at $z = 100$ cm from the original target or source in the treatment head with sufficient number of particles. The phase-space file is then used as an input source (either in DOSRZnrc or DOSXYZnrc user codes). Figure 4.10 is a geometrical representation of a typical photon beam and electron beam.

### 4.2.5. Improvements implemented in the EGSnrc code

In 2000 a new version of the EGS code called the EGSnrc[15] was made available. The new EGSnrc code has implemented improvements to the EGS4 in many different areas. Some subroutines were rewritten to make calculations more efficient, electron transport algorithms have been completely changed, and additional options have been introduced for the user, in addition to including variance reduction techniques as part of the EGS

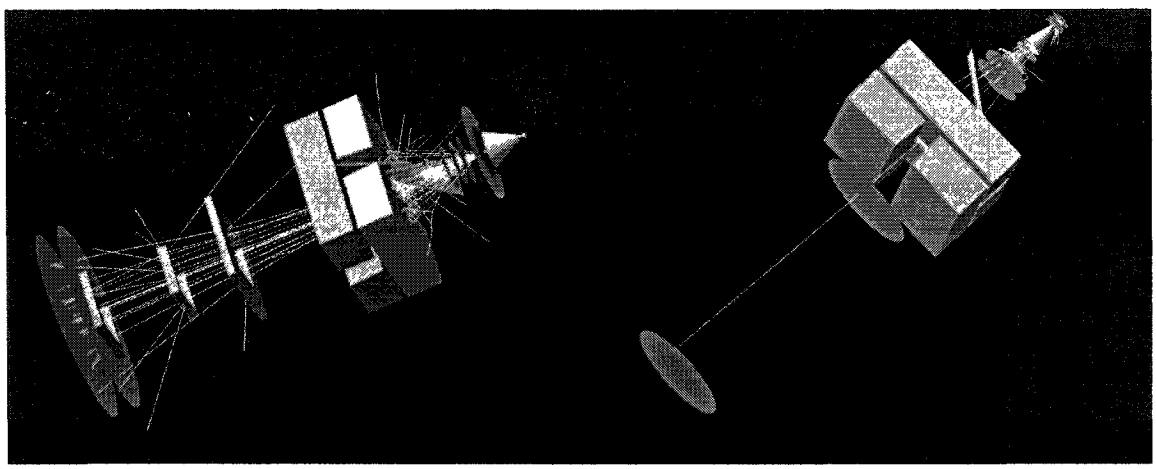

*FIG. 4.10. Illustration of a typical geometrical structure of a linac for use with the BEAMnrc. The linac is constructed using several component modules (CM), each corresponding to a particular component of the treatment beam. The image on the left is for an electron beam showing the primary collimator, scattering foils, monitor chamber, mirror, movable jaws, and electron cone. On the right, the image is for a linac producing a photon beam, showing the primary collimator, flattening filter, monitor chamber, mirror, and movable jaws. Both images also show particular planes of interest that a user may select as a plane for which a phase-space file is generated. The images also show several simulated histories. The electron beam image is produced from modeling a 12 MeV electron beam, and the photon beam is for 6 MV x rays, both modalities produced by a Varian Clinac 2300 C/D linear accelerator.*

code. A complete documentation of the EGSnrc code may be found at the following URL address:*http://www.irs.inms.nrc.ca/inms/irs/EGSnrc/EGSnrc.html*

The following is a list of some of the physics changes in the transport algorithm incorporated in the EGSnrc code:

- A new electron transport algorithm was written. This new algorithm allows electrons to be transported in larger steps with better accuracy than with the EGS4 code. In addition, electrons, as they cross a geometrical boundary, are transported using a single scattering mode for accurate boundary crossing.
- Instead of Molière multiple scattering theory, a new multiple scattering theory for electrons is used which can account for relativistic spin effects in the cross section instead of just the Rutherford cross section which underlies the Molière theory.
- It is possible to create and follow particles resulting from atomic relaxations through fluorescent photons from the K, L, M shells, as well as Auger electrons and Coster-Kronig electrons after photoelectric and Compton scattering photon interactions.
- The angle at which a photoelectron is ejected after a photoelectric interaction is sampled. In EGS4, the photoelectron was emitted in the direction of the incident photon.
- The code can use bound Compton scattering cross-sections instead of the Klein-Nishina Compton scattering cross-sections.
- For bremsstrahlung photons, accurate NIST differential cross sections for energy sampling can be used. Also, angular sampling of bremsstrahlung has been improved.

After the release of the EGSnrc Monte Carlo system code in 2000, the group at the NRC has released several updates. The latest update, called the EGSnrc V3, implemented a new method for calculating the statistical variance of quantities of interest. Previously, the

statistical variance was based on a batch by batch statistical estimator, but after the latest update a history-by-history statistical estimator has been adopted[19]. The history-by-history statistical estimator calculates the statistical variance $\sigma_x$ of quantity $x$ based on the following relationship

$$\sigma_x = \sqrt{\frac{1}{N-1}\left(\frac{\sum_{i=1}^{N} x_i^2}{N} - \left(\frac{\sum_{i=1}^{N} x_i}{N}\right)^2\right)}, \tag{4.3}$$

where $x_i$ is the quantity scored in an independent history $i$ and $N$ is the total number of histories simulated.

For demonstrating polarity effects in the PEEC caused by interaction of radiation with the collecting electrode, the history-by-history statistical estimator has been implemented in a modified DOSRZnrc user code for estimating the statistical variance on the charges landing or leaving the collecting electrode. The details of this approach are discussed further in Section 5.4.

## 4.3. ADDITIONAL APPARATUS

### 4.3.1. Solid Water™ blocks and sheets

Blocks and thin sheets of Solid Water™ material (model 457 and 457-CTG; Gammex-RMI, Middletop, WI) were used as phantom materials in our work. The slabs have a surface area of 30×30 cm$^2$ with thicknesses ranging from 2 mm to 6 cm. The thicknesses of thin slabs were measured with a micrometer. All slabs of the model 457-CTG (Certified Therapy Grade Solid Water) have a serial number engraved on their surface that corresponds to a certificate of conformance provided by the manufacturer. The certification states the particular slab's physical density, elemental composition, effective atomic number, electron density, etc. The manufacturer also provides an x-ray image of all 457-CTG slabs verifying the absence of air bubbles that could be trapped inside the slabs during the manufacturing process of the slab.

## 4.3.2. Ionization chambers

In addition to the PEEC, several other ionization chambers were used at various stages in our experiments.

### *Attix parallel-plate ionization chamber*

The Attix parallel-plate ionization chamber (model 449; Gammex-RMI, Middleton, WI) is a parallel-plate ionization chamber embedded in a 30×30×2.5 $cm^3$ slab of Solid Water$^{TM}$. The chamber's dimensions are 6.0 cm (diameter) × 1.5 cm (height) with an air sensitive volume of 0.125 $cm^3$ open to air temperature and pressure. The front electrode is a 0.0025 cm thick Kapton conductive film ($\rho = 1.92$ g/$cm^3$). The chamber was used, in addition to the PEEC, for measurements in the build-up region for high energy photon beams.

### *Roos parallel-plate ionization chamber*

The Roos chamber (model 34001; PTW, Freiburg, Germany) is a waterproof ionization chamber with a sensitive air-volume vented through its connection cable. The front electrode is a slab of 1 mm thick PMMA (Polymethyl methacrylate) with a density of 1.19 g/$cm^3$ and coated with a graphite conductive layer to form the polarizing electrode. The guard rings are of 4 mm width surrounding a 16 mm diameter collecting electrode. The chamber is suitable for use in water phantoms and was used for measurements in the buildup region of high energy photon beams in water.

### *Farmer thimble ionization chamber*

Some of our measurements required monitoring the radiation output from the linac during irradiation. A Solid Water Farmer-type chamber (model 448; Gammex-RMI, Middleton, WI) connected to a Keithley 6517A electrometer with a triax cable was used for this purpose. The electrometers built-in power supply was used to set a polarizing voltage of +300 V. The electrometer was also connected to the computer controlled-system as shown in FIG. 4.3.

### 4.3.3. Water scanning system

Measurements of the depth ionization curves and beam profiles in water were made using a Wellhöfer water scanner (WP-700; Scanditronix, Schwarzenbruck, Germany) with a Wellhöfer IC-10 ionization chamber having an air-sensitive volume of 0.12 $cm^3$. The IC-10 chamber is made of 0.068 $g/cm^2$ thick C-552 air-equivalent plastic ($\rho = 1.76\,g/cm^3$) and has an inner diameter of 6 mm. Following the AAPM TG-51 protocol[20] or the IAEA TRS-398 code of practice[21] recommendations, the effective point of measurement for the IC-10 chamber is taken to be $0.6r_{inner}$ upstream of the center of the chamber where $r_{inner}$ is the radius of the chamber cavity. The water phantom has a dimension of 50×50×50 $cm^3$. The scanning system has a positional accuracy of 0.5 mm and a reproducibility of 0.2 mm for scanning. In addition, the scanning system uses a separate reference chamber, which is usually mounted on the accelerator head to correct for beam output variations during scanning.

### 4.3.4. Thermoluminescent dosimeters (TLD)

For detecting possible neutrons that may contaminate the 18 MV x-ray beam, thermoluminesent dosimetry (TLD) techniques were used. Two types of $3.2\times3.2\times0.15\,mm^3$ TLD chips were used; TLD-600 (Harshaw Chemical Company, Solon, Ohio) and TLD-700 (Harshaw Chemical Company, Solon, Ohio). Both types are based on the thermoluminescence of LiF chips with the presence of additional impurities. TLD-600 and TLD-700 differ in the relative abundances of isotopes $^6Li$ and $^7Li$ (TABLE. 4.2). The reaction $^6Li(n,\alpha)^3H$ has a high cross-section for thermal neutrons and releases an alpha-particle ($T = 4.8\,MeV$) that deposits all of its energy locally. This makes the TLD-600 dosimeter, which contains concentrated $^6Li$, highly responsive to neutrons. On the other hand, the TLD-700 dosimeter, which contains almost no concentrated $^6Li$, has essentially no response to thermal neutrons. The TLD-100, often less expensive than the TLD-600 and TLD-700, is a third LiF-based TLD containing both $^6Li$ and $^7Li$ in their natural isotopic ratios.

In our work related to detecting the effects of contaminating neutrons of 18 MV x-ray beams on the *PDD*, the measurement of dose with the TLD-600 contains the mixed gamma and neutron dose components. The neutron dose component can be extracted from a cross measurements of the gamma component only using the TLD-700.

TABLE 4.2. RELATIVE CONCENTRATIONS OF $^{6}Li$ AND $^{7}Li$ IN TLD-100, TLD-600, AND TLD-700 THERMOLUMINESENT DOSIMETERS. TLD-100 CONTAINS $^{6}Li$ AND $^{7}Li$ IN THEIR NATURAL ISOTOPIC RATIOS.

| Isotope | TLD-100 | TLD-600 | TLD-700 |
|---|---|---|---|
| $^{6}Li$ | 7.5% | 95.6% | 0.01% |
| $^{7}Li$ | 92.5% | 4.4% | 99.99% |

# REFERENCES


1. C. Zankowski and E. B. Podgorsak, "Determination of saturation charge and collection efficiency for ionization chambers in continuous beams," Med. Phys. 25, 908-915 (1998).
2. C. Zankowski, S. Vatnitsky, J. Siebers et al., "Proton beam output measurement with an extrapolation chamber," Med. Dosim. **23**, 288-291 (1998).
3. C. Zankowski, "Calibration of photon and electron beams with an extrapolation chamber," Ph.D. Thesis, McGill University, 1997.
4. C. Zankowski and E. B. Podgorsak, "Ionization gradient chamber in absolute photon and electron dosimetry," Radiology and Oncology (Slovenia) **30**, 138-141 (1996).
5. C. Zankowski and E. B. Podgorsak, "Calibration of photon and electron beams with an extrapolation chamber," Med. Phys. **24**, 497-503 (1997).
6. C. Constantinou, F. H. Attix, and B. R. Paliwal, "A solid water photonm material for radiotherapy x-ray and gamma-ray beam calibrations," Med. Phys. **9**, 436-441 (1982).
7. C. Constantinou, N. F. Kember, G. Huxtable et al., "Physical measurements with a high energy-proton beam using liquid and solid tissue substitutes," Phys. Med. Biol. **25**, 489-499 (1980).
8. A. K. Ho and B. R. Paliwal," Stopping-power and mass energy-absorption coefficient ratios for Solid Water," Med. Phys. **13**, 403-404 (1986).
9. A. K. Ho, B. R. Paliwal, and F. H. Attix, "Charge storage in electron-irradiation phantom materials," Med. Phys. **13**, 99-100 (1986).
10. C. S. Reft, "Output calibration in solid water for high energy photon beams," Med. Phys. **16**, 299-301 (1989).
11. F. Deblois, W. Abdel-Rahman, J. P. Seuntjens, and E. B. Podgorsak, "Measurement of absorbed dose with a bone-equivalent extrapolation chamber," Med. Phys. **29**, 433-440. (2002).
12. M. J. Berger and S. M. Seltzer, ETRAN, Monte Carlo code system for electron and photon transport through extended media, RISC computer code, package CCC-107 (Oak Ridge National Laboratory, Oak Ridge, TN, 1973).
13. R. L. Ford and W. R. Nelson, "The EGS Code system – Version 3," Standard Linear Accelerator Center Report SLAC-210 (Stanford, CA, 1978).
14. W. R. Nelson, H. Hirayama, and D. W. O. Rogers, "The EGS4 Code system," Stanford Linear Accelerator Center Report SLAC-256 (Stanford, CA, 1985).
15. I. Kawrakow and D. W. O. Rogers, "The EGSnrc Code System: Monte Carlo simulations of electron and photon transport," Technical Report PIRS-701, National Research Council of Canada, Ottawa, Canada (2000).
16. E. Storm and H. I. Israel, "Photon cross sections from 1 keV to 100 MeV for elements from $Z = 1$ to $Z = 100$," In *Nuclear Data Tables*, (Academic Press, New York, NY, 1970), Vol. A7, pp.565-681.
17. M. J. Berger, J. H. Hubbell, and S. M. Seltzer, "XCOM: Photon Cross Sections Database," NIST Standard Reference Database 8 (XGAM), National Institute of Standards and Technology, Gaithersburg, MD (1998).
18. ICRU, "Stopping powers for electrons and positrons," Report 37, International Commission on Radiation Units and Measurements, Bethesda, MD. (1984).

19. B. R. B. Walters, I. Kawrakow, and D. W. O. Rogers, "History by history statistical estimators in the BEAM code system," Med. Phys. **29**, 2745-2752 (2002).

20. P. R. Almond, P. J. Biggs, B. M. Coursey, W. F. Hanson, M. Saiful Huq, R. Nath, and D. W. O. Roger, "AAPM's TG-51 protocol for clinical reference dosimetry of high- energy photon and electron beams," Med. Phys. **26**, 1847-1870 (1999).

21. International Atomic Energy Agency, *Absorbed Dose Determination in External Beam Radiotherapy based on Absorbed-Dose-to-Water Standards: An international code of practice* (IAEA Technical Reports Series No. 398, Vienna, 2000).

# Chapter 5

# COMPTON CURRENT IN THE PEEC

## 5.1. INTRODUCTION

As discussed in Section 3.3.4, ionization chambers when exposed to a constant radiation intensity exhibit a *polarity effect* whereby the magnitude of the measured signal changes when the polarity of the polarizing potential is reversed[1-5]. There are many possible causes for the polarity effects in ionization chambers, and they fall into two categories: voltage-dependent or voltage-independent. In this context, a *voltage-independent polarity effect* always yields the same difference in signals between the two polarities irrespective of the magnitude of the polarizing voltage. One the other hand, in *voltage-dependent polarity effects* the signal difference of the reversed polarity readings varies with the polarizing voltage.

The possible causes for *voltage-dependent polarity effects* are as follows:

*(i)* Appreciable distortion of the electric field caused by a small potential difference between the guard and the collecting electrodes[6]. The polarity effect in this situation decreases with increasing polarizing voltages.

*(ii)* Variation of the gas-sensitive volume with polarity reversal due to space-charge distortion of the electric field lines defining the gas-sensitive volume[7,8]. The signal difference decreases with increasing polarizing voltage. Averaging the absolute positive and negative polarity readings yields the signal collected from a perceived gas-sensitive volume that does not change with the applied voltage. This polarity effect also decreases with an increasing applied voltage.

*(iii)* In cylindrical and spherical ionization chambers, the different mobilities of positive and negative gas ions causes the distribution of space-charge to be dependent on the polarity of the central electrode, leading to differences in the collection efficiency when the polarity is reversed[9]. This polarity effect

decreases with increasing polarizing voltage; however, it will not be eliminated by taking the mean of the absolute signals of the reversed polarity readings.

*(iv)* Low-energy tertiary electrons ejected from the electrodes into the gas-sensitive volume by energetic secondary electrons. In FIG. 5.1 a schematic representation of a parallel-plate chamber operating in the standard configuration is shown; the top electrode is the polarizing electrode and the bottom electrode is the collecting electrode. For simplicity, we assume that the chamber is placed into vacuum. When the chamber is exposed to radiation, tertiary electrons are ejected from the electrodes. In the figure we show the charges of three sets of tertiary electrons of interest: (1) tertiary electrons ejected from the top polarizing electrode into the space between the electrodes (the sensitive volume of the chamber), thus introducing into the sensitive volume a negative charge $-q_1$ and leaving on the top electrode a positive charge $+q_1$; (2) tertiary electrons ejected from the bottom collecting electrode into the sensitive volume bringing a negative charge $-q_2$ and leaving behind in the collecting electrode a positive charge of $+q_2$; and (3) tertiary electrons ejected also from the collecting electrode but through the bottom surface leaving behind a charge of $+q_3$ in the collecting electrode. When the chamber is positively polarized, *i.e.*, the electric field is pointing down, $-q_2$ moves toward the top electrode, while a fraction $f_1$ of $-q_1$, consisting of electrons having sufficient kinetic energies to overcome the electric force, reaches the bottom collecting electrode. Hence, the electrometer will read a current representing the rate of $+q_2+q_3-f_1q_1$. When the polarity of the chamber is reversed (negative polarity), *i.e.*, the electric field is pointing up, all of the charge $-q_1$ will reach the collecting electrode; however, only a fraction $(1-f_2)$ of the $-q_2$ charge consisting of all electrons having an insufficient kinetic energy to overcome the electric force will flow back into the collecting electrode. In this situation, the current read by the electrometer will be given as $-q_1+q_3+f_2q_2$. This obviously will create a polarity effect that cannot be eliminated by taking the average of the two signals, but can be reduced by increasing the polarizing voltage, since

$f_1$ and $f_2$ will both approach 1. This effect was investigated previously at low gas pressures[10,11], however, research has not been carried out under typical clinical irradiation conditions.

*Voltage-independent polarity effects* are principally radiation-induced currents in the ionization chamber caused by the direct interaction of radiation with several chamber components, particularly with the collecting electrode in parallel-plate ionization chambers and with the chamber stem in cylindrical and spherical ionization chambers. Essentially, the magnitude of the induced currents is independent of the chamber polarizing voltage and the true gas ionization in the absence of voltage-dependent polarity effects is equal to the mean of the absolute positive and negative polarity signals provided that the induced current is smaller than the true gas ionization.

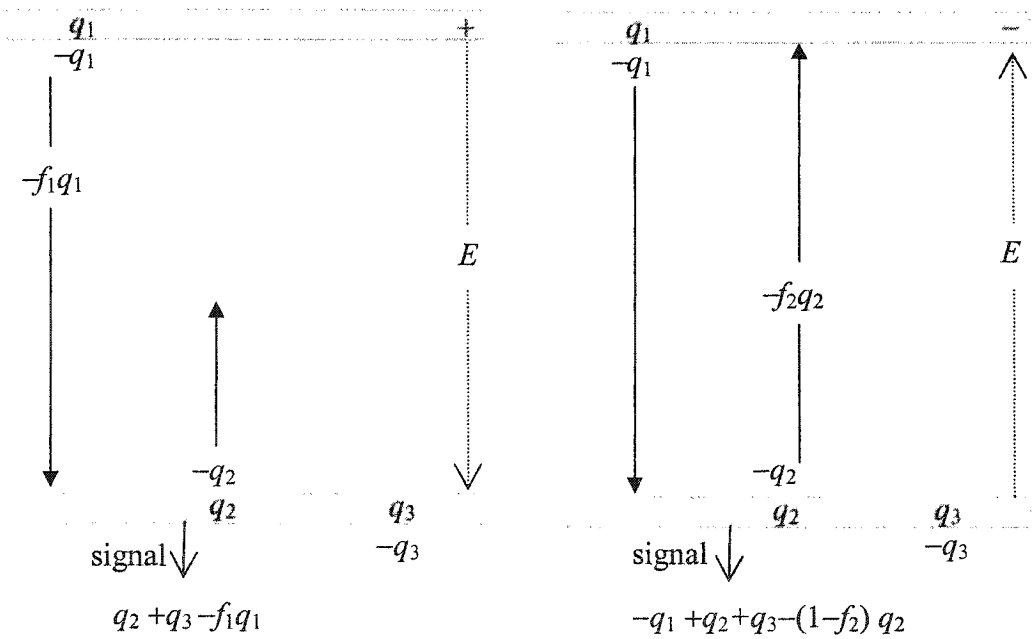


*FIG. 5.1. The polarity effect caused by low-energy tertiary electrons ejected from the electrodes of a parallel-plate ionization chamber.*

Johns *et al.*[12] explained the source of the induced current, often referred to as the *Compton current*, in parallel-plate ionization chambers exposed to photon radiation, attributing the source to a lack of electronic equilibrium in the collecting electrode volume. Their work showed that the magnitude of the Compton current not only depends on the intensity and energy of the photon beam, but is also influenced by many factors including the thickness, area, and angular orientation relative to the incident photon beam of the collecting electrode, as well as the depth of the collecting electrode below the phantom surface or the thickness of the ionization chamber front window. Their study also showed that the Compton current is greatest when the electrodes are oriented at right angles to the radiation beam. Van Dyk and Macdonald[13] investigated the induced currents in parallel-plate ionization chambers exposed to electron beams and showed that the induced currents are caused by the lack of equilibrium between the total number of electrons entering and leaving the collecting electrode volume.

In this chapter we examine the polarity effect of the PEEC in detail. First, we demonstrate that voltage-dependent polarity effects are negligible in the PEEC. At a given applied voltage $V$ the collected gas ionization current $I(V)$ in the PEEC is determined by the following relationship

$$I(V) = \frac{\dot{M}_{\text{pos}}(V) - \dot{M}_{\text{neg}}(V)}{2}, \tag{5.1}$$

where $\dot{M}_{\text{pos}}(V)$ and $\dot{M}_{\text{neg}}(V)$ are the positive and negative currents measured at the positive and negative applied voltages $V$, respectively.

The current $I_{\text{pol}}(V)$ causing the polarity effect in the measurement is given by the following relationship

$$I_{\text{pol}}(V) = \frac{\dot{M}_{\text{pos}}(V) + \dot{M}_{\text{neg}}(V)}{2}. \tag{5.2}$$

To allow a theoretical study of the polarity effect we modified the standard DOSRZnrc/EGSnrc user code. The standard code is optimized for scoring absorbed dose in the predefined geometry. The modified code, called COMPTON/EGSnrc, is optimized for scoring the charge going into, and the charge exiting from, a single region of interest, in addition to the absorbed dose in the full predefined geometry. The COMPTON/EGSnrc

was used in our studies of the polarity effect in the PEEC for our 6 MV x-ray beam as well as for 9 MeV and 12 MeV electron beams.

## 5.2. BACKGROUND

The lack of charged particle equilibrium (CPE) in the collecting electrode volume is the main cause of voltage-independent polarity effects. For CPE to exist, the number of charged particles entering and stopping inside a volume of interest must equal to the number of charged particles created within and escaping that same volume. Along the central axis of radiation beams, the electron fluence in the phantom may increase or decrease in regions with depth, and the CPE generally does not exist at all depths in the phantom. It is expected that the $I_{pol}$ in the chamber will also depend on the measurement depth, varying in magnitude and sign depending on the electron fluence gradient.

In megavoltage external photon beams the interaction of photons in the medium causes the electron fluence to gradually increase in the first layers of the irradiated medium, referred to as the *dose build-up region*, reaching a maximum near the depth of maximum dose $z_{max}$. Hypothetically, if the attenuation and scattering of photons in the medium were ignored, the electron fluence, after saturating at $z_{max}$, would remain constant with increasing depths. If a parallel-plate chamber operating in the standard configuration was placed anywhere in the dose build-up region of this hypothetical photon beam, the number of electrons ejected from its collecting electrode by photons interacting directly in the collecting electrode volume is not replaced by an equal number of electrons that are ejected from the upper layers and stop in the collecting electrode volume. The excess positive charge, *i.e.*, the difference between the number of ejected electrons and the number of electrons landing in the collecting electrode will represent a positive current, often called the *Compton current*, that is read by the measuring electrometer. If the ionization chamber is positively polarized, the positive ions of the ionized gas will arrive at the collecting electrode, adding to the positive current of the collecting electrode ions, and the electrometer will read a signal $\dot{M}_{pos}$ which is the sum of both positive currents. In the situation where the ionization chamber is negatively polarized, the electrometer reads a net current $\dot{M}_{neg}$ representing the positive Compton current and the negative current

due to the negative gas ions arriving at the collecting electrode. At depths beyond $z_{max}$ where CPE exists, there will not be an excess positive charge and the Compton current will equal to zero in the collecting electrode volume. $\dot{M}_{pos}$ and $\dot{M}_{neg}$ in this situation have exactly the same magnitude but opposite signs representing the collected gas currents.

A realistic *photon beam*, with photons scattered and attenuated in the phantom, exhibits an electron fluence build-up similar to that in the hypothetical model reaching a maximum at $z_{max}$. Beyond $z_{max}$, because of the attenuation of photons in the medium, the number of electrons set in motion decreases with increasing depths and the electron fluence decreases accordingly. In parallel-plate ionization chambers placed at depths beyond $z_{max}$, the number of landing electrons exceeds the number of positive ions created within the collecting electrode volume, and the Compton current in this situation is negative. The electron fluences for hypothetical and real photon beams as a function of depth in phantom are shown schematically in FIG. 5.2.

In megavoltage *electron beams* a comparable, but more complicated, Compton current in parallel-plate ionization chambers exists and is also caused by the lack of CPE in the collecting electrode volume. The electron fluence as a function of depth in a typical megavoltage electron beam is shown in FIG. 5.3. At the phantom surface, the electron fluence is essentially equal to the fluence of the primary electrons of the beam. In the first few layers of the phantom the electron fluence increases as δ rays are produced in hard collisions. Most δ rays have a relatively short penetrating depth in the phantom and essentially their fluence saturates not far from the surface. Kessaris[14] showed that the saturation of the secondary electron fluence is at a depth about one fifth of the practical range $R_p$ of the electron beam. With increasing depths, the electron fluence along the beam central axis decreases as a result of: (*i*) the scattering of electrons in the medium away from the beam central axis; and (*ii*) primary electrons losing all their kinetic energy and stopping in the medium. Hence, in electron megavoltage beams the Compton current in a parallel-plate ionization chamber is positive when the chamber is at the surface and decreases with depth; and then reverses sign and becomes negative beyond a particular depth that depends on the electron beam energy.

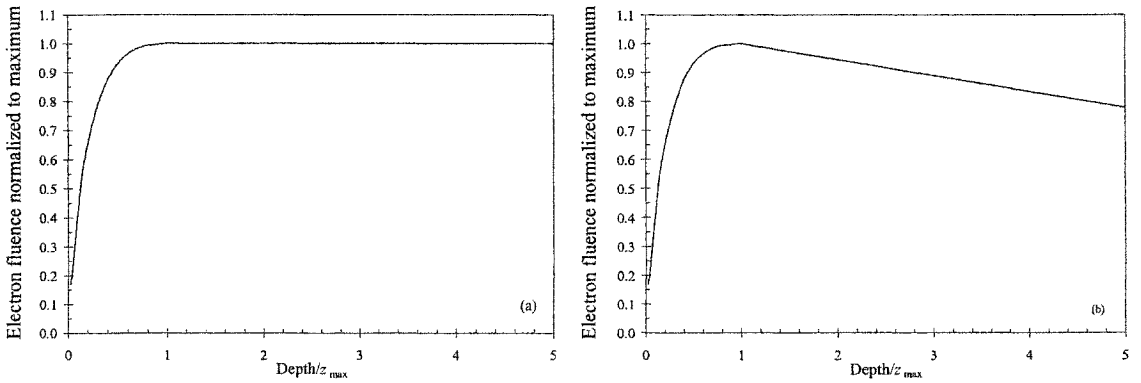


*FIG. 5.2. The electron fluence along beam central axis versus depth in phantom in (a) a hypothetical photon beam in which attenuation and scattering of photons are ignored and (b) a realistic photon beam affected by attenuation and scattering in the phantom.*

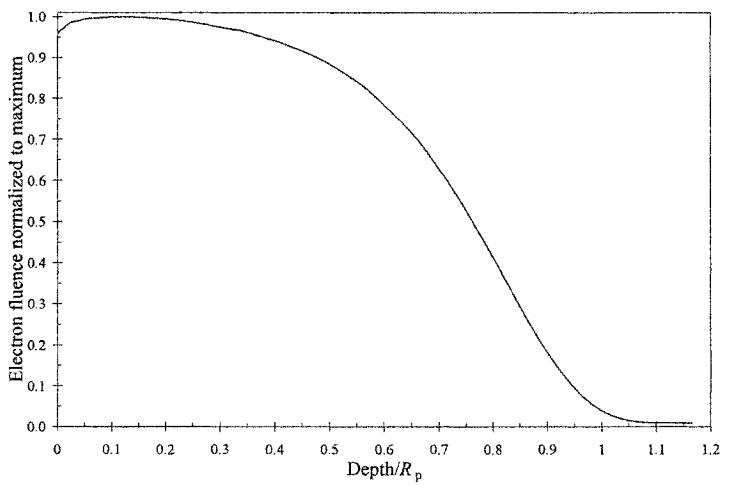


*FIG. 5.3. The electron fluence against depth in phantom along beam central axis in a typical electron beam.*

## 5.3. EQUIPMENT AND EXPERIMENTAL TECHNIQUES

Depth ionization curves along the beam central axis were measured for two pulsed photon beams (6 MV and 18 MV) and two pulsed electron beams (9 MeV and 12 MeV) generated by a clinical linear accelerator (Clinac-2300 C/D; Varian, Palo Alto, CA). In the two *photon beams*, the depth ionization curves were acquired with three parallel-plate ionization chambers: (*i*) the PEEC in Solid Water™ using the aluminized Mylar/Delrin wall front electrode, (*ii*) the commercial Attix chamber (model 449; Gammex-RMI,

Middleton, WI) in Solid Water™, and (*iii*) the Roos commercial chamber (model 34001; PTW, Freiburg, Germany) in water.

Solid Water™ (model 457 and 457-CTG; Gammex-RMI, Middleton, WI) blocks and thin sheets having a 30×30 $cm^2$ surface area with thicknesses ranging from 2 mm to 6 cm were used to set the measurement depths with the PEEC and the Attix ionization chamber, as well as to provide 10 cm thickness of back-scattering material in measurements with the Attix ionization chamber. Measurements with the Roos ionization chamber in water were carried out in a custom made 40×40×40 $cm^2$ acrylic water tank. The chamber was placed in an acrylic mount that protrudes into the center of the tank and runs along an aluminum track, which is part of a manual positioning system.

All measurements in photon beams were carried out in the differential (current) acquisition mode. With its air-sensitive volume covered by the radiation field, a cylindrical reference chamber (model 448; Gammex-RMI, Middleton, WI) positioned below the treatment head PMMA exit window was used to account and compensate for minute variations in the linac output.

The PEEC was operated in the standard configuration; the top polarizing electrode was biased with a variable high voltage power supply (model 248; Keithley, Cleveland, OH); the bottom measuring electrode was grounded through an electrometer (model 35617; Keithley, Cleveland, OH); the guard ring was connected to ground directly. The reference chamber was also operated in the standard configuration; it was grounded and biased by a second electrometer (model 6517A; Keithley, Cleveland, OH). The high voltage power supply and the two electrometers were computer-controlled with an IEEE-488 interface.

The Attix and the Roos ionization chambers were grounded and biased by a Keithley electrometer (model 6517A), while the reference chamber was connected to the Keithley electrometer (model 35617). The Keithley electrometer (model 6517A) provided adjustable polarizing voltages up to 1000 V, whereas the Keithley electrometer (model 35617) could only polarize the ionization chamber at two voltages: 300 V and 150 V.

Appropriate QuickBasic programs were written and used to read the currents registered by both electrometers; to set the voltage magnitude supplied by the high voltage power

source; and to set the voltage magnitude and bias supplied by the Keithley electrometer (model 6517A). The programs, with the biasing voltage on the reference chamber maintained at +300 V, acquired 30 current readings (about 1 current reading per second) from both electrometers for a given voltage setting $V$ on the measuring chambers. The measurements were repeated when the standard deviations on the readings were larger than 0.1% of the averaged currents. Next, the voltage on the measuring chambers was changed to a different setting and the programs delayed the data acquisition for a period of 10 seconds before starting the acquisition of new data.

In the PEEC, the polarizing voltage was varied from 50 V to 450 V in steps of 50 V (a total of 9 voltage settings), whereas for the Roos and Attix ionization chambers the polarizing voltage was varied from 60 V to 300 V in steps of 20 V. After measurements were acquired for all desired voltages, the program output to a text file various parameters including the voltage settings, the average current, and the standard deviation of the measuring chamber, as well as the average current and the standard deviation of the reference chamber signal. Under conditions identical to the first measurement set and after allowing a period of 3-5 min for the measuring chamber to equilibrate, another set of measurements was taken at the reverse bias. All measurements were obtained in a standard *SSD* setup configuration with an *SSD* of 100 cm.

In *electron beams*, depth ionizations curves covering depths from the phantom surface to about 2 cm beyond the practical ranges of the electrons were measured for both bias polarities with the PEEC for $10\times10$ cm$^2$ fields. These measurements were carried out in the integral (charge) acquisition mode and the PEEC polarizing voltage was kept constant at 300 V. At each bias polarity, the mean of 5 readings with a relative error on the average below 3% was taken as the measured signal. Similarly to the procedure in photon beam measurements, in electron beams a period of 3-5 min was allowed for the PEEC to stabilize after the bias reversal, and all measurements were obtained in a standard *SSD* setup with an *SSD* of 100 cm.

Figure 5.3 illustrates the standard *SSD* setup for measurements with the PEEC in photon and electron beams. A 400 MU/min dose output rate was used in all measurements and electrode separation $s$ of the PEEC was maintained at 2 mm.

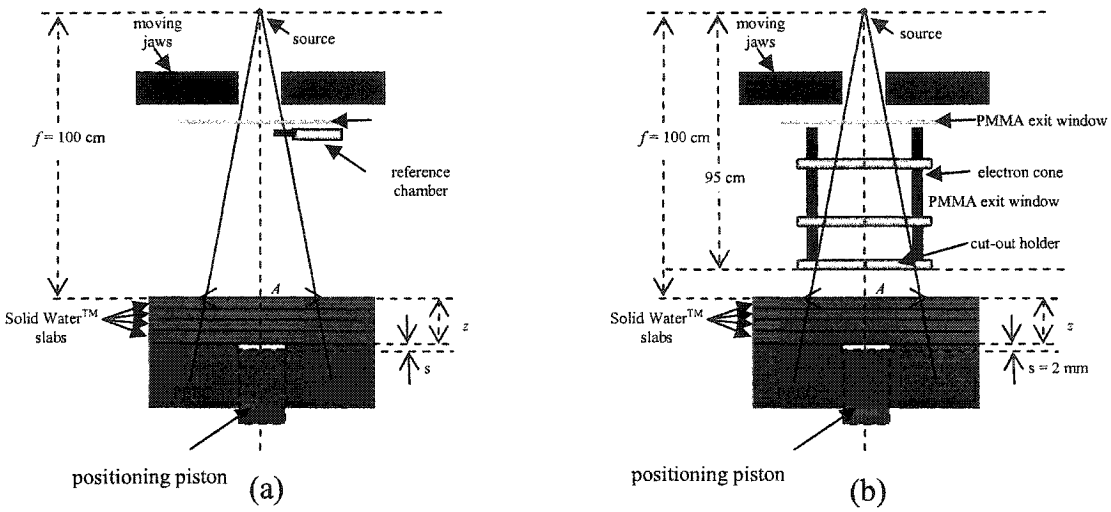


*FIG. 5.4. Standard SSD setup for depth ionization measurements in (a) photon beams and (b) electron beams with the PEEC.*

## 5.4. MONTE CARLO SIMULATIONS AND THE COMPTON/EGSNRC USER CODE

Monte Carlo simulations of the induced current in the collecting electrode of the PEEC were calculated for the 6 MV x-ray beam and 9 MeV and 12 MeV electron beams from our CL-2300 C/D linac using a new user code (COMPTON/EGSnrc user code) developed in our center as part of this PhD work. The COMPTON code, a modification to the standard DOSRZnrc/EGSnrc user code, counts the charge entering and the charge leaving a particular geometrical region of interest (ROI) selected by the user. Appropriate modifications were introduced in the HOWFAR subroutine. As in the standard version 3 EGSnrc system code[15], the *history-by-history* statistical estimator for phase-space sources was implemented[16].

In the EGSnrc system code (version 3) the *history-by-history* statistical estimator is based on defining a single history *i* as the complete history of a primary particle. When using phase-space files in the BEAMnrc and DOSRZnrc user codes, a single history *i* is defined as an initial electron in a linac or one decay event in a radioactive source, *e.g.*, cobalt-60. The simulation of a single history may lead to a number of particles $S_i$ reaching the phase-space geometrical scoring plane. BEAMnrc scores all the particles reaching the scoring plane sequentially and marks the first particle in every $S_i$ group by setting the

particle's energy negative. When the phase-space file is used as a source, the variable IHSTRY keeps track of the number of primary histories used and is incremented only when a particle with negative energy is read. IHSTRY is represented by the generic notation $N$ in the following paragraphs

For a particular ROI selected by the user, the COMPTON user code statistically adds the charge entered into, exited from, and accumulated in the ROI for a single history $i$. In generic variable notations, we represent these quantities by $Q_i^{in}$, $Q_i^{out}$ and $Q_i^{net}$, respectively. A new variable $M$ is used for detecting changes in $N$ and the accumulation of $Q_i^{in}$ and $Q_i^{out}$ takes place only when $M$ and $N$ have equal values.

When the simulation of a new primary history $i$ is started, $N$ is updated to the new value by the EGSnrc system code. Once this update is detected, the values of $Q_i^{in}$ and $Q_i^{out}$ are added, respectively, to two variables (in generic notations) $Q^{in}$ and $Q^{out}$ that store $\sum_i Q_i^{in}$ and $\sum_i Q_i^{out}$, respectively. The code also stores $\sum_i (Q_i^{in})^2$, $\sum_i (Q_i^{out})^2$ and $\sum_i (Q_i^{net})^2$ in the generic variables $Q^{in,2}$, $Q^{out,2}$, and $Q^{net,2}$, respectively, to be used for calculating the statistical uncertainties. Finally, $Q_i^{in}$ and $Q_i^{out}$ are reset to zero, and $M$ is set to the new value of $N$. Figure 5.5 illustrates the above algorithm and the equivalent coding variables of the generic notations are listed in TABLE 5.1.

Once a simulation is completed, the code outputs the values of $Q^{in}$, $Q^{out}$ and their difference $Q^{net}$, the values of $Q^{in,2}$, $Q^{out,2}$, and $Q^{net,2}$, as well as the final value of $M$ into the associated *.*egslog* file.

The COMPTON code is not as user friendly as the DOSRZnrc code, because all outputs of interest are written in the *.*egslog* file hindering the user from easily restarting a simulation. Currently, we overcome this problem by requiring the user to initialize the values of $Q^{in}$, $Q^{out}$, $Q^{in,2}$, $Q^{out,2}$, and $Q^{net,2}$ in the input file, *i.e.*, *.*egsinp*, and the user has to update the input file with values of $Q^{in}$, $Q^{out}$, $Q^{in,2}$, $Q^{out,2}$, and $Q^{net,2}$ from previous simulations for restarting.

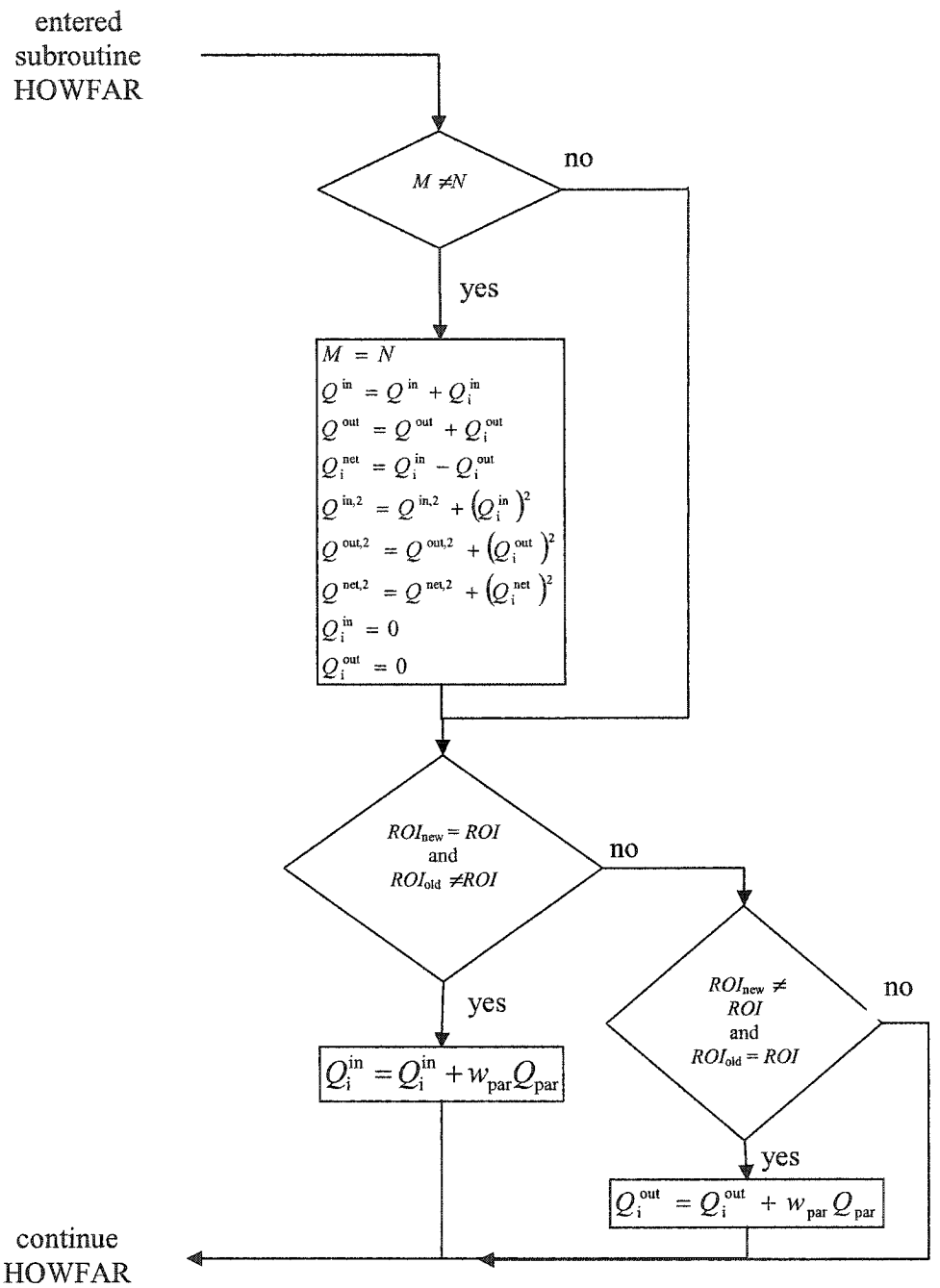


*FIG. 5.5. In generic variable notations, modification implemented in the HOWFAR subroutine of the COMPTON/EGSnrc user code for calculating the charge entered into, exited from, and accumulated in a region of interest (ROI). The generic variable definitions and their equivalent coding variables are given in TABLE 5.1.*

TABLE 5.1. GENERIC VARIABLE NOTATIONS USED IN THE TEXT AND IN FIG. 5.1 FOR THE MODIFICATIONS IMPLENETED IN THE COMPTON/EGSNRC USER CODE. THE EQUIVALET CODING VARIABLE NAMES ARE ALSO GIVEN.

| Generic representation | Stored quantity | Equivalent coding variable |
|---|---|---|
| $N$ | counter for total number of primary histories successfully simulated | IHSTRY |
| $M$ | a variable used for monitoring a change in $N$ | IHSTRY_TEMP1 |
| $ROI$ | the geometrical region of interest corresponding to the collecting electrode | ROI_NUMBER |
| $ROI_{\text{new}}$ | the particle's new region of interest | IRNEW |
| $ROI_{\text{old}}$ | the particle's old region of interest | IRL |
| $Q_{\text{par}}$ | particle charge | IQ(NP) |
| $w_{\text{par}}$ | particle statistical weight | WT(NP) |
| $Q_{\text{i}}^{\text{in}}$ | total charge entered into $ROI$ in history $i$ | INCOMING_TEMP |
| $Q_{\text{i}}^{\text{out}}$ | total charge exited from $ROI$ in history $i$ | OUTGOING_TEMP |
| $Q^{\text{in}}$ | total charge entered into $ROI$ after $N$ primary histories successfully simulated | INCOMING_Q |
| $Q^{\text{out}}$ | total charge exited from $ROI$ after $N$ primary histories successfully simulated | OUTGOING_Q |
| $Q^{\text{net}}$ | $Q^{\text{in}} - Q^{\text{out}}$ after $N$ primary histories successfully simulated | NET_Q |
| $Q^{\text{in,2}}$ | the sum of $\left(Q_{\text{i}}^{\text{in}}\right)^2$ after $N$ primary histories successfully simulated | INCOMING_Q2 |
| $Q^{\text{out,2}}$ | the sum of $\left(Q_{\text{i}}^{\text{out}}\right)^2$ after $N$ primary histories successfully simulated | OUTGOING_Q2 |
| $Q^{\text{net,2}}$ | the sum of $(Q_{\text{i}}^{\text{in}} - Q_{\text{i}}^{\text{out}})^2$ after $N$ primary histories successfully simulated | NET_Q2 |

Furthermore, the user has to manually calculate the following quantities of interest:

- The charge entered into the ROI per history $\overline{Q}^{\text{in}} = Q^{\text{in}} / N$ and the associated statistical uncertainty following the relationship

$$\sigma_{\overline{Q}^{\text{in}}} = \sqrt{\frac{1}{N-1}\left(\frac{Q^{\text{in},2}}{N} - \left(\overline{Q}^{\text{in}}\right)^2\right)}. \tag{5.3}$$

- Analogously, the charge exited from the ROI per history $\overline{Q}^{\text{out}} = Q^{\text{out}} / N$ and the associated statistical uncertainty following the relationship

$$\sigma_{\overline{Q}^{\text{out}}} = \sqrt{\frac{1}{N-1}\left(\frac{Q^{\text{out},2}}{N} - \left(\overline{Q}^{\text{out}}\right)^2\right)}. \tag{5.4}$$

- The accumulated charge in the ROI per history $\overline{Q}^{\text{net}} = \overline{Q}^{\text{in}} - \overline{Q}^{\text{out}}$ and the associated statistical uncertainty following the relationship

$$\sigma_{\overline{Q}^{\text{net}}} = \sqrt{\frac{1}{N-1}\left(\frac{Q^{\text{net},2}}{N} - \left(\overline{Q}^{\text{net}}\right)^2\right)}. \tag{5.5}$$

Because of a number of coding "bugs" initially present in the EGSnrc code that affected calculations when restarting simulations, we decided also to accumulate the absorbed energy in the chamber air-sensitive volume by a method similar to that used for monitoring the charge entering and exiting from the collecting electrode. These modifications were introduced in the AUSGAB subroutine of the DOSRZnrc code.

The EGSnrc code scores the energy deposited by the transported particle in a single step in the coding variable EDEP. The energy deposited $E_i$ in a geometrical region per primary history $i$ is the statistical sum of EDEP deposited in the particular geometrical region. Thus, the energy $\overline{E}$ deposited per primary history after $N$ successfully simulated primary histories is given by the relationship

$$\overline{E} = \frac{\sum_{i}^{N} E_i}{N}, \tag{5.6}$$

and the statistical uncertainty $\sigma_{\overline{E}}$ is given by the following relationship

$$\sigma_{\bar{E}} = \sqrt{\frac{1}{N-1}\left(\frac{\sum_{i}^{N}(E_i)^2}{N} - \bar{E}^2\right)}. \tag{5.7}$$

Lately, these coding "bugs" were fixed and monitoring the absorbed energy became no longer necessary but the modifications still exist in the COMPTON user code. For the interested COMPTON code developer, we are providing in TABLE. 5.2 the coding variables used for accumulating the absorbed energy in the air-sensitive volume.

## 5.5. RESULTS AND DISCUSSION

### 5.5.1. 6 MV and 18 MV photon beams

#### *Polarity current dependence on the applied voltage*

In an ionization chamber, all possible causes of polarity effects in measurements may be present and, to validate that the voltage-independent polarity effect (Compton current) is predominant in the PEEC, we measured the polarity effect current $I_{\text{pol}}$ as a function of the applied voltage. In FIG 5.6 we show the measured absolute positive and negative polarity currents $\left|\dot{M}_{\text{pos}}(V)\right|$ and $\left|\dot{M}_{\text{neg}}(V)\right|$, as well as the collected gas ionization current $I(V)$ against the magnitude of the applied voltage $V$ for the PEEC at the phantom surface.

TABLE 5.2. GENERIC VARIABLE NOTATIONS USED IN THE TEXT AND IN FIG. 5.1 FOR THE MODIFICATIONS IMPLENETED IN THE COMPTON/EGSNRC USER CODE. THE EQUIVALET CODING VARIABLE NAMES ARE ALSO GIVEN.

| Coding variable | Stored quantity |
|---|---|
| IHSTRY_TEMP2 | a variable used for monitoring a change in IHSTRY |
| DOSE_ROI_NUMBER | the geometrical region of interest corresponding to the chamber air-sensitive volume |
| ENERGY_TEMP | energy deposited in MeV in the air sensitive volume in history *i* |
| ENERGY_DOSE_ROI | energy deposited in MeV in the air sensitive volume after *N* primary histories successfully simulated |
| ENERGY2_DOSE_ROI | the sum of (ENERGY_TEMP)$^2$ after IHSTRY primary histories successfully simulated |

Field size was 10×10 cm$^2$, x-ray beam energies 6 MV and 18 MV, electrode gap 2 mm. For an applied voltage $V$ the collected gas ionization current in FIG. 5.6 was calculated following the relationship

$$I(V) = \frac{\dot{M}_{pos}(V) - \dot{M}_{neg}(V)}{2}, \tag{5.8}$$

with the uncertainty $\sigma_I(V)$ related to the standard deviations $\sigma^2_{\dot{M}_{pos}}(V)$ and $\sigma^2_{\dot{M}_{neg}}(V)$ in $\dot{M}_{pos}(V)$ and $\dot{M}_{neg}(V)$ measurements, respectively, and given by the following expression

$$\sigma_I(V) = \frac{\sqrt{\sigma^2_{\dot{M}_{pos}}(V) + \sigma^2_{\dot{M}_{neg}}(V)}}{2}. \tag{5.9}$$

The collected gas ionization $I$(V), as expected, slowly increased with increasing $V$ as the collection efficiency of the chamber approached unity, having a value at 50 V that is about 99% of the value at 450 V.

The polarity effect current $I_{pol}(V)$ at all applied voltages $V$ is calculated from the pairs of measurement signals $\dot{M}_{pos}(V)$ and $\dot{M}_{neg}(V)$ following the relationship

$$I_{pol}(V) = \frac{\dot{M}_{pos}(V) + \dot{M}_{neg}(V)}{2}, \tag{5.10}$$

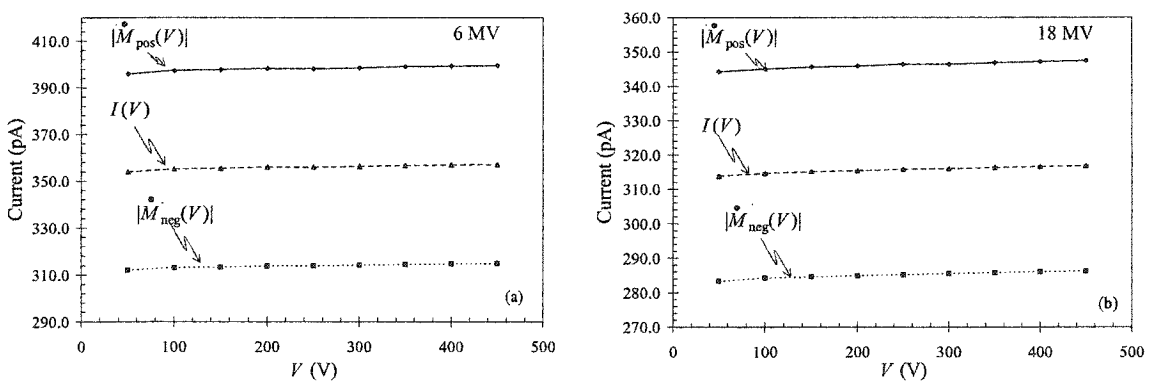


*FIG. 5.6. The absolute values of the positive and negative polarity currents* $|\dot{M}_{pos}(V)|$ *and* $|\dot{M}_{neg}(V)|$ *in the PEEC as a function of the applied voltage V at the phantom surface for a 10×10 cm$^2$ field in (a) 6 MV and (b) 18 MV x-ray beams. The PEEC electrode separation is 2 mm. The figure also shows the collected gas ionization currents I(V) calculated following the expression of Eq. (5.8).*

with an uncertainty given by the expression

$$\sigma_{I_{pol}} = \frac{\sqrt{\sigma^2_{\dot{M}_{pos}}(V) + \sigma^2_{\dot{M}_{neg}}(V)}}{2}. \tag{5.11}$$

In FIG. 5.7 we show the $I_{pol}$ against the applied voltage $V$ in the PEEC for both photon beams calculated from the data presented in FIG. 5.6, clearly showing the independence of the $I_{pol}$ of the applied voltage $V$. Hence, we concluded that the Compton current is the main cause of the polarity effect in the PEEC and voltage-dependent polarity effects are negligible. The Compton current $I_{COMP}$ is considered the statistical average of the $I_{pol}$ measurements and is calculated following the relationship

$$I_{COMP} = \frac{\sum I_{pol}(V)/\sigma^2_{Ipol}(V)}{\sum 1/\sigma^2_{I_{pol}}(V)}, \tag{5.12}$$

with an uncertainty given by the following expression

$$\sigma_{I_{COMP}} = \sqrt{\frac{1}{\sum 1/\sigma^2_{I_{pol}}(V)}}. \tag{5.13}$$

We have also verified the independence of $I_{pol}$ of the applied voltage for the PEEC at all measurement depth and field size configurations and arrived at the same conclusion, namely, that the Compton current is the primary effect causing the polarity asymmetry in the PEEC.

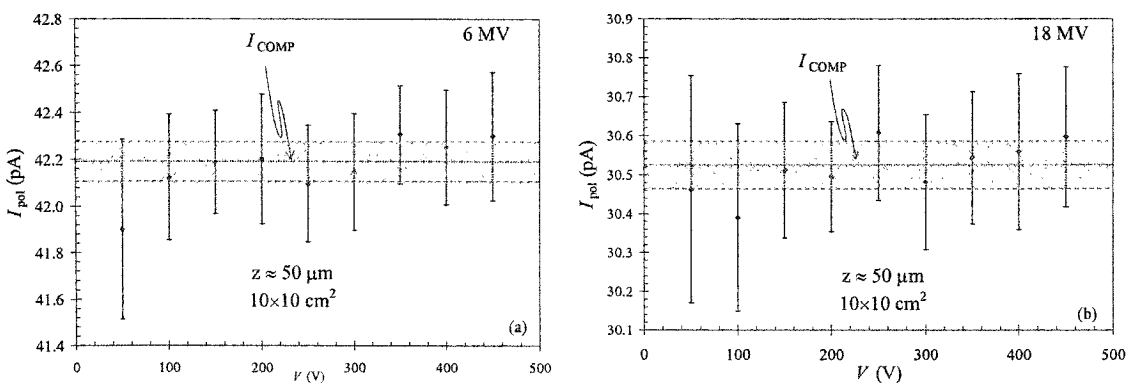


*FIG. 5.7. The polarity effect current $I_{pol}$ in the PEEC at the surface for 10×10 cm² field against the applied voltage V in (a) 6 MV and (b) 18 MV x-ray beams. The data are calculated following the expressions of Eqs. (5.10) and (5.11) from measurements shown in FIG. 5.5. The figures also show the Compton current $I_{COMP}$ and the uncertainty calculated with Eqs. (5.12) and (5.13), respectively.*

The dependence of the $I_{pol}$ on the applied voltage was examined also for the Roos and the Attix ionization chambers in the 18 MV x-ray beam. The $I_{pol}$ at the phantom surface (25 μm for the Attix chamber and 1.0 mm for the Roos chamber), as well as at $z_{max}$ for both ionization chambers as a function of the applied voltage $V$ is shown in FIG. 5.8. Within the experimental uncertainties, the $I_{pol}$ for the Attix ionization chamber [FIG. 5.8(b)] was found to be also voltage-independent similarly to the PEEC and we concluded that (*i*) in the Attix ionization chamber the polarity effect is also primarily caused by the Compton current and (*ii*) voltage-dependent effect also may be ignored.

The $I_{pol}$ of the Roos ionization chamber [FIG. 5.8(a)], on the other hand, is noticeably decreasing with increasing $V$ at both measurement depths, suggesting that for this chamber voltage-dependent polarity effects are not negligible relative to its Compton current. We are not sure what the source of the non-negligible voltage-dependent polarity effects in the Roos ionization chamber is, however, we speculate that space-charge distortion of the electric field or different ionic mobilities of air ions should be ruled out, because measurements with the Roos chamber were acquired at a dose rate and in atmospheric conditions similar to those in measurements with the PEEC and the Attix ionization chamber.

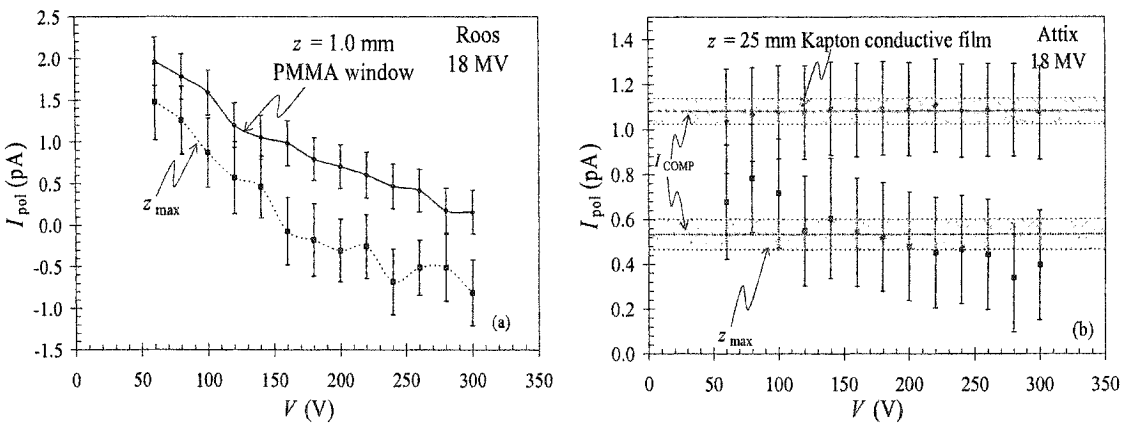


*FIG. 5.8. The $I_{pol}$ at the minimum achievable depths and at $z_{max}$ for (a) the Roos and (b) the Attix parallel-plate ionization chambers against the magnitude of the applied voltage for SSD = 100 cm and 10×10 cm$^2$ 18 MV beam. The $I_{pol}$ in the Attix chamber is voltage independent.*

It is worth mentioning that the design of the Roos ionization chamber incorporates a guard ring with a width relative to the diameter of the collecting electrode considerably smaller than that in the design of the PEEC and the Attix ionization chamber. The Roos chamber has a 16 mm collecting electrode diameter surrounded by a 4 mm width guard ring (ref. 17). The Attix chamber, by comparison, has a 12.7 mm collecting electrode diameter with a 13.5 mm guard ring width (ref. 12), and the PEEC has a 24.2 mm collecting electrode diameter with a 22 mm guard ring width.

To put matters into perspective we note that at a 1.0 mm depth in a 18 MV photon beam the air-sensitive volume of the Roos ionization chamber (2 mm electrode separation and 16 mm collecting electrode diameter) produces a dosimetric current that is about 125 times larger than the maximum $I_{pol}(V)$ value. Its polarity effect current, therefore, contributes to less than 1% of the measured signal at a depth of 1.0 mm, making the chamber still useful for relative dosimetry in the dose build-up region. As an absolute dosimeter, because the dosimetric signal at $z_{max}$ as well as at calibration depths beyond $z_{max}$ recommended by calibration protocols for megavoltage photon beams is higher than that at a 1.0 mm depth, its polarity effect current will have even a smaller contribution to the measured signals, making Eq. (5.8) still practical for accounting for the chamber polarity effect.

### *Compton current dependence on electrode separation*

When exposed to a constant radiation intensity, the collected gas ionization from an ionization chamber is proportional to the size of its air-sensitive volume. Small variations in the gas cavity size for parallel-plate ionization chambers, however, have a negligible impact on the photon and electron fluences traversing the gas cavity and reaching the collecting electrode. Thus, the Compton current in the PEEC should remain independent of the electrode gap size. To validate the above hypothesis we measured the $I_{COMP}$ for the PEEC with electrode separations $s$ varying from 0.89 mm to 10.89 mm in 10×10 $cm^2$ fields for 6 MV and 18 MV photon beams. The results are shown in FIG. 5.9.

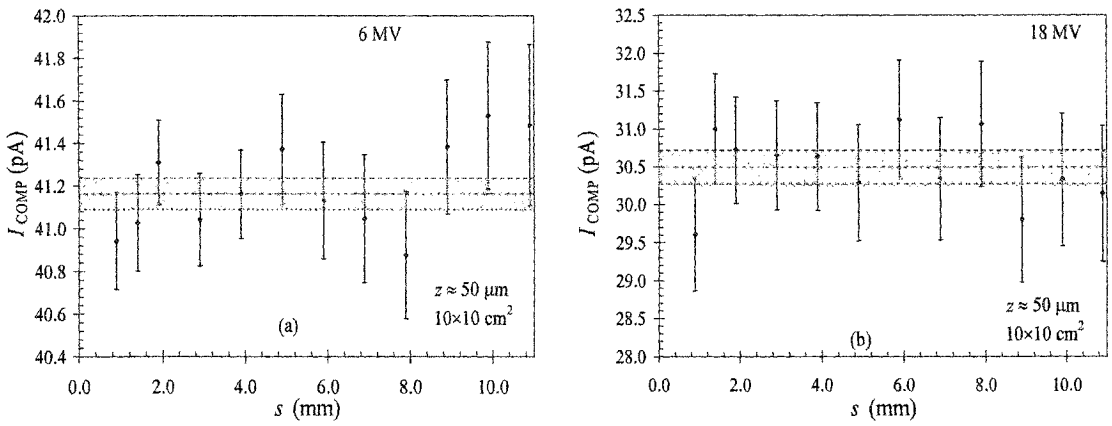


*FIG. 5.9. The $I_{COMP}$ in the PEEC versus electrode separation s measured at the surface under 10×10 cm$^2$ field (a) 6 MV and (b) 18 MV x-ray beams.*

The solid lines in FIG. 5.9(a) and FIG. 5.9(b) represent the Compton current averaged over all measured separations with an uncertainty represented by the half of the width of the shaded areas, clearly showing that the Compton current in the PEEC is independent of the electrode separation $s$.

### *Compton current dependence on depth*

For the PEEC, the $I_{COMP}$ for field sizes of 5×5, 10×10, 15×15, 20×20, and 30×30 cm$^2$ and depths ranging from the surface to 36 mm and 56 mm for 6 MV and 18 MV beams, respectively, is shown in FIG. 5.10. For a given field size, the $I_{COMP}$ versus depth exhibits the following features: (*i*) a maximum positive value at the phantom surface, (*ii*) an exponential-like decrease with increasing depth in the dose build-up region, and (*iii*) a minimum, yet positive, and almost constant value beyond $z_{max}$. Note that for every depth and field size configuration the $I_{COMP}$ and its uncertainty are calculated using Eqs. (5.12) and (5.13), respectively, from the polarity effect current $I_{pol}$ measured at several applied voltages $V$.

In the dose build-up region the $I_{COMP}$ behavior with depth shown in FIG. 5.10 is generally in agreement with the explanation given by Johns *el al.*[12] In this region, the $I_{COMP}$ is always positive having a maximum value when the chamber is at the phantom surface. With larger depths, the $I_{COMP}$ decreases in an exponential manner approaching a minimum positive value at $z_{max}$. At depths beyond $z_{max}$, the $I_{COMP}$ is also positive and is

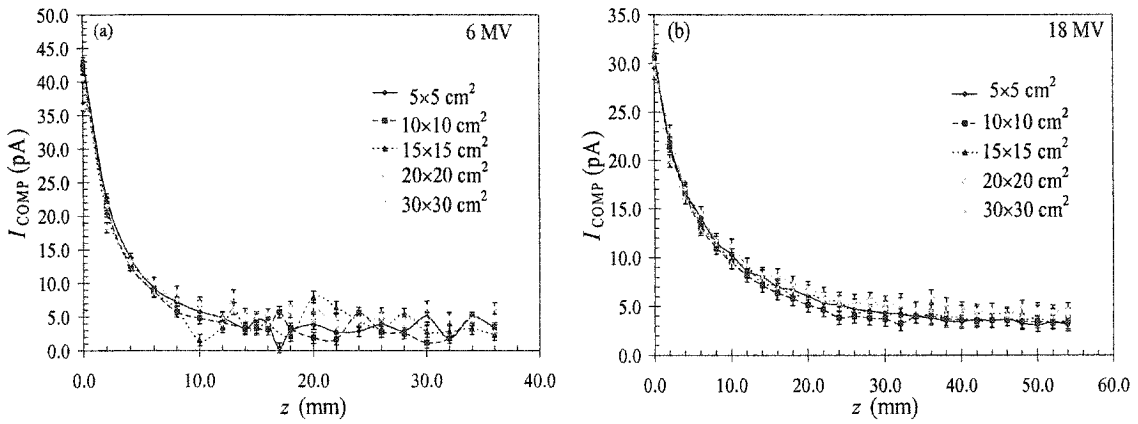


*FIG. 5.10. The Compton current $I_{COMP}(z, A, hv)$ produced in the PEEC as function of depth z in the dose build-up region for CL-2300 C/D (a) 6 MV and (b) 18 MV beams for 5×5, 10×10, 15×15, 20×20, and 30×30 cm² fields. Data were obtained at standard SSD = 100 cm with the PEEC (2 mm electrode separation) using the aluminized Mylar electrode/Delrin walls polarizing electrode.*

independent of the measurement depth, but a small dependence on the field size is observed.

Theoretically, in realistic photon beams we would expect that $I_{COMP}$ becomes zero at $z_{max}$ and negative at depths beyond $z_{max}$, since the decreasing electron fluence beyond $z_{max}$ would essentially generate a negative Compton current in collecting electrodes. In experimental work, however, additional components may potentially become a Compton current source when the chamber is irradiated. Of these possible Compton current sources we speculate that the most significant is the cable connecting the chamber to the electrometer. Although shielded, leakage radiation from the treatment head and scattered radiation from the phantom can still interact with the cable, producing in the event a positive Compton current, since the wire carrying the signal is not surrounded by a sufficient "build-up" solid insulator. Hence, we may separate the $I_{COMP}$ into two components: (*i*) a cable component $I_{COMP}^{cable}(A, hv)$ that is essentially independent of the PEEC position $z$ in the phantom but depends on the field size $A$ as well on as the beam energy $hv$, and (*ii*) a collecting electrode component $I_{COMP}^{elect}(z, A, hv)$ that depends on the parameters $z$, $A$, and $hv$.

To estimate the Compton current cable component $I_{COMP}^{cable}(A,hv)$ we may neglect the negative Compton current $I_{COMP}^{elect}$ produced by the collecting electrode for depths beyond $z_{max}$ and, hence, $I_{COMP}^{cable}(A,hv) \approx I_{COMP}(z,A,hv)$ for $z \geq z_{max}$. In TABLE. 5.3 we list the estimated cable Compton current for the 5×5, 10×10, 15×15, 20×20, and 30×30 $cm^2$ fields and 6 MV and 18 MV x-ray beams, where, for each field, the cable Compton current is obtained by averaging the $I_{COMP}$ data in FIG. 5.10 for depths beyond $z_{max}$. Note that the magnitude of the cable Compton current in large field sizes is greater than that in small fields due to the increased scattered photon fluence.

### *Compton current dependence on the collecting electrode thickness*

An ideal collecting electrode is an electrode with zero thickness. Such electrode produces no wall perturbations in the phantom and generates no Compton current. Hence, a practical approach to an ideal collecting electrode is to make the collecting electrode in parallel-plate ionization chambers as thin as possible, minimizing wall perturbations and considerably reducing the induced currents when the chamber is exposed to radiation.

With our apparatus it was difficult to carry out a systematic study showing the effect of the collecting electrode thickness on the magnitude of the Compton current for the following reasons: (*i*) the method by which the PEEC collecting electrode is constructed, as described in Chapter 4, Section 4.1.2, only allows an estimation of the collecting

TABLE 5.3. ESTIMATED CABLE COMPTON CURRENTS $I_{COMP}^{cable}$ IN NANO-AMPERES FOR SEVERAL FIELD SIZE FOR 6 MV AND 18 MV X-RAY BEAMS.

| Beam \ Field | 5×5 $cm^2$ | 10×10 $cm^2$ | 15×15 $cm^2$ | 20×20 $cm^2$ | 30×30 $cm^2$ |
|---|---|---|---|---|---|
| 6 MV | 3.47 ± 0.25 | 2.85 ± 0.26 | 4.25 ± 0.28 | 4.94 ± 0.29 | 4.72 ± 0.31 |
| 18 MV | 3.41 ± 0.23 | 3.52 ± 0.23 | 3.63 ± 0.23 | 4.61 ± 0.24 | 4.23 ± 0.25 |

electrode thickness and (*ii*) the collecting electrode thicknesses for the Attix and the Roos ionization chambers are not provided by the manufacturers, and references[17] only state the collecting electrode materials (thin graphited polyethylene for the Attix and graphite for the Roos) and sensitive areas without quoting the actual collecting electrode thicknesses. Even so, the small Compton currents produced by the Attix and the Roos ionization chambers in comparison to currents produced in the PEEC suggest that both chambers have a thinner collecting electrode than the PEEC.

One way to validate the above hypothesis is to compare the collecting electrode thicknesses based on the measured Compton currents per unit surface area of the collecting electrodes. For the comparison to be valid the chambers must be exposed to the same radiation intensity and the electrode thicknesses must be small so that electrons are ejected uniformly from the collecting electrode volumes. Under these conditions, it is reasonable to assume that the magnitude of the Compton current would be inversely proportional to the electrode thickness.

Because of the relatively thick front entrance window of the Roos chamber (1 mm), only the collecting electrode thicknesses of the Attix ionization chamber and the PEEC are considered here. When both ionization chambers are at the phantom surface, the mass thicknesses of the front (polarizing) electrodes (0.0048 and 0.0069 g/cm$^2$ for the Attix chamber and the PEEC, respectively) are comparable; hence, the photon and electron fluences in the 10×10 cm$^2$ 18 MV x-ray beam reaching and interacting with the collecting electrodes provide satisfactory conditions for the comparison to be valid. To determine the Compton current generated by the collecting electrodes only, we subtract the cable Compton currents, *i.e.*, the measured Compton currents at $z = z_{max}$, from the Compton currents obtained with surface measurements, as listed in TABLE 5.4 for both ionization chambers. The collecting areas for the Attix chamber and the PEEC are 1.27 cm$^2$ (ref. 17), and 4.60 cm$^2$, respectively; hence, the collecting electrode Compton currents per collecting surface area are (0.41 ± 0.07) nA/cm$^2$ and (5.87 ± 0.13) nA/cm$^2$, respectively. It will be demonstrated with MC simulations in this chapter that the magnitude of the Compton current is proportional to the electrode thickness, and based on this we may conclude here that the collecting electrode thickness of the PEEC is about (14 ± 3) times

TABLE 5.4. COMPARISSON OF THE COLLECTING ELECTRODES COMPTON CURRENTS OF THE ATTIX IONIZATION CHAMBER AND THE PEEC.

| Chamber | $I_{COMP}$ at surface (nA) col(1) | $I_{COMP}$ at $z_{max}$ (nA) col(2) | Collecting electrodes Compton currents at surface (nA) col(1)-col(2) | Collecting electrode front surface area ($cm^2$) | Compton currents per collecting electrode front surface area ($nA/cm^2$) |
|---|---|---|---|---|---|
| Attix | $1.04 \pm 0.06$ | $0.53 \pm 0.07$ | $0.51 \pm 0.09$ | 1.27 | $0.41 \pm 0.07$ |
| PEEC | $30.52 \pm 0.53$ | $3.52 \pm 0.23$ | $27.00 \pm 0.58$ | 4.60 | $5.87 \pm 0.13$ |

larger than that of the Attix ionization chamber, if both collecting electrodes are manufactured from the same material. A more realistic thickness ratio would be about 8 : 1 taking into account the different densities of graphite ($\rho = 1.7$ g/cm$^3$) and polyethylene ($\rho = 0.93$ g/cm$^3$).

### *Compton current dependence on field size*

With increasing field size, the fluences of low-energy scattered photons and contaminating electrons originating from various components in the linac treatment head increase. The low-energy scattered photons and contaminating electrons interact primarily in the dose build-up region and the absorbed dose in this region is expected to increase with increasing field size. When an ionization chamber is placed at the phantom surface or at any depth in the dose build-up region, however, the increase in contaminating electrons would decrease the Compton current (more electrons landing in the collecting electrode volume), while the increase in scattered photons would increase the Compton current. Hence, unlike the situation with the dose, contaminating electrons and scatter photons have opposite effects on the Compton current. Thus, by comparing the Compton current in the PEEC at the surface for various field sizes we can identify which of the two, scattered photons or contaminating electrons, increase significantly with field size, and more importantly affect the absorbed dose in the dose build-up region.

In FIG. 5.11 we plot the collecting electrode Compton current $I_{COMP}^{elect}$ for the PEEC at the surface against field size for 6 MV and 18 MV beams, showing that the collecting electrode Compton current decreases as the fields size is increased from 5×5 up to 30×30 $cm^2$. The $I_{COMP}^{elect}$ at the surface in FIG. 5.11 are calculated by subtracting the corresponding $I_{COMP}^{cable}$ given in TABLE 5.3 from the data points at the surface in FIG. 5.11. Hence, we conclude that the increase in contaminating electrons is more significant than the increase in scattered photons in the dose buildup-region. In a different but more rigorous study of the nature of the head scatter contamination, Sixel[18] showed that low energy photons produced from the linac head have no effect on the dose in the build-up region of open x-ray beams.

### 5.5.2. 9 MeV and 12 MeV electron beams

Measured depth ionizations with the PEEC for 200 MU irradiations for positive and negative polarities, $M_{pos}$ and $M_{neg}$, respectively, for 10×10 $cm^2$ 9 MeV and 12 MeV electron beams are shown in FIG. 5.12. The measured signals $M_{pos}$ and $M_{neg}$ at the same depth $z$ were averaged over 5 repeated 200 MU irradiations at +300 and −300 V polarizing voltages. In clinical physics the electron beam depth ionization curves are determined by taking the average of absolute values from the positive and negative

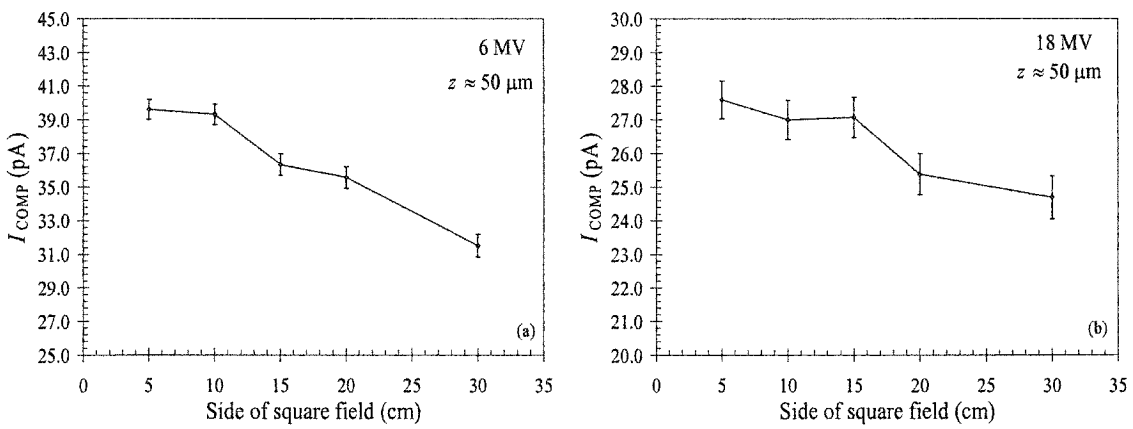


*FIG. 5.11. The collecting electrode Compton current $I_{COMP}$ at $z \approx 50$ μm induced in the PEEC as a function of field size for (a) 6 MV and (b) 18 MV beams for 5×5, 10×10, 15×15, 20×20, and 30×30 $cm^2$ fields.*

readings, $|M_{pos}|$ and $|M_{neg}|$, respectively, at a given depth or more appropriately by the following relationship

$$Q = \frac{M_{pos} - M_{neg}}{2}, \tag{5.14}$$

when the magnitude of the polarity current is larger than the gas collected ionization $Q$. The uncertainty in $Q$ was estimated with the following expression

$$\sigma_Q = \frac{\sqrt{\sigma^2_{M_{pos}} + \sigma^2_{M_{neg}}}}{2}, \tag{5.15}$$

where $\sigma_{M_{pos}}$ and $\sigma_{M_{neg}}$ are the standard deviations of the 5 repeated positive and negative polarity signals, respectively. The uncertainty $\sigma_Q$ was less than 0.1% of the corresponding $Q$ value for most data points but was about 1.0% of the corresponding $Q$ *value* for data collected at depths beyond the practical range of the beams.

The depth ionization curves and the dose curves are correlated by the ratio of restricted stopping powers of Solid Water™ to air evaluated at depth $z$. For data of FIG. 5.12 the percentage depth ionization (*PDI*) curves, normalized to given maximum attained at depth $z_{max}$, are shown in FIG. 5.13. In FIG. 5.13 we also show the percentage depth dose (*PDD*) for both electron beams calculated with the DOSRZnrc/EGSnrc in Solid Water™ using phase-space files that were optimized, based on measurements in water. In FIG. 5.13 we also show some of the important dosimetric beam parameters in Solid Water™,

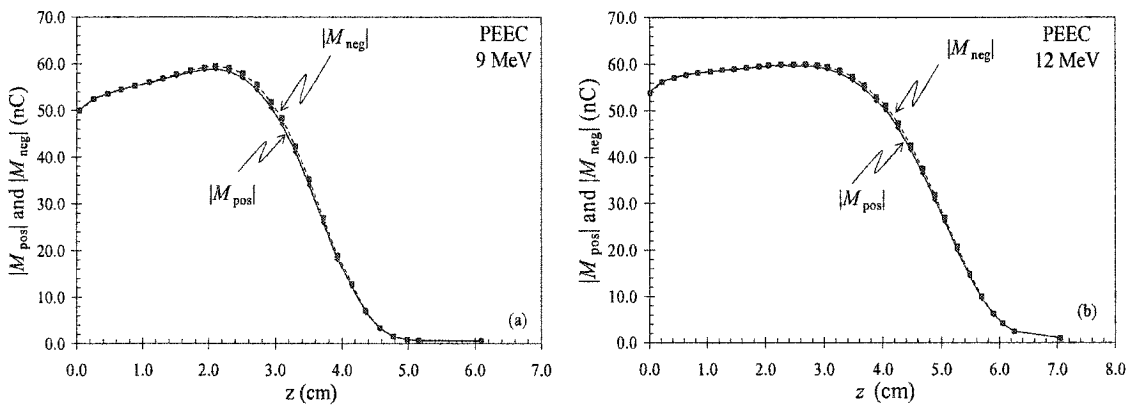


*FIG. 5.12. The PEEC depth ionizations in Solid Water™ for positive and negative polarity settings as a function of depth z for 10×10 cm² field and (a) 9 MeV and (b) 12 MeV electron beams.*

namely, (*i*) the depth of maximum dose ($z_{max}$); (*ii*) the depth at which the dose falls to 50% of maximum ($R_{50}$ in the AAPM TG-51 notation[19]); and (*iii*) the practical range $R_p$ of the electron beam.

The maximum ionization depth ($I_{max}$) and the depth at which the ionization falls to 50% of its maximum value ($I_{50}$) are not equal to $z_{max}$ and $R_{50}$ but are located, respectively, at shallower depths, and the data in FIG 5.13 show that the discrepancy is greater for the lower energy electron beam (9 MeV). The depths of maximum ionization $I_{max}$ are 2.1 and 2.5 cm for the 9 MeV and 12 MeV, respectively, and the depths of maximum dose $z_{max}$ occur roughly 2 mm deeper for both electron beams. The depth at which the ionization ionization falls to 50% of maximum ($I_{50}$) and $R_{50}$ are not as different as $I_{max}$ and $z_{max}$ are. The $R_{50}$ for the 10×10 cm$^2$ field 9 MeV is at 3.7 cm and at 5.0 cm for the 10×10 cm$^2$ field 12 MeV, and the corresponding $I_{50}$ is 3.6 cm and 5.0 cm, respectively. The practical range $R_p$ defined as *the depths at which the tangent plotted through the steepest section of the electron depth dose curve intersects with the extrapolation line of the background due to bremsstrahlung*, are 4.5 cm and 5.1 cm for the 10×10 cm$^2$ field 9 MeV and the 10×10 cm$^2$ field 12 MeV beams, respectively.

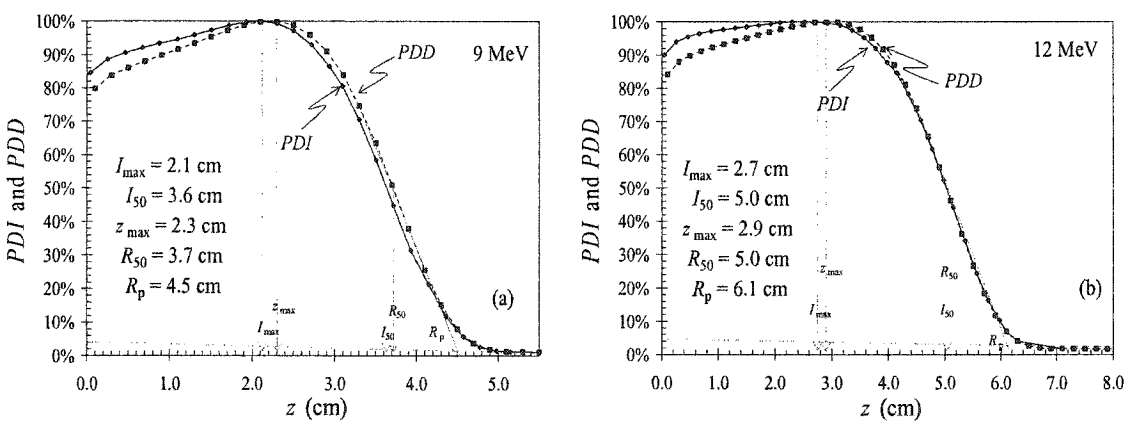


*FIG. 5.13. The percentage depth ionization (PDI) and the percentage depth dose (PDD) in Solid Water™ for a 10×10 cm$^2$ field in (a) 9 MeV and (b) 12 MeV electron beams. In the figure we show several important beam parameters used in electron dosimetry, namely, (i) the depth of maximum dose($z_{max}$); (ii) the depth at which the dose falls to 50% of maximum ($R_{50}$); and (iii) the practical range of the electron beam ($R_p$). The depth of maximum ionization ($I_{max}$) and the depth at which the ionization falls to 50% of maximum ($I_{50}$) are somewhat closer to the phantom surface than $z_{max}$ and $R_{50}$, respectively.*

Charge acquisition mode was used in obtaining our data for the electron beams and we estimated the integral of the Compton current $Q_{COMP}$ or the *Compton charge* at depth $z$ induced in the PEEC collecting electrode during the irradiation following the relationship

$$Q_{COMP} = \frac{M_{pos} + M_{neg}}{2}, \tag{5.16}$$

with an uncertainty $\sigma_{Q_{COMP}}$ estimated by the following relationship

$$\sigma_{Q_{COMP}} = \frac{\sqrt{\sigma^2_{M_{pos}} + \sigma^2_{M_{neg}}}}{2}, \tag{5.17}$$

where $M_{pos}$ and $M_{neg}$ are, respectively, the measured signals at same depth $z$ averaged over 5 repeated 200 MU irradiations at +300 and –300 V polarizing voltages.

In FIG. 5.14 we plot the $Q_{COMP}$ as a function of depth for 10×10 cm$^2$ 9 MeV and 12 MeV electron beams, clearly showing a dependence on depth different from that in the photon beams (FIG. 5.10). The $Q_{COMP}$ has a maximum positive value at the surface; then decreases linearly with depth and becomes negative after a depth of about one fifth of $I_{50}$ for the particular electron beam; then continues to decrease reaching a minimum value at approximately $0.9I_{50}$. Beyond this point $Q_{COMP}$ increases rapidly to reach a zero value at the practical electron beam range $R_p$.

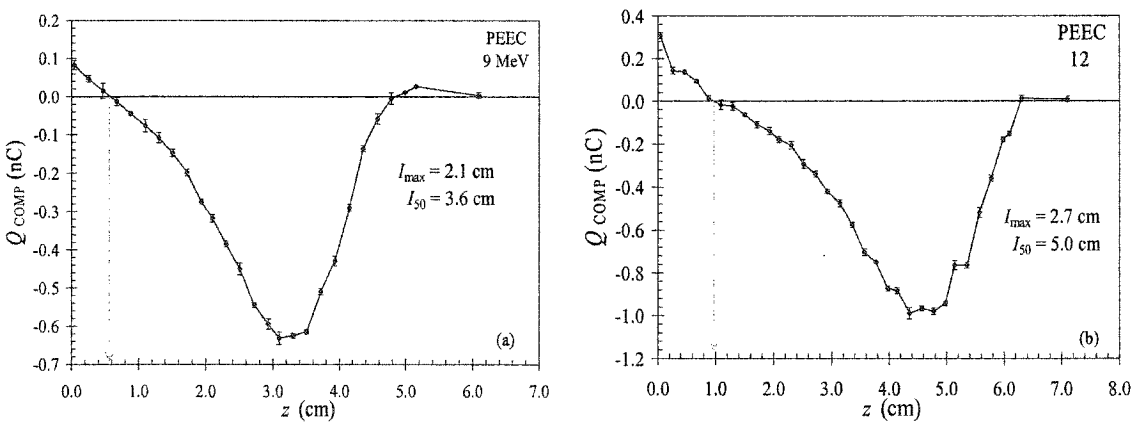


*FIG. 5.14. The PEEC $Q_{COMP}(z, 10\times10\,cm^2)$ for 10×10 cm$^2$ fields (a) 9 MeV and (b) 12 MeV electron beams. The depths at which $Q_{COMP}$ reverses sign is indicated in the figure by the gray arrows, occurring at 0.58 cm and 1.0 cm for 10×10 cm$^2$ fields 9 MeV and 12 MeV, respectively. The minimum $Q_{COMP}$ (maximum negative value) occurs approximately at 3.2 cm for the 9 MeV beam and 4.5 cm for the 12 MeV beam.*

The region near the surface where $Q_{COMP}$ is positive indicates that the number of electrons ejected from the collecting electrode volume exceeds the number of electrons landing and stopping in the collecting electrode volume. The excess positive charge in the collecting electrode can be caused by: (*i*) low-energy contaminating photons that are present in the beam emerging from the linac head and (*ii*) primary electrons that undergo hard collisions within the collecting electrode volume.

The region where $Q_{COMP}$ is negative is caused primarily by the stopping of primary electrons in the collecting electrode volume after they lose their kinetic energy as they penetrate the phantom. In a monoenergetic electron beam and if electrons are not scattered by the medium and travel in a straight path, the Compton charge as a function of chamber depth due to primary electrons would be an inverted delta-like function having essentially a zero value at all depths and a large negative value at the depth at which all primary electrons stop. In a clinical electron beam, however, the Compton charge against chamber depth due to primary electrons landing in the collecting electrode has an inverted Gaussian-like distribution instead.

There are two reasons for this behavior: (1) the scattering of primary electrons in the phantom essentially reduces the penetration depths of the electrons and would result in an inverted Gaussian-like charge deposition distribution centered at the most probable penetrating depth for that particular electron energy and (2) in a realistic clinical electron beam the primary electrons emerge with an energy distribution from a maximum energy down to zero because of the slowing down of electrons in the linac head components, such as the scattering foils and beam monitor chamber, and in the air between the electron source and the phantom surface, as well as the production of electrons from bremsstrahlung photon interactions in all media traversed between the radiation source and the phantom.

At deeper depths in phantom, the electron fluence in the phantom drops significantly, consisting of secondary electrons generated by bremsstrahlung photons which originate from radiative losses of primary electrons in various treatment head components, as well as in the phantom and the Compton charge in this region is approximately zero.

### 5.5.3. COMPTON/EGSnrc Monte Carlo simulations

The Clinac-2300 10×10 $cm^2$ 6 MV x-ray beam treatment head geometry was modeled with the BEAMnrc user code and the initial electron beam parameters were optimized based on ionization measurements in water. The details of the optimization process of the 6 MV beam are presented in Chapter 6. The treatment head geometries for the 10×10 $cm^2$ 9 MeV and 12 MeV electron beams were also modeled with the BEAMnrc user code. Based on measurements in water with a diode, it was found that the optimized energies of the initial electron beams are 9.95 MeV and 13.2 MeV, respectively. For all three beams, phase-space files for a 10×10 $cm^2$ field were obtained at an *SSD* of 100 cm for use as input sources in simulations with the COMPTON user code.

Simulations with the COMPTON user code require the particular user to define a geometry in which the quantities of interest are calculated. The geometry used in our calculations essentially corresponds to the PEEC geometry with which the actual measurements were acquired. In FIG. 5.15, we show the RZ geometry and materials for COMPTON user code simulations in the 6 MV x-ray beam. The RZ geometry and materials used in electron beam calculations are similar to those shown in FIG. 5.15 but the Delrin and Mylar regions are replaced with Solid Water™ and carbon, respectively.

In our calculations with the COMPTON user code, none of the available variance reduction techniques in the EGSnrc code were used. Most of our simulations were calculated using an electron cut-off energy of $\Delta = 189$ keV; however, in some situations $\Delta$ was reduced to 10 keV or 1 keV. For photon particles a 10 keV cut-off energy was used in all calculations. In the following paragraphs the depth in medium is defined by the thickness $z$ of the upper-most geometrical layer, as shown in FIG. 5.15.

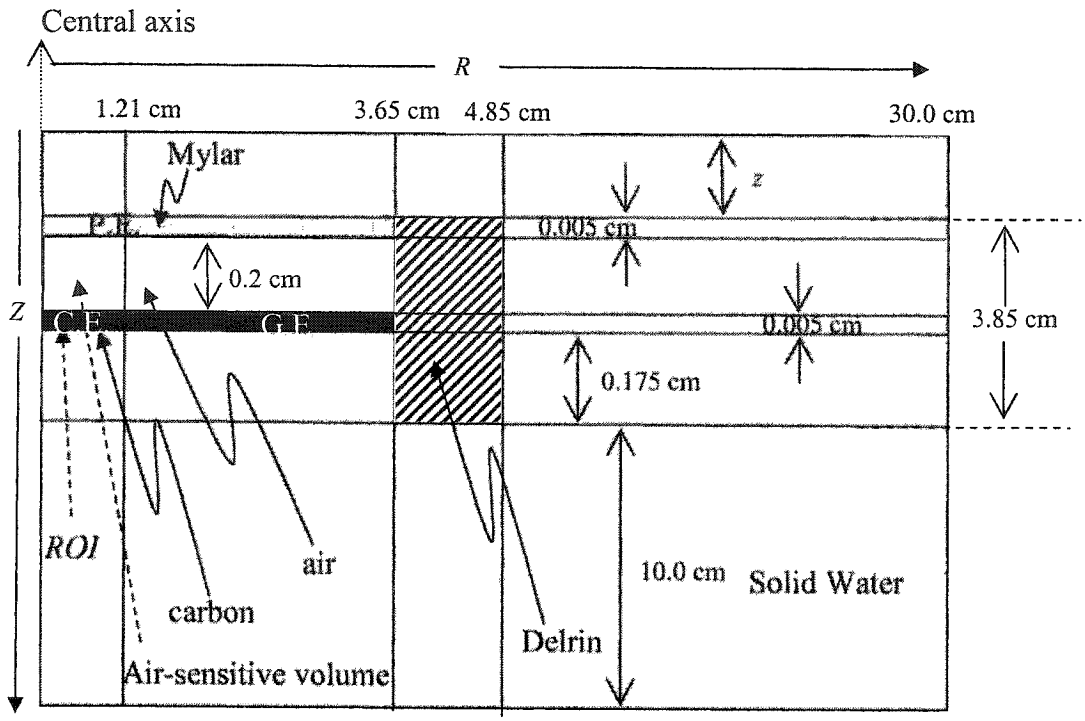


*FIG. 5.15. Schematic PEEC (RZ) geometry and materials used in the COMPTON user code. The ROI corresponds to the collecting electrode of the PEEC and is located below the air-sensitive volume of the cavity.(P.E.= polarizing electrode; C.E.= collecting electrode; and G.E. = guard ring.*

### *6 MV x-ray beam*

The $Q^{in}$ and $Q^{out}$ per primary history, respectively, the $\overline{Q}^{in}$ and the $\overline{Q}^{out}$ in the collecting electrode volume are shown in FIG. 5.16(a) as a function of $z$ in the dose build-up region for the 10×10 cm$^2$ field and cut-off energies $\Delta$ of 189 keV and 10 keV. The accumulated charge per primary history $\overline{Q}^{net}$ from the calculations as a function of $z$ is shown in FIG. 5.16(b), clearly in agreement with theoretical predictions. To compare MC calculations ($\overline{Q}^{net}$) with the PEEC measurements ($I_{COMP}$) directly, we examined two parameters: (*i*) the Compton current depth dependence and (*ii*) the polarity correction factor $P_{pol}$.

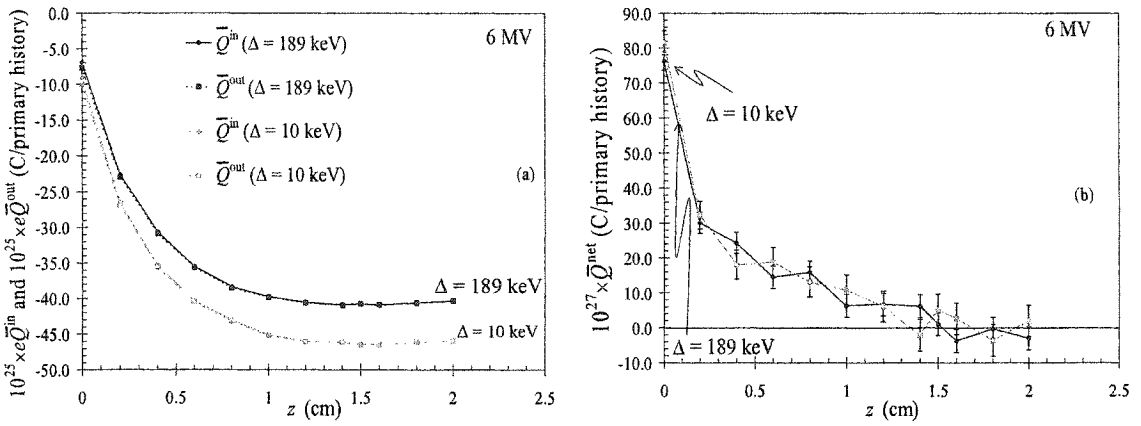


*FIG. 5.16. COMTPON user code results for the PEEC in a 10×10 cm² 6 MV beam. (a) $\bar{Q}^{in}$ and $\bar{Q}^{out}$ in the collecting electrode as a function of depth z calculated with ECUT = 0.700 and 0.521 MeV. (b) $\bar{Q}^{net}$ (the accumulated charge in the collecting electrode) as a function of depth z calculated with Δ = 189 and 10 keV. The calculation is for the PEEC with (i) the aluminized Mylar/Delrin wall front electrode, (ii) a 50 μm carbon collecting electrode, (iii) an electrode separation s = 2 mm, and (iv) 10 keV photon cut-off energy.*

Figure 5.17 presents the normalized $I_{COMP}$ (after removing the cable contribution) and the normalized $\bar{Q}^{net}$ depth curves in the build-up region. The three curves are for: (*i*) the measured $I_{COMP}$, (*ii*) $\bar{Q}^{net}$ calculated with $\Delta = 189$ keV, and (*iii*) $\bar{Q}^{net}$ calculated with $\Delta = 10$ keV. Each curve is normalized at the depth of $z = 0$. This comparison resulted in a satisfactory agreement between the measurements and both MC calculations.

In calibration protocols, such as the AAPM TG-51 (ref. 19) and its predecessors the AAPM TG-21 (ref. 20) and AAPM TG-25 (ref. 21), as well as in the IAEA TRS-398 (ref. 17), the charge used for the reference dosimetry measurement is either $M_{pos}$ or $M_{neg}$ and the protocols require the user to account for the polarity effect of the chamber by applying a polarity effect correction factor $P_{pol}$. This factor is simply the ratio of the collected gas ionization $Q(V)$ to the reference dosimetric signal used (either $M_{pos}$ or $M_{neg}$). Hence, the polarity correction factor $P_{pol}$ for the positive current reading when the ionization chamber is operated near saturation is calculated by the following relationship

$$P_{pol} = \frac{I(V)}{M_{pos}(V)} \approx 1 - \frac{I_{COMP}}{I(V)}. \qquad (5.18)$$

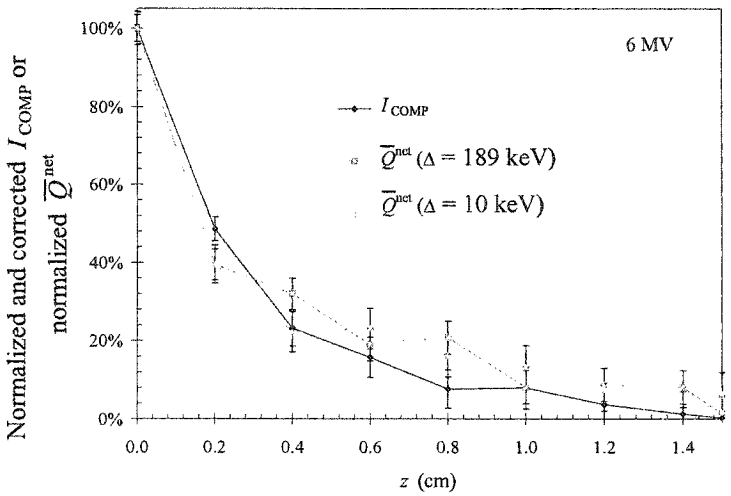


*FIG. 5.17. Comparison of measurements ($I_{COMP}$) and MC calculations ($\overline{Q}^{net}$ for $\Delta$ = 189 keV and 10 keV) of the Compton current in PEEC. The curves are for the relative $I_{COMP}$ and $\overline{Q}^{net}$ depth curves normalized to the value at z = 0 cm.*

The polarity correction factor $P_{pol}$ may also be calculated from our MC simulations. The "gas ionization" $\overline{Q}^{gas}$ per primary history is related to the energy deposited $\overline{E}$ in the air-sensitive volume region per primary history by the following relationship

$$\overline{Q}^{gas} = \overline{E} / \overline{W}_{air}, \tag{5.19}$$

where $\overline{W}_{air}$ is the mean excitation and ionization energy of air expressed in eV/ion pair. Since the positive polarity signal is the sum of the gas ionization and the Compton current, the $P_{pol}$ correction factor calculated from our MC simulations is given by the following relationship

$$P_{pol} = \frac{\overline{Q}^{gas}}{\overline{Q}^{net} + \overline{Q}^{gas}}, \tag{5.20}$$

which may be expressed when $\overline{Q}^{gas} >> \overline{Q}^{net}$ as

$$P_{pol} \approx 1 - \frac{\overline{Q}^{net}}{\overline{Q}^{gas}}. \tag{5.21}$$

While the normalized $\overline{Q}^{net}$ curves are in excellent agreement with measurements (FIG. 5.17), the MC polarity correction factors $P_{pol}$ are not. For $z$ = 0 cm and a 10×10 cm$^2$ 6 MV x-ray beam the MC-calculated $P_{pol}$ for a $\Delta$ of 189 keV and a $\Delta$ of 10 keV

is 0.992 and 0.994, respectively, whereas the $P_{pol}$ from measurements at the same depth, field size and beam quality is 0.897. We even carried-out a single calculation at $z = 0$ with a $\Delta$ of 1 keV but the extra effort did not improve appreciably the calculated $P_{pol}$ value ($P_{pol} = 0.993$).

It is worth mentioning that the uncertainties in the MC-calculated $P_{pol}$ are relatively large (about ±0.083) but the uncertainties also include the correlation between $\overline{Q}^{net}$ and $\overline{Q}^{gas}$. As a possible improvement to the COMPTON code, this correlation could be removed by calculating "on the fly" the polarity correction factor of the chamber for each primary history $i$ essentially treated as a scored quantity $x_i$. Two new variables must be introduced in the COMPTON user code in this situation, one to accumulate the scored quantity "$x_i$" and the other to accumulate "$x_i^2$".

**Effect of collecting electrode thickness on the Compton current in photon beams**

We discussed briefly in Section 5.5.1 the effect of the collecting electrode thickness on the magnitude of the Compton current and, based on several assumptions, we concluded that the collecting electrode of the PEEC is about 8 times thicker than that for the Attix ionization chamber. Our estimation was based on the assumption that the magnitude of the Compton current is proportional to the thickness of the collecting electrode.

To validate this assumption, we varied the thickness of the collecting electrode layer of the RZ geometry in the COMPTON user code from 25 μm to 500 μm. With the calculations carried out with a $\Delta$ of 10 keV, the three quantities of interest, namely, $\overline{Q}^{in}$, $\overline{Q}^{out}$, and $\overline{Q}^{net}$ for the 10×10 cm$^2$ 6 MV beam at $z = 0$ cm are presented in FIG. 5.18, clearly showing that the Compton current increases essentially linearly in this range of collecting electrode thicknesses.

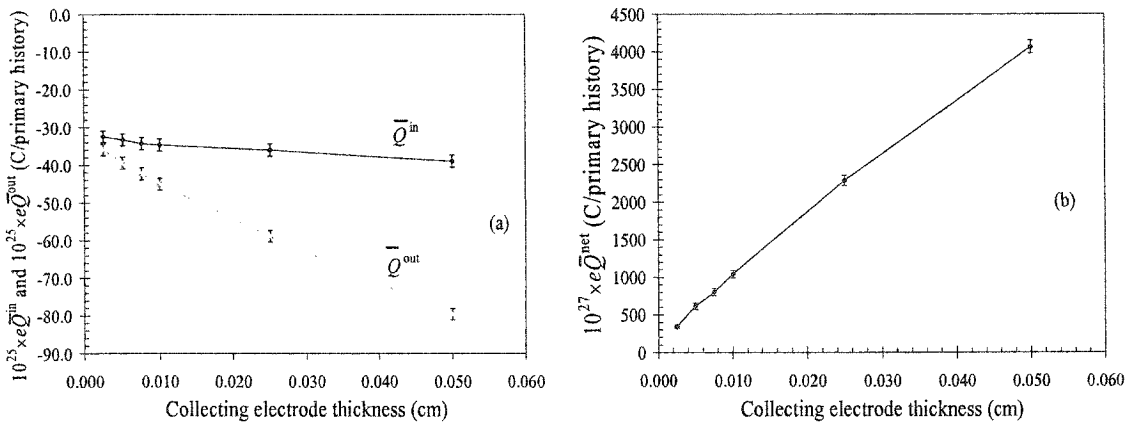


*FIG. 5.18. Calculated (a) $\bar{Q}^{in}$ and $\bar{Q}^{out}$, and (b) $\bar{Q}^{net}$ of the PEEC for 10×10 cm² 6 MV beam and z = 0 as a function of the collecting electrode.*

The y-intercept, *i.e.*, the Compton current of an ideal electrode, in the linear fit to data in FIG. 5.18(b) is (170.5 ± 19.1) C/*primary history* rather than equal to zero. It will be interesting to conduct a comprehensive MC study of the Compton current from the collecting electrode by separating the contributions of photons and energetic electrons to the Compton current and examining the dependence of each component on the electrode thickness. This study might show that while the photon component of the Compton current increases linearly with the collecting electrode thickness, the component related to high energy electrons passing through the collecting electrode does not.

Based on the above MC study we set out to estimate the thickness of the collecting electrode that would give a polarity correction factor $P_{pol}$ matching the measured value of 0.897 with the PEEC. Since $P_{pol}$ couples the gas ionization and the Compton current, we examined the effect of the collecting electrode thickness on the energy deposited in the air-sensitive volume. For the 10×10 cm² 6 MV x-ray beam at $z = 0$ cm the deposited energy per primary history $\bar{E}$ in the air-sensitive volume was calculated as a function of the collecting electrode thickness, and the results are shown in FIG. 5.19. For the range of collecting electrode thicknesses from 25 μm to 500 μm, $\bar{E}$ is constant with a mean value of (1.74 ± 0.04)×10⁻⁸ MeV/*primary history*.

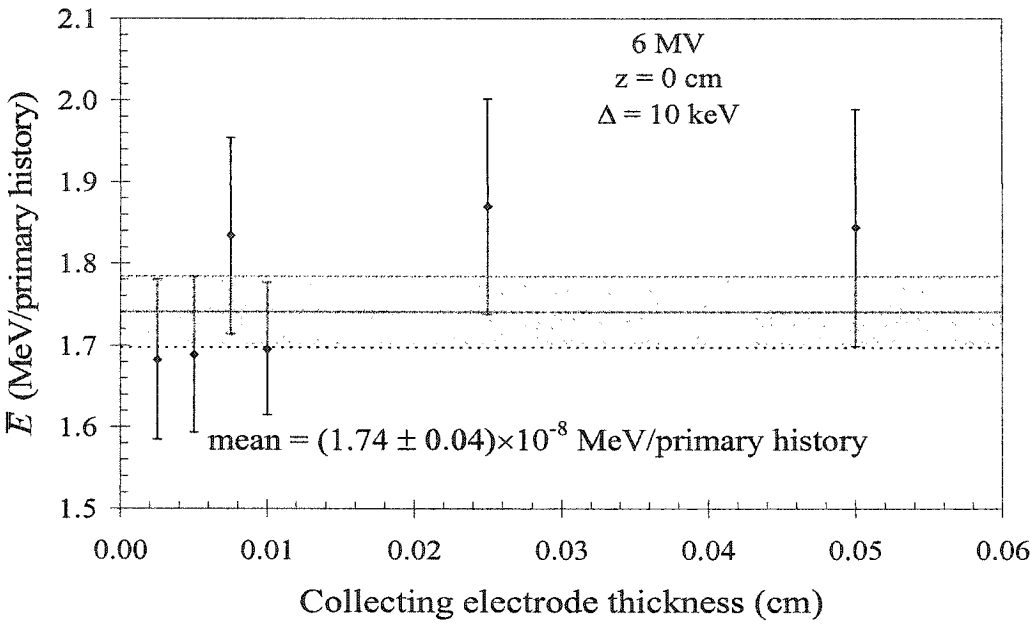


*FIG. 5.19. The energy per primary history $\bar{E}$ deposited in the air-sensitive volume region as a function of the collecting electrode thickness based on calculations with the COMPTON/EGSnrc user code.*

The polarity correction factor $P_{pol}$ calculated with Eq. (5.20) as a function of the collecting electrode thickness is shown in FIG. 5.20. Under the assumptions that the Compton current increases linearly with the collecting electrode thickness, extrapolating the linear fit of the MC-calculated $P_{pol}$ versus the collecting electrode shows that a thickness of about 1 mm, much larger than what was estimated by Zankowski[22] (50 μm) during the construction of the electrode, would produce a calculated $P_{pol}$ of 0.9. Note that in our fit we forced the line to intercept the y-axis at 1.0, which would be the polarity correction factor for the ideal collecting electrode. A 1 mm collecting electrode thickness seems too large, since we got to physically measure a small piece of the guard ring that accidentally fell of the Solid Water disk on which the collecting electrode is spray-painted and concluded that the discrepancy of the measured and MC-calculated $P_{pol}$ cannot be attributed to an uncertainty in the collecting electrode thickness.

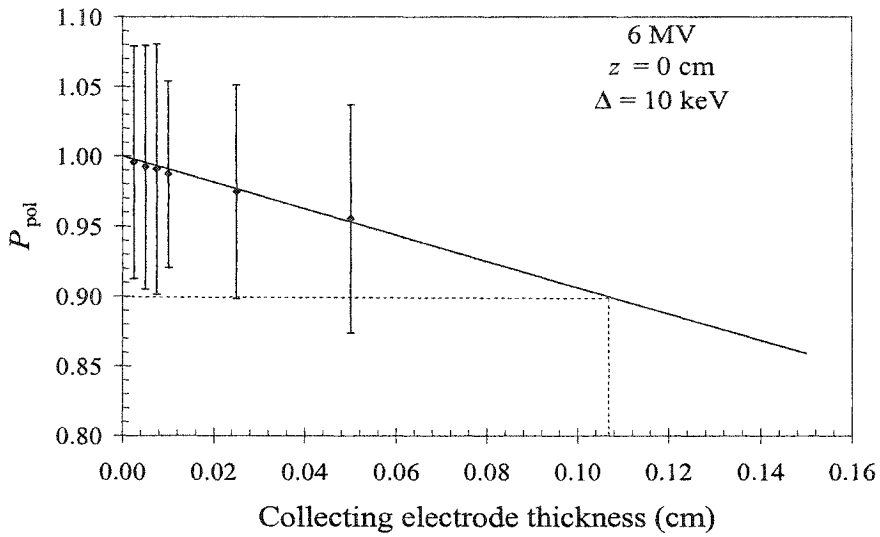


*FIG. 5.20. The MC-calculated $P_{pol}$ correction factor as a function of the collecting electrode thickness. The dotted line shows linear extrapolation of the calculated data predicts that a collecting electrode thickness of 0.107cm would result in a calculated $P_{pol}$ value of 0.9.*

Furthermore, to investigate if the discrepancy between the measured and the MC-calculated $P_{pol}$ could be explained by an uncertainty in the electrode separation $s$, we ran two simulations at $z = 0$ cm for air-sensitive volume thicknesses of 1.9 mm and 2.1 mm, respectively, while keeping the collecting electrode thickness at 50 μm. The MC-calculated $P_{pol}$ for both situations was 0.993, clearly showing that a small uncertainty in the electrode separation cannot explain the discrepancy between the MC-calculated $P_{pol}$ and its measured value.

### *9 MeV and 12 MeV electron beams*

The MC optimization of the 10×10 cm$^2$ field 9 MeV and 12 MeV electron beams was done by our colleagues in the department based on measurements in water with a diode. To verify their optimization, we compared relative depth ionization curves normalized to the maximum measured with the PEEC to the MC relative air-cavity depth dose curves normalized to maximum cavity dose calculated with the COMPTON user code. Simply stated, *the air-cavity depth dose curve* is the MC-calculated sensitive air-cavity dose, *i.e.*, the dose in the geometrical region above the *ROI* in FIG. 5.15, as a function of $z$ normalized to maximum. Since $\overline{W}_{air}/e$ is energy-independent, the relative air-cavity

depth dose curve is essentially equivalent to the relative depth ionization curve of the PEEC.

The verification for the 10×10 cm$^2$ field 9 MeV and 12 MeV electron beams is shown in FIG. 5.21. The MC calculations resulted in relative air-cavity depth dose curves that are in agreement with the measurements, falling to 50% at depths within ±1 mm of $I_{50}$ and within a ±2% relative error in the region between the surface and $I_{max}$. The simulations were carried out using a Δ of 189 keV. Figures 5.22 and 5.23 show $\overline{Q}^{in}$, $\overline{Q}^{out}$, and $\overline{Q}^{net}$ in the collecting electrode region as a function of thickness $z$ for the 10×10 cm$^2$ field 9 MeV and 12 MeV electron beams, respectively.

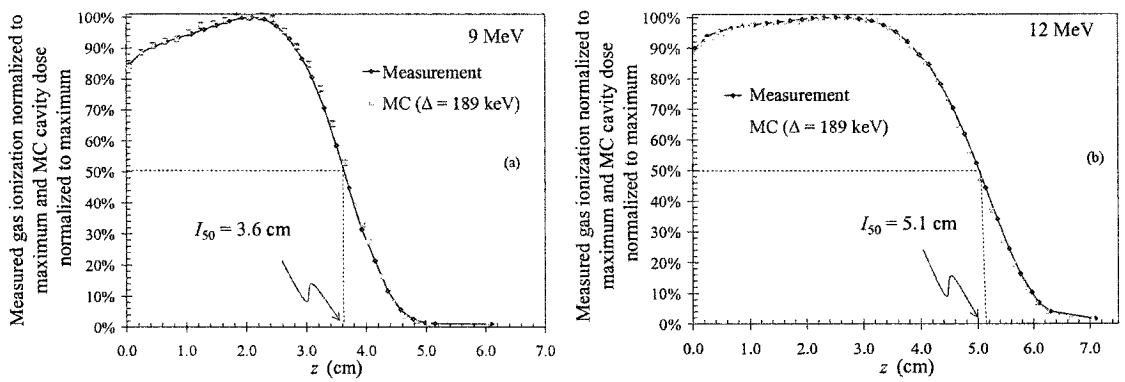


*FIG. 5.21. Comparison of the relative air-cavity depth dose curve calculated with the COMTPON user code and the relative depth ionization curves for the PEEC in the 10×10 cm$^2$ field (a) 9 MeV and (b) 12 MeV electron beams.*

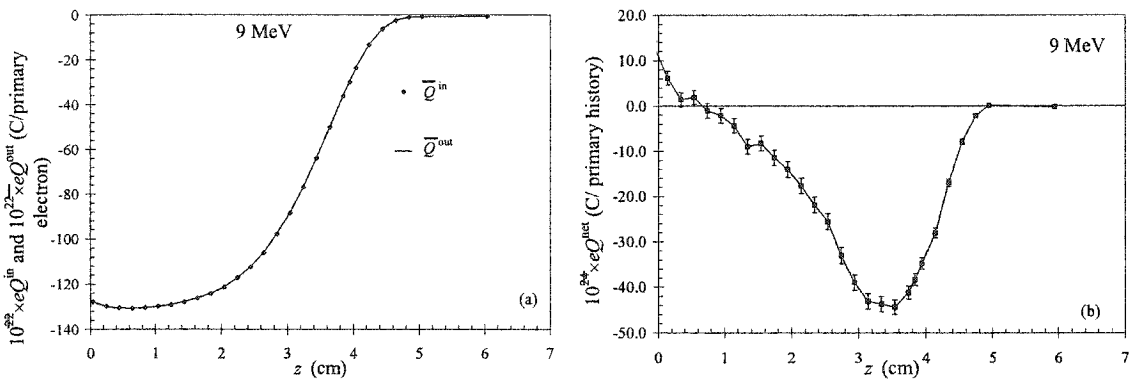


*FIG. 5.22. COMTPON code results for the PEEC in 10×10 cm$^2$ field 9 MeV beam. (a) $\overline{Q}^{in}$ and $\overline{Q}^{out}$ in the collecting electrode as a function of depth z (b) $\overline{Q}^{net}$ (the accumulated charge in the collecting electrode per primary history) as a function of depth z.*

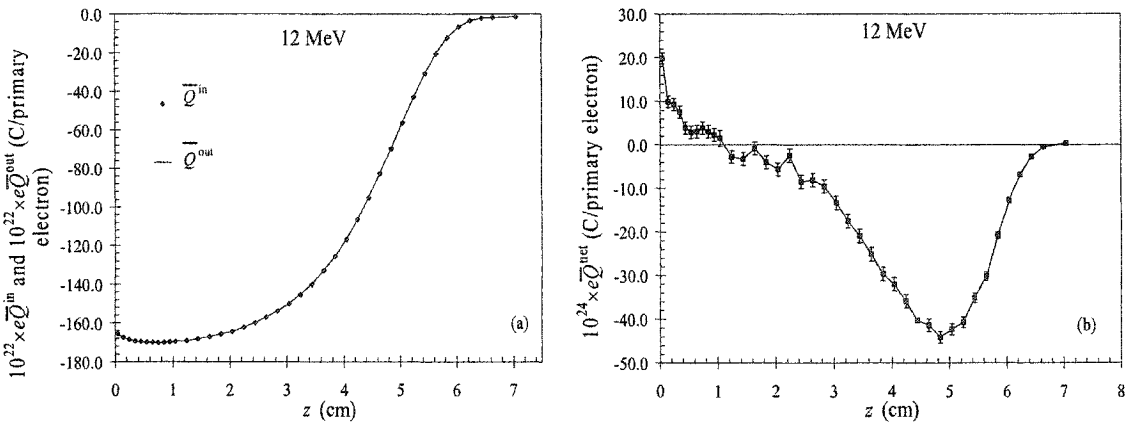


*FIG. 5.23. COMTPON code results for the PEEC in 10×10 cm² field 12 MeV beam. (a) $\overline{Q}^{in}$ and $\overline{Q}^{out}$ in the collecting electrode as a function of depth z (b) $\overline{Q}^{net}$ (the accumulated charge in the collecting electrode per primary history) as a function of depth z.*

The relative $Q_{COMP}$ curves for 10×10 cm² field 9 MeV and 12 MeV electron beams normalized to the Compton charge at depths of 3.4 and 4.8 cm, respectively, are shown in FIG. 5.24. Also shown are the relative $\overline{Q}^{net}$ curves normalized at the same depths. Unlike the situation with the 10×10 cm² 6 MV beam, the MC-calculated curves do not exactly match the measurements but are shifted to shallower depths for the 9 MeV and to larger depths for the 12 MeV beam in the region where the Compton charge is negative. We do not understand the cause of this discrepancy; but we speculate that minute changes to the optimized electron energy of the electron beams would improve the results without affecting the dose distributions.

It would also be useful to repeat the calculations with a smaller Δ to investigate the sensitivity of $\overline{Q}^{net}$ to the electron cut-off energy. Nevertheless, the results in FIG. 5.24 are encouraging and to some extent satisfactory, because the $\overline{Q}^{net}$ curve has the correct shape, predicting correctly the two distinctive positive and negative Compton charge regions, as well as the depths near the surface at which the Compton charge is zero.

Similarly to the situation with the 6 MV beam, the polarity correction factor $P_{pol}$ calculated from MC simulations is different from the measured value. The measured $P_{pol}$ at z = 0.05 cm is 0.998 for 9 MeV and 0.997 for 12 MeV, and has a value of 1.013 at

$z = 3.4$ cm and 1.029 at $z = 4.8$ cm for 9 MeV and 12 MeV, respectively. The COMPTON user code, however, predicted $P_{pol} \approx 1.0$ at all four points.

**Contribution of contaminating photons to the Compton current in electron beams**

Contaminating photons in a typical phase-space file for a clinical electron beam at an *SSD* of 100 cm make up about 50% of all particles contained within the file. These photons will generate a positive Compton charge in ionization chambers placed at the phantom surface in addition to the positive Compton charge that is produced by the primary electrons undergoing hard collisions in the collecting electrode volume. To investigate the effect of contaminating photons on the Compton charge induced in the PEEC, we recalculated $\overline{Q}^{net}$ of the 10×10 cm$^2$ 9 MeV beam as a function of depth using only the photons contained in the phase-space file. In FIG. 5.25(a) we show the results for $\overline{Q}^{in}$ as well as $\overline{Q}^{out}$, and in FIG 5.25(b) we show $\overline{Q}^{net}$ resulting from this calculation.

As shown in FIG. 5.25(b), the $\overline{Q}^{net}$ curve produced by the contaminating photons exhibits behavior that was observed in photon beams before, having a maximum at the surface and quickly decreasing to zero. Our calculations showed, however, that contaminating photons only produced less than 5% of the $\overline{Q}^{net}$ from all particles at $z = 0.04$ cm, essentially indicating that primary electrons through electron-electron hard collisions are the primary source of the Compton current in the PEEC at the surface. At deeper depths the relative contribution of contaminating photons to the Compton charge is even smaller and thus may be considered negligible.

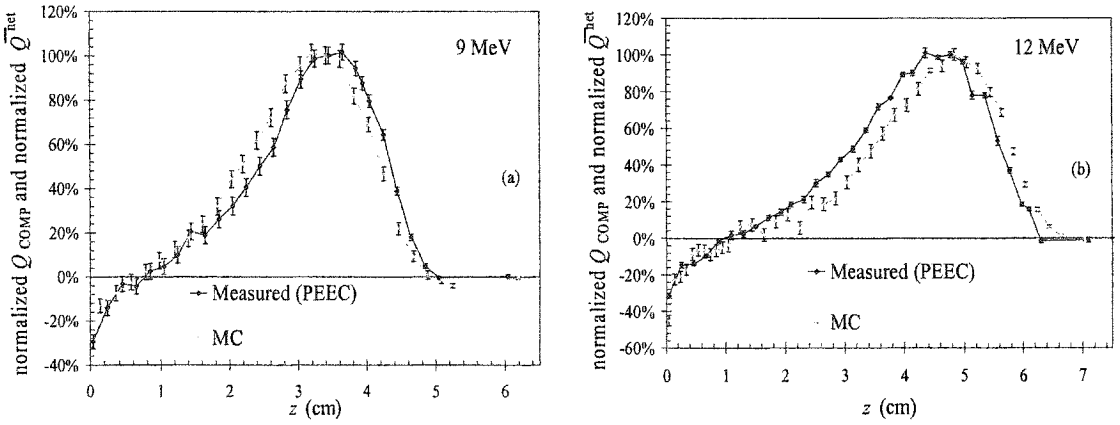


*FIG. 5.24. Compton charge comparison of measurements and MC calculations in the PEEC. The curves are for the relative $I_{COMP}$ and $\overline{Q}^{net}$ normalized to the minimum values.*

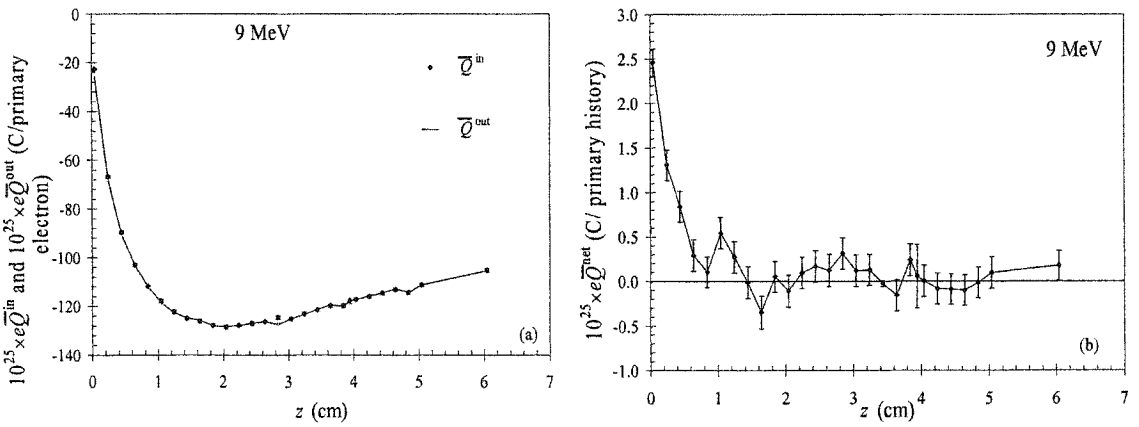


*FIG. 5.25. COMTPON code results for the PEEC in 10×10 cm$^2$ 9 MeV beam using only contaminating photons present in the phase-space file. (a) $\overline{Q}^{in}$ and $\overline{Q}^{out}$ in the collecting electrode as a function of depth z and (b) $\overline{Q}^{net}$ (the accumulated charge in the collecting electrode) as a function of depth z.*

## 5.6. TERMINOLOGY CRITIQUE

In this chapter we used the terminology "*Compton current*" or "*Compton charge*" freely for the induced currents in ionization chamber components irradiated with various types of radiation beams. Understandably, the "Compton current" is commonly used only for photon beams and is avoided for electron beams, but we would like to point out that the "Compton current" is an ambiguous term even for photon beams, since it may lead to the notion that this current is produced only through Compton effect.

Two facts should be noted. Firstly, the magnitude of the current is determined from the number of orbital electrons knocked out from the collecting electrode volume and the number of charges landing and coming to a complete stop in the collecting electrode volume. In fact, at depths where CPE exists at the collecting electrode, the Compton current disappears even though photons continue to interact within the collecting electrode volume through the Compton effect. Secondly, other types of photon interactions, with the exception of Rayleigh scattering, contribute to the "Compton current" either directly through ejected secondary electrons (photoelectron, Compton electron, and triplet production electron) or indirectly through tertiary electrons ejected by the secondary electrons (photoelectric effect, Compton scattering, pair production, and triplet production).

Consequently, we propose "Charged-particle-Fluence-Gradient Current (*CFGC*)" as a better and more descriptive alternative to the "Compton current". This term would describe the induced current irrespective of the radiation source type. The basis for this proposed name can be substantiated from FIGs. 5.16, 5.22, and 5.23, where we plot $\overline{Q}^{in}$, $\overline{Q}^{out}$, and $\overline{Q}^{net}$. Clearly the $\overline{Q}^{net}$ can be related to the gradients of $\overline{Q}^{in}$ or $\overline{Q}^{out}$, having a positive sign when the gradients are negative and visa versa. In addition, the magnitude of $\overline{Q}^{net}$ is also proportional to the magnitude of the gradients.

## 5.7. SUMMARY AND CONCLUSIONS

The polarity effect of ionization chambers can be categorized as: 1) a voltage-dependent effect producing a signal difference between the two polarity readings varying with the polarizing voltage and 2) a voltage-independent polarity effect where the difference between the two polarity readings is independent of the polarizing voltage.

The radiation induced currents (Compton current) were the dominant cause of the polarity effect in the PEEC verifying that the collected gas-ionization in the PEEC can be obtained by averaging the magnitudes of the positive and negative polarity readings, provided that the Compton current is smaller than the collected gas-ionization.

In photon beams, the magnitude of the Compton current was measured in 6 MV and 18 MV x-ray beams as a function of the chamber depths ranging from 0 up to 3.6 cm and 5.6 cm, respectively, and for field sizes of 5×5, 10×10, 15×15 20×20, and 30×30 $cm^2$. The main Compton current source is the collecting electrode of the PEEC. The connecting cable acts as a secondary Compton current source that produces a very small current which depends on the field size and the photon beam, becoming the dominant source when the PEEC is placed at depths greater than $z_{max}$.

The COMPTON/EGSnrc user code which was developed as a modification to the standard NRC DOSRZnrc/EGSnrc user code was introduced in this chapter. The main feature of this code is monitoring the charge entering into, and exiting from, a particular region of interest in the radiation beam simulation, in addition to the absorbed dose in all regions. Satisfactory results showing the variation of the Compton current with chamber depth in the phantom were obtained with the PEEC in a 10×10 $cm^2$ field 6 MV x-ray beam as well as 10×10 $cm^2$ fields 9 MeV and 12 MeV electron beams. The MC-calculated polarity correction factors $P_{pol}$ were different from the measured values for the PEEC, and this has to be investigated further.

The COMPTON/EGSnrc code in its current state is not as user friendly as the standard NRC user codes. We suggest that the additional scored quantities should be written into the **.egsdat* as is the case with the standard user codes and to modify the code accordingly, so that the simulations may be restarted easily. Additional modifications would be required also if the "parallel" option for easily combining the results of simulations processed in a computer cluster, thus allowing the user to simulate more particles without considerably increasing the calculation times.

# REFERENCES


1. B. J. Gerbi and F. M. Khan, "The polarity effect for commercially available plane-parallel ionization chambers," Med. Phys. **14**, 210-215 (1987).
2. A. Nisbet and D. I. Thwaites, "Polarity and ion recombination correction factors for ionization chambers employed in electron beam dosimetry," Phys. Med. Biol. **43**, 435-443 (1998).
3. J. M. Havercroft and S. C. Klevenhagen, "Polarity effect of plane-parallel ionization chambers in electron radiation," Phys. Med. Biol. **39**, 299-304 (1994).
4. C. R. Ramsey, K. M. Spencer, and A. L. Oliver, "Ionization chamber, electrometer, linear accelerator, field size, and energy dependence of the polarity effect in electron dosimetry," Med. Phys. **26**, 214-219 (1999).
5. J. A. Williams and S. K. Agarwal, "Energy-dependent polarity correction factors for four commercial ionization chambers used in electron dosimetry," Med. Phys. **24**, 785-790 (1997).
6. J. W. Boag, "Distortion of the electric field in an ionization chamber due to a difference in potential between guard ring and collector," Phys. Med. Biol. **9**, 25-32 (1964).
7. J. W. Boag, "Space charge distortion of the electric field in a plane-parallel ionization chamber," Phys. Med. Biol. **8**, 461-467 (1963).
8. L. A. W. Kemp and B. Barber, "the construction and use of a guarded-field cavity ionization chamber for the measurement of supervoltage radiation," Phys. Med. Biol. **3**, 149-160 (1963)
9. A. C. Lapsley, "Effect of space charge on saturation properties of ionization chambers," Rev. Sci. Instr. **24**, 602 (1953).
10. J. R. Greening, "A contribution to the theory of ionization chamber measurement at low pressures," Brit. J. Radiol. **27**, 163-170 (1954).
11. C. W. Wilson, "Observation of the ionization produced by radium gamma rays in air-walled ionization chambers at low gas pressures," Brit. J. Radiol. **27**, 159-162 (1954).
12. H. E. Johns, N. Aspin, and R. G. Baker, Radiat. Res. **9**, 573 (1958).
13. J. Van Dyk and J. C. F. MacDonald, "Penetration of high energy electrons in water," Phys. Med. Biol. **17**, 52-55 (1972).
14. N. D. Kessaris, "Penetration of high energy electrons in water," Phys. Rev. **145**, 164-174 (1966).
15. I. Kawrakow and D. W. O. Rogers, "The EGSnrc Code System: Monte Carlo simulations of electron and photon transport," Technical Report PIRS-701, National Research Council of Canada, Ottawa, Canada (2000).
16. B. R. B. Walters, I. Kawrakow, and D. W. O. Rogers, "History by history statistical estimators in the BEAM code system," Med. Phys. **29**, 2745-2752 (2002).
17. International Atomic Energy Agency, Absorbed Dose Determination in External Beam Radiotherapy based on Absorbed-Dose-to-Water Standards: An international code of practice (IAEA Technical Reports Series No. 398, Vienna, 2000).
18. K. E. Sixel, "Measurements and Monte Carlo simulations of x-ray beams in radiosurgery," Ph.D. Thesis, McGill University, 1993.
19. P. R. Almond, P. J. Biggs, B. M. Coursey, W. F. Hanson, M. Saiful Huq, R. Nath, and D. W. O. Roger, "AAPM's TG-51 protocol for clinical reference dosimetry of high- energy photon and electron beams," Med. Phys. **26**, 1847-1870. (1999).

20. AAPM Task Group 21 of the Radiation Therapy Committee, "A protocol for the determination of the absorbed dose from high-energy photon and electron beam," Med. Phys. **10**, 741-771 (1983).

21. Task Group 25 American Association of Physicists in Medicine, "Clinical electron beam dosimetry," Med. Phys. **18**, 73.109 (1991).

22. C. Zankowski, "Calibration of photon and electron beams with an extrapolation chamber," Ph.D. Thesis, McGill University, 1997.

# Chapter 6

# SURFACE DOSE FOR 6 MV AND 18 MV X-RAY BEAMS

## 6.1. INTRODUCTION

Monte Carlo (MC) calculations have been used in studies of numerous radiation dosimetry problems and in many instances served as the "gold" standard for validation of radiation dosimetric measurements. This is evident from radiation dosimetry protocols, such as the AAPM TG-21 (ref. 1), the AAPM TG-25 (ref. 2), the AAPM TG-51 (ref. 3), and the IAEA TRS-398 (ref. 4), all extensively using databases[5-10] obtained through MC calculations. Several recent papers[11-13], however, have reported a significant discrepancy between MC calculations and measurements in the dose build-up region in water for high-energy photon beams and large field sizes. In these papers the MC calculations predicted percentage depth doses (*PDD*) that were appreciably lower than those obtained with measurements.

Hartmann-Siantar *et al.*[13], in commissioning the PEREGRINE MC dose calculation system (NOMOS Corporation, Cranberry Township, PA), hypothesized that the discrepancy was caused by electrons that originate in the accelerator head and are not fully accounted for in the treatment head simulation. They inserted into the PEREGRINE system a hypothetical electron source to increase the calculated dose in the dose build-up region so that it matches the measurements. They also reported that the *PDD*s calculated with the PEREGRINE system in the dose build-up region without the hypothetical electron source matched calculations carried out in the dose build-up region with the BEAM/EGS4 (ref. 14) and DOSXYZ/EGS4 (ref. 14) user codes that are based on the EGS4 MC system[15] confirming that all commercial MC systems exhibit similar discrepancies with measured results.

After the recent release of the EGSnrc MC system code[16], Ding[12] showed that *PDD*s calculated for high-energy photon beams in water with the DOSXYZ/EGS4 (ref. 14) and the DOSRZnrc/EGSnrc[17] agreed with one another; however, both gave significantly

lower results than those obtained through measurements. In order to test the hypothesis put forward by Hartmann-Siantar, Ding[11] compared the calculations with measurements of a treatment head producing a high energy photon beam with a lead attenuator foil placed between the linac head and the water phantom. Since the discrepancy between the MC calculations and measurements in the dose build-up region was still present, Ding[11,12] concluded that this discrepancy cannot be explained by the hypothesis suggested by Hartmann-Siantar[13] and then suggested that contaminating neutrons existing in the beam emerging from a linac head generating high energy photon beams might be responsible for the observed discrepancy between MC calculations and measurements in the dose build-up region. Subsequently, Ding *et al.*[18] refuted this hypothesis by measuring the neutron dose in water with a neutron dosimeter establishing that the measured dose in the build-up region does not contain a significant neutron component. All treatment head modeling in the studies by Ding and Hartmann-Siantar were carried out with the BEAM/EGS4 user code.

In this chapter, MC-calculated doses in the build-up region from a 6 MV and 18 MV x-ray beam are compared to measurements. The accelerator modeling is carried out with the newly released BEAMnrc/EGSnrc user code. During this work, a coding "bug" in the EGSnrc MC system code that considerably affected our calculations for 18 MV beams was found and reported to the NRC group (National Research Council, Canada). This coding "bug" and its effects on our initial calculations are also reported and described in the chapter. Furthermore, since the MC system codes are sensitive to the cross sections for the various interactions of the transported particles in the medium, we also present a comparison of the calculated doses in the medium, especially in the dose build-up region, based on two *photon cross section databases*, namely: (*i*) Storm and Israel[19] (SI) available with the EGSnrc system code and (*ii*) XCOM database compiled by Berger, Hubbell, and Seltzer[20].

## 6.2. BACKGROUND

A variety of dosimeters for determining the dose at a point-of-interest in general and in biological materials in particular exists today. In radiotherapy clinics, cavity ionization chambers are by far the most widely used dosimeters for absolute as well as for relative

dosimetry. Chapter 3 presented a comprehensive discussion of the procedures involved in absolute dosimetry with cavity ionization chambers and based on that discussion the general expression for relative dosimetric techniques with cavity ionization chambers can be given by the following relationship

$$\frac{D_{\text{med}}(Q)}{D_{\text{med}}(P_{\text{ref}})} = \frac{\left[ Q_{\text{sat}} \cdot \left( \frac{\bar{L}_{\Delta}}{\rho} \right)_{\text{air}}^{\text{med}} P_{\text{fl}} P_{\text{wall}} P_{\text{cel}} \right]_{Q}}{\left[ Q_{\text{sat}} \cdot \left( \frac{\bar{L}_{\Delta}}{\rho} \right)_{\text{air}}^{\text{med}} P_{\text{fl}} P_{\text{wall}} P_{\text{cel}} \right]_{P_{\text{ref}}}}, \tag{6.1}$$

where $D_{\text{med}}(Q)$ and $D_{\text{med}}(P_{\text{ref}})$ are the doses in the medium at the point-of-interest $Q$ and at the reference point $P_{\text{ref}}$, respectively. $P_{\text{ref}}$ is usually the point at the depth of maximum dose ($z_{\max}$) along the beam central axis. In most situations, the mean restricted stopping power ratio $(\bar{L}_{\Delta}/\rho)_{\text{air}}^{\text{med}}$ as well as the perturbation factors $P_{\text{fl}}$, $P_{\text{wall}}$, and $P_{\text{cel}}$ do not change between points $Q$ and $P_{\text{ref}}$. As a result, the ratio $D_{\text{med}}(Q)/D_{\text{med}}(P_{\text{ref}})$ is simply the ratio of the gas ionizations ($Q_{\text{sat}}$) at point $Q$ to that at point $P_{\text{ref}}$, considerably simplifying the measurement procedure and the data analysis for these situations.

However, obtaining the percentage depth dose (*PDD*) in the medium in the dose build-up region of high energy photon beams using a cavity ionization chamber is one of the situations where the mean restricted stopping power ratio $(\bar{L}_{\Delta}/\rho)_{\text{air}}^{\text{med}}$ as well as the perturbation factors $P_{\text{fl}}$, $P_{\text{wall}}$, and $P_{\text{cel}}$ must be evaluated separately for points $Q$ and $P_{\text{ref}}$, since they in general may differ at the two points. If the $P_{\text{ref}}$ is the point at $z_{\max}$ and $Q$ is a point along the beam central axis at depth $z$ where $0 \le z \le z_{\max}$ in the phantom at a source-surface distance (*SSD*) of $f$ and field size $A$ at the phantom surface, the left-hand side of Eq. (6.1) is by definition the $PDD(z, A, f, hv)/100$. It is convenient to express the right-hand side of Eq. (6.1) in this situation as the product of three quantities as follows

$$PDD(z,A,f,hv) = PDI(z,A,f,hv) \times RSPR(z,A,f,hv) \times C(z,A,f,hv), \tag{6.2}$$

where $PDI(z,A,f,hv)$, $RSPR(z,A,f,hv)$, and $C(z,A,f,hv)$ are, respectively, *the ratios of the air-cavity ionizations* $Q_{\text{sat}}$, expressed as a percentage; *the mean restricted collision stopping power ratios medium to air* $(\bar{L}_{\Delta}/\rho)_{\text{air}}^{\text{med}}$; and *the combined perturbation factors* $P_{\text{fl}}P_{\text{wall}}P_{\text{cel}}$ at depth $z$ to that at $z_{\max}$.

Measurements in the dose build-up region are usually carried out with parallel-plate ionization chambers or extrapolation chambers, resulting in simplifications to Eq. (6.1). The central electrode perturbation correction factor $P_{cel}$, for example, is applicable only for cylindrical cavity ionization chambers when the material of the central electrode is different from that of the wall. Moreover, because of their thin electrodes, the wall perturbation correction factor $P_{wall}$ for these instruments is small and the correction factor $C$ in Eq. (6.2) is thus dominated by the ratio of the fluence perturbation factors $P_{fl}$ at the two depths $z$ and $z_{max}$.

The electronic fluence perturbation causes ionization chambers to exhibit an "over-response" for measurements carried out in the dose build-up region as well as in all transition zones between two different media. An "over-response" means in this context that the measured *PDI* is larger than the actual *PDD*. The "over-response" in ionization chambers was discussed by Nilsson[21] pointing out that the lack of electronic equilibrium results in a perturbation of the electron fluence in the air-sensitive volume of the cavity ionization chamber.

In FIG. 6.1 we show a schematic representation of a small air cavity embedded in medium near the surface and irradiated by a clinical photon beam. The figure also shows tracks of some particular electrons of interest that ionize the air volume. Electrons of category (a) are the contaminating electrons that are produced in the treatment head as well as in the air between the treatment head and the phantom surface and are the main contributors to the air ionization; electron categories (b), (c), (d), and (e) are secondary electrons produced by various photon interactions in the thin medium layer above the air cavity, in the air cavity itself, in the medium layers below the air cavity, and in the side walls of the air cavity, respectively; and electrons (f) are contaminating electrons scattered into the chamber from the side walls of the air cavity. The fluence perturbation in the air cavity volume is mainly caused by electrons of types (e) and (f). These two electron categories are not equilibrated by an equal number of electrons created within the air cavity and scattered into the side walls. Hence, the cavity presence introduces non-equilibrium in the laterally scattered electrons adding to the lack of electronic equilibrium in the vertical direction that exists near the phantom surface.

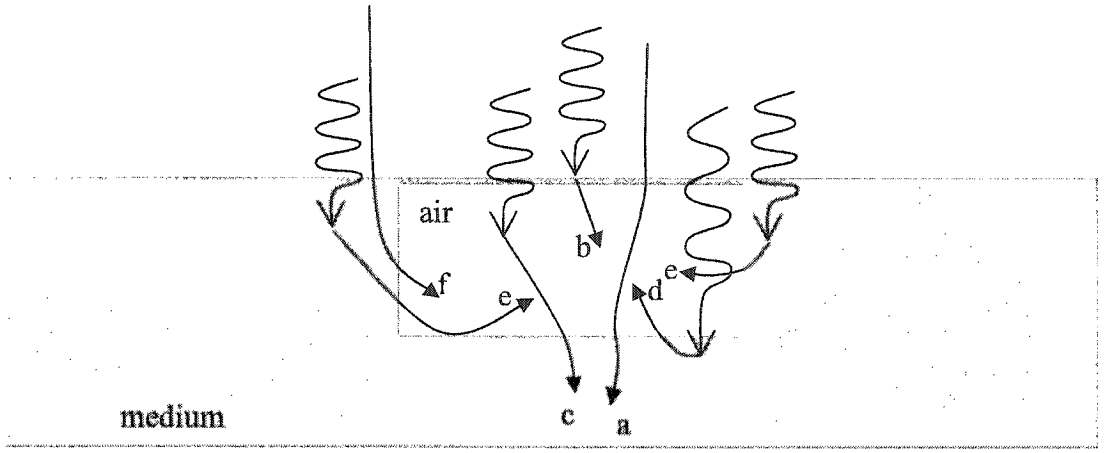


*FIG. 6.1. A number of particular electron categories that contribute to the ionization in an air-cavity volume in high energy clinical photon beams. Electrons (a) are contaminating electrons crossing directly the cavity; electrons (b), (c), (d), and (e) are secondary electrons produced by various photon interactions in the thin layer above the air cavity, in the air cavity itself, in the medium below the air cavity, and in the side walls of the air cavity, respectively; electrons (f) are contaminating electrons scattered from the side walls of the air cavity into the air cavity.*

When located at depths beyond $z_{max}$ in the medium, the fluence perturbation is also present in air cavities but it is small in magnitude and can be ignored in well-guarded parallel-plate ionization chambers and extrapolation chambers, such as our PEEC. For cylindrical and some commercial parallel-plate ionization chambers where fluence perturbations cannot be neglected, the fluence perturbation correction factor $P_{fl}$ is well established at calibration depths (usually at $z = 5$ cm or 10 cm) for numerous cavity ionization chambers used for calibrating high-energy photon beams. Its value can be found in calibration protocols, such as the AAPM TG-21 (ref. 1), the AAPM TG-51 (ref. 3) and the IAEA TRS-398 (ref. 4). Moreover, the well-established values of $P_{fl}$ can be used in absolute dosimetry at depths beyond $z_{max}$ along the beam central axis without considerably affecting the accuracy of the dose measurements. In the dose build-up region, however, the presence of contaminating electrons in clinical photon beams requires in absolute dosimetry with cavity ionization chambers the use of $P_{fl}$s that are very different from those established for depths beyond $z_{max}$ and must be evaluated at the particular measurement depth as well as for the particular linac treatment head. Moreover, because of the significant difference of the $P_{fl}$ for depths in the dose build-up region from that valid at $z_{max}$, the fluence perturbation factors are essential for accurate

relative dosimetry in the dose build-up region, *i.e.*, for measuring the *PDD* in medium with cavity ionization chambers.

A number of references[11-13,18,21-25] in the literature deal with obtaining the *PDD* in the dose build-up region using cavity ionization chambers and extrapolation chambers. These references can be divided into two categories depending on which of the two correction factors of Eq. (6.2) (the *RSPR* or the correction factor *C*) is applied to the measured *PDI*. In their work, Ding[11,12,18] and Hartmann-Siantar[13] assumed that the *RSPR*s are sufficient to convert the *PDI* to the *PDD* in the medium and determined them with MC techniques. The work of Nilsson[21], Velkley[22], Tannous[23], Gerbi[24], and Mellenberg[25], on the other hand, represents an experimental technique whereby the *PDD* in the medium is obtained with an extrapolation chamber. The procedure with extrapolation chambers involves plotting the *PDI* value at a given depth versus the electrode separation *s* and extrapolating the data to zero electrode thickness in order to obtain the *PDD*. We will refer to this extrapolated value by "the zero-volume *PDI*". The correction factor *C* of the zero-volume *PDI* is assumed to be 1.0, hence, the *PDD* in the medium and the zero-volume *PDI* are equal.

In the work of Velkley *et al.*[22], the *PDI*s of their extrapolation chamber were linearly extrapolated to obtain the *PDD* in the build-up region for various clinical photon beams ranging in energy from cobalt-60 to 25 MV and for various field sizes and *SSD*s. Moreover, they derived an empirical correction method that can be used to calculate the *PDD* from the *PDI* measurements with a fixed volume parallel-plate ionization chamber. The empirical relationship is

$$PDD(z, A, f, hv) = PDI(z, A, f, hv) - \xi(hv, z / z_{\max}) \times s, \tag{6.3}$$

where $\xi$ is the slope of the extrapolated curve per millimeter electrode separation *s* as a function of beam energy and the fraction of the depth of maximum dose as given in FIG. 6.2. It was also stated[22] that a functional correlation between $\xi$ and the *SSD* and field size could not be derived from the measured data; nonetheless, the correction $\xi$ for the various *SSD*s and field sizes was within ±15% of the values shown in FIG. 6.2.

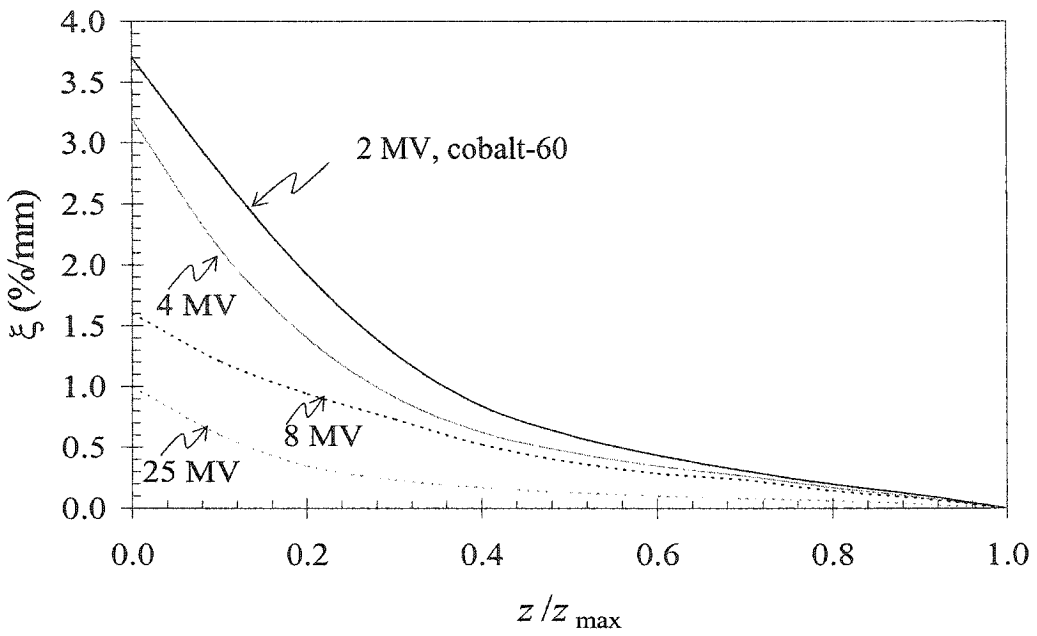


*FIG. 6.2. The correction factor $\xi$ in %/mm electrode separation for converting the PDI at depth z measured with a fixed-volume parallel-plate ionization chamber to the PDD in medium. (Velkley et al.[22])*

In FIG. 6.2 the correction $\xi$ is largest on the phantom surface and decreases with increasing beam energy and increasing depth $z$ until at $z_{max}$ it becomes zero. For a given depth, $\xi$ decreases with beam energy. As the beam energy increases, secondary electrons produced by Compton scattering from the sidewalls of the chamber are less likely to reach and ionize the sensitive-air volume of the ionization chamber, since the scattering of electrons is more forward directed at higher beam energies.

For extrapolation chambers, Nilsson[21] later argued that the relationship between the *PDI* at a given depth in the dose build-up region versus the electrode separation $s$ is only linear for plate separations larger than 2 mm for cobalt-60 beams and 3 mm for higher beam energies. In the nonlinear part of the curve, the slope of the curves increased with increasing electrode separation $s$. The nonlinearity of the *PDI* versus $s$ relationship at small electrode separations $s$ was also attributed to the forward directed scattering of secondary electrons from the sidewalls of the extrapolation chamber, and at very small electrode separations most of these electrons do not reach the sensitive-air volume.

Gerbi[24] showed that the Velkley method given in Eq. (6.3) has the following characteristics:(*i*) it under-estimates the magnitudes of the correction factors required for fixed volume parallel-plate ionization chambers having a sidewall-to-collector edge distance less than 5 mm; (*ii*) it over-corrects for chambers with sidewall-to-collector edge distance greater than 11 mm; and (*iii*) it is accurate to within 2% for chambers whose sidewall-to-collector edge distance is between 5 mm and 11 mm for $s$ = 2 mm to 2.5 mm.

Apart from methods to extrapolate the data, it is logical to multiply the zero-volume *PDI*s by an appropriate *RSPR* evaluated for an extremely small $\Delta$ corresponding to a zero electrode separation to get the *PDD* in medium, since the Spencer-Attix cavity theory requires the $(\bar{L}_\Delta / \rho)^{med}_{air}$ to convert the cavity dose to dose in medium. Generally, the formula of the restricted stopping power $(L_\Delta / \rho)$ given in the ICRU Report 37 (ref. 26) in Section 7 is not recommended for $\Delta$ below 1 keV, and Velkley[22] and Nilsson[21] neither applied the *RSPR* to their measurements nor did they discuss the error resulting from omitting this conversion factor.

## 6.3. EQUIPMENT AND EXPERIMENTAL TECHNIQUES

We measured depth ionization curves in water with the Roos ionization chamber and in Solid Water™ with the PEEC for 6 and 18 MV pulsed photon beams generated by a clinical linear accelerator (Clinac 2300 C/D; Varian, Palo Alto, CA), as discussed in Section 5.3. For both ionization chambers, the dosimetric signals were obtained from an analysis of the saturation curves at the particular depth, whereby the linear portion of the $1/I$ versus $1/V$ curve was extrapolated to $V \rightarrow \infty$, with $V$ the magnitude of the polarizing voltage, and the extrapolated value $1/I_{sat}$ gave the reciprocal of the dosimetric signal used in our analysis.

A Wellhöfer water scanner (WP-700; Scanditronix, Schwarzenbruck, Germany) with a Wellhöfer IC-10 cylindrical ionization chamber having an air-sensitive volume of 0.12 $cm^3$ was also used for measuring depth ionization curves for the 10×10 $cm^2$ and 30×30 $cm^2$ fields covering depths from the surface to z = 20 cm and beam profiles in water extending a few centimeters beyond the penumbra of the fields. The scanning

system has a position resolution of 1 mm with an accuracy of ≤ 0.5 mm and a reproducibility of ≤ 0.2 mm for scanning.

Following recommendations of the AAPM TG-51 protocol[3] and the IAEA TRS-398 code of practice[4], the effective point of measurement for the IC-10 chamber was taken at 1.8 mm upstream of the chamber center. For the parallel-plate chambers (the Roos and the Attix) as well as for the PEEC, the effective point of measurement was taken to be the point just below the top polarizing electrode. All measurements were carried out in the standard *SSD* setup with an *SSD* of 100 cm. The dosimetric signal with the chambers was determined as the average between the positive and negative polarity readings.

The EGSnrc MC system code was used for our MC calculations. The BEAMnrc/EGSnrc user code was used for modeling the treatment heads and to generate phase-space files at an *SSD* of 100 cm. About 15 million particles were accumulated in the phase-space files for the 10×10 $cm^2$ open fields for the 6 MV and 18 MV beams, and for the 30×30 $cm^2$ the number of particles in the phase-space files was about 50 million for both photon beams. The standard DOSRZnrc/EGSnrc and DOSXYZnrc/EGSnrc user codes were used for calculating the absorbed dose and the *PDD*s in water and in Solid Water™ as well as the *PDI* in Solid Water™ for the PEEC using the phase-space files as input sources.

The EGSnrc options and settings used in the BEAMnrc/EGSnrc user code to generate the phase-space files as well as in the DOSRZnrc/EGSnrc and DOSXYZnrc/EGSnrc user codes to calculate the dose were as follows: ECUT = 0.521 MeV; PCUT = 0.010 MeV; Rayleigh scattering OFF; boundary crossing algorithm EXACT; electron-step algorithm PRESTA-II; bound Compton scattering, photoelectron angular sampling, atomic relaxations, and spin effects ON; and pair angular sampling as well as the bremsstrahlung angular sampling KM (Koch and Motz[27]).

To increase the efficiency of our BEAMnrc/EGSnrc user code simulations, a variance reduction technique called uniform bremsstrahlung splitting was used producing 20 bremsstrahlung photons for each bremsstrahlung event. The Russian roulette option was also turned on. A detailed review of all EGSnrc options can be found at the following URL address:

http://www.irs.inms.nrc.ca/inms/irs/EGSnrc/EGSnrc.html

Thermoluminesent dosimetry (TLD) techniques were used for detecting the effect of neutrons that may contaminate the 18 MV x rays on the *PDD* in the dose build-up region. Two types of 3.2×3.2×0.15 $mm^3$ TLD chips were used: TLD-600 (Harshaw Chemical Company, Solon, Ohio) and TLD-700 (Harshaw Chemical Company, Solon, Ohio). In our work related to detecting the effects of contaminating neutrons in 18 MV x-ray beams on the *PDD*, the measurement of dose with the TLD-600 contained the mixed gamma and neutron dose components. The neutron dose component can be extracted from a cross measurement of the gamma component only using the TLD-700.

The reproducibility of individual TLDs was verified using the 10×10 $cm^2$ 6 MV x-ray beam. The reproducibility verification procedure was as follows: (*i*) the TLDs were placed at $z_{max}$ in a Solid Water™ phantom at an *SSD* of 100 cm; (*ii*) the phantom was exposed to 100 Monitor Units (MU) irradiation; (*iii*) the TLDs signals were read with a TLD reader (model 3500; Harshaw Chemical Company, Solon, OH); and (*iv*) the TLDs were annealed in an oven for 1 hour at 400 °C and 2 hours at 100 °C before the next irradiation. The above experiment was repeated 6 times for both TLD types (TLD-700 and TLD-600). Only the individual TLDs having a standard deviation less that 1.5% of the mean readings were selected for neutron detection in the 10×10 $cm^2$ 18 MV x-ray beam. The linearity of the TLDs signal with dose was verified by our colleagues in the department and their experiments showed that the response of the TLDs was linear with dose up to 100 cGy.

## 6.4. RESULTS AND DISCUSSION

### 6.4.1. 6 MV x-ray beam

#### *Beam optimization*

The *PDI*s in water for depths between the surface and $z$ = 20 cm for the 10×10 $cm^2$ and 30×30 $cm^2$ fields 6 MV x-ray beam as well as the *OAR*s in water at depths of 1.5 cm ($z_{max}$) and 10 cm for both fields were obtained using the IC-10 cylindrical chamber. Also, the *PDI* in water from $z$ = 0.1 cm to $z$ = 5.0 cm was measured with the Roos parallel-plate

ionization chamber for the 10×10 $cm^2$ field 6 MV x-ray beam. The positional uncertainties are taken as ±0.5 mm and ±0.1 mm for the IC-10 and the Roos chamber measurements, respectively. The uncertainties in the *PDI* value due to polarity effects as well as ionic recombination are very small and the combined error resulting from both effects was estimated to produce a relative error on the *PDI* value of less than 0.5%.

For the MC calculations, the treatment head of the 6 MV beam was modeled with the BEAMnrc/EGSnrc user code based on the specifications provided by the manufacturer. The electron source as well as the initial kinetic energy of the incident electrons was optimized such that the MC-calculated *PDD* curves in water and the *OAR*s in water obtained with the DOSXYZnrc/EGSnrc and the DOSRZnrc/EGSnrc user codes match, respectively, the measured *PDI* curves in water for depths larger than $z_{max}$ and the measured *OAR*s. The initial electron beam was assumed to be a monoenergetic electron pencil beam of 0.1 cm radius striking the x-ray target and the initial kinetic energy of the electron beam was 6.0 MeV.

In FIGs. 6.3 and 6.4 we show the MC calculations with DOSXYZnrc/EGSnrc in water as well as the IC-10 measurements in water for the 10×10 $cm^2$and 30×30 $cm^2$ fields. The 3-D MC calculation matrix consists of 59×59×59 XYZ voxels with 0.5 cm and 0.7 cm $x$ and $y$ voxel thicknesses in calculations for the 10×10 $cm^2$ field and the 30×30 $cm^2$ field, respectively. The thickness of the $z$ dimension of the calculation voxels varies with depth (about 0.001 cm near the surface, 0.1 cm around $z_{max}$, and larger thicknesses at greater depths). The $z$-coordinate of a voxel is taken as the vertical distance between the surface and the center of the voxel. The $x$ and $y$ coordinates of the voxel are, respectively, the $x$ and $y$ off-axis distances from the beam central axis. The calculated *OAR*s at $z_{max}$ and 10 cm in FIGs. 6.3(a) and 6.4(a) differ from the measurements by less than 1% for the 10×10 $cm^2$ field and less than 2% for the 30×30 $cm^2$ field. The difference between the *PDI*s and the calculated *PDD* in water shown in FIGs. 6.3(b) and 6.4(b) for depths larger that $z_{max}$ is less than 1%.

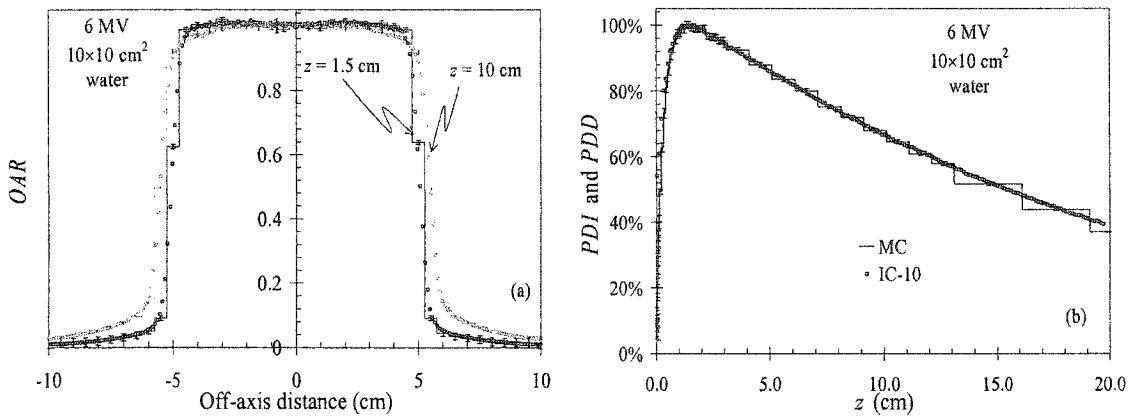


*FIG. 6.3. Measured data in water with the IC-10 cylindrical ionization chamber (data points) and MC calculations in water with the DOSXYZnrc/EGSnrc user code (histograms) for the 10×10 cm² field 6 MV x-ray beam. (a) The OARs at depths $z_{max}$ and 10 cm. (b) The measured PDI and the MC-calculated PDD. z is the depth from the phantom surface to the effective point of measurement of the IC-10 ionization chamber.*

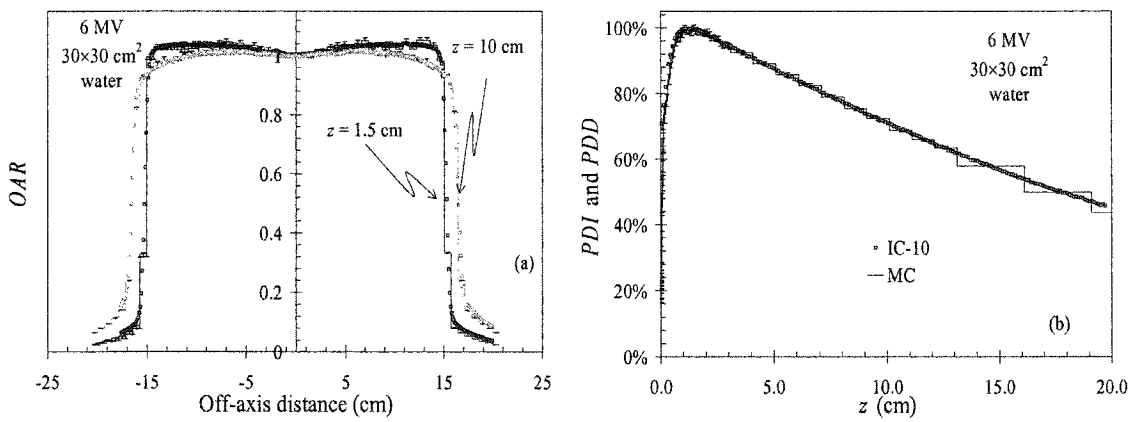


*FIG. 6.4. Measured data in water with the IC-10 cylindrical ionization chamber (data points) and MC calculations in water with the DOSXYZnrc/EGSnrc user code (histograms) for the 30×30 cm² field 6 MV x-ray beam. (a) The OARs at depths $z_{max}$ and 10 cm. (b) The measured PDI and the MC-calculated PDD. z is the depth from the phantom surface to the central transverse plane of the cylindrical voxel in the DOSRZnrc/EGSnrc user code and the effective point of measurement of the PEEC ionization chamber.*

In FIG. 6.5, we plot the data of FIGs. 6.3(b) and 6.4(b) in the dose build-up region, clearly showing a large difference between the MC-calculated *PDD*s and the measured *PDI*s. For the 10×10 cm² field, the *PDI* obtained with the Roos parallel-plate ionization chamber is also included in FIG. 6.5(a). The *PDI*s of the Roos parallel-plate ionization

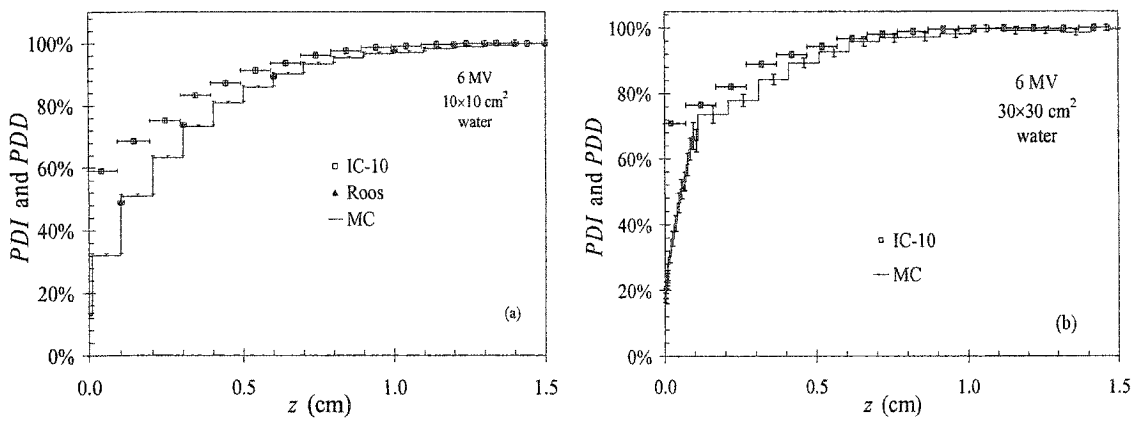


*FIG. 6.5. The PDI in water and the MC-calculated PDD in water in the dose build-up region for the 10×10 cm² and the 30×30 cm² fields 6 MV x-ray beam. (a) The PDIs from the measurement with the IC-10 cylindrical chamber as well as the Roos parallel-plate chamber (data points) and the MC-calculated PDD with DOSXYZnrc/EGSnrc user code (histogram) for the 10×10 cm² field 6 MV x-ray beam. (b) The PDI measured with the IC-10 cylindrical chamber (data points) and the MC-calculated PDD with the DOSXYZnrc/EGSnrc user code (histogram) for the 30×30 cm² field 6 MV x-ray beam. The IC-10 PDIs and the PDDs calculated with MC techniques are taken from FIGs. 6.3(b) and 6.4(b). z is the depth from the phantom surface to the central transverse plane of the cylindrical voxel in the DOSRZnrc/EGSnrc user code and the effective point of measurement of the PEEC ionization chamber.*

chamber and the IC-10 cylindrical ionization chamber from $z_{max}$ to z = 5 cm [not shown in FIG. 6.5(a)] agree with one another but in the dose build-up region the *PDI*s differ and are higher than the MC-calculated *PDD*s.

*PDI*s were also measured in Solid Water™ for depths from the surface ($z \approx 50$ μm) to $z = 20$ cm for the 10×10 cm² and 30×30 cm² fields 6 MV x-ray beam using our PEEC with the aluminized Mylar/Delrin wall front electrode fixed to the chamber. The electrode separation $s$ of the PEEC was maintained at 2 mm, and the PEEC was essentially used as a fixed-volume parallel-plate ionization chamber in these measurements. Using the optimized phase-space files as sources, the *PDD* was calculated in Solid Water™ for the 10×10 cm² and the 30×30 cm² 6 MV x-ray beams using the DOSRZnrc/EGSnrc user code. The RZ calculation voxels in the calculations with the DOSRZnrc/EGSnrc user code represents a 70 cm thick and 30 cm radius Solid Water™ phantom. The *PDD* is calculated for the scored doses in cylindrical voxels with a radius of 0.5 cm along the beam central axis with thicknesses $z$ varying with depth similarly to

the situation with the DOSXYZnrc/EGSnrc user code. Note that the z-coordinate of a particular voxel was taken as the vertical distance from the phantom surface to the central-transverse plane of the cylindrical voxel.

A comparison between the *PDI*s obtained with the PEEC and the MC-calculated *PDD*s in Solid Water™ is shown in FIGs. 6.6 and 6.7 for the 10×10 $cm^2$ and the 30×30 $cm^2$ fields 6 MV x-ray beam, respectively. Although, the agreement between the PEEC *PDI* and the MC-calculated *PDD* in Solid Water™ in the dose build-up region is, in general, improved compared to that of the *PDI* in water for the IC-10 as well as the Roos ionization chambers and the MC-calculated *PDD* in water; an appreciable difference is noticed at the surface for both fields. The numerical values of the PEEC *PDI*s and the MC-calculated *PDD*s in Solid Water™ at the surface are given in TABLE. 6.1.

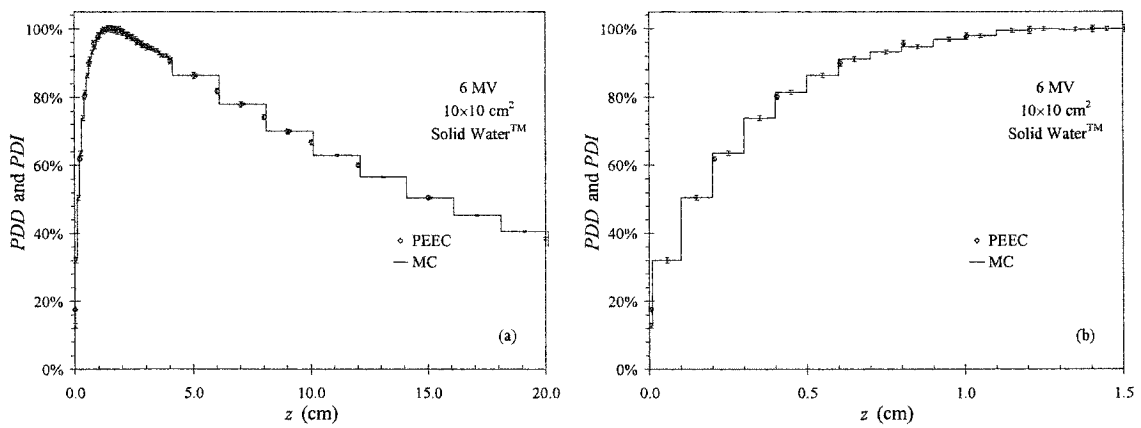


*FIG. 6.6. Measured PDI in Solid Water™ with the PEEC (data points) and the MC-calculated PDD in Solid Water™ with the DOSRZnrc/EGSnrc user code (histogram) for the 10×10 $cm^2$ field 6 MV x-ray beam. (a) Comparison for depths between the surface and 20 cm. (b) Comparison in the dose build-up region. The PDI data are for the PEEC with the aluminized Mylar/Delrin wall front electrode. z is the depth from the phantom surface to the central transverse plane of the cylindrical voxel in the DOSRZnrc/EGSnrc user code and the effective point of measurement of the PEEC ionization chamber.*

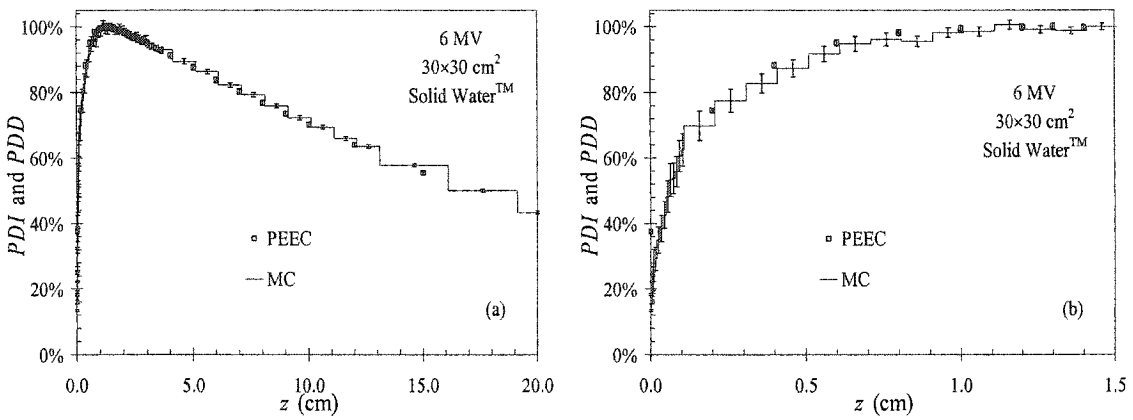


*FIG. 6.7. Measured PDI in Solid Water™ with the PEEC (data points) and the MC-calculated PDD in Solid Water™ with the DOSRZnrc/EGSnrc user code (histogram) for the 30×30 cm² field 6 MV x-ray beam. (a) Comparison for depths between the surface and 20 cm. (b) Comparison in the dose build-up region. The PDI data are for the PEEC with the aluminized Mylar/Delrin wall front electrode. z is the depth from the phantom surface to the central transverse plane of the cylindrical voxel in the DOSRZnrc/EGSnrc user code and the effective point of measurement of the PEEC ionization chamber.*

TABLE. 6.1. COMPARISON OF THE *PDI*s OBTAINED WITH THE PEEC AND THE MC-CALCULATED *PDD*s IN SOLID WATER™ FOR 6 MV X-RAY BEAM AND FIELDS OF 10×10 cm² AND 30×30 cm².

| | 10×10 cm² | | 30×30 cm² | |
|---|---|---|---|---|
| depth | *PDI* (meas.) | *PDD* (calc.) | *PDI* (meas.) | *PDD* (calc.) |
| ≈ 50 μm | 17.5% ± 0.2% | 12.8% ± 0.7% | 37.6% ± 0.4% | 21.2% ± 3.4% |
| 2 mm | 61.9% ± 0.6% | 57.1% ± 0.6% | 74.5% ± 0.7% | 73.4% ± 3.5% |

Experiments in water and Solid Water™ show that the MC-calculated *PDD*s and the measured *PDI*s are not equal to one another in the dose build-up region. It is clear that if the optimized phase-space file for the 6 MV x-ray beam statistically represents the beam emerging from the treatments head, *i.e.*, the calculated *PDD*s are correct, the *PDI*s must be processed first before the *PDD*s in the dose build-up region can be determined experimentally.

### Correction of the PDI using the RSPR

The *RSPR*, given in Eq. (6.2), contains the ratio of the mean restricted mass stopping powers $(\bar{L}_\Delta / \rho)^{med}_{air}$. Since $(\bar{L}_\Delta / \rho)^{med}_{air}$ is relatively independent of the choice of Δ, a Δ of 10 keV was chosen to evaluate the $(\bar{L}_\Delta / \rho)^{med}_{air}$ and consequently the *RSPR*s. The mean restricted stopping power ratio $(\bar{L}_\Delta / \rho)^{med}_{air}$ for Δ of 10 keV in water and solid water as a function of depth $z$ along the beam central axis was calculated for the 10×10 cm$^2$ 6 MV x-ray beam using the SPRRZnrc/EGSnrc user code. The *RSPR* at depths of interest in the dose build-up region, shown in FIG. 6.8, was obtained by dividing the $(\bar{L}_\Delta / \rho)^{med}_{air}$ at the particular depth $z$ with the $(\bar{L}_\Delta / \rho)^{med}_{air}$ at $z_{max}$. Because of the long computational time required, this calculation was carried out only for the 10×10 cm$^2$ field and not for the 30×30 cm$^2$ field.

As expected, the calculations for the 10×10 cm$^2$ 6 MV x-ray beam showed that the *RSPR* for depths greater than $z_{max}$ is 1.0. Furthermore, for depths between 0.7 cm and $z_{max}$, the *RSPR* is also 1.0 and, hence, the *RSPR* can be ignored for when correcting the measured *PDI*s. At the surface, however, the *RSPR* has a value of 1.012 in water and 1.014 in Solid Water$^{TM}$, and then rapidly decreases with increasing $z$ to reach the value of 1.0 at 0.7 cm.

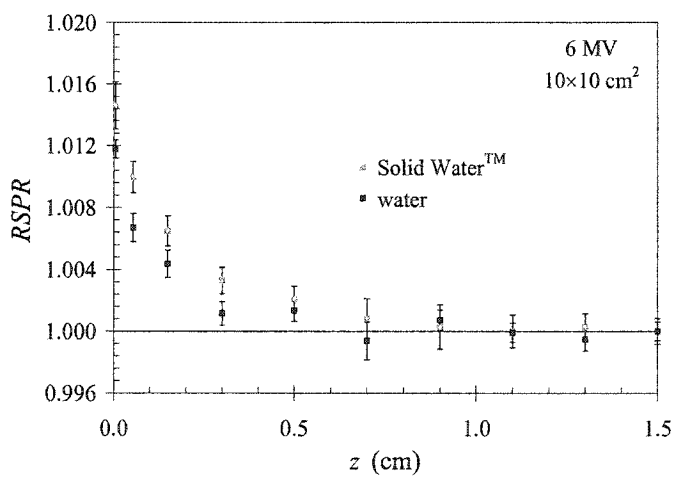


*FIG. 6.8. The RSPR as a function of depth z in water and Solid Water$^{TM}$ for the 10×10 cm$^2$ 6 MV x-ray beam. The data are calculated using the SPRRZnrc/EGSnrc user code.*

In FIG. 6.9 we show the restricted stopping power ratios water-to-air $(L_\Delta/\rho)^{water}_{air}$ and Solid Water$^{TM}$-to-air $(L_\Delta/\rho)^{SW}_{air}$ as a function of electron energy $E_K$ from 1 keV to 20 MeV for $\Delta$ of 1 keV, 10 keV, and 189 keV. The restricted stopping powers of water, Solid Water$^{TM}$, and air were obtained using the PEGS4 user code available with the EGSnrc MC system code (see Section 4.2.3). The $(L_\Delta/\rho)^{water}_{air}$ and $(L_\Delta/\rho)^{SW}_{air}$ are decreasing functions with $E_K$ with an average slope of –0.12 per MeV in the region 1 keV $< E_K <$ 0.4 MeV and an average slope of –0.013 per MeV in the region 0.4 MeV $< E_K <$ 20 MeV. Since the *RSPR*s as a function of depth $z$ in the dose build-up region are larger than 1.0, as shown in FIG. 6.8, we conclude that the mean energy of the electrons traversing the first few millimeters of the phantom is essentially smaller than the mean energy of the electrons that cross the layer at $z_{max}$. This energy diminution results from contaminating electrons and low energy scattered photons that are generated in the treatment head and mainly interact in the dose build-up region.

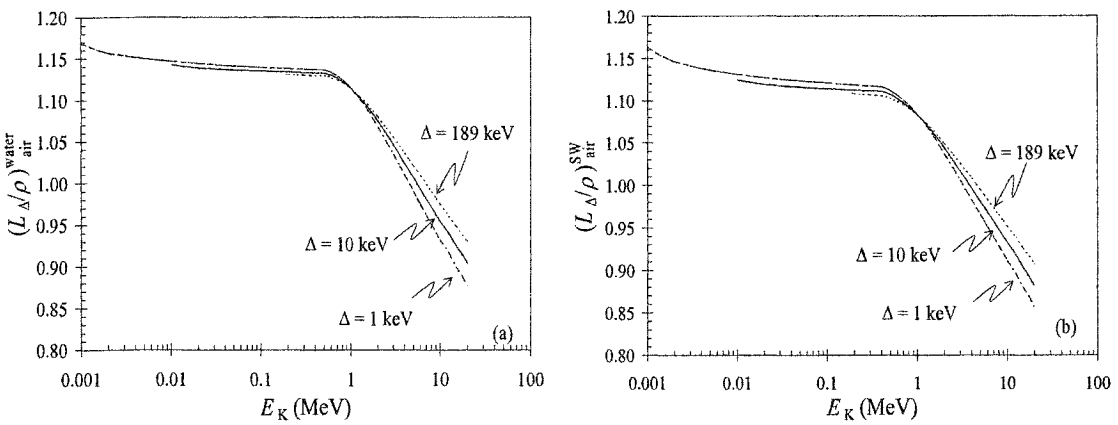


*FIG. 6.9. The restricted stopping power ratio medium-to-air $(L_\Delta/\rho)^{med}_{air}$ as a function of electron kinetic energy $E_K$ for $\Delta$ of 1 keV, 10 keV, and 189 keV calculated with the PEGS4 code. (a) water-to-air. (b) Solid Water$^{TM}$-to-air.*

As shown in FIG. 6.8, the *RSPR* correction factor is relatively small in the build-up region and equal unity for $z > z_{max}$. Thus, multiplying the *PDI* with the *RSPR* for depths in the dose build-up region only slightly affects the difference between the measurements and the calculated *PDD*s. We conclude that, if our MC-calculated *PDD*s are correct, correcting the measured *PDI* only with the *RSPR* does not give the correct *PDD*s in the medium for depths in the dose build-up region, especially, since the correction works in the wrong direction and actually enlarges the discrepancy between the corrected *PDI* and the calculated *PDD*.

### *Extrapolation of ionization density to zero-volume air cavity*

To examine the validity of the extrapolation method, the ionization density of the PEEC was measured for electrode separations between 1 mm and 11 mm at the surface ($z \approx 50$ μm) as well as at $z_{max}$ for the 10×10 cm$^2$ field 6 MV x-ray beam. The ionization density for all electrode separations was obtained from the linear extrapolation of the linear portion of the $1/I$ versus $1/V$ curve where $I$ is the collected current averaged from the positive and negative polarity signals and $V$ is the magnitude of the polarizing voltage. The results are shown in FIG. 6.10 with the ionization densities for all electrode separations normalized to unity at $s = 2$ mm.

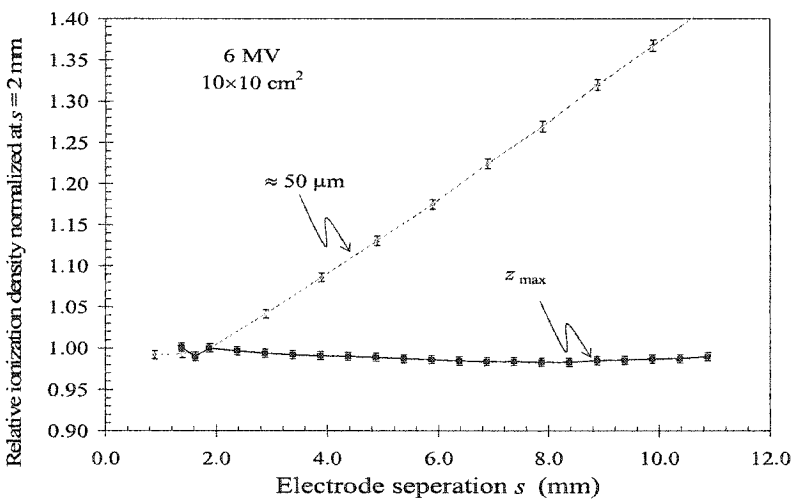


*FIG. 6.10. The relative ionization density for the PEEC as a function of electrode separation s at the surface ($z \approx 50$ μm) and $z_{max}$ for the 10×10 cm$^2$ 6 MV x-ray beam, normalized to 1.00 at $s = 2$ mm.*

Clearly, FIG. 6.10 shows that the ionization density at $z_{max}$ is independent of the electrode separation $s$, implying that the fluence perturbation of the PEEC at that depth (if it exists) is constant. At the surface, however, the influence of the cavity size on the ionization density is noticeable and the *PDI* measured at the phantom surface, consequently, is strongly dependent on $s$.

For measurements on the phantom surface, the relative ionization density for electrode separations larger than 2 mm increases linearly with the electrode separation, and is approximately constant for electrode separations smaller than 2 mm. Results by Nilsson[21] also showed a similar behavior of the relative ionization density at the surface for extrapolation chambers. Nilsson argued that the electronic fluence perturbations in extrapolation chambers should vanish below a threshold electrode separation. This threshold electrode separation will depend on the dimensions of the air-sensitive volume as well as on the width of the guard ring and Nilsson[21] recommended extrapolation of the relative ionization density using only data points for $s$ below that threshold.

We examined both extrapolation methods that were suggested by Velkley *et al.*[22] and Nilsson[21]. Firstly, we linearly extrapolated to zero electrode separation the measurement points of FIG. 6.10 using the data for electrode separations larger than 2 mm. The extrapolated relative ionization density for the surface measurements is 0.908±0.002, and multiplying the extrapolated value and the *PDI* at the surface for $s$ = 2 mm (17.5% ± 0.2%) gives a zero-volume *PDI* of 15.9% ± 0.2%. Secondly, for electrode separations smaller than 2 mm, we linearly extrapolated to zero electrode separation the measurement points of FIG. 6.10, resulting in a zero-volume *PDI* at the surface of 17.3% ± 0.2%, not considerably different from the *PDI* for 2 mm electrode separation. In both situations, the extrapolated zero-volume *PDI* at the surface is larger than the MC-calculated *PDD* (12.8% ± 0.7%) at the same depth. We speculated that the inhomogeneous components of the aluminized Mylar/Delrin wall front chamber window might have increased the surface dose considerably in comparison to that of a full Solid Water™ window and it became important to first validate that the phase-space files of the 6 MV x-ray beam statistically represent the beam emerging from the treatment head.

### *Verification of the MC-calculated PDDs*

Because neither the application of the *RSPR* correction factors nor the extrapolation method with the PEEC resulted in *PDD*s at the phantom surface in good agreement with the MC-calculated *PDD*s, we investigated our beam optimization for the MC calculations. Our hypothesis is that if MC-calculations with optimized beam parameters can predict the direct measurements of the PEEC at the surface and in the dose build-up region, *i.e.*, the *PDI*s, it is reasonable to assume that the MC-calculated *PDD*s are correct. After this step, it would then be interesting to investigate the perturbations caused by the aluminized Mylar/Delrin wall front window that were initially thought to be negligible and were ignored.

The MC-calculated *PDI*s of the PEEC were calculated with the DOSRZnrc/EGSnrc user code. The geometry used in our calculations essentially corresponded to the PEEC geometry with which the actual measurements were acquired, as shown in FIG. 5.15 in Chapter 5. Thus, perturbations caused by the particular design and materials of the PEEC geometry, *i.e.*, the front aluminized Mylar electrode and the Delrin side wall, were incorporated into the MC-calculations for this study, since the calculation geometry included the aluminized Mylar/Delrin wall front electrode. Because the mean ionization and excitation energy of air $\overline{W}_{air}/e$ (33.97 $J \cdot C^{-1}$ for dry air) is independent of the photon and electron beam energies, the scored dose in the region corresponding to the air-sensitive volume in the calculation geometry as a function of the Solid Water™ layer thickness above the aluminized Mylar electrode, as shown in FIG. 5.15, can be used to calculated the *PDI*s. The MC-calculated *PDI*s of the PEEC at depth $z$ are given by multiplying by 100 the ratio of the scored dose in the sensitive air-volume for a front Solid Water™ thickness $z$ to that for thickness $z_{max}$.

Using a full Mylar front electrode in the simulations, FIG. 6.11 plots the MC-calculated *PDI* and the measured *PDI*, clearly in agreement with one another. The MC-calculated *PDI* numerical value at the surface is 16.1% ± 0.7% in good agreement with the measurement (17.5% ± 0.2%). The exact thickness of the conducting aluminum layer in the aluminized Mylar electrode was difficult to determine accurately and we surmise that the conducting aluminum layer can have an effect on our calculations.

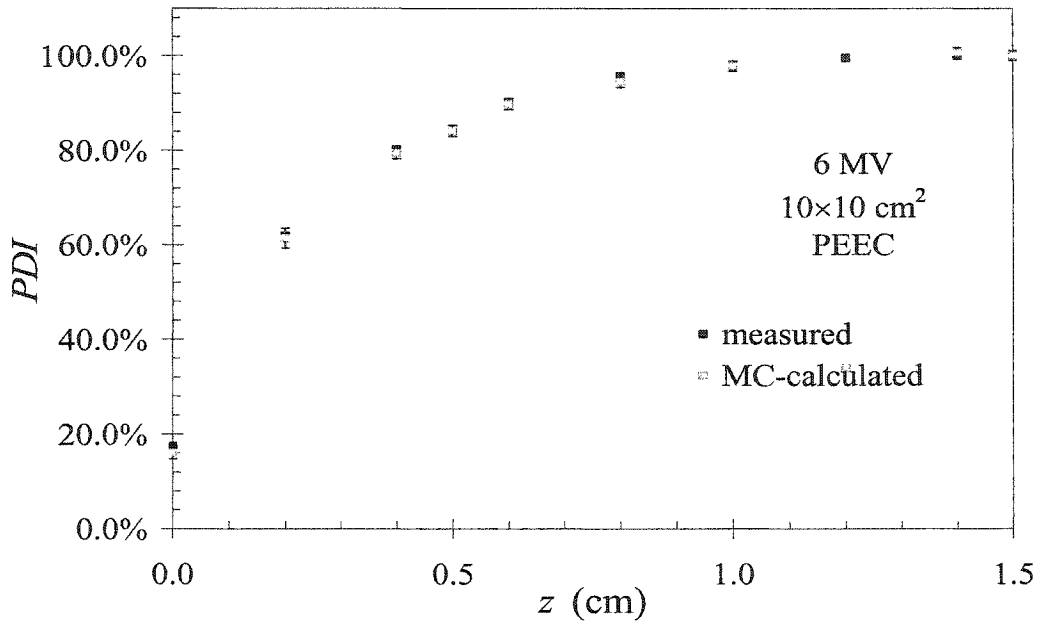


*FIG. 6.11. Comparison of the MC-calculated PDI in Solid Water™ of the PEEC using a Mylar front electrode obtained with the DOSRZnrc/EGSnrc user code and the measured PDI obtained with the PEEC with the aluminized Mylar/Delrin wall front electrode for the 10×10 cm² field 6 MV x-ray beam. z is the Solid Water™ thickness above the polarizing electrode.*

To examine the effect of the conducting aluminum layer, we calculated the *PDI*s at the surface for a full 50 μm aluminum layer and a combination 25 μm Mylar/ 25 μm aluminum layer replacing the Mylar layer of FIG. 5.15. The calculated *PDI* for these simulations are given in TABLE. 6.2, showing about a 3% increase in the calculated *PDI* in comparison to the value obtained for a full Mylar layer. The measured *PDI* at the surface falls between the calculated *PDI*s at the surface for a 50 μm Mylar and the 25 μm Mylar/ 25 μm aluminum electrodes, validating our MC modeling and optimization of the 6 MV beam.

TABLE 6.2. THE EFFECT OF THE ALUMINUM LAYER FORMING THE TOP ELECTRODE ON THE CALCULATED *PDI* FOR THE 10×10 $cm^2$ FIELD 6 MV X-RAY BEAM.

| simulated electrode layer(s) | 50 μm Mylar | 25 μm Mylar/25 μm aluminum | 50 μm aluminum |
|---|---|---|---|
| MC-calculated *PDI* | 16.1% ± 0.7% | 19.6% ± 0.7 % | 19.6% ± 0.9 % |
| Measured *PDI* | 17.5 % ± 0.2% | | |

Using the PEEC with the graphite/Solid Water™ front window attached to the chamber, the *PDI* in Solid Water™ at $z = 2$ mm was also measured for the 10×10 $cm^2$ field. The electrode separation $s$ in this measurement was also set to 2 mm. The measured *PDI* at $z = 2$ mm is 31.4% ± 0.2%. Using the graphite/Solid Water™ front window geometry, the calculated *PDI* at $z = 2$ mm and $s = 2$ mm for the graphite/Solid Water™ front window is 32.7% ± 1.2%, agreeing with the measurement. It is worth mentioning that the *PDI* using the aluminized Mylar/Delrin wall front window at 2 mm is 61.9% ± 0.3%, agreeing well with the MC-calculated *PDI* of 61.4% ± 1.2%.

Similarly to the situation for the 10×10 $cm^2$ field, the MC-calculated *PDI* for the 30×30 $cm^2$ field was obtained assuming a Mylar front electrode. The *PDI* was calculated at depths of 0.5 cm and 1.0 cm as well as at the surface. In FIG. 6.12 we show the calculated *PDI* as well as the measured data for the 30×30 $cm^2$ field. The numerical *PDI* values at the surface are 37.6% ± 0.4% and 35.0% ± 2.5% for the measurements and the MC calculation, respectively. The effect of the conducting aluminum layer on the aluminized Mylar electrode was not studied for this field; however, we think that, similarly to the situation with the 10×10 $cm^2$ field, the MC-calculated *PDI* including an aluminum layer will improve the agreement between the MC calculations and measured data.

Based on the above results, we conclude that our optimized 6 MV beam statistically represents the beam emerging from the 6 MV treatment head; hence, the calculated *PDD*s as well as the *RSPR*s, shown in FIG. 6.8, are correct.

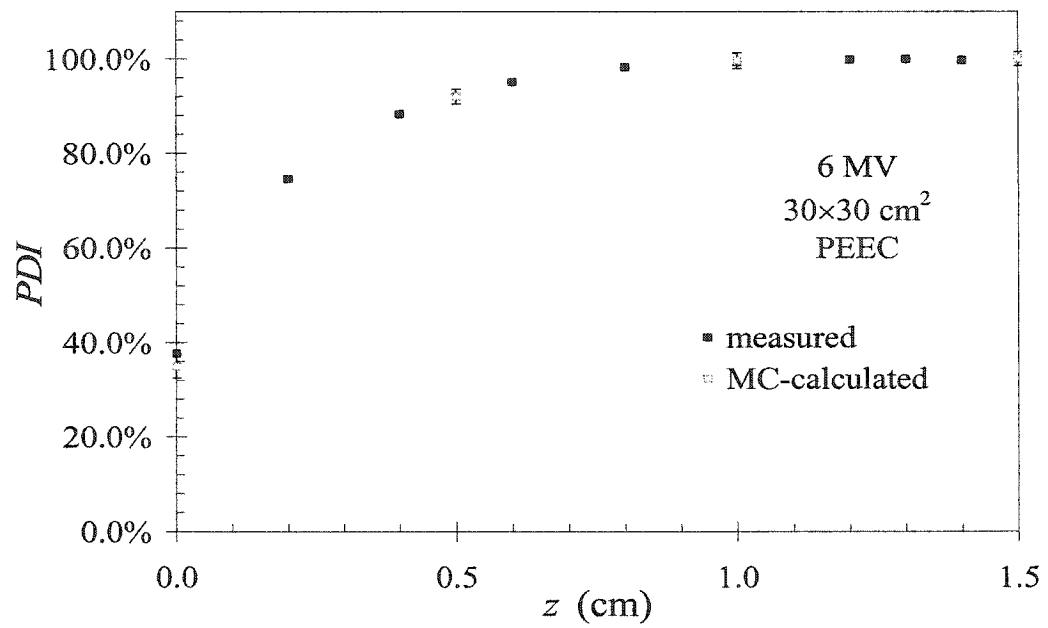


*FIG. 6.12. Comparison of the MC-calculated PDI in Solid Water™ of the PEEC using a Mylar front electrode obtained with the DOSRZnrc/EGSnrc user code and the measured PDI obtained with the PEEC with the aluminized Mylar/Delrin wall front electrode for the 30×30 cm² field 6 MV x-ray beam. z is the Solid Water™ thickness above the polarizing electrode.*

To understand why our zero-volume *PDI* differs from the *PDD* in the medium, we undertook a number of calculations to investigate the effect of the aluminized Mylar/Delrin wall front window on our measurements. This would establish that the extrapolation technique may still be a practical means for obtaining the *PDD*s directly without the need of further data processing when no inhomogeneities are present.

In an absolute sense, we postulated that, if the extrapolation technique removes the electronic fluence perturbations caused by the air cavity, our measured zero-volume *PDI*/100 should equal the ratio of the dose in Solid Water™ at point A on the surface to that at point B at $z_{max}$ with the front window electrode present, as shown in FIG. 6.13.

For this study, the DOSRZnrc/EGSnrc user code and the optimized phase-space file of the 10×10 cm² field 6 MV x-ray beam were used. The inhomogeneities considered in this calculation were a 50 μm Mylar layer and a 3.85 cm thick Delrin ring, while the graphite collecting electrode and the conducting aluminum layer were ignored. The doses at points

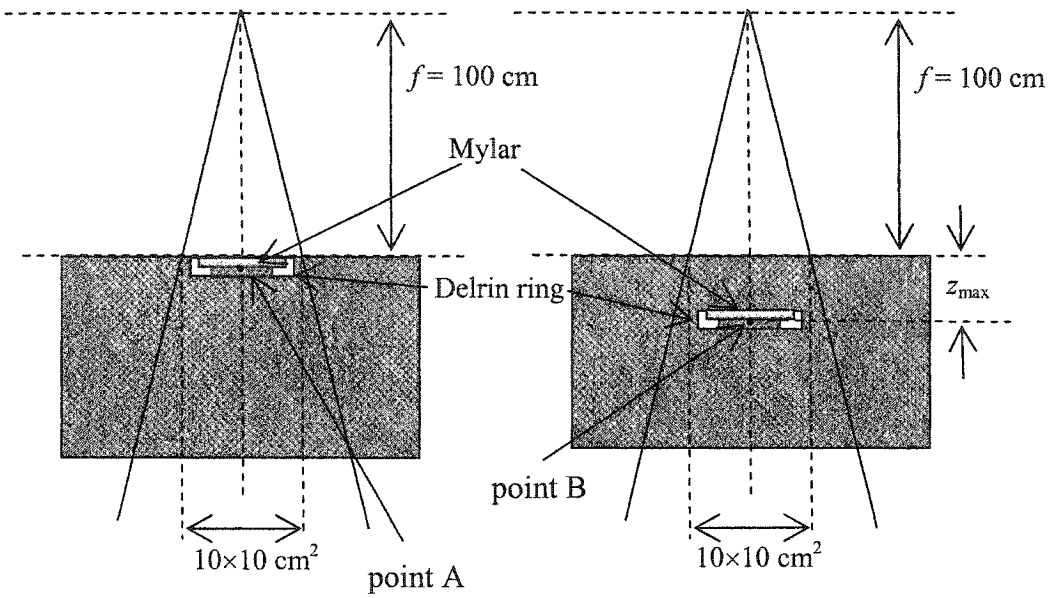


*FIG. 6.13. Schematic representation of the MC calculation for studying the effect of the Delrin wall and the aluminized Mylar electrode on the PDD for the 10×10 cm² field 6 MV x-ray beam.*

A and B are taken as the scored doses in a Solid Water™ layer of 50 μm thickness and 1.21 cm radius just below the Mylar layer.

Based on this study, the ratio of the dose at point A to that at point B, expressed as a percentage, when the Delrin ring only was included in the calculation geometry is 15.9% ± 0.4%, approximating nicely the zero-volume *PDI* of 15.9% ± 0.2% obtained by linearly extrapolating the relative density ionizations for electrode separations larger than 2 mm.

When both the Mylar layer and the Delrin ring wall were considered, the ratio of the dose at point A to that at point B, expressed as a percentage, was 16.4% ± 0.4%. We speculate that the conducting aluminum layer deposited onto the Mylar will also have an effect on the doses at points A and B, increasing the dose ratio, similarly to the situation with the *PDI* in the 2 mm thick air cavity study (TABLE. 6.2). This suggests that the measured zero-volume *PDI* of 17.5% ± 0.2% obtained with linearly extrapolating the relative density ionizations for electrode separations smaller than 2 mm removes the fluence perturbations, suggesting that the wall perturbation factor $P_{wall}$, not as initially thought,

must also be considered in evaluating the dose in medium at the phantom surface with our PEEC.

Thus, in the dose build-up region, the MC-calculated *PDD*s in water and in Solid Water™ can be trusted for our 6 MV x-ray beam, since the MC-calculations: (*i*) correctly predict the *PDI*s measured with the PEEC and (*ii*) explain why our measured *PDI*s and the *PDD*s in water do not match.

### 6.4.2. 18 MV x-ray beam

Our MC study of the dose in the build-up region for the 18 MV x-ray beam led us to find a coding error ("bug") in the EGSnrc code related to the bremsstrahlung production of positrons that may produce erroneous results when optimizing high-energy photon beams. One of the many physics input parameters in the EGSnrc MC system code, called the bremsstrahlung cross section option, allows the user to select two different differential cross sections for energy sampling of the radiative losses of transported electrons and positrons. The bremsstrahlung cross section option can be set to: either (*i*) the NIST (the National Institute of Standards and Technology) differential cross sections modeled according to the NIST bremsstrahlung cross section database[28,29] (the basis of the ICRU Report 37 (ref. 26)) or (*ii*) the BH (Bethe-Heitler) differential cross sections modeled according to the first Born approximation Bethe-Heitler cross sections with an empirical correction factor below 50 MeV (ref. 27). The coding "bug" affects the bremsstrahlung production as well as the annihilation of positrons when the bremsstrahlung cross section option in the physics input parameters is set to "NIST".

In the following section, the incorrect transport of positrons by the EGSnrc MC system when the NIST option is selected caused by this coding error is explained, and its effect on the initial beam optimization for our 18 MV x-ray beam is reported.

#### *The NIST coding error*

During the source optimization for the MC calculations using the 10×10 $cm^2$ field 18 MV x-ray beam, the optimized energy of the electron source was found to be considerably different when the bremsstrahlung cross sections are set to the NIST option compared to

when it was set to the BH option. Note that each of the two options was used in the BEAMnrc/EGSnrc user code to generate the phase-space files at an *SSD* of 100 cm and in the DOSRZnrc/EGSnrc as well as the DOSXYZnrc/EGSnrc user codes to calculate the *PDD*s and the *OAR*s in a water phantom. Moreover, the geometrical models of the treatment head in our 18 MV beam in the BEAMnrc/EGSnrc simulations for both options were identical and so were the initial electron sources (a 0.1 cm radius electron pencil beam striking the x-ray target).

In FIG. 6.14(a) we show the 10×10 $cm^2$ field *PDD*s in water obtained with the NIST bremsstrahlung cross section option and an initial kinetic energy of the electron pencil beam of 17.0 MeV [NIST(17.0 MeV)] as well as with the BH bremsstrahlung cross section option and a 17.8 MeV electron pencil beam [BH(17.8 MeV)]. The *PDI* in water measured with the IC-10 cylindrical ionization chamber is also shown in FIG. 6.14(a). It is interesting to note that, while the calculated *PDD* in water with BH(17.8 MeV) matched the measured *PDI* in water for $z \geq z_{max}$, a significantly lower initial kinetic energy of the electron beam of 17.0 MeV is necessary for the calculated *PDD* in water with the NIST option and the *PDI* to match. The scored doses in water per initial electron along the beam central axis as a function of depth $z$ for the NIST(17.0 MeV) and the BH(17.8 MeV) calculations are compared in FIG. 6.14(b), showing that the two differ by about 15% with the NIST(17.0 MeV) calculation consistently providing lower values than the BH(17.8 MeV) calculation.

The decrease in the scored doses in water [FIG. 6.14(b)] may be caused by the lower kinetic energy of the electron pencil beam or by the bremsstrahlung cross sections option. To eliminate the effect of the energy of the electron pencil beam for the comparison, an additional BH(17.0 MeV) *PDD* in water was obtained. The scored doses in water per initial electron for the BH(17.0 MeV) and the NIST(17.0 MeV) calculations are displayed in FIG. 6.15(a), clearly showing that the difference in the scored doses of FIG. 6.14(b) is mainly caused by the different energies of the electron pencil beam. Figure 6.15(b) shows that the scored doses from the BH(17.0 MeV) calculation are about 2% to 5% higher than the values from the NIST(17.0 MeV) calculations at a given depth in the dose build-up region; however, for $z \geq z_{max}$ the situation was reversed and the BH(17.0 MeV)

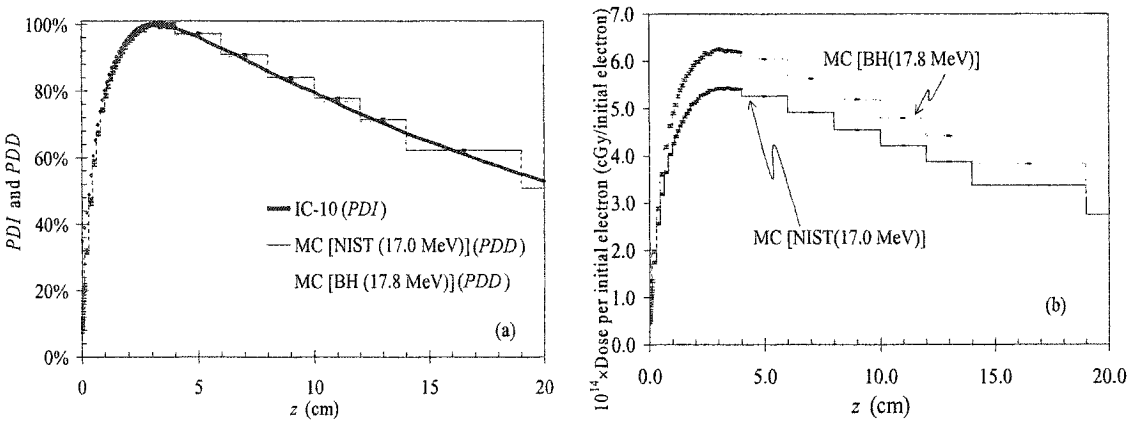


*FIG. 6.14. Comparison of the PDDs in water for the 10×10 cm² field 18 MV x-ray beam for the NIST and BH bremsstrahlung cross sections options in the EGSnrc physics input parameters. (a) The PDI in water with the IC-10 cylindrical ionization chamber (data points), the MC-calculated PDD in water using NIST bremsstrahlung cross sections with a 17.0 MeV electron pencil beam [NIST(17.0 MeV)] (histograms), and the MC-calculated PDD in water using BH bremsstrahlung cross sections with a 17.8 MeV electron pencil beam [BH(17.8 MeV)] (histograms).(b) The scored dose in water along beam central axis per initial electron as a function of depth resulting from the NIST(17.0 MeV) and BH(17.8 MeV) calculations.*

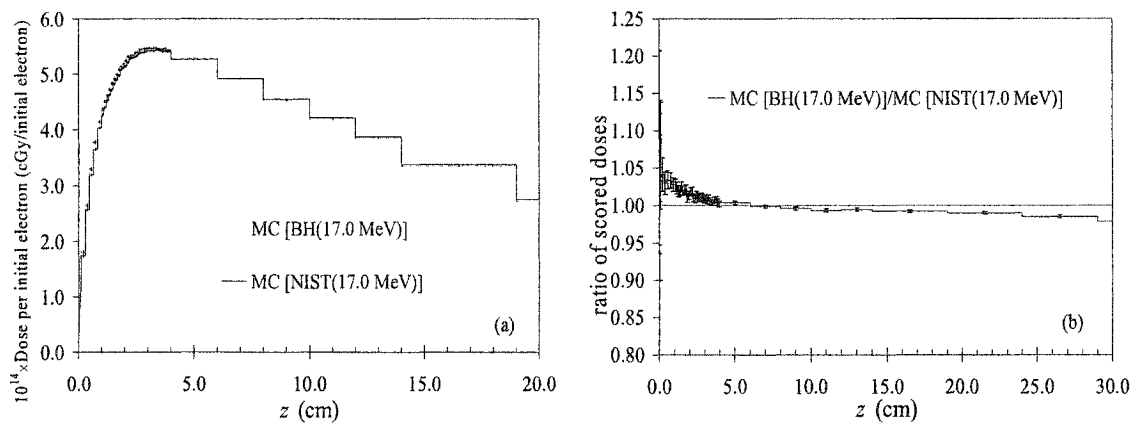


*FIG. 6.15. Comparison of the scored dose in water along beam central axis per initial electron for the 10×10 cm² field 18 MV x-ray beam for the NIST and BH bremsstrahlung cross sections options in the EGSnrc physics input parameters with a 17.0 MeV initial pencil beam. (a) The scored dose in water along beam central axis per initial electron as a function of depth. (b) The scored dose ratios of the data in (a) as a function of depth.*

calculation produced lower scored doses than the NIST(17.0 MeV) calculation. Thus, the following problem remains unanswered: the NIST(17.0 MeV) and the BH(17.8 MeV) calculations, while producing similar *PDD*s in water (FIG. 6.14(a)), beyond $z_{max}$ produce considerably different scored doses, as shown in FIG. 6.14(b).

Since the differences in FIG. 6.14 are linked to bremsstrahlung production, it is logical to compare the bremsstrahlung $g$ factors for monoenegetic photon beams, (see Section 2.3.9), obtained with the EGSnrc MC system code for both bremsstrahlung cross section options. The g/EGSnrc user code, written by the NRC group and used for this comparison, transports photons in a specified medium, tracks the secondary particles in the medium, and reports two $g$ factors: (*i*) $g_{rad}$, the fraction of kinetic energy of secondary electrons and positrons lost to bremsstrahlung production only and (*ii*) $g_{all}$, the fraction of kinetic energy of secondary electrons and positrons lost to bremsstrahlung production and annihilation.

To illustrate the above definitions of the $g_{rad}$ and the $g_{all}$ for positrons, suppose a high energy photon transfers a kinetic energy of 5 MeV to a positron after undergoing pair production interaction in the medium. The energetic positron, before annihilating in-flight with an orbital electron, loses 3 MeV in hard and soft collisions and 1 MeV in bremsstrahlung production. In the g/EGSnrc user code, the 1 MeV energy lost to bremsstrahlung production is used for evaluating the $g_{rad}$ factor and a total of 2 MeV energy lost in bremsstrahlung production and in annihilation is used for evaluating the $g_{all}$ factor.

The $g_{rad}$ and the $g_{all}$ factors in water for photon energies between 1 MeV and 18 MeV, calculated with the NIST option, are shown in FIG. 6.16. It was surprising to observe that above 3 MeV the $g_{all}$ in water is much higher than the $g_{rad}$ , since it is much more likely for the positrons to annihilate with an orbital electron after losing all of their kinetic energy than undergoing an in-flight annihilation. We took a close look at the EGSnrc code and found that, in calculations with the NIST option selected, most positrons will undergo in-flight annihilation. This obvious transporting error was reported to the NRC group, and they confirmed our findings, found the coding error that caused this problem, and instructed all users of the EGSnrc MC system code to correct the coding error.

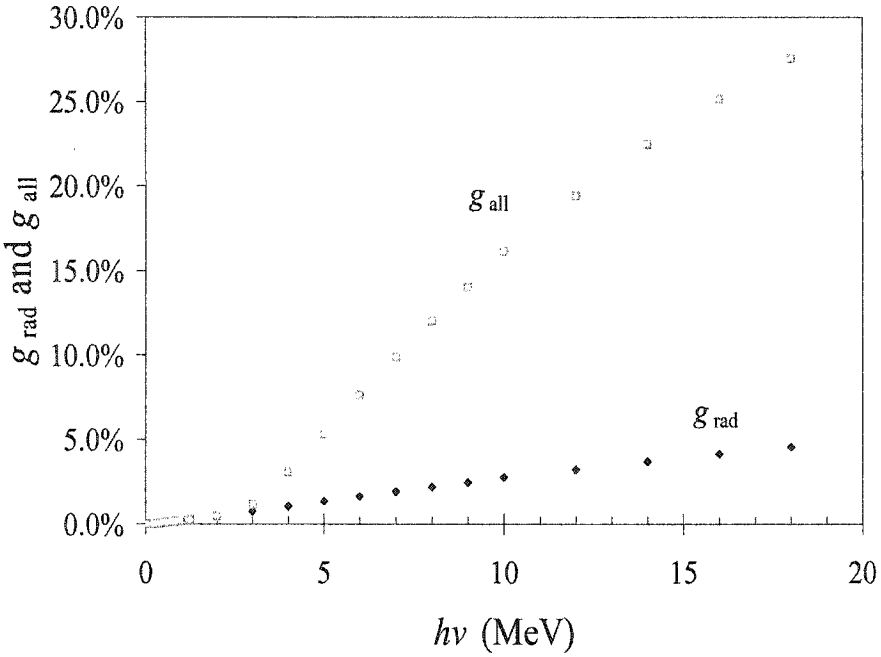


*FIG. 6.16. The $g_{rad}$ and $g_{all}$ in water as a function of photon energy calculated with the g/EGSnrc MC user code using the "incorrect" NIST option for the bremsstrahlung production differential cross sections.*

Photons in clinical photon beams produced by linear accelerators are primarily bremsstrahlung photons produced by electron beams striking the x-ray target. Bremsstrahlung photons generated in the x-ray target with energies greater than 1.022 MeV may subsequently interact with the various components of the treatment head and may undergo a pair or triplet interaction resulting in an electron-positron pair in pair production or two electrons and a positron in triplet production. Most positrons after annihilation with an orbital electron produce 0.511 MeV photons that become part of the photon fluence exiting the treatment head. Thus, treatment head simulations with the "incorrect" NIST bremsstrahlung cross section option will produce a smaller number of 0.511 MeV photons and increase the relative number of higher energy photons, because of the erroneous increased probability for in-flight annihilation of positrons.

In FIG. 6.17, we show the 10×10 $cm^2$ field 18 MV x-ray photon fluence spectra in the phase-space files obtained with the BH(17.0 MeV), the "corrected" NIST(17.0 MeV), and the "incorrect" NIST(17.0 MeV) calculations. The photon fluence spectra resulting

from the BH(17.0 MeV) and the "corrected" NIST(17.0 MeV) calculations are similar to one another and differ from the "incorrect" NIST(17.0 MeV) calculations in the number of predicted photons per initial electron striking the target. In the "incorrect" NIST(17.0 MeV) spectrum the number of photons with energies above 1 MeV is larger and the number of photons in the 0.511 MeV peak is smaller when compared to the "corrected" NIST(17.0 MeV) and the BH(17.0 MeV) fluence spectra. This explains the differences in the *PDD*s in water shown in FIG. 6.15(a), where the reduced 0.511 MeV peak decreased the scored dose in the dose build-up region and the extra high energy photons increased the scored doses at deeper depths. Thus, for the *PDD*s in water for the 18 MV beam from the "incorrect" NIST and the BH calculations to match one another for $z \geq z_{max}$, a lower kinetic energy of the initial electron pencil beam must be used with the "incorrect" NIST calculation, causing substantial differences in the scored doses, as shown in FIG. 6.14.

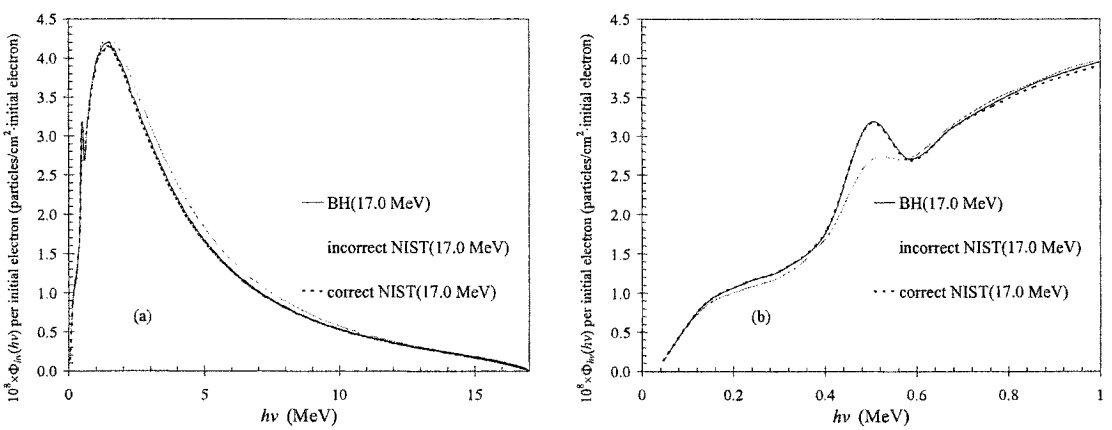


*FIG. 6.17. The photon fluence spectrum at 100 cm from the electron source of the 18 MV x-ray treatment head obtained with the BEAMnrc/EGSnrc user code using the BH option, the "corrected" NIST option, and the "incorrect" NIST option for the bremsstrahlung production differential cross sections. The initial electron source is a 0.1 cm radius 17.0 MeV pencil beam striking the x-ray target. Part (b) shows data of part (a) in an expanded scale.*

It should be noted that the "incorrect" NIST calculation is only noticed at relatively high photon energies (18 MV) where the pair production cross sections become important. For 6 MV photons the contribution of pair production interactions is much less pronounced and thus has a negligible effect on the fluence spectrum. The use of the "incorrect" NIST in calculations for 6 MV beams does not appreciably affect the optimization and the scored doses and therefore the problem was not noticed in our study of the 6 MV x-ray beam.

### *Beam optimization*

Following the steps discussed in Section 6.4.1, the *PDI*s and the beam profiles at $z_{max}$ (3.0 cm) as well as 10 cm in water were measured for the 10×10 $cm^2$ and the 30×30 $cm^2$ fields 18 MV x-ray beam with the IC-10 cylindrical ionization chamber. The *PDI* in water for the 10×10 $cm^2$ field 18 MV x-ray beam was also obtained with the Roos parallel-plate ionization chamber in the dose build-up region and down to 5 cm depth in water.

Similarly to the situation with the 6 MV beam, the treatment head for the 18 MV x-ray beam is modeled in the BEAMnrc/EGSnrc user code based on specifications provided by the manufacturer. The optimization of the electron source beam striking the x-ray target and the kinetic energy of the electron source was based on matching the calculated *PDD*s and the *PDI*s in water for depths larger than $z_{max}$ as well as the calculated and measured *OAR*s at selected depths. For the 10×10 $cm^2$ field, FIGs. 6.18(a) and 6.18(b) compare the calculated and measured *OAR*s at $z_{max}$ as well as depth of 10 cm in water and the calculated *PDD*s with the measured *PDI*s in water, respectively, clearly showing a satisfactory agreement between the measurements and the MC calculation. The MC calculations are obtained using a 17.8 MeV electron pencil beam of radius 1.0 mm striking the x-ray target, and the bremsstrahlung cross section option is set to BH. The calculated *OAR*s at $z_{max}$ and 10 cm, shown in FIG. 6.18(a), differ from the measurements by less than 1% for the 10×10 $cm^2$ field. Also, the difference between the *PDI*s and the calculated *PDD* in water shown in FIGs. 6.18(b) for depths larger than $z_{max}$ is less than 1%. In the dose build-up region, as expected, the *PDI*s in water obtained with the IC-10

cylindrical ionization chamber as well as with the Roos parallel-plate ionization chamber are larger than the corresponding MC-calculated *PDD*s in water, as shown in FIG. 6.19.

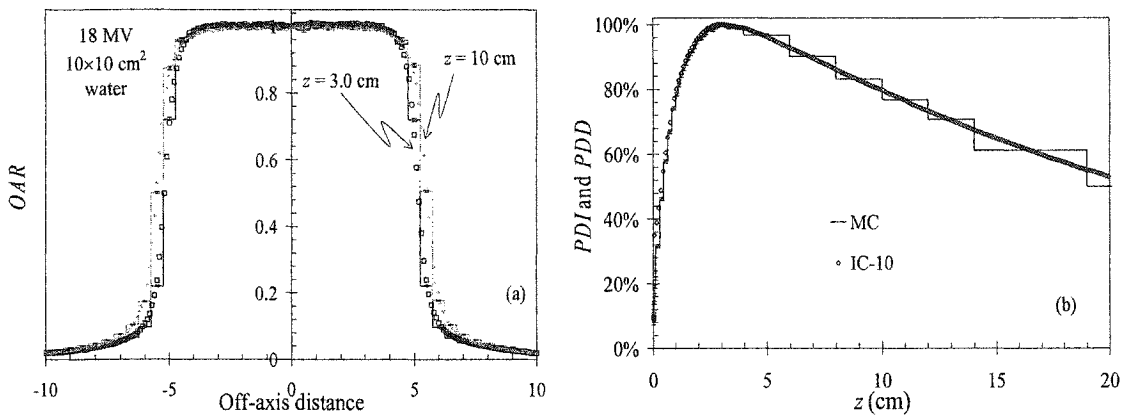


*FIG. 6.18. Measured data in water with the IC-10 cylindrical ionization chamber (solid lines) and MC calculations in water with the DOSXYZnrc/EGSnrc user code (data points) for the 10×10 cm² field 18 MV x-ray beam. (a) The OARs at depths $z_{max}$ and 10 cm. (b) The measured PDI (data points) and the MC-calculated PDD (histogram). z is the depth from the phantom surface to the center of the calculation voxel in the DOSXYZnrc/EGSnrc user code and the effective point of measurement of the IC-10 ionization chamber.*

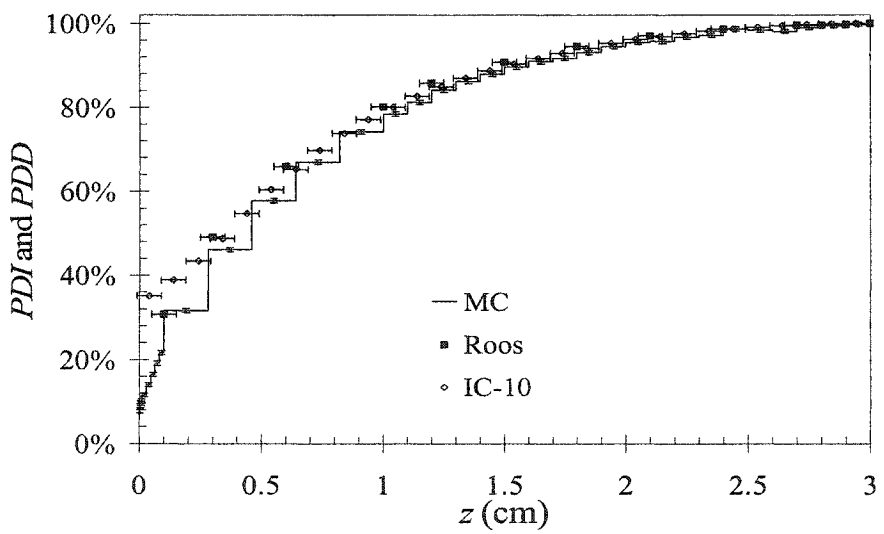


*FIG. 6.19. The PDIs in water and the MC-calculated PDD in water in the dose build-up region for the 10×10 cm² field 18 MV x-ray beam. The measured PDIs with the IC-10 cylindrical chamber as well as with the Roos parallel-plate chamber are shown with data points and the MC-calculated PDD using the DOSXYZnrc/EGSnrc user code shown with a histogram. z is the depth from the phantom surface.*

The *PDI*s in Solid Water™ were also measured with the PEEC for the 10×10 cm$^2$ 18 MV x-ray beam. The MC-calculated *PDD*s in Solid Water™ with the phase-space file optimized in water and the PEEC *PDI*s in Solid Water™ for the 10×10 cm$^2$ field are displayed for comparison in FIG. 6.20, showing a satisfactory agreement between measurement and MC calculation at depths larger than $z_{max}$; however, in the build-up region measurements and MC calculation differ; the largest discrepancy on phantom surface and thus there is a gradual improvement until at $z_{max}$ and beyond the measurement and MC calculation agree.

Using the SPRRZnrc/EGSnrc user code, the stopping power ratios Solid Water™ to air as a function of depth were calculated for the 10×10 cm$^2$ field 18 MV x-ray beam. The *RSPR*s defined by Eq. (6.2) are plotted in FIG. 6.21 as a function of depth. Unlike the situation for the 10×10 cm$^2$ field for the 6 MV beam (FIG. 6.8), the *RSPR* in the dose build-up region for the 18 MV beam has a value at the surface of 0.93, *increasing* rapidly in the dose build-up region to reach a value of 1.0 for all depths larger than 0.5 cm. Although the *RSPR*s corrections for the 18 MV beam are in the appropriate direction, reducing the discrepancy between the MC-calculated *PDD* and the measurements, their magnitudes are small and will not completely account for the difference between the measured *PDI*s and MC calculated depth doses.

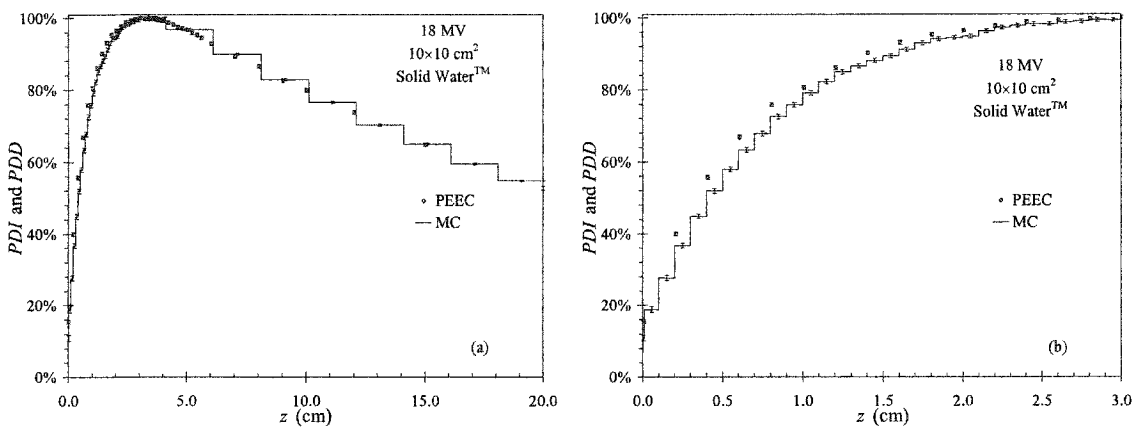


*FIG. 6.20. Measured PDI in Solid Water™ with the PEEC (data points) and the MC-calculated PDD in Solid Water™ with the DOSRZnrc/EGSnrc user code (histogram) for the 10×10 cm$^2$ field 18 MV x-ray beam. (a) Comparison for depths between the surface and 20 cm. (b) Comparison in the dose build-up region.*

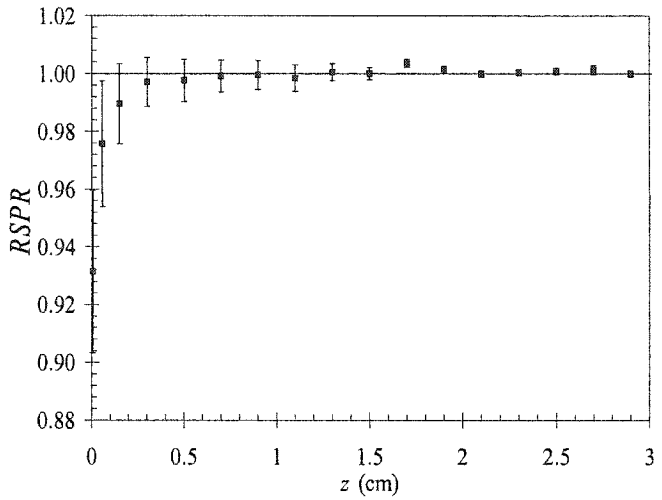


*FIG. 6.21. The RSPR as a function of depth z in Solid Water™ for the 10×10 cm² 18 MV x-ray beam. The data are calculated using the SPRRZnrc/EGSnrc user code.*

The ionization density as a function of electrode separation $s$ was measured at the surface as well as at $z_{max}$ with the PEEC for the 10×10 cm² 18 MV x-ray beam. The ionization density normalized to 1.0 at $s$ = 2 mm is shown in FIG. 6.22. From these measurements, the zero-volume *PDI* at the phantom surface determined from the linear extrapolation of the data points for electrode separations larger than 2 mm is 14.4% ± 0.2% in contrast to 15.2% ± 0.2% from the linear extrapolation of the data points for electrode separations smaller than 2 mm. Both zero-volume *PDI* values on the phantom surface are substantially larger than the MC-calculated *PDD* in Solid Water™ at 50 μm (9.6% ± 0.5%).

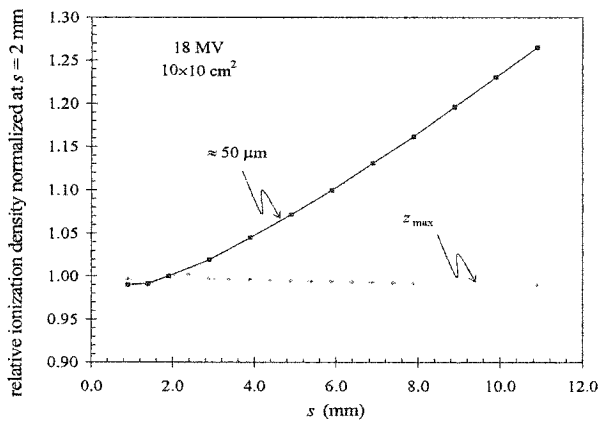


*FIG. 6.22. The relative ionization density for the PEEC as a function of electrode separation s at the surface (z ≈ 50 μm) and $z_{max}$ for the 10×10 cm² 18 MV x-ray beam.*

Similarly to the situation with the 6 MV x-ray beam, the *PDI* in the dose build-up region for the PEEC geometry, with a 2 mm electrode separation and a 50 μm Mylar layer and the 10×10 $cm^2$ field 18 MV x-ray beam, were calculated. In FIG. 6.23, the MC calculation and the measurements of the *PDI* in the dose build-up region for the 10×10 $cm^2$ field 18 MV x-ray beam are compared, showing lower MC-calculated *PDI*s than the corresponding values in the dose build-up region. For example, on the phantom surface ($z$ = 50 μm) measurements show a *PDI* of 15.5% ± 0.2% while the MC-calculated *PDI* is 10.4 % ± 0.6%.

To establish whether or not this discrepancy is caused by the conducting aluminum layer on the aluminized Mylar electrode, we calculated the *PDI* at the surface for a combination 25 μm Mylar/25 μm aluminum layer as well as a 50 μm aluminum layer replacing the 50 μm Mylar layer, and the results are shown in TABLE. 6.3. The MC-calculated *PDI*s at the surface for the various front electrode geometries are all about 10.5%, still lower than the measured value of 15.5% ± 0.2%. Hence, we conclude that the conducting aluminum layer in the aluminized Mylar electrode is not the source of the discrepancy between the measurement and the calculation.

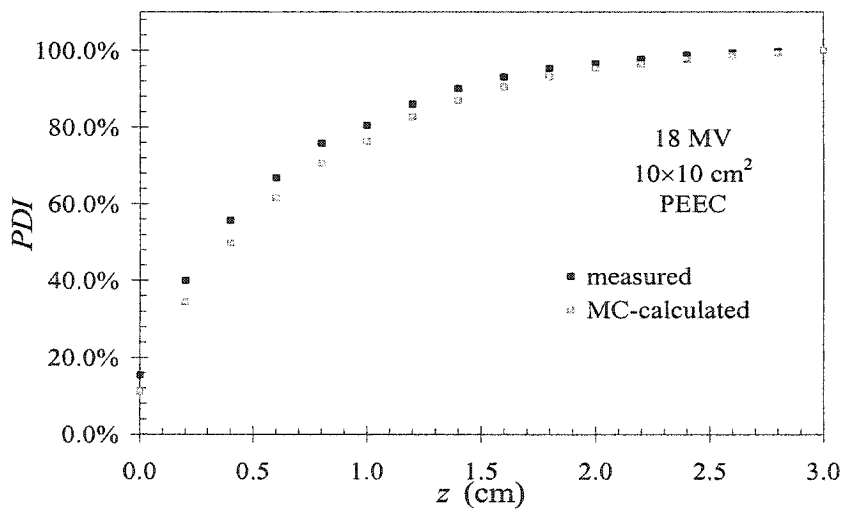


*FIG. 6.23. Comparison of the MC-calculated PDI in Solid Water™ of the PEEC using a Mylar front electrode obtained with the DOSRZnrc/EGSnrc user code and the measured PDI obtained with the PEEC with the aluminized Mylar/Delrin wall front electrode for the 10×10 $cm^2$ field 18 MV x-ray beam. z is the Solid Water™ thickness above the polarizing electrode.*

TABLE 6.3. THE EFFECT OF THE ALUMINUM LAYER ON THE TOP ELECTRODE ON THE CALCULATED *PDI* FOR THE 10×10 $cm^2$ FIELD 18 MV X-RAY BEAM.

| simulated electrode layer(s) | 50 μm Mylar | 25 μm Mylar/25 μm aluminum | 50 μm aluminum |
|---|---|---|---|
| MC-calculated *PDI* | 10.4 % ± 0.6% | 10.3% ± 0.5 % | 10.4% ± 0.5 % |
| Measured *PDI* | 15.5% ± 0.2% | | |

The *PDI* in Solid Water™ at 2 mm depth and 10×10 $cm^2$ field was also measured with the PEEC using the graphite/Solid Water™ front window. While the measured *PDI* at 2 mm is 21.2% ± 0.2%, the MC-calculated *PDI* for this front window at 2 mm gives 16.5% ± 0.7% again lower than the measured value.

Because the MC-calculated *PDI*s in the build-up region are lower than the measurements, our optimization of the 18 MV x-ray beam, although correctly giving the *PDD* in water and Solid Water™ for $z \geq z_{max}$, produced calculated *PDI*s significantly lower than the measurements. We investigated three possible causes for this discrepancy: (*i*) *inadequate geometrical modeling* of the 18 MV x-ray beam treatment head that may not have accounted for some contaminating electrons that contribute to the dose in the dose build-up region, (*ii*) *contaminating neutrons* produced in the treatment head of the 18 MV x-ray beam significantly affecting our measurements in the dose build-up region, and (*iii*) *lower pair production photon cross sections* in the SI photon cross sections database than that in the XCOM database. It should be noted that the first two possible causes were investigated previously by Ding[11,12,18] who concluded that they did not explain the discrepancy between MC calculations and measurements for an 18 MV x-ray beam.

### *An evaluation of a possible electron source in the treatment head model*

Hartmann-Siantar *et al.*[13] suggest in their work the possibility that the beam model does not fully account for all contaminating electrons in the radiation beam. To eliminate this possibility, we placed a number of Solid Water™ blocks having a total thickness of 12.0 cm below the exit window of the treatment head on a 0.63 cm thick Lucite blocking tray and measured the *PDI* in Solid Water™ with the PEEC and the aluminized Mylar/Delrin

wall front window at an *SSD* of 100 cm for the 10×10 $cm^2$ field 18 MV x-ray beam. The distance between the phantom surface and the bottom of the Lucite blocking tray was 35.5 cm.

All contaminating electrons produced within the treatment head are stopped in the 12 cm Solid Water™ attenuator, essentially reducing errors caused by improper modeling of the treatment head. A Solid Water™ attenuator was selected in this experiment because of its low atomic number *Z*, hence, minimizing the radiative losses in the attenuator of contaminating electrons from the treatment head. Contaminating electrons reaching the phantom surface are essentially produced within the Solid Water™ attenuator and the air between the Solid Water™ attenuator and the phantom surface. Because of the simplicity of the geometry, MC calculations should properly account for contaminating electrons reaching the phantom surface at *SSD* = 100 cm.

A phase-space file was generated for the modified 18 MV x-ray beam treatment head geometry that included the 12 cm Solid Water™ attenuator as well as the Lucite blocking tray, and the *PDI* of the PEEC geometry was consequently calculated. In FIG. 6.24, we plot the measured *PDI*s in Solid Water™ in the dose build-region for the open and blocked 10×10 $cm^2$ fields 18 MV x-ray beam. At the surface, the measured *PDI* of the blocked field is 22.3% ± 0.3%, actually higher than the measured *PDI* for the open field which was 15.5% ± 0.2%. The MC-calculated *PDI* for the blocked field is 15.3% ± 0.7% also higher than the MC-calculated *PDI* for the open field (10.4 % ± 0.6%), yet the MC calculations are again significantly lower than the measurements. Thus, we conclude that an incorrect modeling of the treatment head that would reduce the contaminating electron fluence of the open beam is not the source of the discrepancy between our MC calculations and measurements in the dose build-up region.

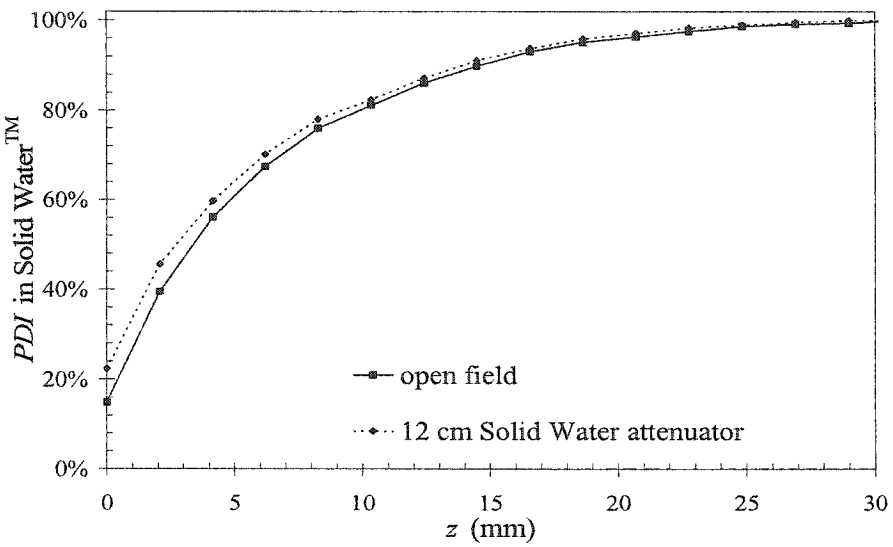


*FIG. 6.24. Comparison of the measured PDI in Solid Water™ of the open and blocked 10×10 cm² fields 18 MV x-ray beam. The 12.0 cm Solid Water™ attenuator was placed below the exit window of the treatment head. The PDIs at z = 50 μm for the open field and the blocked field are 15.5% ± 0.2% and 22.3% ± 0.3%, respectively .*

### *An evaluation of the effect of contaminating neutrons on the PDD*

To investigate the possible effect of contaminating neutrons on the *PDD* of the 18 MV x-ray beam, 3.2×3.2×0.15 mm$^3$ TLD-600 and TLD-700 thermoluminesent chips were used. If contaminating neutrons affect the dose in the build-up region, the relative dosimetry measurements obtained with TLD-600 and TLD-700 chips should be different, since in addition to the x-ray and electron dose components, the measurements with TLD-600 are sensitive to the neutron dose component, while those with TLD-700 are not.

Three TLD-600 and three TLD-700 chips were placed at each measurement depth in the dose build-up region and exposed to 100 MU irradiation from the 10×10 cm$^2$ field 18 MV x-ray beam. The measurement depths were: at the surface, and depths of 0.2 cm, and 1.0 cm. After reading the signal of each TLD chip, all chips were placed at $z_{max}$ and exposed to 100 MU irradiation from the 10×10 cm$^2$ field 18 MV x-ray beam. The relative response as a function of depth was taken as the averaged ratio of TLD signals at depth $z$ to that at $z_{max}$ for the three TLDs at that particular depth, and the standard deviation was used as the error estimator.

The relative response of TLD-600 and TLD-700 chips at the surface, and depths of 0.2 cm, 1.0 cm is given in FIG. 6.25. The results show quite clearly that the relative dosimetry measurements with TLD-600 and TLD-700 chips are almost identical, leading us to the conclusion that contaminating neutrons, existing in the 18 MV beam, have no effect on the *PDD* measured in the dose build-up region.

Moreover, the relative response, expressed as a percentage, at the surface for both types of TLDs is 18.8% ± 0.6%. The sensitive point of measurement for the chips is usually taken at the center of the TLD chip (75 μm for our chips) and the MC-calculated *PDD* in Solid Water™ for the 18 MV x-ray beam at $z$ = 75 μm is 11.2% ± 0.7%. The depth at which the MC-calculated *PDD* is 18.8% is at z = 550 μm, yet again confirming our findings with ionization chambers that the MC-calculated *PDD*s are lower than the measurements for the 18 MV x-ray beam.

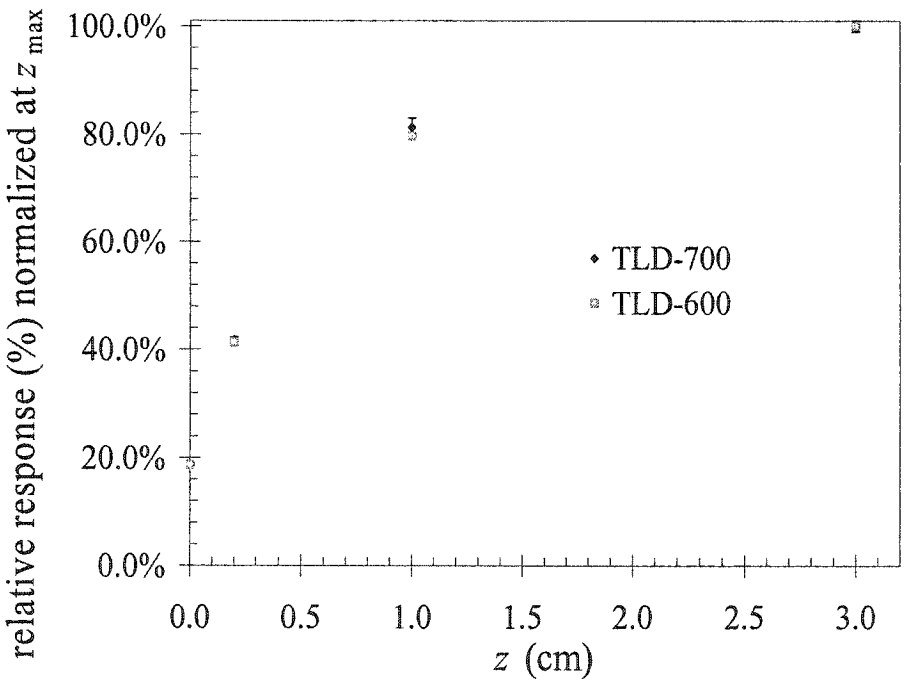


*FIG. 6.25. Comparison of TLD-700 and TLD-600 relative response as a function of depth in Solid Water™, normalized at $z_{max}$ for the 10×10 cm² field 18 MV x-ray beam.*

The TLD measurements thus showed that neutrons contaminating out 18 MV x-ray beam are not the source of the discrepancy between the measured and calculated doses in the dose build-up region. Moreover, the TLD measurements provide an independent confirmation of our measurement results obtained with our PEEC and parallel plate ionization chambers.

### *The effect of the XCOM photon cross database on the MC calculations for 18 MV beam*

The EGSnrc MC system makes use of the *photon cross section database* compiled by Storm and Israel[19] (SI) in 1970 to transport photons in given calculation geometries. A second *photon cross section database*, known as XCOM and compiled recently by Berger, Hubbell, and Seltzer[20] also exists and contains significantly different photoelectric effect photon interaction cross sections for low energy photons. Hobeila[30] conducted a MC study of ionization chamber response in low energy (orthovoltage) photon beams, showing that using the XCOM rather than the SI photoelectric cross sections significantly improved the MC calculations.

It turns out that, the pair production cross sections for high energy photons are also different in the SI and XCOM databases. As FIG. 6.26 demonstrates with a plot of the ratio of the atomic cross sections of the two databases $\kappa_{XCOM}/\kappa_{SI}$, the XCOM pair production cross sections $\kappa_{XCOM}$ for tungsten are about 6% higher than the SI pair production cross sections $\kappa_{SI}$ for photon energies up to 2 MeV and about 1% higher for photon energies between 5 and 20 MeV, and, for water, the $\kappa_{XCOM}$ and $\kappa_{SI}$ are within 1% of one another for all photon energies up to 20 MeV. In general, high $Z$ materials have higher pair production cross sections in the XCOM database than in the SI database. Note that $\kappa$ is the combined pair and triplet production cross section.

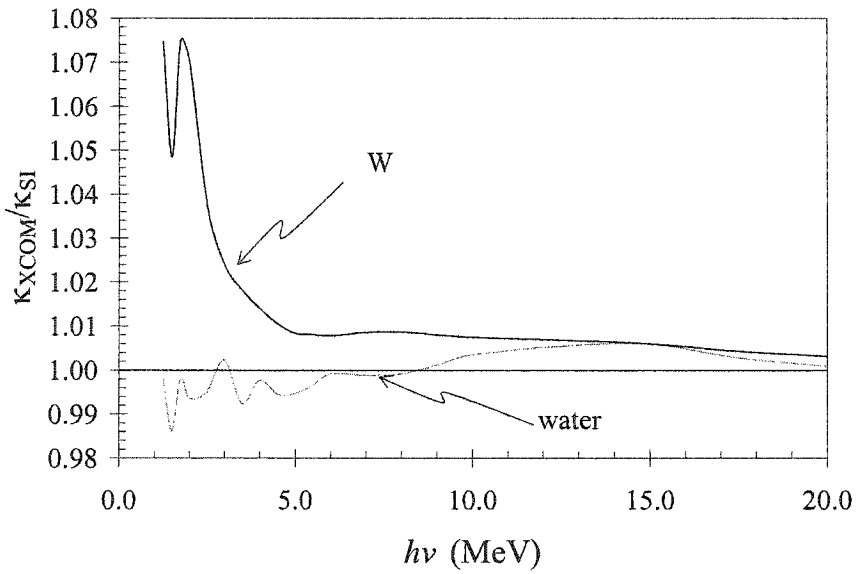


*FIG. 6.26. A comparison of pair production atomic cross sections ${}_a\kappa$. The ratio of the atomic cross sections of the two databases $\kappa_{XCOM}/\kappa_{SI}$ are plotted against photon energy for two materials: tungsten and water.*

Most of the components in a linac head are made of high $Z$ materials and we speculated that using the SI database in comparison with the XCOM database in BEAMnrc/EGSnrc simulations for the 18 MV x-ray beam produces: (*i*) a higher spectral fluence for high energy photons and (*ii*) a reduced 0.511 MeV photons fluence, hence both effect reducing the dose in the build-up region.

To investigate this hypothesis the XCOM photon cross sections for elements with $Z = 1$ to $Z = 100$ were downloaded from the following URL address:

*http://physics.nist.gov/PhysRefData/Xcom/Text/XCOM.html*

and entered in a text file, called *pgs4pepr_xcom-full.dat*. This file is equivalent to the *pgs4pepr.dat* text file containing photon cross sections from the SI database and used by the PEGS4 user code. With the PEGS4 user code we generated all the necessary data required for the simulations with the XCOM photon cross sections and obtained a phase-space file for the 10×10 cm$^2$ field 18 MV x-ray beam using the NIST bremsstrahlung cross section option as well as the XCOM photon cross sections. The electron source (0.1 cm radius pencil beam) and kinetic energy of the initial electrons (17.8 MeV) were identical to those in our previous calculations.

In the following paragraphs we compare the effects of the NIST and BH bremsstrahlung cross sections as well as the SI and XCOM databases photon cross sections on: (*i*) the photon fluence spectra that is produced in the treatment head model at an *SSD* of 100 cm, (*ii*) the scored dose in water along the beam central axis, (*iii*) the *PDD*s in water, and (*iv*) the MC-calculated *PDI* at the surface for the PEEC geometry.

*(i)* *Photon fluence spectra*

The calculated photon fluence spectra at an *SSD* of 100 cm for the 10×10 $cm^2$ field 18 MV beam model is shown in FIG. 6.27. In general, the four calculations using different cross section combinations – the BH(SI), the BH(XCOM), the NIST(SI), and the NIST(XCOM) – produced photon fluence spectra that are similar to one another; however, small differences in the fluence spectra were observed, especially in the energy region between 2 MeV and 5 MeV. Note that NIST(XCOM) stands for calculations with the NIST bremsstrahlung cross section option and the XCOM photon cross sections

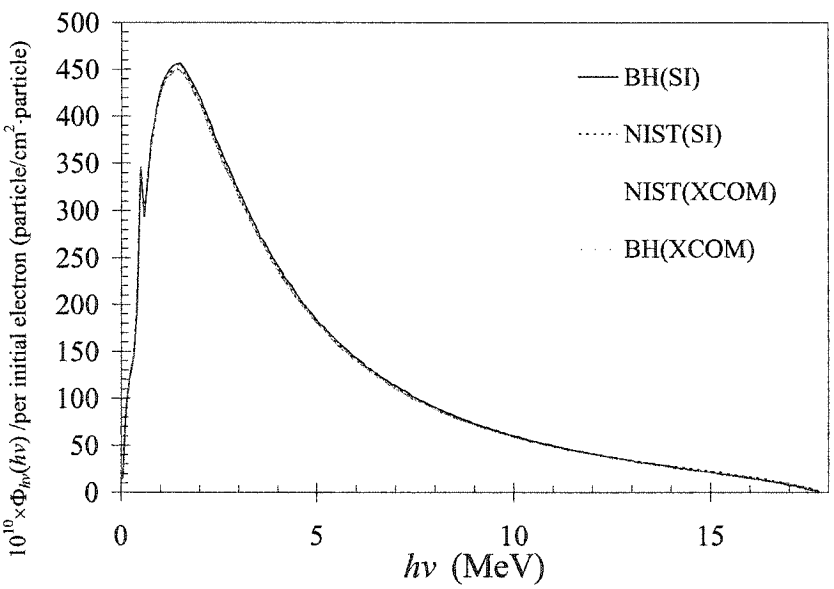


*FIG. 6.27. The photon fluence spectra at an SSD of 100 cm of the treatment head simulations of the 10×10 $cm^2$ field 18 MV x-ray beam. NIST(XCOM) stands for calculations using the NIST bremsstrahlung cross section option and the XCOM photon cross sections database; NIST(SI) stands for calculations using the NIST bremsstrahlung cross section option and the SI photon cross sections database; and BH(SI) stands for calculations using the BH bremsstrahlung cross section option and the SI photon cross sections database.*

database, NIST(SI) stands for calculations with the NIST bremsstrahlung cross section option and the SI photon cross sections database, and so forth. The contaminating electron fluence spectra at an *SSD* of 100 cm obtained from the phase-space files of the four calculations are statistically identical; hence, they were ignored in this study.

In FIG. 6.28(a) we compare the effect of *the differential Bremsstrahlung cross section options NIST* and *BH* on the photon fluence spectra. Note that each curve in FIG. 6.28(a) represent the difference in the photon fluence spectra "BH( ) – NIST( )" for the same photon cross section database. To examine the effect of cross sections used in our beam modeling, FIG. 6.28(a) compares the photon fluence spectral differences of the treatment head simulations performed with the two differential bremsstrahlung cross sections, BH and NIST, when the XCOM and SI photon cross section databases are used. *Firstly*, the primary electrons when undergoing bremsstrahlung production in the x-ray target are likely to lose a larger amount of their kinetic energies to bremsstrahlung radiation with the NIST option in comparison with the BH option. Irrespective of the photon cross section database, the fluence spectra with the NIST calculations are characteristically: (1) greater at photon energies above 12 MeV and (2) lower for photon energies between 1 MeV and 8 MeV.

The NIST and BH options also govern photon energies of radiative losses from secondary electrons that are produced through photon interactions as well as electron hard collisions. However, because of their lower kinetic energy in comparison to that of the primary electrons, the different bremsstrahlung photon energies produced from radiative losses of secondary electrons also slightly alter the photon fluence spectra but to a much lesser degree. *In addition*, since a larger number of higher energy photons is produced with the NIST option, the number of pair production interactions taking place in the treatment head geometry increases. This generates more positrons and consequently more 0.511 MeV annihilation photons, as the positrons eventually annihilate with orbital electrons of the medium. As demonstrated in FIG. 6.28(a), the 0.511 MeV photon peaks from the NIST(XCOM) and the NIST(SI) calculations are greater than those in the BH(XCOM) and BH(SI) calculations, respectively.

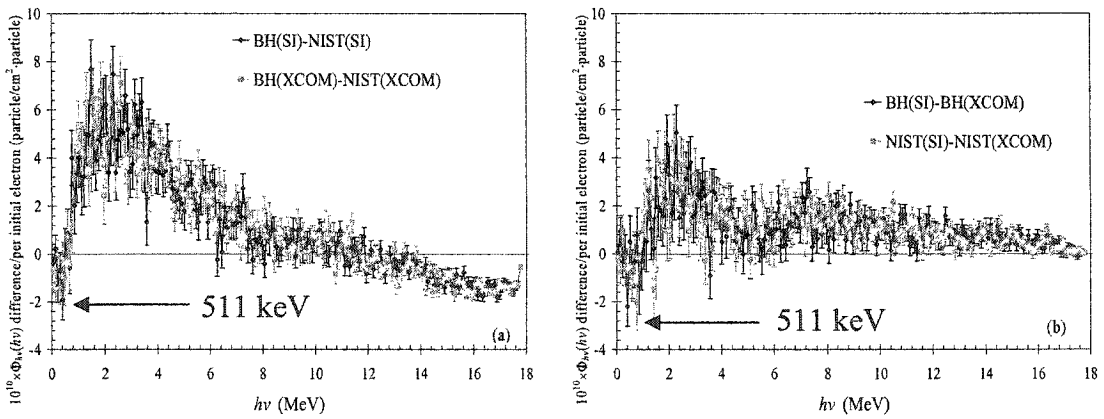


*FIG. 6.28. Comparison of the photon fluence spectra of the treatment head simulations of the 10×10 cm² field 18 MV x-ray beam.(a) The effect of the differential Bremsstrahlung cross sections NIST and BH on the photon fluence spectra. (b) The effect of the photon cross section databases XCOM and SI on the photon fluence spectra. Note that the photon fluence spectra for all calculations are shown in FIG. 6.27.*

In FIG. 6.28(b) we compare the effect of *the photon cross section databases XCOM* and *SI* on the photon fluence spectra. Note that each curve in FIG. 6.28(b) represent the difference in the photon fluence spectra "[ ](SI) – [ ](XCOM)" for the same differential Bremsstrahlung cross section option. For the 18 MV beam, a number of high energy photons that are produced from the x-ray target may undergo pair production interaction particularly in the various treatment head components with a high atomic number *Z*. The number of pair production interactions is essentially proportional to the pair production cross section.

As expected, more photons are undergoing pair production interactions in the various treatment head components when the XCOM database is used, thus reducing the number of high energy photons emerging from the treatment head and essentially producing in most situations two 0.511 MeV photons as the secondary positrons annihilate with an orbital electron. Because the angular distribution probability of a single 0.511 MeV annihilation photon is isotropic and the other photon is essentially emitted in the opposite direction, positron annihilation does not necessarily result in 0.511 MeV at the phase-space file plane. Hence, the increase of 0.511 MeV peak in the photon fluence spectrum for calculations with the XCOM photon cross section database is proportional to the

decrease in the photon fluence spectrum for photons with energies greater than 1.022 MeV.

As FIG. 6.28 demonstrates, the photon fluence spectra of the 18 MV beam is more sensitive to the differential Bremsstrahlung cross section option compared to the photon cross section database. Referring to FIGs. 6.27 and 6.28, at about 2 MeV the difference in photon fluence is about ±1.3% of the photon fluence magnitude when the Bremsstrahlung differential cross sections is changed and the BH setting always produces the higher photon fluence. By comparison, the XCOM photon cross section database increases the photon fluence by about 0.6% of that with the SI photon cross section database at 2 MeV.

*(ii)* *The scored doses along the beam central axis*

A comparison of the scored doses in water for the 10×10 $cm^2$ field 18 MV x-ray beam from the BH(SI), the BH(XCOM), the NIST(SI), and the NIST(XCOM) calculations is shown in FIG. 6.29. The scored doses were calculated with the dosrznrc/EGSnrc user code using the respective phasespace files as input sources, thus, representing the combined effect of the bremsstrahlung differential cross sections and the photon cross section databases from the treatment head as well as the phantom. The results show that beyond $z_{max}$, the scored dose in water is not sensitive to the bremsstrahlung differential cross section used (the NIST and the BH options) if the photon cross section database is

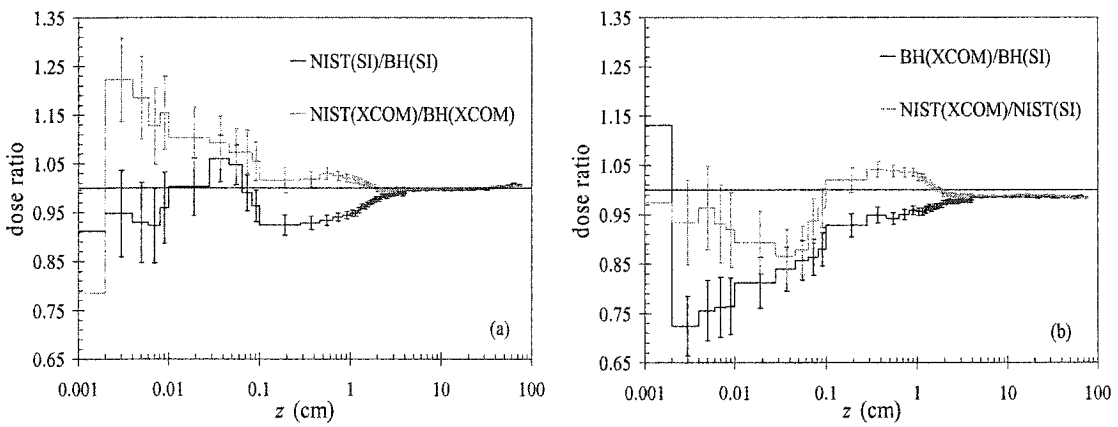


*FIG. 6.29. Comparison of the scored dose in water for the 10×10 $cm^2$ field 18 MV x-ray beam obtained using the different combinations of the BH(SI), the BH(XCOM), the NIST(SI), and the NIST(XCOM). (a) The effect of the Bremsstrahlung cross section option. (b) The effect of the photon cross section database.*

unchanged, as shown in FIG. 6.29(a). On the other hand, the scored dose in water beyond $z_{max}$ using the XCOM photon cross section database is about 2% lower than that using the SI photon cross section database [FIG. 6.29(b)] if the bremsstrahlung differential cross section is not changed.

The BH(SI) calculation produced considerably higher doses in the dose build-up region than did the NIST(SI) calculation, as shown by the BH(SI)/NIST(SI) curve in FIG. 6.29(a). For example, at a depth of 50 μm, the scored dose ratio is 1.20 ± 0.12. We attribute the decrease in the scored doses in the dose build-up region with the NIST(SI) calculation to two reasons: (*i*) the lower photon spectrum fluence for photon energies between 1 MeV and 7 MeV, as shown in FIG. 6.28, and (*ii*) the increased bremsstrahlung production in the phantom by electrons moving in the dose build-up region. Also, the scored doses in the build-up region with the NIST(XCOM) are appreciably higher than those with the NIST(SI) calculation. The scored dose at 50 μm depth in water with the NIST(SI) is 0.749 ± 0.061 of that with the NIST(XCOM) calculations, caused by the higher pair production cross sections in the XCOM databases. The higher pair production cross sections with the NIST(XCOM), in addition to altering the photon fluence spectrum, generate more positron-electron pairs in the phantom as high energy photons interact in the phantom. In the dose build-up region, the increased charge particle fluence with the NIST(XCOM) calculation also deposits a larger dose in the dose build-up region. In FIG. 6.30, the BH(SI)/NIST(XCOM) calculation is almost 1.0 in the dose build-up and it seems that the decrease in absorbed dose when the NIST option is used is off-set by the increase in the absorbed dose produced by the higher pair production XCOM database cross sections.

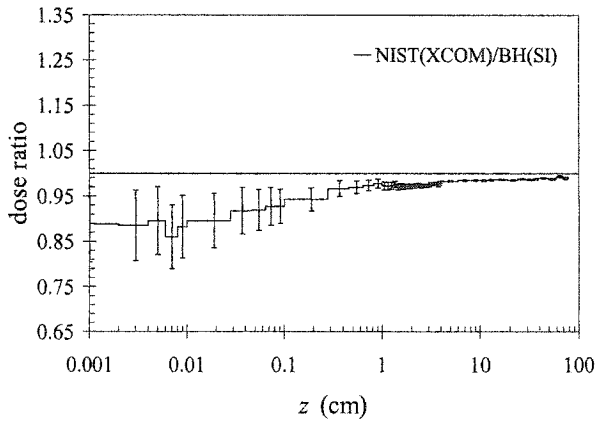


*FIG. 6.30. Comparison of the scored dose in water for the 10×10 cm² field 18 MV x-ray beam obtained using the different combinations of the BH(SI) and the NIST(XCOM).*

*(iii)* *The PDDs in water*

The *PDD*s in water for the 10×10 cm² field 18 MV x-ray beam from the NIST(XCOM), the NIST(SI), and the BH(SI) calculations are shown in FIG. 6.31. While the calculated *PDD*s from the NIST(XCOM) and the BH(SI) calculations are similar to one another in the dose build-up region, they are higher than those calculated with the NIST(SI) calculation. At the 50 μm depth in water, for example, the *PDD*s for the the BH(SI), the BH(XCOM), the NIST(SI), and the NIST(XCOM) calculations are 9.0% ± 0.5%, 7.3% ± 0.4%, 6.6% ± 0.4%, and 9.6 ± 0.5%, respectively.

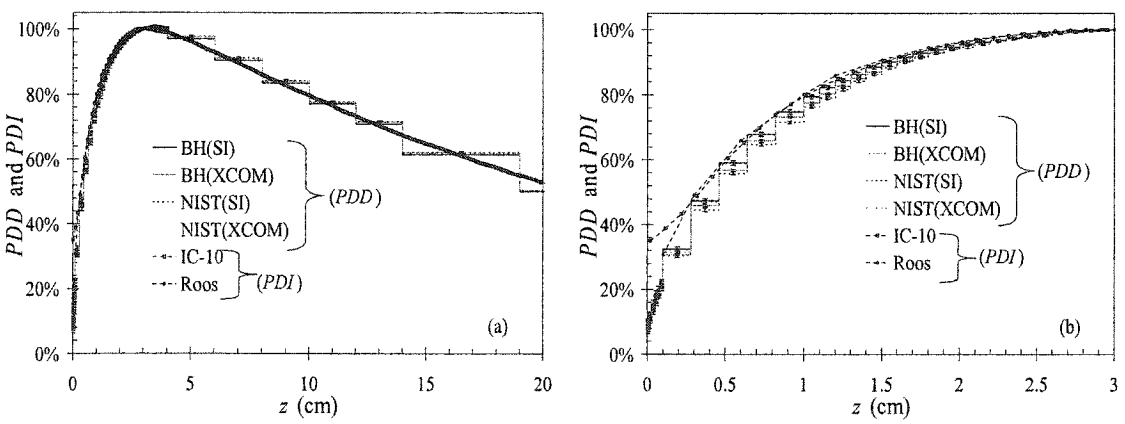


*FIG. 6.31. Comparison of the PDDs in water for of the 10×10 cm² field 18 MV x-ray beam obtained with the BH(SI), the BH(XCOM), the NIST(SI), and the NIST(XCOM) calculations.(a) the PDDs in water for depths up to 30.0 cm. (b) the PDDs in the dose buildup-region.*

*(iv)* *The PDIs at the surface for the PEEC geomtery*

For the PEEC geometry, the *PDI* in Solid Water™ for the 10×10 $cm^2$ field 18 MV x-ray beam from the the BH(SI), the BH(XCOM), the NIST(SI), and the NIST(XCOM) calculations are given in TABLE. 6.4. They are all higher than the *PDD*s in Solid Water™, but still smaller than the measured *PDI*. Thus, using the XCOM photon cross section database does not reduce the discrepancy between the MC calculations and our measurements.

Based on the results of TABLE 6.4 as well as the data in FIG. 6.31(b) in the dose build-up region, the calculations with the NIST(XCOM) and the BH(SI) produced similar *PDI*s and *PDD*s at the phantom surface yet higher than calculations with the NIST(SI) and the BH(XCOM). We speculate that the compatibility of the bremsstrahlung cross sections and the pair production cross sections used in the calculations is the source of these differences. Because the bremsstrahlung production and pair production processes are cross-symmetric, their cross sections are related to one another. In the EGSnrc MC system code, the BH option models bremsstrahlung processes for energies below 50 MeV as well as the SI pair production photon cross sections based on the first Born approximation Bethe-Heitler cross sections with an empirical cross section factor. On the other hand, the NIST option models bremsstrahlung processes according to the NIST bremsstrahlung cross section database on which the pair production cross sections in the XCOM database is based.

TABLE 6.4. THE CALCULATED *PDI* AT 50 μm IN SOLID WATER™ FOR THE PEEC GEOMETRY FOR THE 10×10 $cm^2$ FIELD 18 MV X-RAY BEAM.

| MC calculation | BH(SI) | BH(XCOM) | NIST(SI) | NIST(XCOM) |
|---|---|---|---|---|
| MC-calculated *PDI* | 10.4% ± 0.6% | 10.0% ± 0.3% | 7.6% ± 0.5 % | 10.3% ± 0.5 % |
| Measured *PDI* | 15.5% ± 0.2% | | | |

### *The effect of protons production through photonuclear reactions*

In high energy clinical photon beams, it is generally assumed that the absorbed dose in media as well as the ionization in cavity ionization chambers results only from the interaction of light charged particles, *i.e.*, electrons and positrons. In an 18 MV x-ray beam, heavier charged particles, *i.e.*, protons, alpha particles, *etc.*, may also be produced through photonuclear interactions, since the photon fluence of the beam contains photons with energies exceeding the threshold energy for photonuclear interactions to take place. The magnitudes of the nuclear cross sections for the $(h\nu,e)$ and the $(h\nu,\alpha)$ interactions are of the order of a $10^{-27}$ cm$^2$ and $10^{-28}$ cm$^2$, respectively. Both photon nuclear interactions have nuclear cross sections considerably smaller than are the atomic cross sections for the $(h\nu,e)$ interactions which are on the order of $10^{-24}$ cm$^2$. Thus, the fluence of protons and alpha particles is usually insignificant in comparison to that of electrons in an 18 MV x-ray beam. Since the collisional stopping powers $(S/\rho)_{col}$ for heavy charged particles are much larger than for light charged particles (for example, the $(S/\rho)_{col}$ in air is 222.9 MeV·cm$^2$/g for 1 MeV protons and 1.66 MeV·cm$^2$/g for 1 MeV electrons), we were concerned that a small non-negligible fluence of heavy charged particles entering the air cavity of the ionization chamber may substantially ionize the air molecules; and thus explain the discrepancy between the MC calculations and our measurements in the dose build-up region.

To evaluate the above hypothesis, we note that the MC-calculated *PDI*s for our 18 MV x-ray beam are essentially based on the dose deposition of light charged particles in the air cavity of our PEEC since, the EGSnrc MC system only considers the $(h\nu,e)$ interactions when transporting photons. Based on the results given in TABLE 6.4, the $(h\nu,e)$ interactions produce a cavity dose at $z_{max}$ about 10 times greater than at the phantom surface. On the other hand, because of their relatively small range, the fluence of heavier charged particles as a function of depth $z$ exhibits a maximum near the phantom surface and then decreases with depth in phantom as the photon beam is attenuated. If the cavity ionization at the phantom surface from the heavy charged particles is 50% of that produced through the $(h\nu,e)$ interactions, assuming (*i*) a 10 fold cavity dose increase from $(h\nu,e)$ interactions and (*ii*) neglecting the decrease in the fluence of the heavy charged

particles in the dose build-up region, the *PDI* resulting from (*hv*,*e*) interactions and heavy charged particles at the phantom surface is given by $100\times(100+50)/(1000+50)=14.3\%$, significantly higher than our MC results and closer to our measurements with the PEEC.

To test the above hypothesis, we wrote a simple FORTRAN program to calculate same basic quantities of interest in a 2 mm thick air layer positioned below a medium m, as shown in FIG. 6.32. The quantities of interest are: (1) the fraction $f$ of photon interactions in m through a particular interaction mechanism, (2) the mean energy transferred $\overline{(E_{tr})_i}$ to charged particles through interaction $i$, (3) the mean kinetic energy of the charged particles $\overline{(E_K)_i}$ through interaction $i$ per incident photon, and (4) the mean energy absorbed $\overline{(E_{ab})_i}$ per incident photon in a 2 mm thick air layer through interaction $i$. All quantities were calculated for the photon fluence spectrum of our 18 MV x-ray beam, shown in FIG. 6.27. For this calculation we only considered the (*hv*,p) interactions in addition to the photoelectric effect (PE), Rayleigh scattering, Compton scattering, pair production (PP), and triplet production (TP) interactions. All secondary particles (electrons, positrons and protons) depositing the dose in the 2 mm air layer are emitted from the medium m (the polarizing electrode) above the air layer (sensitive volume of the PEEC). The photonuclear cross section data are obtained from the IAEA-TECDOC-1178 report[31] downloadable from the following URL:
*http://iaeand.iaea.or.at/photonuclear/app-b2.pdf.*

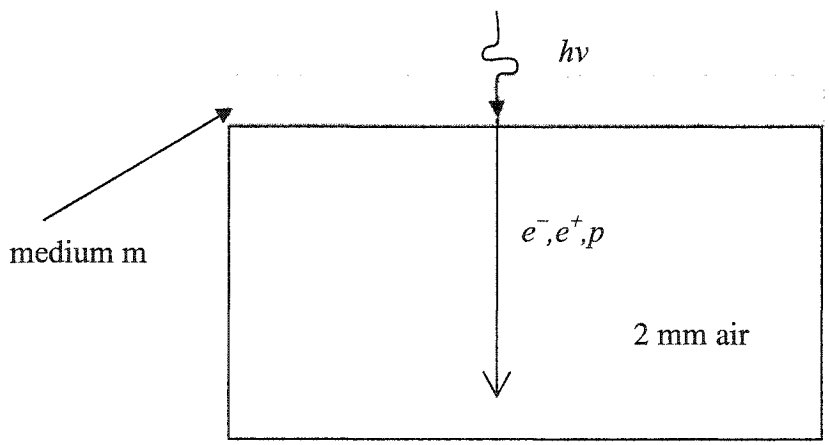


*FIG. 6.32. A simple geometry for calculating the contribution of protons to the ionization in a 2 mm air cavity.*

The atomic cross sections for the PE, Compton, Rayliegh, PP, and TP are taken from the XCOM photon cross section database and the collisional stopping powers in air for electrons and protons are from the ETRAN and PTRAN databases compiled by Berger *et al.*[32] and can be downloaded from the following URL:

*http://www.physics.nist.gov/PhysRefData/Star/Text/contents.html*

TABLEs 6.5 and 6.6 give the calculation results for $f$, $\overline{(E_{tr})_i}$, $\overline{(E_K)_i}$, and $\overline{(E_{ab})_i}$ for an aluminum and a Mylar medium above the 2 mm air layer,respectively, clearly showing that most of the absorbed dose in air is produced by the Compton electrons followed by the electron-positron pair produced in PP interactions, while the PE interaction contributes the lowest fraction to the dose. The calculations also show that the absorbed doses from the ($h\nu$,p) photonuclear reaction is comparable to that from TP but contributes to about 1% of the absorbed dose in the cavity. Since heavy charged particles produced in photonuclear reactions in our 18 MV beam cannot contribute significantly to the cavity dose, we conclude that they cannot explain the discrepancy between the MC-calculated *PDI* and our measurements.

TABLE 6.5. ESTIMATION OF THE EFFECT OF ($h\nu$,p) PHOTONUCLEAR INTERACTIONS ON THE ABSORBED DOSE IN A 2 mm THICK AIR CAVITY LOCATED BELOW AN ALUMINUM ELECTRODE. ALL QUANTITIES ARE CALCULATED FOR A PHOTON FLUENCE SPECTRUM OF AN 18 MV X-RAY BEAM.

| | PE | Rayleigh | Compton | PP | TP | ($h\nu$,p) |
|---|---|---|---|---|---|---|
| $f$(%) | 0.14 | 0.16 | 87.30 | 11.95 | 0.41 | 0.04 |
| $\overline{(E_{tr})_i}$ (MeV) | 0.41 | 0 | 2.39 | 7.48 | 7.85 | 5.47 |
| $\overline{(E_K)_i}$ (MeV) per photon | 0.0006 | 0 | 2.09 | 0.45 | 0.011 | 0.002 |
| $\overline{(E_{ab})_i}$ (eV) per photon | 1.34 | 0 | 489 | 102 | 5.18 | 6.27 |
| $\sum\overline{(E_{ab})_i}$ (eV) per photon | 603.79 | | | | | |
| $\overline{(E_{ab})_{(h\nu,p)}} / \sum\overline{(E_{ab})_i}$ | 1.04% | | | | | |

TABLE 6.6. ESTIMATION OF THE EFFECT OF ($h\nu$,p) PHOTONUCLEAR INTERACTIONS ON THE ABSORBED DOSE IN A 2 mm THICK AIR CAVITY LOCATED BELOW A MYLAR ELECTRODE. ALL QUANTITIES ARE CALCULATED FOR A PHOTON FLUENCE SPECTRUM OF AN 18 MV X-RAY BEAM.

| | PE | Rayleigh | Compton | PP | TP | (hv,p) |
|---|---|---|---|---|---|---|
| $f(\%)$ | 0.018 | 0.06 | 92.16 | 7.25 | 0.49 | 0.013 |
| $\overline{(E_{tr})_i}$ (MeV) | 0.11 | 0 | 2.53 | 7.75 | 8.08 | 2.54 |
| $\overline{(E_K)_i}$ (MeV) per photon | 0.00002 | 0 | 2.33 | 0.28 | 0.013 | 0.003 |
| $\overline{(E_{ab})_i}$ (eV) per photon | 0.22 | 0 | 516 | 62.2 | 6.12 | 4.34 |
| $\sum\overline{(E_{ab})_i}$ (eV) per photon | 588.88 | | | | | |
| $\overline{(E_{ab})}_{(h\nu,p)} / \sum\overline{(E_{ab})_i}$ | 0.7% | | | | | |

## 6.5. SUMMARY AND CONCLUSIONS

The type and design of ionization chambers must be considered in relative dosimetry in the dose build-up region for clinical high energy photon beams. Well-guarded extrapolation chambers built from same material as the medium are the ideal instrument for measuring directly the *PDD*s in the dose build-region. Using extrapolation chambers with components made of material other than the medium requires processing the measurement with additional correction factors in order to remove the effect of those inhomogeneities on the measurements. The correction factors are generally not universal and depend on many parameters, such as the beam energy, the particular treatment head design, and the measurement depth but can be determined with MC techniques.

In this chapter we investigated the MC-calculated *PDD*s in Solid Water™ at an *SSD* of 100 cm for the 10×10 $cm^2$ and the 30×30 $cm^2$ fields 6 MV x-ray beam generated by a Varian Clinac 2300 C/D treatment head by calculating the *PDI*s in Solid Water™. The MC-calculated *PDI*s matched the direct measurements with the PEEC. Moreover, the

zero-volume *PDI* at the surface obtained with the PEEC was very close to the MC-calculated dose ratios in Solid Water™ at the surface and $z_{max}$ when the PEEC inhomogeneities (the Delrin wall and the aluminized Mylar electrode) are included in the calculation geometries. Finally, the MC-calculated *PDD* in water and solid water at the surface ($\approx$ 50 μm depth) are, respectively, 12.9 ± 0.8% and 12.8% ± 0.7% for the 10×10 $cm^2$ 6 MV x-ray beam and, respectively, 22.4% ± 1.9% and 21.2% ± 3.4% for the 30×30 $cm^2$ field.

For the 18 MV x-ray beam significant discrepancies between the MC calculations and the measurements in the dose build-up region were observed. Although this was reported for large fields by previous investigators, we found that these discrepancies were also present in the 10×10 $cm^2$. We then undertook a number of experiments and theoretical studies of various possible effects which could be the source of the discrepancy. The experiments included: (*i*) comparing the measurements and calculations under a thick Solid Water™ attenuator between the treatment head and the phantom and (*ii*) evaluating the effect of contaminating neutrons produced from the 18 MV treatment head on the measurements in the dose build-up regions. The theoretical studies focused on the effect of: (*i*) the XCOM and the SI photon cross sections databases, (*ii*) the NIST and the BH options for evaluating the bremsstrahlung differential cross sections on our MC calculations, and (*iii*) the effect of heavy charged particles on our measurements. We concluded from this work that all of those possible sources cannot explain the discrepancy between the MC calculations and measurement in the dose build-up region and this discrepancy will have to be is yet to be further investigated to be understood.

# REFERENCES


1. AAPM Task Group 21 of the Radiation Therapy Committee, "A protocol for the determination of the absorbed dose from high-energy photon and electron beam," Med. Phys. **10**, 741-771 (1983).
2. Task Group 25 American Association of Physicists in Medicine, "Clinical electron beam dosimetry," Med. Phys. **18**, 73-109 (1991).
3. P. R. Almond, P. J. Biggs, B. M. Coursey, W. F. Hanson, M. Saiful Huq, R. Nath, and D. W. O. Roger, "AAPM's TG-51 protocol for clinical reference dosimetry of high- energy photon and electron beams," Med. Phys. **26**, 1847-1870. (1999).
4. International Atomic Energy Agency, Absorbed Dose Determination in External Beam Radiotherapy based on Absorbed-Dose-to-Water Standards: An international code of practice (IAEA Technical Reports Series No. 398, Vienna, 2000).
5. M. J. Berger and S. M. Seltzer, *Internal Report 82-2451*, 1982 Natl. Bur. Stand. (US).
6. P. Andreo and A. E. Nahum, "Stopping-power ratio for a photon spectrum as a weighted sum of the values for monoenergetic photon beams," Phys. Med. Biol. **30**, 429-443 (1985).
7. D. T. Burns, G. X. Ding, and D. W. O. Rogers, "R50 as a beam quality specifier for selecting stopping power-ratios and reference depths for electron dosimetry," Med. Phys. **23**, 383-388 (1996).
8. D. W. O. Rogers, A. F. Bielajew, and A. Nahum, "Ion chamber response and a wall correction factors in a Co-60 beam by Monte Carlo simulation," Phys. Med. Biol. **31**, 839-858 (1986).
9. G. X. Ding, D. W. O. Rogers, and T. R. Mackie, "Calculation of stopping-power ratios using realistic clinical electron beams," Med. Phys. **22**, 489-501 (1995).
10. D. W. O. Rogers and C. L. Yang, "Corrected relationship between $\%dd(10)_x$ and stopping-power ratios," Med. Phys. **26**, 538-540 (1999).
11. G. X. Ding, "Dose discrepancies between Monte Carlo calculation and measurement for high-energy photon beam at buildup region" *Int. Workshop on Recent Developments in Accurate Radiation Dosimetry* (Montreal, Canada, 10-13 OCT. 2001).
12. G. X. Ding, "Dose discrepancies between Monte Carlo calculations and measurements in the buildup region for a high-energy photon beam," Med. Phys. **29**, 2459-2463 (2002).
13. C. L. Hartmann-Siantar *et al*, "Description and dosimetric verification of the PEREGRINE Monte Carlo dose calculation system for photon beams incident on a water phantom," Med. Phys. **28**, 1322-1337 (2001).
14. D. W. O. Rogers, B. A. Faddegon, G. X. Ding, C. M. Ma, J. We, and T. R. Mackie, "BEAM: a Monte Carlo code to simulate radiotherapy treatments units," Med. Phys. **22**, 503-524 (1995).
15. W. R. Nelson, H. Hirayama, and D. W. O. Rogers, "The EGS4 Code System," Report SLAC-356, Stanford Linear Accelerator Center, Stanford, California, 1985.
16. I. Kawrakow, "Accurate condensed history Monte Carlo simulation of electron transport. I. EGSnrc, the new EGS4 version," Med. Phys. **27**, 485-498 (2000).
17. D. W. O. Rogers, I. Kawrakow, J. P. Seuntjens, and B. R. Walters, NRC User Codes for EGSnrc. 2001, National Research Council of Canada, Report No. PIRS-702, Ottawa.

18. G. X. Ding, C. Duzenli, and N. I. Kalach, "Are neutrons responsible for the dose discrepancies between Monte Carlo calculations and measurements in the build-up region for a high-energy photon beam?," Phys. Med. Biol. **47**, 3251–3261 (2002).

19. E. Storm and H. I. Israel, "Photon cross sections from 1 keV to 100 MeV for elements from $Z$ = 1 to $Z$ = 100," In *Nuclear Data Tables*, (Academic Press, New York, NY, 1970), Vol. A7, pp.565-681.

20. M. J. Berger, J. H. Hubbell, and S. M. Seltzer, "XCOM: Photon Cross Sections Database," NIST Standard Reference Database 8 (XGAM), National Institute of Standards and Technology, Gaithersburg, MD (1998).

21. B. Nilsson and A. Montelius, "Fluence perturbation in photon beams under nonequilibrium conditions," Med. Phys. **13**, 191-195 (1986).

22. D. E. Velkley, D. J. Manson, J. A. Purdy, and G. D. Oliver, "Build-up region of megavoltage photon radiation sources," Med. Phys. **2**, 14-19 (1975).

23. N. B. J. Tannous, W. F. Gagnon, and P. R. Almond, "Buildup region and skin-dose measurements for the Therac 6 Linear Accelerator for radiation therapy," Med. Phys. **8**, 378-381 (1981).

24. B. J. Gerbi and F. M. Khan, "Measurement of dose in buildup region using fixed-separation plane-parallel ionization chambers," Med. Phys. **17**, 17-26 (1990).

25. D. E. Mellenberg, "Determination of build-up region over-response corrections for a Markus-type chamber," Med. Phys. **17**, 1041-1044 (1990).

26. ICRU, "Stopping powers for electrons and positrons," Report 37, International Commission on Radiation Units and Measurements, Bethesda, MD. (1984).

27. H. W. Koch and J. W. Motz, "Bremsstrahlung cross-section formulas and related data." Rev. Mod. Phys. **31**, 920-955 (1959).

28. S. M. Seltzer and M. J. Berger, "Bremsstrahlung spectra from electron interactions with screened atomic nuclei and orbital electrons," Mucl. Inst. Meth. Phys. Res. B **12 12**, 95-134 (1985).

29. S. M. Seltzer and M. J. Berger, "Bremsstrahlung energy spectra from electrons with kinetic energy from 1 keV to 10 GeV incident on screened nuclei and orbital electrons of neutral atoms with Z = 1-100," Atomic Data and Nuclear Data Tables **35**, 345-418 (1986)

30. F. Hobeila, "Monte Carlo study of ion chamber response in low energy photon beams," M.S. Thesis, McGill University, 2003.

31. International Atomic Energy Agency, Handbook of photonuclear data for applications: Cross sections and spectra (IAEA Report TECDOC-1178 398, Vienna, 2000).

32. M. J. Berger, J. S. Coursey, and M. A. Zucker, "ESTAR, PSTAR, and ASTAR: Computer Programs for Calculating Stopping-Power and Range Tables for Electrons, Protons, and Helium Ions (version 1.2.2)," National Institute of Standards and Technology, Gaithersburg, MD (2000).

# Chapter 7

# CONCLUSIONS

## 7.1. SUMMARY

The main objective of the thesis work was to investigate the discrepancy between EGSnrc Monte Carlo (MC) system code calculations and cavity ionization chambers measurements in the dose build-up region for megavoltage photon beams in water and water-equivalent materials. The approach undertaken in this thesis work to validate MC calculations in the dose build-up region of megavoltage photon beams was to compare the MC-calculated percentage depth ionizations (*PDI*) and the direct measurements of a geometrically well defined cavity ionization chamber.

The principal ionization chamber used in our work was a phantom-embedded extrapolation chamber (PEEC) initially built by Zankowski for calibrating clinical photon and electron beams. The device was then modified by Deblois by motorizing the chamber piston and integrating the chamber piston control into a computer-controlled system that also controlled the electrometers as well as the high voltage power supply, thus completely automatizing data acquisition. For surface dose measurements, we replaced the PEEC original graphite/Solid Water$^{TM}$ entrance widow with an aluminized Mylar/ Delrin window, allowing measurements at 50 μm depth from the surface.

Because our validation approach hinges on knowing accurately the geometry as well as materials of the PEEC components, we conducted a comprehensive study of a number of important aspects of the PEEC which included: (*i*) the linearity and reproducibility of the piston control system, (*ii*) the accuracy in determination of the collecting electrode area, and (*iii*) evaluation of the chamber leakage current. The conclusion from the above studies was that uncertainties on the piston motion control and collecting electrode area, as well as the chamber leakage current, do not appreciably affect the measurements and are thus negligible.

We examined the polarity effect of the PEEC when irradiated with two megavoltage photon beams (6 MV and 18 MV) and two megavoltage electron beams (9 MeV and 12 MeV) and showed that voltage-dependent polarity effects are negligible and radiation induced currents, known as the Compton current, are the dominant cause of the polarity effect in the PEEC. Thus, the collected gas-ionization in the PEEC can be obtained by averaging the magnitudes of the positive and negative polarity readings, provided that the Compton current is smaller than the collected gas-ionization.

In the 6 MV and the 18 MV x-ray beams, the collecting electrode of the PEEC is the primary source of radiation-induced currents in measurements in the dose build-up region and the magnitude of the Compton current depends on the measurement depth $z$, the field size $A$, and the beam energy $hv$. The connecting cable acts as a secondary Compton current source producing a very small current that depends on the field size $A$ and the beam energy $hv$, becoming the dominant Compton current source when the measurement depth is greater than the depth of maximum dose $z_{max}$. The magnitude of the Compton current of the PEEC for a given field size $A$ and beam energy $hv$ is maximum at the surface and rapidly decreases with depth $z$ in the dose build-up region, reaching a minimum positive value at the depth of maximum dose $z_{max}$ and remains constant for $z \geq z_{max}$. We also showed that the magnitude of the Compton current of the PEEC in the dose build-up region is independent of the electrode separation $s$. Because of the significant increase of contaminating electrons originating from the treatment head in comparison to the increase in the photon fluence, the Compton current decreases with an increasing field size $A$.

In the 9 MeV and 12 MeV electron beams, for a 10×10 cm$^2$ field, the Compton current has a maximum positive value at the surface; then decreases linearly with depth and becomes negative after a depth of about one fifth of the depth $I_{50}$ (the depth at which ionization falls to 50% of maximum ionization) for the particular electron beam; then continues to decrease reaching a minimum value at approximately $0.9I_{50}$; then increases rapidly to reach a zero value at the practical electron beam range $R_p$.

To allow a theoretical study of the polarity effect in the PEEC, we developed the COMPTON/EGSnrc user code which is a modification to the standard NRC

DOSRZnrc/EGSnrc user code. The COMPTON/EGSnrc user code is optimized for scoring the charge going into and the charge exiting from a single region of interest, in addition to the absorbed dose in the full predefined geometry. Monte Carlo techniques were used to model the 10×10 $cm^2$ fields for the 6 MV, 9 MeV, and 12 MeV beams. Satisfactory results showing the variation of the Compton current with chamber depth in the phantom were obtained with the PEEC in a 10×10 $cm^2$ field 6 MV x-ray beam as well as 10×10 $cm^2$ fields 9 MeV and 12 MeV electron beams. However, the polarity correction factors $P_{pol}$ calculated by the COMPTON/EGSnrc were different from the measurements.

We then compared the MC-calculated percentage depth dose (*PDD*) in water and the *PDI* in water for an IC-10 thimble ionization chamber for the 10×10 $cm^2$ and 30×30 $cm^2$ fields 6 MV x-ray beam. While Ding and Hartmann-Sinatar reported discrepancies between the MC calculation and the measurements in the dose build-up region in water for large field size in 18 MV x-ray beams, we observed a difference between the MC-calculated *PDD* and the measured *PDI* in the dose build-up region for the 10×10 $cm^2$ and the 30×30 $cm^2$ fields for 6 MV, when following the comparison procedures used in their reports. The MC-calculated *PDD*s in Solid Water™ and the measured *PDI* with the PEEC for the 6 MV x-ray beam were also different; however, the MC-calculated and measured *PDI* were in agreement with one another. We have shown that fluence perturbations caused by inhomogeneous materials of a number of components in the PEEC (the Delrin wall and the aluminized Mylar polarizing electrode) can affect appreciably the measurements in the dose build-up region.

For the 18 MV x-ray beam, the MC-calculated *PDD* in water for the 10×10 $cm^2$ field and the measured *PDI* in water with the IC-10 ionization chamber were different in the dose build-up region. Moreover, neither the MC-calculated *PDD* in Solid Water™ nor the MC-calculated *PDI* in Solid Water™ were in agreement with the *PDI* measured with the PEEC in the dose build-up region for the 10×10 $cm^2$ field 18 MV x-ray beam. We then undertook a number of experiments and theoretical studies of various possible effects which could be the source of this discrepancy. The experiments included: (*i*) comparing the measurements and calculations under a thick Solid Water™ attenuator between the

treatment head and the phantom and (*ii*) evaluating the effect of contaminating neutrons produced from the 18 MV treatment head on the measurements in the dose build-up regions. The theoretical studies focused on the effect of: (*i*) the XCOM and the SI photon cross section databases and (*ii*) the NIST and the BH options for evaluating the bremsstrahlung differential cross sections on our MC. We also examined the effect of heavy charged particles produced in photonuclear reactions on our measurements. We showed through a simple calculation that the heavy charged particles contribution to the cavity dose at the phantom surface is only about 1% of the total cavity dose. We concluded from this work that all of these possible sources do not explain the discrepancy between the MC calculations and measurement in the dose build-up region and this discrepancy is yet to be further investigated.

## 7.2. FUTURE WORK

Although our COMPTON/EGSnrc user code as it stands today is a useful tool for understanding induced currents in ionization chambers, the user code could be developed so that it can correctly predict the polarity correction factors of cavity ionization chambers irradiated with photon and electron beams. This can be a useful tool for manufacturers in designing cavity ionization chambers, analogous to the BEAM user code in aiding in the design of treatment units. One area we suggest for the interested developers to look into is the transport of low energy electrons (below 1 keV) in conductors and insulators used in manufacturing cavity ionization chambers. Since the ionization energy for conductors (about 3 eV) is much smaller than for air (33.97 eV), the EGSnrc MC system code may underestimate the electronic fluence when evaluating the polarity currents and residual charges in collecting electrodes.

Furthermore, we have shown that the MC-calculated and the measured *PDI* for the 6 MV x-ray are different in the dose build-up region where a state of electronic disequilibrium exists. It will be fitting to also investigate the response of cavity ionization chambers near the radiation field penumbra in open fields or in situations when the cavity ionization chamber is partially irradiated with the open radiation field. This may lead to an improvement in the dosimetry in radiotherapy especially in the recently developed technique known by intensity modulated radiotherapy treatments (IMRT).

The remaining discrepancy between the MC calculation and the measurements in the dose build-up region for the 18 MV x-ray beam still requires investigation. Since the EGSnrc MC system code currently does not explicitly model triplet production interactions, it will be interesting to include these interactions in the photon transport algorithm and to evaluate their contribution to contaminating electrons in the phasespace file at an *SSD* of 100 cm.

Although our MC simulations for the 18 MV x-ray beam did not match our measurements in the dose build-up region, the response of ionization chambers or any measurements device should be taken into account when validating MC calculations in the dose build-up region for megavoltage photon beams.

# List of tables

## Chapter 1 : Introduction



## Chapter 2 : Basic radiation physics



## Chapter 4 : Experimental apparatus



## Chapter 5 : Compton current in the PEEC

## Chapter 6 : Surface dose for 6 and 18 MV x-ray beams

# List of figures

## Chapter 1 : Introduction

## Chapter 2 : Basic radiation physics

## Chapter 3 : Dose determination with ionization chambers

## Chapter 4 : Experimental apparatus

## Chapter 5 : Compton current in the PEEC

## Chapter 6 : Surface dose for 6 and 18 MV x-ray beams

# Bibliography


AAPM Task Group 21 of the Radiation Therapy Committee, "A protocol for the determination of the absorbed dose from high-energy photon and electron beam," Med. Phys. 10, 741-771 (1983) ..... [12,13,16,75,154,168,172]

AAPM Task Group 25, "Clinical electron beam dosimetry," Med. Phys. **18**, 73.109 (1991)..... [75,154,168]

F. Ajzenberg-Selove and T. Lauritsen, "Energy levels of light nuclei," Nucl. Phys. **11**, 1 (1959) ..... [37]

P. R. Almond, P. J. Biggs, B. M. Coursey, W. F. Hanson, M. Saiful Huq, R. Nath, and D. W. O. Roger, "AAPM's TG-51 protocol for clinical reference dosimetry of high- energy photon and electron beams," Med. Phys. **26**, 1847-1870. (1999) ..... [75,119,149,154,168,172,176]

H. H. Andersen, J. F. Bak, H. Knudsen, and B. R. Nielsen, "Stopping power of Al, Cu, Ag, and Au for MeV hydrogen , helium, and lithium ions. $Z_1^3$ and $Z_1$ proportional deviations from the Bethe formula," Phys. Rew. **B16**, 1929 (1977) ..... [43]

P. Andreo and A. E. Nahum, "Stopping-power ratio for a photon spectrum as a weighted sum of the values for monoenergetic photon beams," Phys. Med. Biol. **30**, 429-443 (1985)..... [168]

G. Arcovito, A. Pieramattei, G. D'Abramo, and R. Andreassi, "Dose measurement and calculation of small fields for 9 MV x-ray" Med. Phys. **12**: 779-784 (1994)..... [12]

J. C. Ashley, R. H. Ritchie, and W. Brandt, "$Z_1^3$ dependents stopping power and range contributions," Phys. Rev. **A8**, 2402 (1973) ..... [43]

J. C. Ashley, R. H. Ritchie, and W. Brandt, "$Z_1^3$ effect in the stopping power of matter for charged particles," Phys. Rev. **B5**, 2393 (1972) ..... [43]

F. H. Attix, Introduction to radiological physics and radiological dosimtry (John Wiley & Sons, New York, 1986) ..... [61]

F. H. Attix, L. De La Vergne, and V. H. Ritz, "Cavity ionization as a function of wall material," J. Res. **60**, 235 (1958) ..... [67]

H. Bethe and W. Heitler, "On the stopping of fast particles and on the creation of positive electrons," Proc. Roy. Soc. A. **146**, 83-112 (1934) ..... [28,44]

H. Bethe," Zur Theorie des Durchgangs schneller Korpuskularstrahlen durch Materie," Ann. Physik. **5**, 325 (1930) ..... [44]

M. J. Berger, J. H. Hubbell, and S. M. Seltzer, "XCOM: Photon Cross Sections Database," NIST Standard Reference Database 8 (XGAM), National Institute of Standards and Technology, Gaithersburg, MD (1998) ..... [112,169,176,207]

M. J. Berger and S. M. Seltzer, *Internal Report 82-2451*, 1982 Natl. Bur. Stand. (US). ..... [168]

M. J. Berger and S. M. Seltzer, ETRAN, Monte Carlo code system for electron and photon transport through extended media, RISC computer code, package CCC-107 (Oak Ridge National Laboratory, Oak Ridge, TN, 1973) ..... [109]

P.J. Biggs and C. C. Ling, "Electrons as the cause of the observed $d_{max}$ shift with field size in high energy photon beams" Med. Phys. **6**: 291-295 (1979). [12]

M. D. Blaufox, "Becquerel and the discovery of radioactivity: early concepts," Semin. Nucl. Med. **26**, 145-154 (1996). [1]

F. Bloch, "Zur bremsung rasch bewegter Teilchen beim Durchgang durch Materie," Ann. Phys. **16**, 285 (1933) [43]

J. W. Boag, "Ionization chambers," in *Radiation dosimetry*, edited by F. H. Attix, W. C. Roesch and Tochilin (Academic Press, Ney Yory, 1966), Vol. 2, pp. 1-72 [85]

J. W. Boag, "Distortion of the electric field in an ionization chamber due to a difference in potential between guard ring and collector," Phys. Med. Bio. **9**, 25-32 (1964a) [88,123]

J. W. Boag, "Space charge distortion of the electric field in a plane parallel ionization chamber," Phys. Med. Bio. **8**, 461-467 (1963) [88,123]

J. Böhm and U. Schneider, "Review of extrapolation chamber measurements of beta rays and low energy x-rays," Radiat. Prot. Dosim. **14**, 193-198 (1986) [80]

M. Boutillon and A.-M. Perroche, "Effect of a change in the stopping-power values on the $W$ value recommended by ICRU for electrons in dry air," Bureau International des poids et Mesures, Sèvres, Rept. CCEMRI(I)/85-8 [83]

A. L. Bradshow, "The variation of percentage depth dose and scatter factor with beam quality" Br. J. Radiol. Supplement 25 Appendix D: 125-130 (1996) [13]

W. H. Bragg, "Consequences of the corpuscular hypothesis of the gamma and x rays, and the ranges of beta rays," Phil. Mag. **20**, 385 (1910) [62]

P. R. J. Burch, "Cavity ionization chamber theory," Rad. Res. **4**, 361 (1955) [68]

T. E. Burlin, "The measurement of exposure dose for high energy radiation with cavity ionization chambers," Phys. Med. Biol. **3**, 197-206 (1959) [70]

D. T. Burns, G. X. Ding, and D. W. O. Rogers, "R50 as a beam quality specifier for selecting stopping power-ratios and reference depths for electron dosimetry," Med. Phys. **23**, 383-388 (1996) ... [168]

R. S. Caswell, J. J. Coyne, and M. L. Randolph, "Kerma factors for neutron energies below 30 MeV," Rad. Res. **83**, 217 (1966) [39]

C. Constantinou, F. H. Attix, and B. R. Paliwal, "A solid water photonm material for radiotherapy x-ray and gamma-ray beam calibrations," Med. Phys. 9, 436-441 (1982) [93]

C. Constantinou, N. F. Kember, G. Huxtable et al., "Physical measurements with a high energy-proton beam using liquid and solid tissue substitutes," Phys. Med. Biol. 25, 489-499 (1980) [93]

F. Deblois, W. Abdel-Rahman, J. P. Seuntjens, and E. B. Podgorsak, "Measurement of absorbed dose with a bone-equivalent extrapolation chamber," Med. Phys. **29**, 433-440 (2002) [59,80,93]

G. X. Ding, C. Duzenli, and N. I. Kalach, "Are neutrons responsible for the dose discrepancies between Monte Carlo calculations and measurements in the build-up region for a high-energy photon beam?," Phys. Med. Biol. **47**, 3251–3261 (2002). [169,173,203]

G. X. Ding, "Dose discrepancies between Monte Carlo calculations and measurements in the buildup region for a high-energy photon beam," Med. Phys. **29**, 2459-2463 (2002).....[168,169,173,203]

G. X. Ding, "Dose discrepancies between Monte Carlo calculation and measurement for high-energy photon beam at buildup region" *Int. Workshop on Recent Developments in Accurate Radiation Dosimetry* (Montreal, Canada, 10-13 OCT. 2001).....[18,168,169,173,203]

G. X. Ding, D. W. O. Rogers, and T. R. Mackie, "Calculation of stopping-power ratios using realistic clinical electron beams," Med. Phys. **22**, 489-501 (1995).....[168]

J. Dutreix, "From x-rays to radioactivity and radium. The discovery and works of herni Becuerel (1851-1908)," Bull. Acad. Natl. Med. **180**, 109-181 (1996).....[1]

J. Dutreix and A. Dutreix, "Henri Becquerel (1852-1908)," Med. Phys. **22**, 1869-1875 (1995).....[1]

G. G. Eichholz and J. W. Poston, *Principles of Nuclear Radiation Detection* (Ann Arbor Science, Ann Arbor, Michigan, 1979).....[53]

E. W. Emery, "Geiger-Mueller and proportional counters," in *Radiation dosimetry*, edited by F. H. Attix, W. C. Roesch, and E. Tochilin (Academic Press, New York, 1966), Vol. 2, pp. 73.121 .....[53]

R. D. Evans, *The Atomic Nucleus* ( McGraw-Hill, Malabar, Florida, 1982).....[26]

R. D. Evans, "X-ray and gamma ray interactions," In *Radiation dosimetry*, edited by F. H. Attix and W. C. Roesch (Academic Press, New York, 1968), Vol. 1, pp. 93-155.....[24]

G. Failla, "Measurement of tissue dose in terms of the same unit for all ionizing radiations," Radiology **29**, 202-215 (1937).....[80]

R. L. Ford and W. R. Nelson, "The EGS Code system – Version 3," Standard Linear Accelerator Center Report SLAC-210 (Stanford, CA, 1978).....[109,110]

S. Genna and J. S. Laghlin, "Absolute calibration of cobalt 60 gamma-ray beam," Radiology **65**, 394-405 (1955).....[80]

B. J. Gerbi and F. M. Khan, "Measurement of dose in buildup region using fixed-separation plane-parallel ionization chambers," Med. Phys. 17, 17-26 (1990).....[173,175]

B. J. Gerbi and F. M. Khan, "The polarity effect for commercially available plane-parallel ionization chambers," Med. Phys. **14**, 210-215 (1987).....[123]

O. Glasser and W. C. Röntgen, *Dr. W. C. Röntgen* (C. C. Thomas, Springfield, I11., 1945).....[1]

O. Glasser, J. C. Tucker, and M. Boveri, Wilhelm Conrad Röntgen and the early history of the Roentgen rays (Bale & Danielsson, London, 1933).....[1]

M. D. Goldberg, V. M. Way, and J. R. Stehn, *Angular distributions in neutron-induced reactions* Brookhaven Natl. Lab. Rept. BNL-400 2nd ed., Vol. I (1962) .....[37]

L. H. Gray, "Absorption of penetrating radiation," Proc. Roy. Soc. A. (London) **122**, 647 (1929).....[62]

J. R. Greening, "A contribution to the theory of ionization chamber measurement at low pressures," Brit. J. Radiol. **27**, 163-170 (1954).....[125]

D. Harder, "Einfluss der Vielfachstreuung von Elektronen auf die Ionization in gas gefüllten Hohlräumen," Biophysik **5**, 157 (1968) ..... [74]

C. L. Hartmann-Siantar *et al*, "Description and dosimetric verification of the PEREGRINE Monte Carlo dose calculation system for photon beams incident on a water phantom," Med. Phys. **28**, 1322-1337 (2001) ..... [18,168,169,173,203]]

J. M. Havercroft and S. C. Klevenhagen, "Polarity effect of plane-parallel ionization chambers in electron radiation," Phys. Med. Biol. **39**, 299-304 (1994) ..... [123]

A. K. Ho and B. R. Paliwal," Stopping-power and mass energy-absorption coefficient ratios for Solid Water," Med. Phys. 13, 403-404 (1986) ..... [93]

A. K. Ho, B. R. Paliwal, and F. H. Attix, "Charge storage in electron-irradiation phantom materials," Med. Phys. 13, 99-100 (1986) ..... [93]

F. Hobeila, "Monte Carlo study of ion chamber response in low energy photon beams," M.S. Thesis, McGill University, 2003. ..... [207]

J. H. Hubbell, "Photon mass attenuation and energy absorption coefficients from 1 keV to 20 MeV," Int. J. Appl. Rad. Isot. **33**, 1269-1290 (1982) ..... [33]

J. H. Hubbell, H. A. Gimm, and I. Øverbø, "Pair, triplet and total cross sections for 1 MeV-100 GeV photons in elements $Z$ = 1-100," J. Phys. Chem. Ref. Data **9**, 1023-1147 (1980) ..... [33]

J. H. Hubbell, W. J. Veigele, E. A. Briggs et al., "Atomic form factors, incoherent scattering functions and photon scattering cross section," J. Phys. Chem. Ref. Data **4**, 471-538 (1975) ..... [30]

J. H. Hubbell, "Photon Cross Sections, Attenuation Coefficients and Energy Absorption Coefficients from 10 keV to 100 GeV," Report NSRDS-NBS29, U.S. National Bureau of Standards (1969) ..... [24]

D. J Hughes, B. A. Magurno, and M. K. Brussel, *Neutron cross sections* Brookhaven Natl. Lab. Rept. BNL-325 Suppl. 1 2$^{nd}$ ed. (1960) ..... [37]

D. J. Hughes and R. B. Schwatrz, *Neutron cross sections* Brookhaven Natl. Lab. Rept. BNL-325 2$^{nd}$ ed. (1958) ..... [37]

International Atomic Energy Agency, Absorbed Dose Determination in External Beam Radiotherapy based on Absorbed-Dose-to-Water Standards: An international code of practice (IAEA Technical Reports Series No. 398, Vienna, 2000) ..... [75,119,141,145,154,168,172,176]

International Atomic Energy Agency, *Absorbed dose determination in photon and electron beams: An international code of practice* (IAEA Technical Reports Series No. 277, Vienna, 1987) ..... [753]

Institute of Physics & Engineering in Medicine & Biology, "The IPEMB code of practice for the determination of absorbed dose for x-rays below 300 kV generating potential (0.035 mm AL-4mm Cu HVL; 10-300 kV generating potential). Institution of Physics and Engineering in Medicine and Biology," Phys. Med. Biol. **41**, 2605-2625 (1996) ..... [75]

Institute of Physics & Engineering in Medicine & Biology, "The IPEMB code of practice for electron dosimetry for radiotherapy beams of initial energy from 2 to 50 MeV based on air-kerma calibration. Institution of Physics and Engineering in Medicine and Biology," Phys. Med. Biol. **41**, 2557-2603 (1996) ..... [75]

ICRP, "1990 Recommendations of the ICRP," Publication 60, International Commission on Radiological Protection, Pergamon Press, Oxford and New York (1991) ..... [6]

ICRU, "Fundamental quantities and units for ionizing radiation," Report 60, International Commission on Radiation Units and Measurements, Bethesda, MD. (1998) ..... [5]

ICRU, "Quantities and units in radiation protection dosimetry," Report 51, International Commission on Radiation Units and Measurements, Bethesda, MD. (1991) ..... [5,6]

ICRU, "Stopping powers for electrons and positrons," Report 37, International Commission on Radiation Units and Measurements, Bethesda, MD. (1984) .....[43,44,45,47,113,175,192]

ICRU, "Radiation dosimetry: Electrons with energies between 1 and 50 MeV," Report 35, International Commission on Radiation Units and Measurements, Washington, D. C. (1972) ..... [74]

ICRU, "Radiation quantities and units," Report 33, International Commission on Radiation Units and Measurements, Washington, DC. (1980)..... [5]

ICRU, "Average energy required to produce an ion pair," Report 31, International Commission on Radiation Units and Measurements, Washington, D. C. (1979b)..... [83]

ICRU, "Determination of absorbed dose in a patient irradiated by beams of X or gamma rays in radiotherapy procedures," ICRU Report 24, International Commission on Radiation Units and Measurements, Washington, D. C. (1976) ..... [75]

ICRU, "Radiation quantities and units," Report 19, International Commission on Radiation Units and Measurements, Bethesda, MD (1971) ..... [21,82]

ICRU, "Neutron fluence, neutron spectra and kerma," Report 13, International Commission on Radiation Units and Measurements, Washington, D.C. (1969)..... [39, 40]

K. Johansson, L. Mattson, L. Lindborg, and H. Svensson, "Absorbed-dose determination with ionization chambers in electron and photon beams having energies between 1 and 50 MeV," Report IAEA-SM 222/35, International Atomic Energy Agency, Vienna (1977) ..... [74]

H. E. Johns, N. Aspin, and R. G. Baker, Radiat. Res. **9**, 573 (1958)..... [126,142]

I. Kawrakow and D. W. O. Rogers, "The EGSnrc Code System: Monte Carlo simulations of electron and photon transport," Technical Report PIRS-701, National Research Council of Canada, Ottawa, Canada (2000) .....[18,109,110,115,132]

I. Kawrakow, "Accurate condensed history Monte Carlo simulation of electron transport. I. EGSnrc, the new EGS4 version," Med. Phys. **27**, 485-498 (2000)..... [168]

L. A. W. Kemp and B. Barber, "the construction and use of a guarded-field cavity ionization chamber for the measurement of supervoltage radiation," Phys. Med. Biol. **3**, 149-160 (1963) ..... [123]

N. D. Kessaris, "Penetration of high energy electrons in water," Phys. Rev. **145**, 164-174 (1966)..... [128]

O. Klein and Y. Nishina, "Über die streuung von Strahlung durch freie Elktronen nach der neuen relativistischen Quantendynamik von Dirac," Physik **52**, 853-868 (1929) ..... [26]

C. Klevenhagen, "Determination of absorbed dose in high-energy electron and photon radiations by means of an uncalibrated ionization chamber," Phys. Med. Biol. **36**, 239-253 (1991) ..... [80]

H. W. Koch and J. W. Motz, "Bremsstrahlung cross-section formulas and related data." Rev. Mod. Phys. **31**, 920-955 (1959). ..... [176,192

K. S. Krane, *Introductory Nuclear Physics* (John Wiley & Sons, Toronto, Canada, 1988) ..... [53]

A. C. Lapsley, "Effect of space charge on saturation properties of ionization chambers," Rev. Sci. Instr. **24**, 602 (1953) ..... [88,123]

G. Lempert, R. Nath, and R. J. Schulz, "Fraction of ionization from electrons arising in the wall of an ionization chamber," Med. Phys. **10**, 1-3 (1983) ..... [73]

J. Lindhard, "The Barkas effect, or $Z_1^3 - Z_1^4$ corrections to stopping of swift charged particles," Nucl. Instrum. Meth. **132**, 1 (1976) ..... [43]

M. S. Livingston and H. A. Bethe, "Nuclear physics," Rev. Mod. Phys. **9**, 282 (1937) ..... [43]

R. Loevinger, "Extrapolation chamber for measurement of beta sources," Sci. Instr. **24**, 907-914 (1953) ..... [80]

D. J. Manson, D. Velkley, J. A. Purdy et al., "Measurements of surface dose using build-up curves obtained with an extrapolation chamber," Radiology **15**, 473.474 (1975) ..... [80]

W. H. McMaster, N. K. Del Grande, J. R. Mallett, and J. H. Hubbell, "Compilation of x-ray cross sections," Report UCRL-50174, Section 11, Rev.1, Univ. of Calif., Livermore, CA (1969) ..... [33]

D. E. Mellenberg, "Determination of build-up region over-response corrections for a Markus- type chamber", Med. Phys. **17**, 1041-1044 (1990) ..... [81,173]

A. E. Nahum, "Extension of the Spencer-Attix Cavity Theory to 3 media situation for Electron beams," in *Dosimetry in Radiotherapy*, edited by IAEA (IAEA, Vienna, 1988), Vol. 1, pp. 87-115 ..... [69]

NCRP, "Conceptual Basis for Calculations of Absorbed-Dose Distributions," Report 108, National Council on Radiation Protection and Measurements, Bethesda, MD (1991). ..... [6]

W. R. Nelson, H. Hirayama, and D. W. O. Rogers, "The EGS4 Code system," Stanford Linear Accelerator Center Report SLAC-256 (Stanford, CA, 1985) ..... [109,110,168]

M. T. Niatel, "Etude experimentale de l'influence de la vapeur d'eau sur l'ionisation produite dans l'air," Comptes Rendus Acad. Sci. Paris 268, 1650 (1969) ..... [83]

B. Nilsson and A. Montelius, "Fluence perturbation in photon beams under nonequilibrium conditions," Med. Phys. **13**, 191-195 (1986) ..... [81,171,173,174,175,186]

A. Nisbet and D. I. Thwaites, "Polarity and ion recombination correction factors for ionization chambers employed in electron beam dosimetry," Phys. Med. Biol. **43**, 435-443 (1998) ..... [123]

C. R. Ramsey, K. M. Spencer, and A. L. Oliver, "Ionization chamber, electrometer, linear accelerator, field size, and energy dependence of the polarity effect in electron dosimetry," Med. Phys. **26**, 214-219 (1999) ..... [123]

C. S. Reft, "Output calibration in solid water for high energy photon beams," Med. Phys. 16, 299-301 (1989) ..... [93]

R. H. Ritchie and W. Brandt, "Projectile charge dependence of stopping powers," Phys. Rev. **A17**, 2102 (1978) ..... [43]

F. Rohrlich and B. C. Carlson, "Positron-electron differences in energy loss and multiple scattering," Phys. Rev. **93**, 38 (1953) ..... [44]

D. W. O. Rogers, I. Kawrakow, J. P. Seuntjens, and B. R. Walters, NRC User Codes for EGSnrc. 2001, National Research Council of Canada, Report No. PIRS-702, Ottawa. ..... [168]

D. W. O. Rogers and C. L. Yang, "Corrected relationship between %dd(10)$_x$ and stopping-power ratios," Med. Phys. **26**, 538-540 (1999). ..... [168]

D. W. O. Rogers, B. A. Faddegon, G. X. Ding, C. M. Ma, J. We, and T. R. Mackie, "BEAM: a Monte Carlo code to simulate radiotherapy treatments units," Med. Phys. **22**, 503-524 (1995)..... [168]

D. W. O. Rogers, A. F. Bielajew, and A. Nahum, "Ion chamber response and a wall correction factors in a Co-60 beam by Monte Carlo simulation," Phys. Med. Biol. **31**, 839-858 (1986). ..... [168]

W. C. Röntgen, A, Thomas, I. Isherwood et al., *The Invisible Light: 100 years of medical radiology* (Blackwell Science Ltd, Oxford; Cambridge, Mass., 1995)..... [1]

S. M. Seltzer and M. J. Berger, "Bremsstrahlung energy spectra from electrons with kinetic energy from 1 keV to 10 GeV incident on screened nuclei and orbital electrons of neutral atoms with Z = 1-100," Atomic Data and Nuclear Data Tables **35**, 345-418 (1986). ..... [192]

S. M. Seltzer and M. J. Berger, "Bremsstrahlung spectra from electron interactions with screened atomic nuclei and orbital electrons," Mucl. Inst. Meth. Phys. Res. B **12 12**, 95-134 (1985) ..... [192]

K. E. Sixel, and E. B. Podgorsak, "Build-up region and depth of dose maximum of megavoltage x-ray beams" Med. Phys. **21**: 411-416 (1994)..... [12]

K. E. Sixel, "Measurements and Monte Carlo simulations of x-ray beams in radiosurgery," Ph.D. Thesis, McGill University, 1993 ..... [147]

C. G. Soares, "Calibration of ophthalmic applicators at NIST: a revised approach," Med. Phys. **18**, 787-793 (1991)..... [80]

L. V. Spencer and F. H. Attix, "A theory of cavity ionization," Radiat. Res. **3**, 239-254 (1955) ..... [62,66]

J. R. Stehn, M. D. Goldberg, B. A. Magurno, and R. Wiener-Chasman, *Neutron cross sections* Brookhaven Natl. Lab. Rept. BNL-325 Suppl. 2. Vol. I (1964)..... [37]

E. Storm and H. I. Israel, "Photon cross sections from 1 keV to 100 MeV for elements from Z = 1 to Z = 100," In Nuclear Data Tables, (Academic Press, New York, NY, 1970), Vol. A7, pp.565-681 ..... [33,1112,169,207]

N. B. J. Tannous, W. F. Gagnon, and P. R. Almond, "Buildup region and skin-dose measurements for Therac 6 linear accelerator for radiation therapy," Med. Phys. **8** 378-381 (1981) ..... [81,173]

E. A. Uehling, "Penetration of heavy charged particles in matter," Annual Rev. Nucl. Sci. **4**, 315 (1954) ..... [44]

J. Van Dyk and J. C. F. MacDonald, "Penetration of high energy electrons in water," Phys. Med. Biol. **17**, 52-55 (1972)..... [126]

D. E. Velkley, D. J. Manson, J. A. Purdy, and G. D. Oliver, "Build-up region of megavoltage photon radiation sources," Med. Phys. **2**, 14-19 (1975)..... [81,173,175,186]

B. R. B. Walters, I. Kawrakow, and D. W. O. Rogers, "History by history statistical estimators in the BEAM code system," Med. Phys. 29, 2745-2752 (2002) ..... [117,132]

F. H. Williams, The Roentgen rays in medicine and surgery: as an aid in diagnosis and as a therapeutic agent designed for the use of practitioners and students (Macmillan, New York, 1901). ..... [1]

J. A. Williams and S. K. Agarwal, "Energy-dependent polarity correction factors for four commercial ionization chambers used in electron dosimetry," Med. Phys. **24**, 785-790 (1997) ..... [123]

C. W. Wilson, "Observation of the ionization produced by radium gamma rays in air-walled ionization chambers at low gas pressures," Brit. J. Radiol. **27**, 159-162 (1954) ..... [125]

H. Wyckoff and F. H. Attix, "Design of free-air ionization chambers," Handbook 64, National Bureau of Standards, Washington, D.C.,(1957) ..... [59]

C. Zankowski and E. B. Podgorsak, "Determination of saturation charge and collection efficiency for ionization chambers in continuous beams," Med. Phys. 25, 908-915 (1998) ..... [93]

C. Zankowski, S. Vatnitsky, J. Siebers et al., "Proton beam output measurement with an extrapolation chamber," Med. Dosim. 23, 288-291 (1998) ..... [93]

C. Zankowski, "Calibration of photon and electron beams with an extrapolation chamber," Ph.D. Thesis, McGill University, 1997 ..... [93,158]

C. Zankowski and E. B. Podgorsak, "Calibration of photon and electron beams with an extrapolation chamber," Med. Phys. 24, 497-503 (1997) ..... [59,80,93]

C. Zankowski and E. B. Podgorsak, "Ionization gradient chamber in absolute photon and electron dosimetry," Radiology and Oncology (Slovenia) 30, 138-141 (1996) ..... [93]